Water and Volatile Element Accretion to the Inner Planets

by

Adam Robert Sarafian

B.Sc., University of Georgia, 2009

M.Sc., University of Georgia, 2012

Submitted in partial fulfillment of the requirements for the degree of
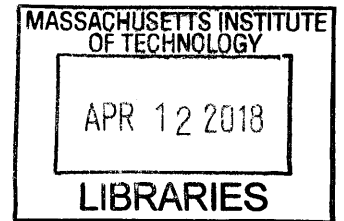Doctor of Philosophy
at the
MASSACHUSETTS INSTITUTE OF TECHNOLOGY
and the
WOODS HOLE OCEANOGRAPHIC INSTITUTION
February 2018

Signature of Author **Signature redacted**
Joint Program in Oceanography/Applied Ocean Science and Engineering
Massachusetts Institute of Technology and Woods Hole Oceanographic Institution
November 3, 2017

Certified by **Signature redacted**
Sune G. Nielsen
Associate Scientist, Department of Geology and Geophysics, WHOI
Thesis Supervisor

Certified by **Signature redacted**
Horst R. Marschall
Professor, Department of Earth Sciences, University of Frankfurt
Thesis Supervisor

Accepted by **Signature redacted**
Mark D. Behn
Senior Scientist, Department of Geology and Geophysics, WHOI
Chairman, Joint Committee for Marine Geology and Geophysics

1

Water and Volatile Element Accretion to the Inner Planets

by

Adam Robert Sarafian

Submitted to the Department of Marine Geology and Geophysics,
MIT/WHOI Joint Program in Oceanography/Applied Ocean Science and Engineering
on November 3, 2017 in partial fulfillment of the requirements
for the degree of Doctor of Philosophy

Abstract

This thesis investigates the timing and source(s) of water and volatile elements to the inner solar system by studying the basaltic meteorites angrites and eucrites. In chapters 2 and 3, I present the results from angrite meteorites. Chapter 2 examines the water and volatile element content of the angrite parent body and I suggest that some water and other volatile elements accreted to inner solar system bodies by ~2 Myr after the start of the solar system. Chapter 3 examines the D/H of this water and I suggest it is derived from carbonaceous chondrites. Chapter 4, 5, 6, and 7 addresses eucrite meteorites. Chapter 4 expands on existing models to explain geochemical trends observed in eucrites. In Chapter 5, I examine the water and F content of the eucrite parent body, 4 Vesta. In chapter 6, I determine the source of water for 4 Vesta and determine that carbonaceous chondrites delivered water to this body. Chapter 7 discusses degassing on 4 Vesta while it was forming.

Thesis Supervisors:
Sune G. Nielsen
Title: Associate Scientist, Department of Geology and Geophysics, WHOI
Horst R. Marschall
Title: Professor, Department of Earth Sciences, University of Frankfurt

Acknowledgments

First, I must thank my advisors Horst and Sune. They have always been an e-mail, call, text, or roll-of-the-chair away. Without these two believing me, supporting me from the beginning, and allowing me to weigh them down, I would not have been able to start this venture. In addition, Kevin Righter and Erik Hauri opened their hearts and labs to an unknown punk student studying planetary science at an oceanographic institution. This thesis could not and would not have happened without the above four people. Other people who have been extremely helpful are Evel Berger, Anne Peslier, Francis "the" McCubbin(ator), Duck Mittlefehldt, Tom Lapen, Martin Whitehouse, Timm John, Juia Roszjar, Ben Weiss, Tim Grove, Brian Monteleone, Veronique Le Roux, Freider Klein, Christian Vollmer and others I likely didn't mention, opened their office doors and email inboxes to guide me and allow me to follow my passion. Finally, I thank the 15 co-authors of the manuscript-chapters in this thesis without you, I would have had to actually write the bulk of this thesis.

To my friends, who will remain nameless, I thank you for your encouragement, distractions, and getting me into unquantifiable amounts of trouble.

My family, including Mom, Dad, brother and sister have also been instrumental in keeping me sane (or making me go insane) in this experience.

Most of all, I cannot thank Emily Sarafian enough for dragging me, usually kicking and screaming, away from science to explore "anywhere off cape". Most of the quantitative work in this thesis could not have happened without you. Finally, Adeline (aka D-line, Dolorous Addie, Bug, Addington, Booger, Monster), you have provided me with the time of my life. I appreciate you spending your afternoons with me. You make doing all of this worth it. Thomas, I look forward to changing your poopie diapers, also, keep kicking the crap out of Mom.

Table of Contents

9

Chapter 1

Introduction: Thesis objective and summary of chapters

Where did Earth's water come from and when did it get here? I don't know the full answer to that question, but this thesis attempts to address this long standing question. Since the mid 1900s when it has been debated as to when Earth accreted water. It was first suggested that Earth and the rest of the inner solar system must have received its current water relatively late, after planet formation, because the high energies associated with planetary accretion. Another, far less likely option is "cold accretion", by which planets accrete at low enough temperatures for volatile elements, like H, to remain.

Using the chemical composition of extremely old rocks and isotope geochemistry makes determining where our water and other volatiles elements derived from is a slightly simpler task than determining when these elements got here. Since the 1980's theorists and solar system observationalists suggested that Earth's (and likely the rest of the inner solar system's) water was derived from comets, dirty ice balls. In the 2000s, after observations of several comets showed that the H-isotope composition of most comets did not match the H-isotope compositions of Earth's water, it was found that the H-isotope composition of Earth matches carbonaceous chondrites, a type of wet meteorite.

This thesis focuses on when water and other volatile elements, F, P, S and Cl, arrived to the inner solar system, including Earth. Here, I employ advanced analytical techniques to help constrain the timing of hydrous accretion to the inner solar system and pinpoint the source these volatile element I use the light isotopes of hydrogen and chlorine, as well as the concentrations of H, F, P, S, Cl to elucidate accretion events in the early inner solar system. In conjunction with the volatile isotopes/element concentrations, I also used major element concentrations and radiometric dating to constrain the timing of wet accretion to the inner solar system.

Chapter 2 and 3 focuses on the oldest and best-preserved basaltic meteorites, angrites. These meteorites are also classified as ultra-volatile element depleted. In order to understand the

volatile elements I employed ion probe techniques to measure D/H and volatile element concentrations of olivine and basaltic glass. Using volatile element concentrations I was able to determine that an accretion event occurred earlier than 2.5 million years after the start of the solar system and using D/H I was able to show carbonaceous chondrites accounted for 99% of all water for the inner solar system.

In chapter 4, I turn my attention to eucrite meteorites. Eucrites can be separated into two distinct groups based on geochemistry, the main group and the Stannern trend. In this chapter I add to and modify existing models, which describe the genesis of the main group and Stannern trend. I argue that Stannern trend eucrites formed from contamination of a main group magma with a low degree melt.

In chapter 5, I address the water content of 4 Vesta by studying rare *unequilibrated* eucrite meteorites. These unique samples have no evidence of thermal alteration and preserve the best record to determine the water and volatile element content of 4 Vesta. In this chapter I provide a minimum estimate for the water and F content of 4 Vesta.

In chapter 6, I measure the hydrogen isotope composition of eucrite meteorites and infer the hydrogen isotope composition of 4 Vesta. This contribution was the first hydrogen isotope study of an asteroidal basalt and opened the field for the entire thesis.

In chapter 7, I focus on the Cl isotope composition of eucrite meteorites. This chapter provides urges authors to use caution when interpreting volatile element data because volatile elements often degas. I show that 4 Vesta likely had a magma ocean that was continually degassing Cl and H throughout its history.

Chapter 2

Angrite meteorites record the onset and flux of water to the inner solar system

2.1 Abstract

Earth and the other rocky bodies that make up the inner solar system are systematically depleted in hydrogen (H) and other cosmochemically volatile elements (e.g., carbon (C), fluorine (F), chlorine (Cl), and thallium (Tl)) relative to primitive undifferentiated meteorites known as carbonaceous chondrites. If we are to understand how and when Earth gained its life-essential elements, it is critical to determine the timing, flux, and nature of the delivery of condensed volatiles into the presumed hot and dry early inner solar system. Here we present evidence preserved in ancient basaltic angrite meteorites for an addition of volatiles to the hot and dry inner solar system within the first two million years of solar system history. Our data demonstrate that the angrite parent body was enriched in highly volatile elements (H, C, F, and Tl) relative to those predicted on the basis of the angrite parent body's overall volatile depletion trend (e.g., H is enriched by up to a factor of 10^6).This relative enrichment is best explained by mixing of extremely volatile-depleted material, located well inside the snow line, with volatile-rich material derived from outside the snow line.

2.2 Introduction

To better understand when Earth – and, potentially, the other rocky planets – became habitable it is necessary to establish a time dependent flux of volatiles to inner solar system bodies. The Earth's total volatile contents are debated (*1-3*), and any record of the timing of volatile addition has been erased by ongoing geologic processes. On Mars, geologic processing that may have erased the record of early H_2O accretion history is much less extensive than on Earth, but Martian meteorites with ages sufficiently old to study volatile accretion in the early solar system have yet to be found (*4*). The H_2O content of the Moon has also been examined (*5, 6*), but its relatively young age (*7-10*) limits the time window of volatile addition that can be investigated with lunar rocks to younger than 4450 Ma. Hence, if we are to determine how much, if any, H_2O and other volatiles entered the inner early solar system before the Moon accreted, ancient rocks with simple geologic histories need to be studied.

Angrites are the oldest basaltic meteorites known and likely originate from the first generation of differentiated bodies in the solar system (*11, 12*). Angrites can be divided into two groups, volcanic (basaltic) and plutonic (gabbroic). Volcanic angrites are unique among other basaltic meteorites because they contain vesicles and show little-to-no evidence of post-crystallization alteration (*11, 13*), although some suggest angrites represent metasomatized nebular condensates (*14, 15*). The volcanic quenched angrites, D'Orbigny and Sahara 99555 have concordant magmatic crystallization ages of 4563.6 ± 0.2 Ma with respect to ^{207}Pb-^{206}Pb (*16-20*). Quenched angrites also have relatively simple and rapid cooling histories (*11*), thus lowering the possibility that inter–mineral diffusion may have taken place during or after crystallization. Importantly, angrites contain the primary crystallizing phase olivine. Olivine is a well-studied and robust mineral that can preserve a record of primitive magmatic H content as well as other volatile species (e.g., C, F, and Cl) (*21-23*), as long as post crystallization diffusion did not alter or reset the original concentrations and degassing did not occur prior to olivine crystallization.

Here we report the first measurements of H, C, F, Cl, and S in olivine from two angrites, D'Orbigny and Sahara 99555. We also report bulk meteorite concentration data for the volatile

metal Tl in D'Orbigny. We calculate the composition of the angrite parent body (APB) mantle by combining our new data with literature values for other elements. We show that the APB is extremely depleted in moderately volatile elements, the highly volatile elements are relatively enriched.

2.3 Samples

D'Orbigny is a coarse grained (major minerals ca. 100 μm –1000 μm in the long direction) volcanic rock comprised of highly zoned calcic olivine, zoned subsilicic aluminian-ferrian diopside, and Ca-rich plagioclase, with minor kirschsteinite/monticellite, spinel, troilite, whitlockite, baddeleyite, and an unspecified silica-phosphate (*11, 24*). Sahara 99555 is a fine-grained basaltic rock (major minerals ca. 50 μm – 200 μm in the long direction) that contains intergrowths of zoned olivine and anorthite, which could indicate quench growth, as well as subsilicic aluminian-ferrian diopside, minor phases include spinel, troilite, and silica-phosphate.

2.3.1 Late stage features in angrites

Some have suggested that angrites represent heavily metasomatized materials (*14, 15*) instead of pristine magmatic rocks (*11, 13*). For example, Varela et al. (2003) used observations of interstitial regions of D'Orbigny to suggest a non-magmatic origin of D'Orbigny, while Mittlefehldt et al. (2002) used core-rim composition transects to demonstrate these rocks crystallized from a melt. During the late stages of crystallization angrites likely exsolved a fluid phase, which resulted in vesiculation (*25*). The late stage fluid phase, which was rich in C (*25*) and other incompatible elements, could have metasomatized the outermost rims of the major silicate crystals in angrites. If the mesostasis crystallized after fluid exsolution, then the mesostasis was likely severely affected by the fluid. Petrologic evidence, e.g., vesicles, and non-igneous textures (Fig. A1) clearly points to fluid exsolution at some point. Therefore, for this study we avoided all olivine that had evidence of fluid interaction and only analyzed olivine smooth zoning patterns in Mg-Fe (Fig A2).

2.4 Analytical methods

2.4.1 Secondary ion mass spectrometry

Meteorite chips were polished with a water-based diamond suspension to 0.3 μm, followed by colloidal silica. The polished chips of D'Orbigny and Sahara 99555 were then pressed into a single indium metal sample holder to reduce backgrounds of H, C, and Cl. Our indium metal sample mount was cleaned with distilled water and dried in a vacuum oven for a week at 50°C. Prior to analysis, the sample was taken out of the vacuum oven and gold coated. After gold coating, the sample was placed into the airlock on the Cameca 6f ion probe at the Carnegie Institute of Washington, Department of Terrestrial Magnetism and held under a vacuum of < 6 x 10^{-6} Pa for > 12 hrs (~5 x 10^{-8} Torr). The sample was then transferred to the analysis chamber and analyzed after the analysis chamber achieved a vacuum better than 1 x 10^{-7} Pa (~5 x 10^{-10} Torr). Three external reference materials were also affixed to the angrite indium mount: 1) a low water reference material (Suprasil 3002 pure SiO_2 glass, 1 μg/g H_2O, purchased from Heraeus Quarzglas, Switzerland) to monitor machine background stability, 2) a mid-water concentration reference material (Herasil 102 pure SiO_2 glass, 55 μg/g H_2O, purchased from Heraeus) to examine reproducibility close to angritic olivine H_2O, F and Cl concentrations, and 3) a high H_2O reference material (ALV 519-4-1 mid ocean ridge basalt glass, 1700 μg/g H_2O) to correct for instrumental drift throughout the session.

We used well-established methods to measure volatiles in olivine (*21*). Briefly, a focused 15 nA Cs^+ primary beam was rastered to produce a 50 x 50 μm^2 pre-sputter crater. During our analysis we used a 20 x 20 μm^2 raster and a circular field aperture to decrease the measured area to the central 10 μm of the sputter crater (78 μm^2). Mass resolving power (MRP) was nominally 4500, sufficient to separate ^{17}O from $^{16}O^1H$. We measured masses ^{12}C, $^{16}O^1H$, ^{19}F, ^{30}Si, ^{32}S, and ^{35}Cl using ^{30}Si as a normalization mass to generate calibration curves. Background was assumed to be negligible for F, S, and Cl because these elements strongly co-correlate at relatively high and low concentrations. H_2O and C background was removed by subtracting the value determined from our blank reference material, Suprasil 3002 quartz glass. Instrumental background was found to be 0.7 ± 0.1 μg/g (2σ) H_2O, which is similar to or better than other analytical sessions with this

16

setup (*21*). A correction was applied to account for an instrumental drift of 6 % over the three-day analytical session.

Contamination of H_2O and other volatiles is possible on the surface of the olivine or in cracks because SIMS is a surface analytical technique. Surface contamination was sufficiently removed from the sample surface by presputtering the sample for 5 minutes prior to analysis (*5, 26, 27*). A five-minute presputter is sufficient because after this time the ion intensities of the measured isotopes remain constant, meaning all surface contaminates have been removed. All measured masses were checked on the image plate for small-scale heterogeneities with high volatile concentrations, which could represent cracks or heterogeneous surface contamination (*28*). Additionally, the consistent relationship between volatiles and major elements strongly argues against most surface contamination of volatiles in this study.

2.4.2 Electron microprobe analysis

Major and minor element compositions of olivine in D'Orbigny and Sahara 99555 were determined using the Cameca SX100 electron microprobe (EPMA) at NASA-Johnson Space Center, Houston, TX. Accelerating voltage of 20 kV and a beam current of 40 nA were used for quantitative major and minor element concentration analyses throughout. The elements Al, Ca, Ti, Cr, Fe, Mn, Ni, Si, and Mg were measured with a focused (1 µm) beam and calibrated with natural and synthetic reference materials: oligoclase, diopside, rutile, chromite, fayalite, rhodonite, NiO, fayalite and forsterite, respectively. Analyses were rejected if analytical totals were >101% and <99%. Detection limits were: MgO (0.02), Al_2O_3 (0.01), SiO_2 (0.02), CaO (0.01), TiO_2 (0.02), Cr_2O_3 (0.02), MnO (0.02), FeO (0.04), NiO (0.02).

2.4.3 Isotope Dilution

D'Orbigny was measured for Tl abundance by isotope dilution (ID). All sample preparation was performed in the class 1000 NIRVANA trace metal clean lab facility at the Woods Hole Oceanographic Institution. Approximately 5 g of D'Orbigny with no fusion crust was ground in

an agate mortar and pestle. Three 50 mg aliquots of the homogenized powder were prepared for digestion. Prior to digestion, the three D'Orbigny aliquots, along with two aliquots of the USGS Iceland basalt reference material BIR-1a, were leached for one hour in 1M HCl in an ultrasonic bath, which has been shown to remove Tl from low temperature alteration products from magmatic rocks (*29*). The leaching procedure was performed on D'Orbigny in order to remove any potential terrestrial contamination, while leaching of BIR-1a was performed in order to investigate the effect of leaching on an otherwise contamination-free basalt (table A1). All samples were mixed with a ^{203}Tl-enriched spike (*30*) and digested in 0.3 ml of concentrated HF and 2 ml of concentrated HNO_3. Samples were dried and then fluxed repeatedly in 3+3 ml of concentrated HNO_3 and HCl until samples were fully dissolved. Subsequently, samples were reconstituted in 1M HCl and Tl was oxidized with Br_2-saturated nanopure water. Thallium was separated from the sample matrix via liquid anion exchange chromatography using previously described methods (*30*). Thallium isotope compositions of purified and spiked samples were measured at the WHOI plasma facility using a Thermo Scientific Neptune multiple collector inductively coupled plasma mass spectrometer coupled to an Aridus II desolvating nebulizer. Instrumental mass bias was corrected for by adding NIST SRM981 Pb to the purified Tl solutions and monitoring the ^{208}Pb/^{206}Pb isotope ratio during measurements assuming that mass bias followed an exponential law. Procedural blanks processed were 12 - 17 pg Tl, which constituted between 36 and 54% of the measured natural Tl and were subtracted during data processing. The uncertainty on Tl concentration measurements by ID is generally on the order of 2% (2σ) (*30*). However, the reproducibility of the concentrations of the leached samples was 23% (2σ), which is likely due to variable efficiency of the leaching procedure and the high proportion and variability in our reagent blanks.

2.5 Results

We performed systematic rim-core-rim transects across several euhedral olivine grains to measure major and minor elements by EPMA and highly volatile elements by SIMS, (tables 1, A2 & A3). For D'Orbigny, the olivine MgO content varied from 29.2 to 0.1 wt% (Fo 60-0) and water content varied from 6.2 to 20.6 μg/g. The most MgO-rich olivine core that was found contained 6.2 μg/g H_2O, 0.8 μg/g C, 60 ng/g F, and 27 ng/g Cl.

In Sahara 99555 olivine MgO content systemically varied from 30.9 to 0.2 wt% (Fo 63-1) and water content systemically varied from 7.4 to 12.3 µg/g. The Sahara 99555 olivine with the lowest H_2O contents has 7.4 µg/g H_2O, 1 µg/g C, 60 ng/g F, and 43 ng/g Cl. Importantly, minor and volatile element concentrations in olivine from D'Orbigny and Sahara 99555 correlate strongly with MgO content (Figs. 2 & 3).

The blank-corrected Tl concentration of BIR-1a was 960 ± 150 pg/g (2σ), which is within error of a previous measurement of BIR-1a, 1.3 ± 0.4 ng/g (2σ) (31). Therefore, we conclude that the leaching procedure did not remove a measurable fraction of the Tl in the rock powder (29). With these leaching results in hand, the blank corrected Tl content measured in D'Orbigny is 340 ± 80 pg/g Tl (2σ). The bulk Tl content of D'Orbigny fits along the same trend that was found for the other highly volatile elements measured here (Fig. 1).

2.6 Discussion

2.6.1 Volatile element content of a primitive melt

If the variability observed in the olivines results from fractional crystallization (11), the core concentrations can be used to determine the volatile content of the primitive melt. To test the fractional crystallization hypothesis, we performed a forward fractional crystallization model (32) to determine if fractional crystallization can explain the observed chemical variations in the olivine grains from D'Orbigny and Sahara 99555. We must assume that D'Orbigny and Sahara 99555 represent very similar magmas in order to use a single crystallization model to describe both angrites. This assumption is valid, as D'Orbigny and Sahara 99555 have nearly identical major and trace element compositions (13, 15, 33-35). The input parameters for the model include bulk composition, pressure, and oxygen fugacity. A D'Orbigny bulk composition, 100 kPa, and a log(fO₂) of IW-1 for the onset of crystallization were used. We chose the D'Orbigny bulk composition because most of our EPMA and SIMS data come from D'Orbigny, which is thought to represent a melt composition (11),. The pressure of 100 kPa was used because angrites crystallized at very low pressure (11) and the olivine crystallization model is best suited

for terrestrial ambient pressure (*32*). The log(fO$_2$) of IW-1 was used for the crystallization model because early crystallizing phases are relatively reduced (*11, 36*) and metal has been predicted (*37*) and observed (*38*) in mantle restites. If a more oxidizing fO$_2$ is used, similar to late crystallizing phases, e.g., druse pyroxenes (*39*) and phosphates (*40*), model outputs are comparable, but less consistent with the observed major element olivine compositions in D'Orbigny. The model output predicts the first olivine that crystallizes from a D'Orbigny composition to be Fo$_{67.7}$ and the most primitive olivine phenocryst found is Fo$_{64.4}$ (*15*). The excellent agreement between the composition of the first olivine that crystallized in our model and the most primitive olivine found in D'Orbigny shows that the model adequately accounts for the early stages of fractional crystallization from the D'Orbigny melt. In addition, the close correspondence between the observed major and volatile elements in D'Orbigny and Sahara 99555 and those predicted with the forward model suggests that we can use the model to determine the volatile content of the most primitive olivine composition.

Our best–fit model, which predicts the trends observed in H, C, F, and Cl, has a primitive (MgO-rich) olivine volatile content of 7.3 ± 1.6 µg/g H$_2$O, 0.75 ± 0.3 µg/g C, 50 ± 20 ng/g F, 31 ± 9 Cl ng/g, which is within error of the most primitive (MgO-rich) olivine that we measured (Ol-11; Fig 3, table 1 & A3). We convert the most MgO-rich and H$_2$O-poor measured olivine data to primitive melt composition using published olivine-melt partition coefficients (*21-23*), because the model olivine and our most primitive olivine are within error of one another. The resulting primitive melt volatile contents are 1500 ± 190 µg/g H$_2$O, 1100 ± 260 µg/g C, 0.52 ± 0.16 µg/g F, and 23 ± 3.4 µg/g Cl (2σ) (table A4).

2.6.2 Post crystallization alteration of olivine

The strong correlation between volatile concentrations and MgO content in olivine suggests that fractional crystallization played a major role in producing the observed co-variations. However, there are several other processes that could have altered the initial distribution of elements – including H – in olivine such that the measured concentrations would not reflect that of the parent melt. Possible processes include (i) intracrystalline diffusion and (ii) degassing.

(i) Hydrogen diffusion could occur on the APB if the basaltic angrites cooled relatively slowly or if subsequent lava flows buried and heated D'Orbigny and Sahara 99555. The diffusivity of H in olivine is ~5 orders of magnitude faster than Mg and Fe and ~10 orders of magnitude faster than Si (41, 42). The large difference in diffusivities would cause predictable and measurable profiles across large euhedral olivine grains, such that fast diffusing elements (e.g., H) would be equilibrated and show little or no compositional variation, whereas slower diffusing elements such as Si, Fe, Mg, and Ca would be partially equilibrated or unequilibrated (43). The strong correlation between major, minor, and volatile elements from the olivine core to the olivine rim is inconsistent with a slow cooling history, which would cause H to become decoupled from the other elements with slower diffusion coefficients. Additionally, the observation that the cores of all olivines, regardless of crystal size, cluster around 6 µg/g H_2O argues against a relaxation of the H_2O profile, as smaller crystals should relax their concentration profile faster than large crystals. Instead, fractional crystallization is a more plausible explanation for the observed major, minor, and volatile element distribution in olivine (see below). The lack of post-crystallization H diffusion in olivine places strong constraints on the thermal regime that D'Orbigny and Sahara 99555 could have experienced over the last 4563 Ma. We use a diffusion rule of thumb (44):

$$X_i \propto (D_i t)^{1/2} \tag{1}$$

Where X_i is the diffusion length of element i during diffusion, D_i is the diffusion coefficient of element i (in m^2/s), and t is time in seconds. Assuming we could not detect H diffusion in olivine if it traveled <60 µm, about the size of our presputter spot, and if a later heating event did occur, then it must have been <5 years at 600 °C, or <500 years at 500 °C in order to leave the disturbance of the H_2O concentration profiles undetectable, assuming a diffusivity of 1.97×10^{-17} m/s^2 at 600 °C (41).

(ii) Large vesicles in D'Orbigny have been interpreted as evidence for a fluid phase that exsolved from the melt at some point during crystallization (i.e. degassing) (25). It has been documented that the volatile species fractionate strongly when a vapor exsolves from a melt. In particular, a preferential loss of H_2O, C, and Cl compared to F (45) would be observed if olivine had been crystallizing while the hypothetical vapor phase was exsolving. H_2O and C contents remain well correlated with MgO in most of the olivine core-rim profile, however a detectable decrease in H_2O and C contents of the most Mg-poor olivine (at the crystal rim) is indeed observed, whereas Cl and F appear to remain undepleted (Fig. 3). This observation implies that degassing could have occurred during the last stages of crystallization. Alternatively, the fractional crystallization models can be inaccurate during the late stages of crystallization due to the uncertainties involved in predicting the saturation of the melt in trace phases as well as when degassing occurs (46).

We conclude that neither degassing nor diffusion affected the major, minor, or volatile contents of olivine grains in D'Orbigny and Sahara 99555, except at their outermost rims and in mesostasis regions (Fig. 3). Therefore, we can use the measured volatile element contents of the most primitive olivine cores to determine the melt composition in equilibrium with the olivine.

2.6.3 APB mantle composition

The APB has often been referred to as an ultra-volatile depleted body (14, 15, 24). For example, the APB is highly depleted in Rb and Na compared to the Moon, Earth, and chondrites (Fig. 4) (14). Here, we use our new data for highly volatile elements in conjunction with published data on D'Orbigny and Sahara 99555 (13, 15, 34, 47) to reconstruct the composition of the APB mantle (Table A4). We assume that the bulk meteorite concentrations of non-volatile elements correspond to the primitive melt concentrations, because D'Orbigny and Sahara 99555 have major element compositions that closely resemble primitive melt (11). The bulk rock elemental concentrations determined in D'Orbigny and Sahara 99555 have the possibility of terrestrial contamination (12), but the bulk rock concentration measurements were conducted in labs that regularly measure extra-terrestrial samples, and terrestrial contamination was removed as best as

possible (*13, 15, 34, 47*). Regardless of terrestrial contaminating removal steps, minute amounts of contamination often persists that can be seen in isotopic measurements (*12*). We are unable to fully account for the minute amounts of terrestrial contamination that are inherent to bulk rock measurements, but minute amounts of terrestrial contamination will not alter our conclusions because we compare concentrations in log space. To estimate the bulk composition of the APB mantle we assumed D'Orbigny and Sahara 99555 represent 15 % partial melting of the APB mantle (*11, 48*), which would likely leave just olivine and orthopyroxene as a residual phase in the mantle. For the model we used an orthopyroxene:olivine ratio of 30:70. If this ratio is adjusted from 0:100 (pure olivine) to 60:40 (more orthopyroxene than olivine) the resulting trace element contents will vary only by ~10 % because the partition coefficients in the two minerals for the considered elements are relatively similar. Combining the primitive melt composition with published olivine- and orthopyroxene-melt partition coefficients (*21-23, 49-59*) we determine the bulk composition of the APB mantle assuming batch melting which is likely appropriate for low gravity conditions (*60*):

$$C_l/C_o = (1-(1-F)^{(1/D)}) * F^{-1} \qquad (2)$$

Where C_l is the liquid composition in equilibrium with the mantle i.e., the primary melt, C_o is the concentration of the original system, F is the fraction of melt produced and D is the partition coefficient for the element of interest. Using the above assumptions and equation we calculate the bulk composition of the silicate portion of the APB (Table A4).

Rare olivines, interpreted as xenocrysts, with core compositions of $Fo_{\sim90}$ have been found in D'Orbigny (*15*). If the APB mantle olivine content was Fo_{90} instead of ca. Fo_{70}, then all of our best estimate mantle values would decrease by ca. 25 % due to additional fractionation of olivine. However, these olivines could also be xenocrystic residues of partial melting on the APB, in which case our estimates would be unchanged.

We can convert the bulk Tl content of 340 ± 80 pg/g (2σ) measured in D'Orbigny into that of the APB mantle by applying the bulk mantle melting partition coefficient for Tl (*56*), which produces Tl_{APB} = 51 ± 20 pg/g. Based on the moderately volatile element depletion trend (Fig 1), the expected Tl content of an angrite would be 0.11 pg/g Tl. However, the bulk rock Tl content of D'Orbigny likely does not represent the primitive melt composition because of degassing, which as been observed in a glass associated with D'Orbigny (*35*). As stated above, the vesicles in D'Orbigny strongly suggest that D'Orbigny degassed at some point during crystallization (*11*, *25*), and Tl likely degasses as efficiently as S (*61*). Additionally, Tl may partition into the core during core formation (*62*), thereby increasing the depletion of Tl in the silicate portion of the APB. Therefore, while we cannot take into account the possibility of a minor terrestrial contamination signal, the Tl content of the APB mantle derived from D'Orbigny likely represents a lower limit.

2.6.4 Timing of volatile addition to the inner solar system

We obtain a volatility trend for the APB by plotting lithophile and atmophile element concentrations relative to Si and CI chondrite concentrations and against their respective half-mass condensation temperatures (*63*) (Fig. 1). The plot shows very steep depletion in moderately volatile elements, while depletion of highly volatile elements is relatively flat. We suggest that the most plausible explanation for the step-wise pattern observed for the volatile element depletion in the APB is that the steep depletion in moderately volatile elements is inherited from nebular or accretion processes (*12*, *64*, *65*) that formed the main mass of the APB. Subsequently, a small amount of volatile-rich material was added to the APB before it fully solidified, which was sufficient to augment its complement of highly volatile elements, for example H_2O is enriched by a factor of 10^6 relative to the initial volatile element depletion trend, while leaving the moderately volatile and refractory element budgets unaffected. To determine the source of the highly volatile elements we compared volatile element ratios from several different solar system bodies (Fig. 4). The element ratios involving H overlap only with the field of carbonaceous chondrites (Figs. 4a and 4c), suggesting that the APB has a carbonaceous chondrite-like volatile signature, which agree with H, C, and N isotope composition of angrites

(*35, 47*). Additionally, a cometary origin for most volatiles on the APB can be rejected based on mixing models of H and N isotopes (*35*).

Mixing calculations between an average composition of CI, CM, CO, and CV carbonaceous chondrites (*66, 67*) and the volatile element depleted APB (black line, Fig. 1) show that the observed volatile element pattern can be reproduced by the addition of 0.1–1 % (by weight) average carbonaceous chondrite to the APB mantle (Fig. 1). Our interpretation is in agreement with refractory highly siderophile element (HSE) concentrations in angrites that are also present in chondritic relative proportions (*34*), which suggests that the APB must have received chondritic material some time after its core formed at ~4565 Ma (*37*). Given that basalts on the APB had crystallized and locked in their geochemical signature at 4563.6 ± 0.2 Ma (*16-20*) it follows that the addition that led to chondritic proportions of the HSE and highly volatile elements happened some time between the maximum age of core formation, which could have happened about the same time as CAI formation (*37*), and the age of the oldest angrites, 4563.6 ± 0.2 Ma (*16-20*).

Additional evidence of early accretion of chondritic material to the inner solar system comes from eucrite meteorites (*68-72*), some of which crystallized as early as 4563.7 ± 2.1 Ma (*73*). Interpretations of the eucrite meteorite volatile data suggest that material with H, N, and C isotopic signatures similar to carbonaceous chondrite was abundant enough to hydrate apatites in eucrites and also form veins and veinlets in eucrites (*68, 74*). Although the eucrite data provide evidence for early accretion of volatiles in the inner solar system, these data cannot be used to deduce a robust estimate of the amount of water accreted to the eucrite parent body (*69, 74*). All the same, our new data for D'Orbigny and Sahara 99555 angrites, in conjunction with the H isotope composition of D'Orbigny and Sahara 99555 (*35*), shows that volatile accretion in the very early solar system was not a stochastic event limited to stray collisions. We now have evidence from two major bodies in the inner solar system that volatile-rich material was added to differentiated bodies inside the snowline earlier than 4563 Ma.

2.7 Conclusions

We measured highly volatile elements in olivine in the angrites D'Orbigny and Sahara 99555. These concentrations imply that water and C are enriched by factor of 1 million compared to the expected volatile element depletion based on moderately volatile elements. We conclude that the APB accreted 0.1 – 1 % by mass of ice-free carbonaceous chondrites, which equates to a APB mantle concentration of ~230 μg/g H_2O. Based on angrite chronological data, the addition of carbonaceous chondrites must have occurred between 4566.8 Ma and 4562.9 ± 0.6 Ma. Therefore, inner solar system bodies could have received elements necessary for terrestrial life (H, C, and N) throughout their accretion history and delivery of volatiles during accretion does not appear to have been the limiting factor for establishing life on Earth.

2.8 Acknowledgements

2.9 References

1. F. Albarède, Volatile accretion history of the terrestrial planets and dynamic implications. *Nature*. **461**, 1227–1233 (2009).

2. B. Marty, The origins and concentrations of water, carbon, nitrogen and noble gases on Earth. *Earth and Planetary Science Letters*. **313**, 56–66 (2012).

3. M. M. Hirschmann, Constraints on the early delivery and fractionation of Earth's major volatiles from C/H, C/N, and C/S ratios : American Mineralogist. **101**, 540–553 (2016).

4. M. Humayun *et al.*, Origin and age of the earliest Martian crust from meteorite NWA 7533. *Nature*. **503**, 513–516 (2013).

5. A. E. Saal *et al.*, Volatile content of lunar volcanic glasses and the presence of water in the Moon's interior. *Nature*. **454**, 192–195 (2008).

6. F. M. McCubbin *et al.*, Magmatic volatiles (H, C, N, F, S, Cl) in the lunar mantle, crust, and regolith: Abundances, distributions, processes, and reservoirs. *American Mineralogist*. **100**, 1668–1707 (2015).

7. S. A. Jacobson *et al.*, Highly siderophile elements in Earth's mantle as a clock for the Moon-forming impact. *Nature*. **508**, 84–87 (2014).

8. L. E. Borg, J. N. Connelly, M. Boyet, R. W. Carlson, Chronological evidence that the Moon is either young or did not have a global magma ocean. *Nature*. **477**, 70–72 (2011).

9. M. Barboni *et al.*, Early formation of the Moon 4.51 billion years ago. *Science Advances*, 1–9 (2017).

10. M. Touboul, T. Kleine, B. Bourdon, H. Palme, R. Wieler, Late formation and prolonged differentiation of the Moon inferred from W isotopes in lunar metals. *Nature*. **450**, 1206–1209 (2007).

11. K. Keil, Angrites, a small but diverse suite of ancient, silica-undersaturated volcanic-plutonic mafic meteorites, and the history of their parent asteroid. *Chemie der Erde - Geochemistry*. **72**, 191–218 (2012).

12. U. Hans, T. Kleine, B. Bourdon, Rb–Sr chronology of volatile depletion in differentiated protoplanets: BABI, ADOR and ALL revisited. *Earth and Planetary Science Letters*. **374**, 204–214 (2013).

13. D. W. Mittlefehldt, M. Killgore, M. T. Lee, Petrology and geochemistry of D'Orbigny, geochemistry of Sahara 99555, and the origin of angrites. *Meteoritics & Planetary Science*. **37**, 345–369 (2002).

14. M. E. Varela *et al.*, Glasses in the D'Orbigny angrite. *Geochimica et Cosmochimica Acta.* **67**, 5027–5046 (2003).

15. G. Kurat *et al.*, D'Orbigny: A non-igneous angritic achondrite? *Geochimica et Cosmochimica Acta.* **68**, 1901–1921 (2004).

16. Y. Amelin, The U–Pb systematics of angrite Sahara 99555. *Geochimica et Cosmochimica Acta.* **72**, 4874–4885 (2008).

17. Y. Amelin, U–Pb ages of angrites. *Geochimica et Cosmochimica Acta.* **72**, 221–232 (2008).

18. J. N. Connelly, M. Bizzarro, K. Thrane, J. A. Baker, The Pb–Pb age of angrite Sah99555 revisited. *Geochimica et Cosmochimica Acta.* **72**, 4813–4824 (2008).

19. F. Thiessen, A. A. Nemchin, J. F. Snape, M. J. Whitehouse, J. J. Bellucci, Impact history of the Apollo 17 landing site revealed by U-Pb SIMS ages. *Meteoritics & Planetary Science.* **1**, 2040–28 (2017).

20. K. K. Larsen *et al.*, Evidence for Magnesium Isotope Heterogeneity in the Solar Protoplanetary Disk. *ApJL.* **735**, L37 (2011).

21. E. H. Hauri *et al.*, Matrix effects in hydrogen isotope analysis of silicate glasses by SIMS. *Chemical Geology.* **235**, 352–365 (2006).

22. C. Dalou, K. T. Koga, N. Shimizu, J. Boulon, J.-L. Devidal, Experimental determination of F and Cl partitioning between lherzolite and basaltic melt. *Contributions to Mineralogy and Petrology.* **163**, 591–609 (2012).

23. A. Rosenthal, E. H. Hauri, M. M. Hirschmann, Experimental determination of C, F, and H partitioning between mantle minerals and carbonated basalt, $CO2/Ba$ and $CO2/Nb$ systematics of partial melting, and the $CO2$ contents of basaltic source regions. *Earth and Planetary Science Letters.* **412**, 77–87 (2015).

24. D. W. Mittlefehldt, T. J. McCoy, C. A. Goodrich, A. Kracher, in *Reviews in Mineralogy*, J. J. Papike, Ed. (Mineralogical Society of America, 1998), vol. 36, pp. 4–1–4–195.

25. T. J. McCoy *et al.*, Formation of vesicles in asteroidal basaltic meteorites. *Earth and Planetary Science Letters.* **246**, 102–108 (2006).

26. A. E. Saal, E. H. Hauri, J. A. Van Orman, M. J. Rutherford, Hydrogen Isotopes in Lunar Volcanic Glasses and Melt Inclusions Reveal a Carbonaceous Chondrite Heritage. *Science.* **340**, 1317–1320 (2013).

27. E. H. Hauri, T. Weinreich, A. E. Saal, M. C. Rutherford, J. A. Van Orman, High pre-eruptive water contents preserved in lunar melt inclusions. *Science.* **333**, 213–215 (2011).

28.   J. P. Greenwood *et al.*, Hydrogen isotope ratios in lunar rocks indicate delivery of cometary water to the Moon. *Nature Geoscience*. **4**, 79–82 (2011).

29.   S. G. Nielsen *et al.*, Tracking along-arc sediment inputs to the Aleutian arc using thallium isotopes. *Geochimica et Cosmochimica Acta*. **181**, 217–237 (2016).

30.   S. G. Nielsen, M. Rehkämper, J. Baker, A. N. Halliday, The precise and accurate determination of thallium isotope compositions and concentrations for water samples by MC-ICPMS. *Chemical Geology*. **204**, 109–124 (2004).

31.   S. G. Nielsen *et al.*, Thallium isotopes in Iceland and Azores lavas—implications for the role of altered crust and mantle geochemistry. *Earth and Planetary Science Letters*. **264**, 332–345 (2007).

32.   L. V. Danyushevsky, P. Plechov, Petrolog3: Integrated software for modeling crystallization processes. *Geochemistry, Geophysics, Geosystems*. **12**, 1–32 (2011).

33.   D. P. Glavin, A. Kubny, E. Jagoutz, G. W. Lugmair, Mn-Cr isotope systematics of the D'Orbigny angrite. *Meteoritics & Planetary Science*. **39**, 693–700 (2004).

34.   A. J. V. Riches *et al.*, Rhenium–osmium isotope and highly-siderophile-element abundance systematics of angrite meteorites. *Earth and Planetary Science Letters*. **353**, 208–218 (2012).

35.   A. R. Sarafian *et al.*, Early accretion of water and volatile elements to the inner Solar System: evidence from angrites. *Philosophical Transactions of the Royal Society of London A: Mathematical, Physical and Engineering Sciences*, 1–27 (2017).

36.   P. L. King *et al.*, Redox History of Early Solar System Planetismals Recorded in the D'Orbigny Angrite. *Lunar and Planetary Science Conference*. **43**, 2436 (2012).

37.   T. Kleine, U. Hans, A. J. Irving, B. Bourdon, Chronology of the angrite parent body and implications for core formation in protoplanets. *Geochimica et Cosmochimica Acta*. **84**, 186–203 (2012).

38.   A. R. Santos *et al.*, Northwest Africa 8535: Sampling a New Portion of the Angrite Parent Body. *Lunar and Planetary Science Conference*. **48**, 2266 (2017).

39.   Y. A. Abdu *et al.*, Druse clinopyroxene in D'Orbigny angritic meteorite studied by single-crystal X-ray diffraction, electron microprobe analysis, and Mössbauer spectroscopy. *Meteoritics & Planetary Science*. **44**, 581–587 (2009).

40.   T. Mikouchi, K. Sugiyama, W. Satake, Y. Amelin, Mineralogy and crystallography of calcium silico-phosphate in Northwest Africa 4590 angrite. *Lunar and Planetary Science Conference*. **42**, 2026 (2011).

41. S. Demouchy, S. Mackwell, Mechanisms of hydrogen incorporation and diffusion in iron-bearing olivine. *Phys Chem Minerals.* **33**, 347–355 (2006).

42. S. Chakraborty, Diffusion Coefficients in Olivine, Wadsleyite and Ringwoodite. *Reviews in Mineralogy and Geochemistry.* **72**, 603–639 (2010).

43. E. B. Watson, D. J. Cherniak, Quantitative cooling histories from stranded diffusion profiles. *Contributions to Mineralogy and Petrology.* **169**, 1–14 (2015).

44. J. Crank, *The mathematics of diffusion* (Oxford university press, 1979).

45. M. R. Carroll, J. D. Webster, in *Volatiles in Magmas, Reviews in Mineralogy*, M. R. Carroll, J. R. Holloway, Eds. (Washington, DC, 1994), vol. 30, pp. 231–279.

46. H. D. Nathan, C. K. Vankirk, A Model of Magmatic Crystallization. *Journal of Petrology.* **19**, 66–94 (1978).

47. F. A. J. Abernethy *et al.*, Stable isotope analysis of carbon and nitrogen in angrites. *Meteoritics & Planetary Science.* **48**, 1590–1606 (2013).

48. A. J. G. Jurewicz, D. W. Mittlefehldt, J. H. Jones, Experimental partial melting of the Allende (CV) and Murchison (CM) chondrites and the origin of asteroidal basalts. *Geochimica et Cosmochimica Acta.* **57**, 2123–2139 (1993).

49. R. L. Nielsen, W. E. Gallahan, F. Newberger, Experimentally determined mineral-melt partition coefficients for Sc, Y and REE for olivine, orthopyroxene, pigeonite, magnetite and ilmenite. *Contributions to Mineralogy and Petrology.* **110**, 488–499 (1992).

50. P. Beattie, The generation of uranium series disequilibria by partial melting of spinel peridotite: constraints from partitioning studies. *Earth and Planetary Science Letters.* **117**, 379–391 (1993).

51. A. K. Kennedy, G. E. Lofgren, G. J. Wasserburg, An experimental study of trace element partitioning between olivine, orthopyroxene and melt in chondrules: equilibrium values and kinetic effects. *Earth and Planetary Science Letters.* **115**, 177–195 (1993).

52. T. Dunn, C. Sen, Mineral/matrix partition coefficients for orthopyroxene, plagioclase, and olivine in basaltic to andesitic systems: a combined analytical and experimental study. *Geochimica et Cosmochimica Acta.* **58**, 717–733 (1994).

53. F. Brunet, G. Chazot, Partitioning of phosphorus between olivine, clinopyroxene and silicate glass in a spinel lherzolite xenolith from Yemen. *Chemical Geology.* **176**, 51–72 (2001).

54. K. Mibe, Y. Orihashi, S. Nakai, T. Fujii, Element partitioning between transition-zone minerals and ultramafic melt under hydrous conditions. *Geophys. Res. Lett.* **33**, L16307

(2006).

55. A. Borisov, A. Pack, A. Kropf, H. Palme, Partitioning of Na between olivine and melt: An experimental study with application to the formation of meteoritic Na 2 O-rich chondrule glass and refractory forsterite grains. *Geochimica et Cosmochimica Acta*. **72**, 5558–5573 (2008).

56. S. G. Nielsen, N. Shimizu, C. T. A. Lee, M. D. Behn, Chalcophile behavior of thallium during MORB melting and implications for the sulfur content of the mantle. *Geochemistry, Geophysics, Geosystems*. **15**, 4905–4919 (2014).

57. V. Le Roux, R. Dasgupta, C. T. A. Lee, Recommended mineral-melt partition coefficients for FRTEs (Cu), Ga, and Ge during mantle melting. *American Mineralogist*. **100**, 2533–2544 (2015).

58. T. H. Green, J. D. Blundy, J. Adam, G. M. Yaxley, SIMS determination of trace element partition coefficients between garnet, clinopyroxene and hydrous basaltic liquids at 2–7.5 GPa and 1080–1200°C. *Lithos*. **53**, 165–187 (2000).

59. S. Klemme, D. Günther, K. Hametner, S. Prowatke, T. Zack, The partitioning of trace elements between ilmenite, ulvospinel, armalcolite and silicate melts with implications for the early differentiation of the moon. *Chemical Geology*. **234**, 251–263 (2006).

60. B. E. Mandler, L. T. Elkins-Tanton, The origin of eucrites, diogenites, and olivine diogenites: Magma ocean crystallization and shallow magma chamber processes on Vesta. *Meteoritics & Planetary Science*. **48**, 2333–2349 (2013).

61. R. G. A. Baker, M. Rehkämper, T. K. Hinkley, S. G. Nielsen, J. P. Toutain, Investigation of thallium fluxes from subaerial volcanism—implications for the present and past mass balance of thallium in the oceans. *Geochimica et Cosmochimica Acta*. **73**, 6340–6359 (2009).

62. B. J. Wood, S. G. Nielsen, M. Rehkämper, A. N. Halliday, The effects of core formation on the Pb-and Tl-isotopic composition of the silicate Earth. *Earth and Planetary Science Letters*. **269**, 326–336 (2008).

63. K. Lodders, Solar system abundances and condensation temperatures of the elements. *The Astrophysical Journal*. **591**, 1220–1247 (2003).

64. A. N. Halliday, Mixing, volatile loss and compositional change during impact-driven accretion of the Earth. *Nature*. **427**, 505–509 (2004).

65. A. Hubbard, D. S. Ebel, Protoplanetary dust porosity and FU Orionis outbursts: Solving the mystery of Earth's missing volatiles. *Icarus*. **237**, 84–96 (2014).

66.   J. T. Wasson, G. W. Kallemeyn, Compositions of Chondrites. *Philosophical Transactions of the Royal Society of London. Series A, Mathematical and Physical Sciences*. **325**, 535–544 (1988).

67.   C. M. O. Alexander *et al.*, The provenances of asteroids, and their contributions to the volatile inventories of the terrestrial planets. *Science*. **337**, 721–723 (2012).

68.   A. R. Sarafian, S. G. Nielsen, H. R. Marschall, F. M. McCubbin, B. D. Monteleone, Early accretion of water in the inner solar system from a carbonaceous chondrite–like source. *Science*. **346**, 623–626 (2014).

69.   A. R. Sarafian, T. John, J. Roszjar, M. J. Whitehouse, Chlorine and hydrogen degassing in Vesta's magma ocean. *Earth and Planetary Science Letters*. **459**, 311–319 (2017).

70.   J. M. D. Day, R. J. Walker, L. Qin, D. Rumble Iii, Late accretion as a natural consequence of planetary growth. *Nature Geoscience*. **5**, 614–617 (2012).

71.   C. W. Dale *et al.*, Late Accretion on the Earliest Planetesimals Revealed by the Highly Siderophile Elements. *Science*. **336**, 72–75 (2012).

72.   T. J. Barrett *et al.*, The abundance and isotopic composition of water in eucrites. *Meteoritics & Planetary Science*. **51**, 110–1124 (2016).

73.   M. Touboul, P. Sprung, S. A. Aciego, B. Bourdon, T. Kleine, Hf-W chronology of the eucrite parent body. *Geochimica et Cosmochimica Acta*. **73**, 5150–5188 (2015).

74.   A. R. Sarafian, M. F. Roden, A. E. Patiño Douce, The nature of volatiles in eucrites: Clues from apatite. *Meteoritics & Planetary Science*. **48**, 2135–2154 (2013).

75.   W. F. McDonough, S. S. Sun, The Composition of the Earth. *Chemical Geology*. **120**, 223–253 (1995).

76.   A. E. Saal, E. H. Hauri, C. H. Langmuir, M. R. Perfit, Vapour undersaturation in primitive mid-ocean-ridge basalt and the volatile content of Earth's upper mantle. *Nature*. **419**, 451–455 (2002).

77.   F. Robert, in *Solar System History from Isotopic Signatures of Volatile Elements* (Springer, Dordrecht, 2003), vol. 16 of *Space Sciences Series of ISSI*, pp. 87–101.

78.   D. L. Kohlstedt, S. J. Mackwell, Diffusion of hydrogen and intrinsic point defects in olivine. *Zeitschrift für Physikalische Chemie*. **207**, 147–162 (1998).

79.   A. J. Berry, J. Hermann, H. S. C. O'Neill, G. J. Foran, Fingerprinting the water site in mantle olivine. *Geology*. **33**, 869–872 (2005).

80.   G. A. Gaetani *et al.*, Hydration of mantle olivine under variable water and oxygen fugacity

conditions. *Contributions to Mineralogy and Petrology*. **167**, 1–14 (2014).

81.   I. Kovács, H. S. C. O'Neill, J. Hermann, H. Hauri, Site-specific infrared OH absorption coefficients for water substitution into olivine. *American Mineralogist*. **95**, 292–299 (2010).

2.10 Figures & Tables

Figure 1

Silicon and CI normalized concentrations of lithophile elements in the primitive terrestrial mantle and the calculated mantle of the angrite parent body (APB) vs. half-mass condensation temperature in the solar nebula (*63*). Notice the exponential trends for Earth and the APB. Highly volatile elements in the APB are enriched compared to the expected trend, dashed line. Model curves indicate mixing of depleted APB with average CI, CM, CO, CV carbonaceous chondrite composition (*66, 67*). Black arrows indicate lower limit for N and Tl because both of these elements are based on bulk-rock analyses and therefore prone to degassing. Earth data from (*75*)
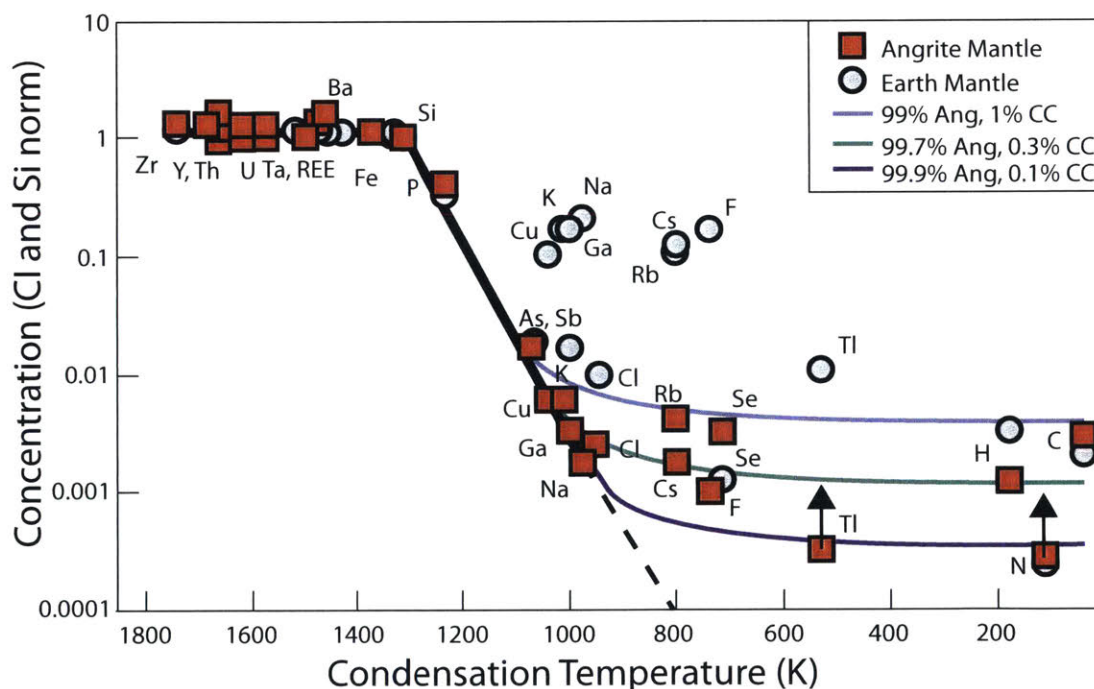
Figure 2

Transect across large euhedral olivine grain in D'Orbigny, olivine 2. Hydrogen (cast as H_2O), C × 5, F ×100, Cl ×100, and MgO vs. distance across grain.
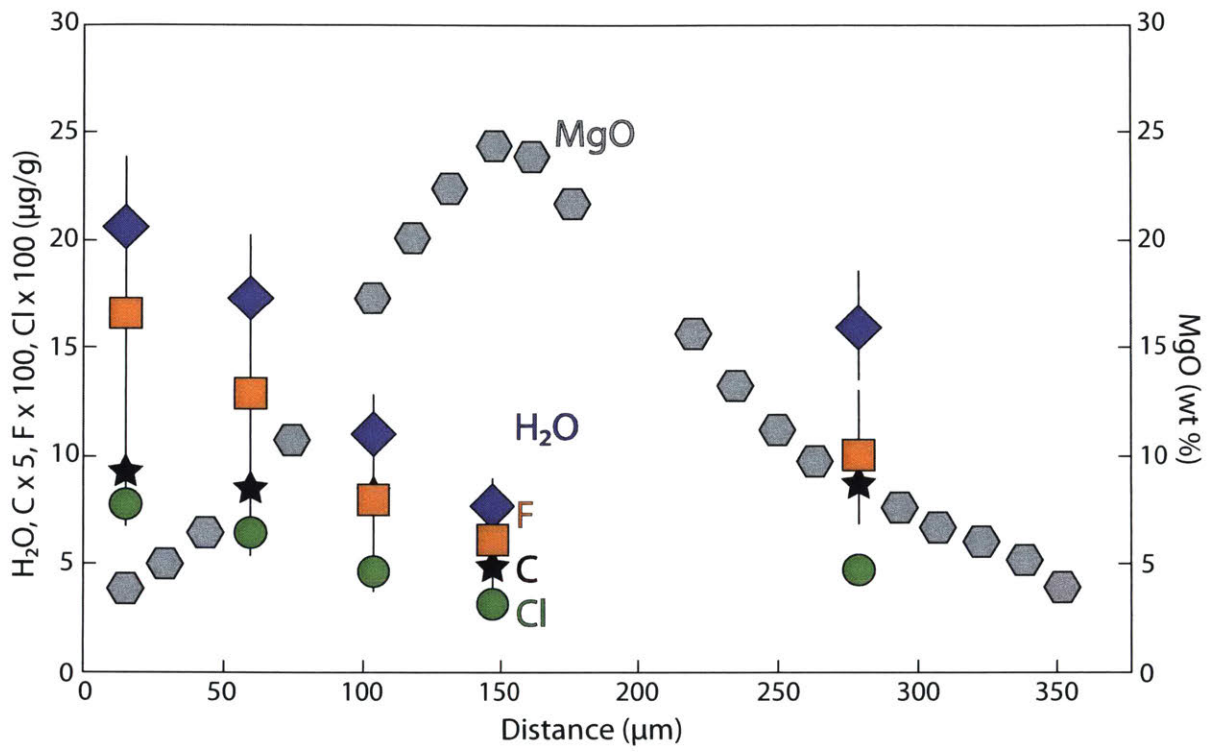
Figure 3

A: Fluorine and Cl vs MgO content of olivine from D'Orbigny (solid symbols) and Sahara 99555 (hollow symbols). B: Hydrogen (cast as H_2O) and C vs MgO content of olivine from D'Orbigny (solid symbols) and Sahara 99555 (hollow symbols). Top axis is percent melt remaining from forward fractional crystallization model. Symbols with black outlines are measured data. Solid lines and shaded regions are forward fractional crystallization model. Shaded region represents possible model outputs that fit data and represents the uncertainty of our calculated primitive melt volatile contents. During the latter part of crystallization C and H_2O have lower concentrations than expected due to degassing. Initial melt H_2O, C, F, and Cl contents can be constrained, because model and data fit for the early stages of crystallization.
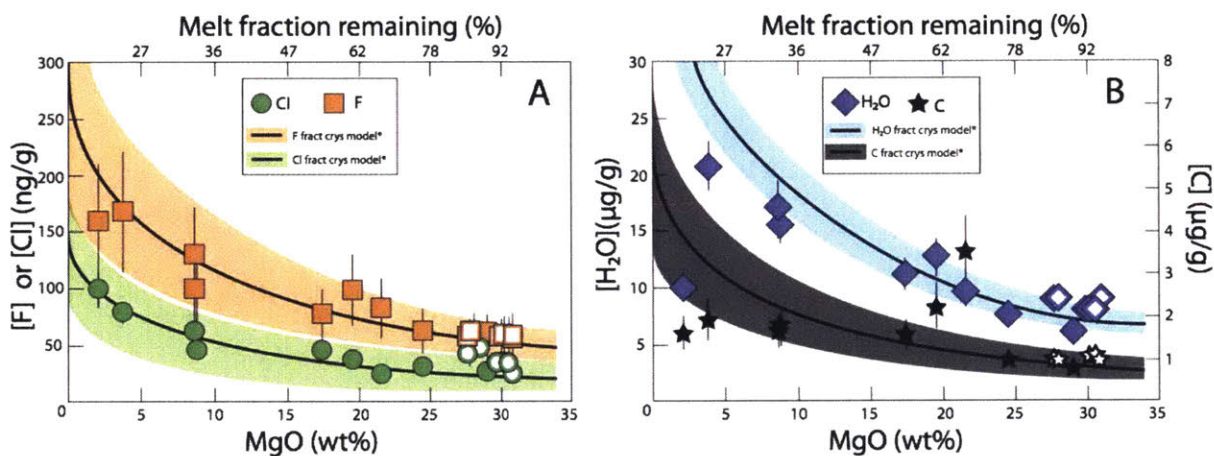
Figure 4

Volatile discrimination diagrams. APB = angrite parent body (A) log F/H$_2$O vs log Cl/H$_2$O, APB plots within the carbonaceous chondrite field. (B) log Rb vs log Na, APB is highly depleted in the volatile metals Rb and Na compared to the Moon, Earth, and chondrites. (C) Log Rb/H$_2$O vs log Na/H$_2$O, note, APB plots within the carbonaceous chondrite field, which agree with N and H isotope compositions (35). Data can be found in table A5 and from (34, 66, 67, 75-77). Error bars are smaller than the symbols.
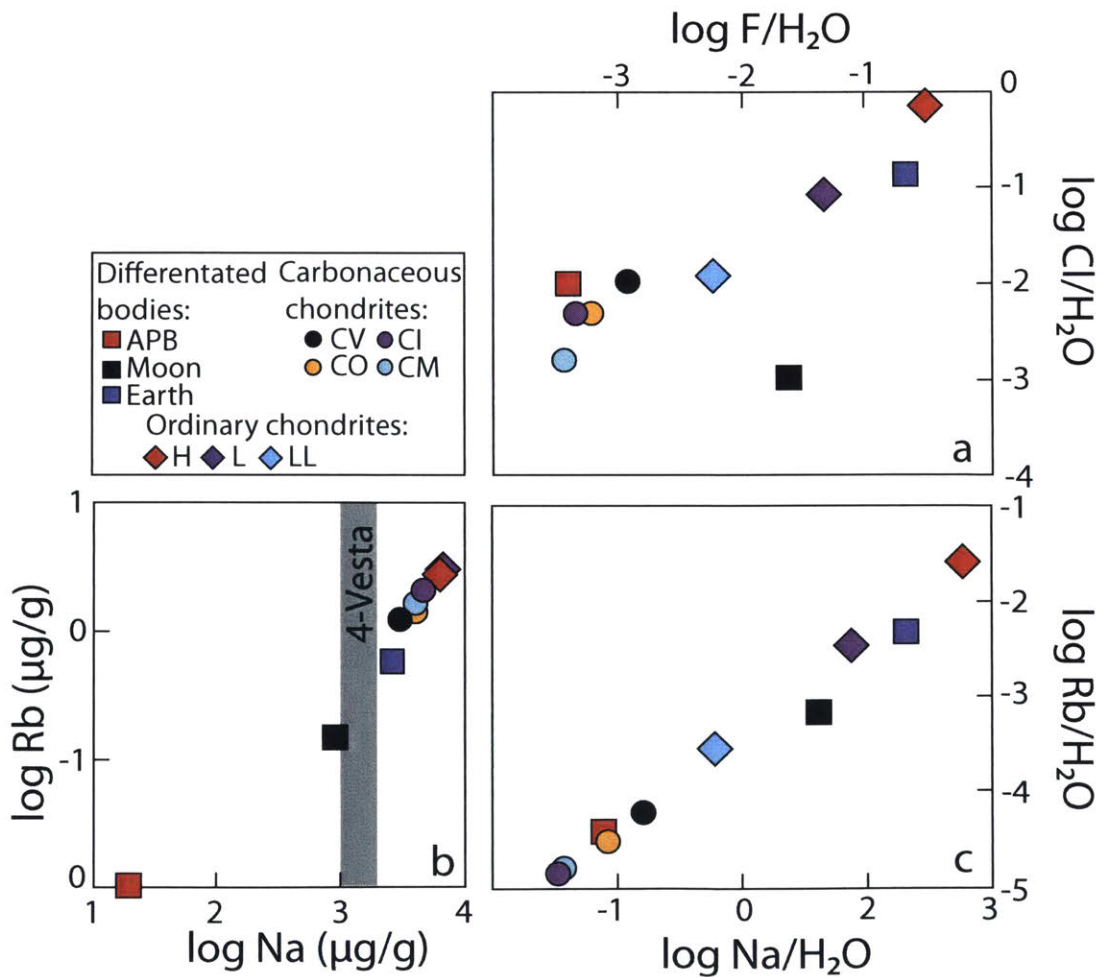
Table 1.

Coordinated EPMA and SIMS analyses of D'Orbigny and Sahara 99555.

Major elements in wt. %, C, H_2O, and S in μg/g, and F and Cl are in ng/g. C and H_2O are background subtracted, while S, F, and Cl are not. bdl is below detection limit

Sample	MgO	Al_2O_3	SiO_2	CaO	TiO_2	Cr_2O_3	MnO	FeO	NiO	Total
D'Orbigny										
ol-11	29.01	0.10	35.81	0.95	0.03	0.05	0.37	34.37	bdl	100.7
ol3-186	19.55	0.03	34.02	1.86	0.03	0.02	0.56	44.16	0.02	100.3
ol3-187	21.58	0.04	34.52	1.68	0.03	bdl	0.52	42.54	bdl	100.9
ol3-188	2.13	0.02	30.41	9.37	0.11	bdl	0.80	56.74	bdl	99.60
ol2-1	3.86	0.03	30.79	9.34	0.08	bdl	0.84	55.21	bdl	100.2
ol2-4	8.65	0.03	31.51	4.00	0.06	bdl	0.77	55.73	bdl	100.8
ol2-6	17.43	0.03	33.09	2.00	0.03	0.02	0.59	46.99	bdl	100.2
ol2-9	24.53	0.07	35.08	1.26	0.02	0.02	0.46	39.64	bdl	101.1
ol2-16	8.80	0.03	31.50	3.47	0.08	bdl	0.80	55.97	bdl	100.7
Sahara 99555										
ol5-67	27.75	0.10	35.87	1.01	0.04	0.04	0.37	35.74	0.03	101.0
ol5-68	28.02	0.08	35.87	0.99	0.04	0.05	0.38	35.37	0.02	100.8
ol1-124	30.16	0.11	36.32	0.88	0.03	0.03	0.36	32.73	0.03	100.7
ol1-125	30.58	0.10	36.34	0.89	0.03	0.04	0.35	32.60	0.04	101.0
ol1-126	30.87	0.11	36.48	0.88	0.03	0.03	0.35	32.13	0.02	100.9
ol1-127	29.91	0.08	36.21	0.91	bdl	0.04	0.36	33.43	bdl	101.0

Sample	[C] μg/g	2SD	[H_2O] μg/g	2SD	[F] ng/g	2SD	[S] μg/g	2SD	[Cl] ng/g	2SD
D'Orbigny										
ol-11	0.8	0.2	6.2	0.8	60	19	0.37	0.09	27	4
ol3-186	2.3	0.5	12.8	1.6	98	31	0.71	0.17	37	5
ol3-187	3.6	0.8	9.7	1.2	83	26	0.56	0.13	25	4
ol3-188	1.6	0.4	10.1	1.3	160	50	10.0	2.36	98	15
ol2-1	1.8	0.4	20.6	2.6	168	53	2.60	0.61	79	12
ol2-4	1.7	0.4	17.4	2.2	131	41	1.39	0.33	63	9
ol2-6	1.6	0.4	11.3	1.4	78	24	0.63	0.15	45	7
ol2-9	0.9	0.2	7.7	1.0	62	20	0.44	0.10	31	5
ol2-16	1.7	0.4	16.0	2.0	100	31	1.04	0.24	48	7
Sahara 99555										
ol5-67	1.0	0.2	9.1	1.2	57	18	0.46	0.11	43	6
ol5-68	0.9	0.2	9.2	1.2	60	19	0.32	0.08	45	7
ol1-124	1.1	0.3	8.3	1.1	59	18	0.37	0.09	35	5
ol1-125	1.1	0.3	8.1	1.0	57	18	0.33	0.08	36	5
ol1-126	1.0	0.2	9.2	1.2	59	19	0.35	0.08	25	4
ol1-127	6.3	1.5	8.2	1.0	57	18	0.37	0.09	36	5

Chapter 3

Early accretion of water and volatile elements to the inner solar system: Evidence from angrites

3.1 Abstract

Inner solar system bodies are depleted in volatile elements relative to chondrite meteorites, yet the source(s) and mechanism(s) of volatile element depletion and/or enrichment are poorly constrained. The timing, mechanisms, and quantities of volatile elements present in the early inner solar system have vast implications for diverse processes from planetary differentiation to the emergence of life. We report major, trace, and volatile element contents of a glass bead derived from the D'Orbigny angrite, the hydrogen isotopic composition of this glass bead and that of coexisting olivine and silicophosphates, and the ^{207}Pb–^{206}Pb age of the silicophosphates, 4568 ±20 Ma. We use volatile saturation models to demonstrate that the angrite parent body must have been a major body in the early inner solar system. We further show via mixing calculations that all inner solar system bodies accreted volatile elements with carbonaceous chondrite H and N isotope signatures extremely early in solar system history. Only a small portion (if any) of comets and gaseous nebular H-species contributed to the volatile content of the inner solar system bodies.

3.2 Introduction

The Earth and Mars are depleted in all volatile metals, e.g., rubidium, cesium, and sodium, compared to the most primitive carbonaceous chondrites. This volatile element depletion is also seen in the elements with extremely low condensation temperatures, e.g., hydrogen (H) and carbon (C) (1, 2). Although some inner solar system bodies such as the moon, these extremely volatile elements may not be as depleted as expected based on volatile metal trends (3). The systematic depletion of volatile elements has long been observed in the inner solar system bodies (2), but the precise mechanism for the volatile element depletion is debated (4-6). Two main hypotheses suggest that either high-energy events during accretion or solar processes caused volatile element depletion in the terrestrial planets. The accretion end-member hypothesis suggests that impacts during accretion were energetic enough to cause evaporative loss of volatile elements compared to refractory elements (5). In such a model, the inner planets may or may not have accreted volatile elements early, but those volatile elements would have been lost during accretion and a later stage of volatile accretion would be needed (4, 5, 7). However, this hypothesis may not be consistent with the lack of fractionation in volatile metals that is expected during evaporation (4, 8), and the more recent dynamical models suggest that volatile loss, specifically volatile-metal loss, is not a requirement during large planetary-scale impacts (3, 9-11).

The second end-member hypothesis, which assumes solar processes caused volatile-element depletion, assumes that accretion processes did not significantly fractionate the volatile elements, but the protoplanetary disc was inherently heterogeneous in volatile elements. The heterogeneity in the solar nebula was purportedly a function of heliocentric distance, such that the disc was more volatile-element depleted in the inner solar system and less volatile-element depleted in the outer solar system (6, 12). The systematic heterogeneity in the disc could be due to high energy solar outbursts (6) or due to other high-temperature processes. While both the accretionary and solar process models provide a mechanism for volatile depletion, neither model satisfies the observed enrichment in H and C relative to other volatile elements for Earth and the moon (3, 13, 14). Therefore, independent of which depletion mechanism is evoked, a subsequent enrichment mechanism must also have taken place e.g., an addition of volatile-rich carbonaceous chondrites

(*3*, *15-22*), comets (*23-26*), or potentially gaseous H-species from the solar nebula (*16*). To understand how and when inner solar system planet(s) became habitable, the processes that depleted/enriched the bio-essential elements H and C to the terrestrial planets must be known.

We can infer volatile enrichment of inner solar system bodies from the systematic behavior of volatile elements with respect to their condensation temperature, but the mechanisms of volatile element accretion and the source(s) of accreted water remain enigmatic. Determining the origin and abundance of water for differentiated planetary bodies is essential to resolve when volatile elements entered the inner solar system. Existing models attempt to explain the mechanism(s) that may have delivered volatile elements to the inner solar system (*27-31*), but they are relatively unconstrained by observations. For instance, many dynamic models invoke formation and migration of the giant planets to seed the inner solar system with volatile elements, including H, thus providing possible mechanisms for inner solar system hydration (*27-31*). However, critical observations are needed to constrain the timing of this process and the source(s) of the volatile elements.

Relatively few observations on the timing of volatile element accretion exist. The oldest evidence of water on Earth comes from an enriched ^{18}O signature in 4.4 Ga detrital zircons (*32*), but this is indirect evidence and long after planetary accretion began (*33, 34*). Only recently has the Moon been studied for its water and volatile element contents (*3, 19, 35-38*). The oldest lunar rocks are ca. 4.5 Ga (*39*), which is still too young to provide insights into the main phase of planetary accretion that occurred within the first 1-20 million years of solar system history (*34*). Recent evidence from eucrite meteorites suggests that volatile elements accreted to the inner solar system extremely early (*40*), e.g., the eucrite Stannern crystallized at 4563.7 ± 2.1 Ma and has a hydrogen isotope signature that matches that of the known terrestrial planets (*20, 41*). These studies push back the earliest time that differentiated bodies in the inner solar system obtained volatile elements. The early-accreted volatile elements in the differentiated bodies have H-, C-, and N-isotopic signatures that are indistinguishable from primitive, unprocessed carbonaceous chondrites, but only a crude estimate of the amount of water added to the eucrite parent body has been made. More recently it was determined through the study of angrite

41

meteorites that the amount of water and volatile elements accreted to the angrite parent body (APB) led to abundances of about 250 µg/g H_2O by 4563.3 Ma (42), in agreement with the timing indicated by the eucrite parent body (20, 22, 41).

Angrites are a small group of meteorites (~24, many paired) that have are subdivided into two groups, slowly cooled and quenched. The quenched angrites are silica undersaturated basaltic rocks that crystallized within the first few million years of solar system history (e.g. 43-45). Quenched angrites are unique among basaltic meteorites in that they show virtually no evidence of brecciation, shock, or subsolidus diffusion (46). Early crystallizing phases in angrites are relatively reduced, while late-crystallizing phases are more oxidized, suggesting that degassing, or some other mechanism oxidized angrite magmas during crystallization (44, 47, 48). The size of the APB is unknown, but a radius of >100 km has been suggested, based on the retention of volatile-bearing, vesiculated basalts that may have been emplaced in a pyroclastic eruption (44). Despite its proposed substantial size, the APB has not been physically observed, although there are smaller asteroids that exhibit spectral features that are very similar to the angrites [69]. Consequently, the APB was likely disrupted or destroyed (49).

Here we first provide additional constraints on the size of the APB based on angrite volatile element concentration data. We then interpret major and trace element concentrations and H isotope compositions in a glass melt bead recovered from the quenched angrite D'Orbigny. We also report H isotope data in olivines from D'Orbigny and silicophosphates from D'Orbigny and Sahara 99555 to characterize the degassing history on the APB. The H isotope data is complemented by ^{207}Pb-^{206}Pb ages measured in some of the silicophosphate grains to provide additional constraints on the thermal history of D'Orbigny. We put our measurements in geologic context and provide an internally consistent model to determine the hydrogen isotopic composition of an angritic primitive melt and the H isotope composition of the APB. Finally, we use these constraints to determine the maximum amount of cometary and gaseous nebular H-species that could have accreted to the APB and other objects in the inner solar system.

3.3 Samples

The volcanic (quenched) angrites D'Orbigny (relatively coarse grained; *44*) and Sahara 99555 (relatively fine grained; *44*) contain chemically zoned calcic olivine, zoned subsilicic aluminian-ferrian diopside, and Ca-rich plagioclase with minor phases of silica, kirschsteinite/monticellite, spinel, troilite, whitlockite, baddeleyite, and an unspecified silico-phosphate (*44, 46*), which may have been identified as Tsangpoite (*50*). D'Orbigny is characterized by an ophitic texture whereas the texture of Sahara 99555 is characterized by ca. 200–400 μm^2 intergrowths of zoned olivine and plagioclase (Fig. 1A & B).

D'Orbigny is a unique angrite because of its large mass (16.55 kg) and the occurrence of glass spheres. The main mass of D'Orbigny consists of two dense fractions separated by a low density, porous/vuggy, possibly caused by subsequent lava flows, where the dense fractions represent the lower part of a lava flow and the porous/vuggy fraction likely represents the top part of a degassed flow. Given the similarity between the composition of the glass and the whole rock, the glasses do not represent an evolved quenched melt (*51*). Additionally, the homogeneity of the beads and lack of any flow features (*51*) show that it is unlikely to be quenched impact melt (*52*). In this paper, we focus our analyses on several rock chips of D'Orbigny and Sahara 99555 and one 4–5 mm diameter glass bead from D'Orbigny (Fig. 1).

3.4. Methods

3.4.1 Preparation

Rock chips of D'Orbigny and Sahara 99555, as well as the D'Orbigny glass bead were prepared at the Woods Hole Oceanographic Institution for analysis by first embedding the samples in epoxy resin. The rock and glass chips were then polished using SiC followed by water-based diamond suspensions. Samples were polished to 0.25 μm quality and finished with colloidal silica. Rock chips of Sahara 99555 and D'Orbigny were plucked from the epoxy and embedded in a single indium metal sample holder. The D'Orbigny glass bead was also removed from the epoxy and mounted in a separate indium metal sample holder. Three reference materials were added to the indium mounted samples: Suprasil 3002 pure SiO_2 glass (1 $\mu g/g$ H_2O, provided by

43

Heraeus Quarzglas, Switzerland), Herasil 102 pure SiO_2 glass (55 μg/g H_2O, provided by Heraeus), and ALV 519-4-1 mid-ocean ridge basalt glass (1700 μg/g H_2O).

3.4.2 SEM

Scanning electron microscope (SEM) mapping was conducted on chips of D'Orbigny and Sahara 99555. We used the JEOL 8600F field emission SEM at the NASA Johnson Space Center in Houston equipped with an energy dispersive spectroscopy (EDS) detector. The sample was coated before analysis with a layer ca. 10 nm of carbon using a sputter coater. EDS maps were collected and processed with the JEOL manufacturer's software. Element maps of P, S, and Ca were used to identify silicophosphates in this study. Maps were collected using 15 kV and 700 pA accelerating voltage and beam current, respectively. Care was taken to expose the silicophosphates for a minimum amount of time to ensure the least amount of H migration possible (*53*). Regardless, the amount of H-isotope fractionation caused by electron beam exposure is <50 ‰ for several minutes of exposure to a beam current of 20 nA (*53*); therefore a 700 pA beam will likely cause less H isotope fractionation than a 20 nA beam.

3.4.3 EPMA

Electron probe microanalysis (EPMA) was conducted on the D'Orbigny glass bead to measure major and minor element concentrations. We used a JEOL JXA-8530F Hyperprobe equipped with 5 wavelength dispersive spectrometers housed at NASA Johnson Space Center in Houston. The sample was coated before analysis with ca. 15 nm of carbon using a sputter coater. Data were collected using the JEOL manufacturer's software, and matrix corrections were implemented using a ZAF correction procedure. The D'Orbigny glass bead was analyzed using 15 kV and 15 nA accelerating voltage and beam current, respectively. A beam diameter of 10 μm was used for all analyses. We analyzed the glass bead for the elements Si, Ti, Al, Cr, Fe, Mn, Mg, Ca, Na, K, and P. We standardized using a number of in-house standards including VG2 MORB (Si), rutile (Ti), A99 Hawaiian basalt (Al, Fe), chromite (Cr), rhodonite (Mn), diopside (Mg, Ca), albite (Na), orthoclase (K), and Wilberforce apatite (P). The quality of all glass analyses was assessed and analyses were discarded if they had totals below 99 % or above 101

%. Out of the 163 analyses conducted for this study, we discarded 4 analyses due to totals that were >101 %. Backscattered electron images and secondary electron images were also collected with the JEOL JXA-8530F Hyperprobe.

3.4.4 LA-ICP-MS

3.4.4.1 Major and Trace element analyses: Major and trace elements were measured in the D'Orbigny glass bead by laser ablation inductively coupled plasma mass spectrometry (LA-ICP-MS) using a Photon Machines 193 nm excimer laser into a Thermo iCapQ quadrupole mass spectrometer located at the Carnegie Institution of Washington. No reaction gas was used in the collision cell. Backgrounds were measured for 20 s with the laser off, and intensities were measured for 30 s with the laser ablating after signal ramp-up; wash-out time between successive analyses was 90 s. The crater diameter was 75 µm and 4 µm deep (100 nm/shot ablation rate). Major and trace element data were reduced using the LasyBoy v3.77g software for MS Excel provided by Joel Sparks (Boston University), with calibrations provided by analysis of MPG-DING glasses (GOR128g, GOR132g, KL2g, ML3Bg, BM90-21g) (*54*) and USGS glasses (BHVO-2g, BCR-2g, BIR-1g, GSD-1g, GSC-1g, GSA-1g) (*55*). Secondary standard glass WASVNTR-032 and MORB from the East Pacific Rise (*56*) were analyzed 8 times interspersed with analysis of D'Orbigny glass. The results yielded relative standard deviations (RSD) of 2% or better for all major elements; RSD for trace elements was Sc (2.5%), V (0.5%), Cr (0.9%), Co and Rb (0.6%), Ni and Ba (2.2%), Cu (0.8%), Zn (1.0% above 50 µg/g), Sr (3.6%), Y (2.8%), Zr (3.0%), Nb (2.0%), Cs (3.1%), 4% or better for REE, Hf, Ta, W, Pb, Th and U (table S1). Major element data of D'Orbigny glass obtained by laser ablation were adjusted by multiplication factors based on ratios of reported-to-measured values for WASVNTR-032 (*56*), whereas trace element data are reported as measured; trace element data for WASVNTR-032 agreed with reported values (*56*) to within 10 % except for Nb for which our measured values were 14 % higher.

3.4.4.2 *U-Pb isotope analysis:* Uranium and Pb isotope compositions of 10 silicophosphate grains in D'Orbigny were measured by LA-ICP-MS. Measurements were made with a

PhotonMachines *Analyte 193* laser ablation system coupled to a Varian *810* quadrupole ICP-MS located at the University of Houston. Data were acquired with a laser spot size of 15 μm, 8 Hz repetition rate, an energy density of 3 J/cm^2, and He carrier gas flow rate of 0.500 L/min. On-peak backgrounds were measured for 20 s with the laser off prior to each 20 s of sample ablation. Isotopes of ^{201}Hg, ^{202}Hg, ^{204}(Hg+Pb), ^{206}Pb, ^{207}Pb, ^{208}Pb, ^{232}Th, and ^{238}U were measured. The ^{204}Hg backgrounds were 968 ± 110 (2 σ) counts per second (cps); ^{204}Pb ion intensities of less than 100 cps were not accurately measured. Isotope data were corrected for instrumental element and isotope fractionations with in-house standards of 958 ±13 Ma Bear Lake apatite (*57*) and 473.5 ±0.7 Ma Madagascar apatite (*58*) following methods outlined in ref (*59*). Terrestrial standards were corrected for common Pb by monitoring ^{204}Pb. Silicophosphate grains were not corrected for common Pb because ^{204}Pb intensities were too low for accurate measurements and the corrections are small considering the overall low ^{204}Pb/^{206}Pb ratios. All systematic and random uncertainties are propagated following methods outlined in (*59*).

3.4.5 NanoSIMS

The isotopes of H (deuterium, D and H) were measured in olivine and silicophosphate, from D'Orbigny and Sahara 99555. The D'Orbigny glass bead was measured for H isotope compositions as well as H, C, F, and Cl concentrations. NanoSIMS measurements were conducted on a Cameca NanoSIMS 50L at the Carnegie Institution of Washington. Before measuring, our indium metal sample mount was cleaned with distilled water and ethanol and dried in a vacuum oven for a week at 50 °C. The samples were then taken out of the vacuum oven and gold coated. After gold coating, the sample was placed into the instrument to obtain a pressure of lower than 9 x 10^{-8} Pa (~7 x 10^{-10} torr) in the analysis chamber.

We used methods of (*19*) to measure D/H in olivine, glass, and phosphates. Briefly, a focused 15 nA Cs$^+$ primary beam was rastered to produce a 20 x 20 μm^2 pre-sputter crater. During our analysis, we used a 10 x 10 μm^2 raster and used the Cameca software to eliminate the outer portions of our crater such that we counted ions from the central 4 x 4 μm^2 of the SIMS pit. Mass resolving power (MRP) was nominally 2000 using the Cameca definition, or an MRP of ~2000

m/Δm at 10% peak height. Separation of H_2 from D is unnecessary, as the production of H_2 is less than 1.5 x 10^{-3}, which permits high precision (2–3 ‰) measurements at low mass resolving power (60). Using multi-collection mode, we counted on masses ^1H, ^2H, and ^{12}C. Hydrogen (^1H) background measured throughout the session was ~ 1 x 10^6 counts/s, which translates to 8 μg/g H_2O, and the D/H of the background was roughly terrestrial. Backgrounds were corrected by subtracting counts of H and D from our low water reference material, Suprasil, from our olivine, glass, and phosphate measurements. All errors were propagated from measured backgrounds and analytical uncertainties. Instrumental drift and D/H instrumental mass fractionation was corrected daily by measuring an internal reference basaltic glass, ALV 519-4-1 (1700 μg/g H_2O, δD = -72 ‰) at regular intervals throughout each analytical session. Drift was ~160 ‰ throughout a given day.

3.5. Results

3.5.1 Major element concentrations of the glass bead

In addition to glass, we identified anhedral to subhedral spinel crystals ($MgAl_2O_4$) by EDS as a minor phase within the glass bead (Fig. 1C). We avoided the spinel crystals during the glass analyses. We conducted two roughly perpendicular core-rim traverses on the bead by EPMA. All of the EPMA analyses from both traverses are available in the supplementary materials (table S2). The glass bead was homogenous from core to rim and did not exhibit detectable zoning. We determined the average composition of the bead from all 159 analyses from both traverses (table 1). The composition of the glass bead is that of an alkali-depleted metaluminous foidite with a Mg# (100 x molar Mg/(Mg+Fe)) of 35. The composition of the glass bead analyzed here is similar in composition to other glass beads reported from D'Orbigny (51, 61).

3.5.2 Trace element content of glass bead

We performed one LA-ICP-MS transect across the D'Orbigny glass bead, adjacent to the EPMA transect. The glass is relatively homogeneous in most elements (tables 1 & 2), except for the alkali metals at the crystallized end of the bead and Ni at both edges. The chondrite-normalized rare-earth element content decreases with increasing atomic number, and shows a small positive

Eu anomaly. Our trace element data agree with that of (*61*), except our glass bead is enriched in MgO and Ni.

3.5.3 Pb-isotope composition of phosphates

Uranium-Pb isotope analyses of silicophosphate grains from D'Orbigny yielded a weighted average ^{207}Pb/^{206}Pb age of 4568 ±20 Ma (n = 10, MSWD = 1.0) and an upper intercept U-Pb concordia age of 4572 ±49 Ma (n = 10; MSWD = 1.1) (table 3, Fig 2). Analyses of our in-house external standard of Yates Mine (equals Otter Lake of ref *62*), yielded a weighted average age of 932 ±19 Ma, which is in agreement with previous studies (*62*) (all uncertainties are listed as 2σ).

3.5.4 Volatile element analyses

3.5.4.1 Olivine: We performed several core to rim transects and individual analyses on olivine grains in D'Orbigny and Sahara 99555. Our spallation correction for D/H uses the data of Füri and Deloule (*63*) forcing the relationship between counts on D and exposure age through the origin and propagating error on the slope. This spallation correction method is different from previous studies (*17, 19, 64, 65*), which use the D production rate of Merlivat et al. (*66*), and assume an arbitrary uncertainty to the D production rate. The spallation correction for olivine was ≦179 ‰, given the low water content of olivine and the young exposure age of angrites (*67*). The spallation corrected δD (δD = (((D/H$_{sample}$)/(D/H$_{VSMOW}$)) − 1) x 1000, where VSMOW = Vienna standard mean ocean water D/H = 0.00015576) in olivine range from -146 to +61 ‰, with a weighted mean of -31 ± 39 ‰ (2 SE, n=13), excluding our 1 olivine measurement adjacent to a mesostasis region (table 4; Fig. 3). The observed range in values is relatively large (table 4), but measuring D/H at <19 μg/g H$_2$O is expected to be afflicted with large uncertainties (*19*).

3.5.4.2 Silicophosphate: We measured the D/H of several silicophosphate grains in D'Orbigny and Sahara 99555. The δD varies from -205 to +1034 ‰ for D'Orbigny and -262 to -35 ‰ in silicophosphates from Sahara 99555 (table 5; Fig. 3). The water content estimated from raw

counts on ^1H range from 85 to 1892 μg/g for silicophosphates in D'Orbigny and 36–255 μg/g in silicophosphates in Sahara 99555, but these values are approximations because no internal reference mass was measured (such as ^{18}O) to account for variations in ion yield.

3.5.4.3 D'Orbigny glass bead: We measured one transect across the glass bead to measure volatile element concentrations and another transect to measure D/H, both of which were parallel and adjacent to one of the EPMA and LA-ICP-MS transects. The glass bead is nearly homogeneous in volatile element concentrations (table 6). The spallation corrected δD of the glass bead does not correlate with H_2O content, and water concentration and D/H do not vary systematically with distance across the glass bead (table 6 & 7). Therefore, we conclude that the bead is homogenous in D/H and volatile concentrations, 69 ± 1 μg/g H_2O, 3 ± 0.3 μg/g C, 5 ± 0.03 μg/g F, 2 ± 0.08 μg/g Cl (uncertainty 2 SE, n=31).. δD analyses in the glass bead range from -154 to +115 ‰. The weighted average δD of the glass bead is -16 ± 26 ‰ (2 SE n=29).

3.6. Discussion

3.6.1 Size of the Angrite Parent Body

The size of the APB is poorly constrained, unlike the parent body of the eucrite-howardite-diogenite (HED) clan, which is likely the asteroid 4-Vesta (R = 262.7 km) (*68-70*). Asteroids that have similar reflectance spectra as angrites are limited to bodies with radii of <34 km (*71*), therefore the main parent body has not been observed or the APB is extremely small. Accretion and melting models suggest that melting could occur in parent asteroids as small as ~60 km in radius, if the APB accreted within the first ~2 Myr of solar system history (*72*). Some have suggested that the APB was a major body in the early solar system based on the metamorphic history of plutonic angrites (*73, 74*). A quantitative estimate of the minimum size of the APB can be inferred from the fact that gravity was strong enough on the APB for basalts to be preserved and not lost to space during eruption and degassing (*44, 75, 76*). Previous studies of igneous meteorite groups that lack basalts, e.g., aubrites, ureilites, and acapulcolites, concluded that these were derived from parent bodies that likely had a radius smaller than 100 km if the parental liquids of the basalts had at least hundreds of μg/g volatiles (*44, 75, 76*). Following the same

49

logic, the APB must have had a radius >100 km because basalts were present on its surface (*44*). Further, we can estimate the size of the APB by using the solubility of H and C in basaltic melts. To obtain a conservative estimate of the minimum size of the APB we assume that melting occurred vapor saturated and that melting occurred at the base of the mantle, i.e., at the core-mantle boundary. We use a primitive melt H_2O and C content of 1500 µg/g H_2O and 1100 µg/g C (*42*), which were obtained by measuring the cores of olivine that were zoned in H and C and using experimentally determined partition coefficients (*77, 78*). The olivine water content strongly correlates with olivine major elements; therefore a primitive melt composition was calculated. We used a vapor saturation model for basaltic melts (*79*), which assumes OH (which degasses as H_2O) and CO_3 (which degasses as CO_2) are the most soluble H-C-O species. At low oxygen fugacity H_2, CH_4, and CO would likely be stable, although the solubility and speciation of reduced H and C species are highly dependent on pressure, temperature, and oxygen fugacity (*80-83*). These reduced H and C species have substantially lower solubility in silicate melts relative to OH and CO_3 (*80-82, 84*), meaning that if we assume any C and H in the primitive angrite melt were reduced H-C-O species, the required confining pressure would be substantially higher and, thereby, require a larger planetary body. For example, if we incorporate CH_4 as the primary C-bearing volatile species and extrapolate the solubility from experimental data (*82*), then an enormous minimum pressure of ~ 8 GPa is required. In addition to the assumption of primarily oxidized C-H-O volatile species, we also assume that no loss of volatiles took place before the first olivines in D'Orbigny and Sahara 99555 crystallized, which is reasonable given that olivine cores from both meteorites have identical C and H contents (REF). However, any degassing that occurred between melting and crystallization of the first olivines would act to lower the volatile concentrations, which would yield a lower confining pressure of melting and, thereby, underestimate the size of the parent body. Therefore, all the assumptions that we use in the model calculation act to produce a minimum size estimate of the APB.

Based on the solubility model (*79*) a confining pressure of at least 166 MPa is required to maintain primary D'Orbigny and Sahara 99555 volatile abundances. We calculate a depth vs. radius of planetesimals, where all melting occurs at 166 MPa, using different size estimates for the core of the APB (15%, 25% and 40% of the total radius). We assume a homogenous core

density of 8000 kg/m^3 and a homogeneous mantle density of 3200 kg/m^3 (*85, 86*) and calculate the pressure vs. depth for the APB as a function of the size of the total body. The smallest possible parent body is obtained by melting at the core-mantle boundary (at the edge of the forbidden zone in Figure 4) for the largest core size, because of the higher density of the core compared to the silicate mantle. We assume that the largest likely core size of the APB is ~40%, which produces a minimum APB radius of 270 km (Fig. 4). If instead, we use the bulk density of 4-Vesta (3456 kg/m3; *87*) for the APB, then the APB radius is estimated to be ≧340 km, compared to a radius of ~263 km for 4-Vesta. Therefore, the APB was likely a major body in the inner solar system, and our most conservative estimates place the APB (≧270 km) at approximately the size of 4-Vesta (~263 km). Following previous studies (*49*), we suggest that the APB must have been disrupted early in its history so that no evidence of shock or brecciation is preserved in angrites.

3.6.2 Degassing on the Angrite Parent Body

The melt that formed D'Orbigny, Sahara 99555 and the D'Orbigny glass bead, along with other angrites was likely reduced but transitioned to a more oxidized magma during crystallization and subsequent degassing (*44, 47, 48, 88*). The hydrous species in a reduced basaltic melt with low water contents is H_2O, OH, and H_2 (*80, 89*), but hydrous species have limited solubility in magmas at low pressure (*79*). Therefore, degassing is likely to occur in asteroidal settings. However due to their different petrologic formation histories, bulk D'Orbigny, bulk Sahara 99555 and the D'Orbigny glass bead are unlikely to have experienced the same degassing histories.

3.6.2.1 Major and trace element content of the D'Orbigny glass bead and the case for missing volatile elements: As mentioned previously, the bulk composition of the D'Orbigny rock and the D'Orbigny glass bead are all very similar (tables 1 & 2); the average major element (MgO, Al_2O_3, SiO_2, P_2O_5, CaO, TiO_2, and FeO) difference between the D'Orbigny bead and D'Orbigny bulk rock is only ~3 % relative. However, the difference in MgO is 18 % relative. If we assume the D'Orbigny rock and glass bead were co-magmatic, then we can employ a fractional

51

crystallization model (*90*) to directly compare the composition of the glass to the bulk rock. We modeled fractionation of olivine in equilibrium with the parental melt from the more primitive glass bead to reach the MgO content of the D'Orbigny whole rock; fractionating just olivine keeps the difference between the average major element contents of the glass bead and the D'Orbigny bulk rock composition at a minimum. The D'Orbigny glass composition must fractionate 4% olivine to obtain a major element difference of less than 2%, including MgO. Because only 4% olivine fractionation is required, elements that are compatible in olivine (e.g., Ni) are expected to be depleted in the D'Orbigny whole rock relative to the D'Orbigny glass bead (table 2), whereas incompatible elements in olivine should remain practically unchanged (table 1). For example, if the partition coefficient for Ni between ~Fo_{60} olivine and D'Orbigny melt is on the order of 17 (*91*), then fractionation of olivine *reduces* the Ni content of primitive melt (glass bead) from 122 to 63 μg/g (the more evolved D'Orbigny whole rock), whereas an incompatible element will only *increase* its concentration by roughly 4% relative. The refractory lithophile incompatible element content of the D'Orbigny glass bead are ~3% lower than the D'Orbigny whole rock, consistent with the modeled amount of olivine fractionation. Based on these results, it seems likely that the D'Orbigny glass bead and D'Orbigny whole rock were co-magmatic. Interestingly, the W concentration is roughly a factor of two higher in the glass bead relative to the D'Orbigny whole rock, this elevation in a siderophile element may imply a minor chondritic contamination incorporated into the glass bead.

In contrast to the major and most trace elements, which show similar concentrations between the D'Orbigny glass bead and the D'Orbigny whole rock, volatile elements are depleted in the glass bead. For example H_2O (95% depleted), C (99.9% depleted), Na (36% depleted), Cl (90% depleted), K (87% depleted), Cu (63% depleted), Rb (90% depleted), Cs (87% depleted), Pb (83% depleted – glass vs Sahara 99555) are depleted (table 2, Fig. 5), whereas F is enriched by a factor of ~30. Volatile element ratios, such as H_2O/Ce and C/Nb, should remain invariant during partial melting and crystallization processes (*92, 93*), but H_2O/Ce and CO_2/Nb are depleted in the glass bead relative to the D'Orbigny host rock, which strongly indicates degassing. Intriguingly, the C/Nb of the D'Orbigny whole rock (1100) is higher than the C/Nb of Earth (240) (*92*). This relatively high C/Nb of the APB can be explained by less partitioning of C into the APB core

compared to the Earth, which would require lower mean pressure and/or higher mean fO_2 prevailing during APB core formation than on Earth (*94*).

Degassing is known to fractionate the volatile species, such that H_2O, C, and Cl readily enter the fluid or vapor phase, whereas F remains in the melt (*95*). Therefore, we propose that the parent melt to the D'Orbigny glass bead experienced degassing that depleted H, C, and Cl (as well as volatile metals) in the melt prior to quenching. The high F content of the glass relative to the D'Orbigny bulk rock is intriguing. One possible explanation is that the estimate of the D'Orbigny primitive melt is under-estimated because the partition coefficient used (*96*) was not calibrated for low-pressure basalts.

3.6.2.2 The H isotope composition of the D'Orbigny glass bead and silicophosphates: The parent melt to the D'Orbigny glass bead and the Sahara 99555 melt contained dissolved H_2 and H_2O (inferred from ref *80*), and during quenching probably degassed these species in their original proportions. Here we attempt to model degassing from a primitive melt composition of 1500 µg/g H_2O with an olivine δD of -31 ‰ to a D'Orbigny glass bead H_2O content of 69 µg/g and a δD of -16 ‰. Modeling multiphase degassing is complex because H_2 and H_2O fractionate the H-isotopes in opposite directions, i.e., degassing of H_2 leads to a D-rich melt [89] whereas degassing of H_2O leads to a D-depleted melt (*97*). Isotope fractionation factors (α) of 0.816 for H_2 degassing (*89*) and 1.049 for degassing H_2O (*97*) were used in the degassing modeling. The initial melt must have had an H_2:H_2O molar ratio of ca. 17:83 in the vapor phase to satisfy these isotopic constraints (Fig. 6), which is within the range of thermodynamic predictions of melts with ~1500 µg/g H_2O at an fO_2 near the IW buffer (*80*). Our isotope fractionation model assumes a constant α throughout H_2O degassing, although α should change with the H content of the melt (*97*). A full parameterization of the relationship of H_2O hydrogen isotope fractionation between silicate melt and vapor that takes into account all of these factors simultaneously is not available. An additional complication arises if CH_4 is taken into account, but H-isotope fractionation associated with CH_4 degassing is unkown.

For the slower-cooling D'Orbigny whole rock, a different degassing process is expected. Instead of degassing H_2O and H_2, equilibrium between the hydrous species is expected, and H_2 was probably the only hydrous species lost because the fugacity of H_2 is highest, so that H_2 is the least soluble hydrous species, even though the concentration of H_2 is relatively low compared to H_2O (80, 89). The preferential loss of H_2 during degassing leads to a conversion of H_2O or OH to H_2, which oxidizes the system or consumes an oxygen buffer, e.g., Fe $\rightarrow$ FeO (89). Newly formed H_2 will continue to degas at the expense of OH and H_2O, which continually releases oxygen to the remaining melt in the process (89). If this degassing process took place on the APB, then late-crystallizing phases in slowly cooled angrites that allowed for equilibrium between the hydrous species to be maintained should have an elevated D/H and be relatively oxidized. Indeed, the $Fe^{3+}/\Sigma Fe$ of silicophosphate in the slowly cooled angrite NWA 4590 is 0.8 (98), indicating an oxidizing environment during silicophosphate crystallization and the D/H of some silicophosphates in D'Orbigny are extremely elevated (Fig. 3). The oxidizing nature and elevated D/H of silicophosphates are consistent with degassing of H_2 (48, 89, 99).

To ensure the elevated D/H of the silicophosphates were not an alteration product of a post-crystallization heating event, we determined the age of the silicophoshates in D'Orbigny by [207]Pb–[206]Pb dating, as the Pb system would likely be relatively easily disturbed, as the closure temperature of the U-Pb system in apatite is approximately 500 °C [93]. Although the Pb diffusion characteristics of the silicophosphate grains may be different from those of apatite, significant thermal heating events should cause U-Pb disturbance in these grains. We determined a [207]Pb–[206]Pb date of 4568 ±20 Ma, which we interpret as an igneous crystallization age. This crystallization age is within error of the igneous crystallization age of D'Orbigny determined by bulk techniques, e.g., U–Pb and Hf–W (43, 44, 100), indicating that no high-temperature processes reset these isotope systems after crystallization. Given the [207]Pb–[206]Pb crystallization age of the silicophosphates and undisturbed H concentration gradients in olivine (42), it is likely that the H isotopes in the silicophosphates are also undisturbed, providing further support to the hypothesis that the parent melt of the D'Orbigny whole rock experienced degassing of H_2.

3.6.3 D/H of olivine and the APB

54

The earliest crystallizing phase, olivine, is the best recorder of the H-isotopic composition of a primitive melt if degassing before olivine crystallization and post-crystallization diffusion did not occur. The olivine in D'Orbigny and Sahara 99555 show no evidence for early-stage degassing or post-crystallization diffusion (42, 44). For example, several studies have measured EPMA transects across olivine grains and found that major and minor element zoning in euhedral olivines is consistent with fractional crystallization from a basaltic liquid (44, 101). Olivine is usually the liquidus phase; hence it provides an excellent record of the D/H of the primitive melt. Olivine does not incorporate high abundances of H; therefore D/H measurements are less precise even though they provide the most accurate representation of a primitive melt. The weighted mean δD for our olivine measurements is -31 ± 39 ‰ (2SE n=13), which is our best estimate of the bulk APB δD.

3.6.4 Origin of water in the inner solar system

Here we have derived our best estimate for the δD of the APB, -31 ± 39‰, which is based on the weighted average of olivine D/H measurements. Our estimate for the δD of the APB is within error of the best estimates for δD of Earth and Vesta, and possibly Mars and the Moon (Fig. 7) (17, 19, 20, 89, 99, 102-104). We add literature N isotope data from angrites (105) to our comparison of our H isotope data with those of other inner solar system bodies. Thus far, the best estimate for primitive D/H and $^{15}N/^{14}N$ for all measured inner solar system bodies closely cluster in the carbonaceous chondrite field and well outside the field for protosolar hydrogen and comets (Fig. 7). Degassing models have shown that an unrealistic amount of H_2 loss would have to occur to evolve from a nebular gaseous H-species source signature to a carbonaceous chondrite source signature in D/H–$^{15}N/^{14}N$ space (blue line; Fig. 7)(20). A protosolar-source of water can thus be excluded as the primary source of water for the inner solar system. Here, we present mixing calculations between nebular gaseous H-, carbonaceous chondrite-, and comet-sources of H and N (Figs. 7 & 8) based on published H and N isotope and abundance data for these components (106-116):

$$D/H_m = \frac{f \times M_a \times D/H_a + [(1-f) \times D/H_b \times (1-M_a)]}{f \times M_a + (1-f) \times (1-M_a)} \tag{1}$$

where D/H_m is the hydrogen (or nitrogen) isotope ratio of the mixture, f is the fraction mixed, M_a is the mass fraction of component a in the total (component a and b together comprise the total) and D/H_a and D/H_b are the hydrogen or nitrogen isotope ratios of the reservoirs. We found that no mixture of protosolar and comet H and N is compatible with the isotopic signature of carbonaceous chondrite sources or that of the differentiated bodies (13, 19, 20, 64, 105, 117, 118) (red line; Fig. 7). Taking into account the mixing models, all inner solar system bodies likely received the same main source signature of water and other volatile elements, and this source has the same H and N isotope signature as carbonaceous chondrites, although the question remains, where did carbonaceous chondrites get their water? Some authors have attempted to address this using physical chemical modeling (119), but the precise mechanisms that imparted the H and N isotope signature in carbonaceous chondrites have remained elusive. Regardless, mixing carbonaceous chondrites and a protosolar source or carbonaceous chondrites and comet sources indicate that small amounts of comet material (<0.3% of the accreting mass) and solar material (<0.5%) could make up the volatile compliment of accreted planetary material (see orange and purple lines; Fig. 8). Comet material and the protosolar nebula could not have contributed substantial H and N to the inner planets, which are different from some previous estimates that suggested significantly larger contributions from comets or protosolar material (23, 24, 26, 120).

The highest value of 0.3% addition of cometary material to the terrestrial planets (Figs. 7 & 8) provides an upper limit for the total mass of comets that may have been added to a particular inner solar system body. For example, a conservative estimate for the maximum amount of water from comets that could have been added to Earth can be estimated. The bulk water content of 2000 µg/g H_2O for the silicate Earth is equivalent to approximately 8×10^{21} kg of H_2O, and 0.3% of this would mean that the total mass of cometary water that could have been added was 2.4×10^{19} kg. If we assume comets in the early solar system had similar compositions as they do now, then at most hundreds of thousands of comets may have impacted earth. If Earth has a lower H_2O content than 2000 µg/g, about 400 µg/g (4) then only tens of thousands of comets could have been added to Earth. Our estimate of the maximum number of comet impactors may allow for

the delivery of small amounts of complex organic molecules (*121*), but it does not allow for comets to comprise significant contributors to the H or N budget of differentiated bodies in the inner solar system.

3.7. Conclusions

Based on the volatile concentrations in the D'Orbigny and Sahara 99555 primitive melt, we have estimated the radius of the APB of at least 270 km, and probably $\geqq 340$ km. Major and trace elements in the D'Orbigny glass bead and the D'Orbigny whole rock show that the parent melt of the D'Orbigny glass bead degassed >95 % of its H_2O, C, and Cl, yet F contents were enriched. We suggest that olivine is the best recorder of the D/H of the APB, and its δD was -31 ± 39 ‰. Finally, the maximum amount of comet material (<0.3 %) and protosolar material (<0.5 %) that could have accreted to the inner solar system bodies is constrained through isotope mixing. These are maximum values, and no comet or protosolar material is required to pair the isotope signature of inner solar system differentiated bodies with that of carbonaceous chondrites.

3.8. Acknowledgments

3.9 References

1.   K. Lodders, Solar system abundances and condensation temperatures of the elements. *The Astrophysical Journal*. **591**, 1220–1247 (2003).

2.   H. Wänke, T. Gold, Constitution of terrestrial planets [and discussion]. *Philosophical Transactions of the Royal Society of London A: Mathematical, Physical and Engineering Sciences*. **303**, 287–302 (1981).

3.   E. H. Hauri, A. E. Saal, M. J. Rutherford, J. A. Van Orman, Water in the Moon's interior: Truth and consequences. *Earth and Planetary Science Letters*. **409**, 252–264 (2015).

4.   F. Albarède, Volatile accretion history of the terrestrial planets and dynamic implications. *Nature*. **461**, 1227–1233 (2009).

5.   A. N. Halliday, Mixing, volatile loss and compositional change during impact-driven accretion of the Earth. *Nature*. **427**, 505–509 (2004).

6.   A. Hubbard, D. S. Ebel, Protoplanetary dust porosity and FU Orionis outbursts: Solving the mystery of Earth's missing volatiles. *Icarus*. **237**, 84–96 (2014).

7.   H. E. Schlichting, R. Sari, A. Yalinewich, Atmospheric mass loss during planet formation: The importance of planetesimal impacts. *Icarus*. **247**, 81–94 (2015).

8.   M. Humayun, R. N. Clayton, Potassium isotope cosmochemistry: Genetic implications of volatile element depletion. *Geochimica et Cosmochimica Acta*. **59**, 2131–2148 (1995).

9.   M. Ćuk, S. T. Stewart, Making the Moon from a Fast-Spinning Earth: A Giant Impact Followed by Resonant Despinning. *Science*. **338**, 1047–1052 (2012).

10.   K. Pahlevan, S.-I. Karato, B. Fegley, Speciation and dissolution of hydrogen in the proto-lunar disk. *Earth and Planetary Science Letters*. **445**, 104–113 (2016).

11.   D. C. Rubie *et al.*, Heterogeneous accretion, composition and core–mantle differentiation of the Earth. *Earth and Planetary Science Letters*. **301**, 31–42 (2011).

12.   F. J. Ciesla, G. D. Mulders, I. Pascucci, D. Apai, VOLATILE DELIVERY TO PLANETS FROM WATER-RICH PLANETESIMALS AROUND LOW-MASS STARS. *The Astrophysical Journal*. **804**, 9 (2015).

13.   B. Marty, The origins and concentrations of water, carbon, nitrogen and noble gases on Earth. *Earth and Planetary Science Letters*. **313**, 56–66 (2012).

14.   M. M. Hirschmann, R. Dasgupta, The H/C ratios of Earth's near-surface and deep

reservoirs, and consequences for deep Earth volatile cycles. *Chemical Geology*. **262**, 4–16 (2009).

15. J. J. Barnes *et al.*, An asteroidal origin for water in the Moon. *Nature Communications*. **7**, 11684 (2016).

16. K. L. Robinson *et al.*, Water in evolved lunar rocks: Evidence for multiple reservoirs. *Geochimica et Cosmochimica Acta*. **188**, 244–260 (2016).

17. J. J. Barnes *et al.*, The origin of water in the primitive Moon as revealed by the lunar highlands samples. *Earth and Planetary Science Letters*. **390**, 244–252 (2014).

18. K. Shimizu *et al.*, Two-component mantle melting-mixing model for the generation of mid-ocean ridge basalts: Implications for the volatile content of the Pacific upper mantle. *Geochimica et Cosmochimica Acta*. **176**, 44–80 (2016).

19. A. E. Saal, E. H. Hauri, J. A. Van Orman, M. J. Rutherford, Hydrogen Isotopes in Lunar Volcanic Glasses and Melt Inclusions Reveal a Carbonaceous Chondrite Heritage. *Science*. **340**, 1317–1320 (2013).

20. A. R. Sarafian, S. G. Nielsen, H. R. Marschall, F. M. McCubbin, B. D. Monteleone, Early accretion of water in the inner solar system from a carbonaceous chondrite–like source. *Science*. **346**, 623–626 (2014).

21. T. J. Barrett *et al.*, The abundance and isotopic composition of water in eucrites. *Meteoritics & Planetary Science*. **51**, 110–1124 (2016).

22. A. R. Sarafian, T. John, J. Roszjar, M. J. Whitehouse, Chlorine and hydrogen degassing in Vesta's magma ocean. *Earth and Planetary Science Letters*, 1–9 (2016).

23. A. H. Delsemme, Cometary origin of carbon and water on the terrestrial planets. *Advances in Space Research*. **12**, 5–12 (1992).

24. A. H. Delsemme, The deuterium enrichment observed in recent comets is consistent with the cometary origin of seawater. *Planetary and Space Science*. **47**, 125–131 (1998).

25. A. Delsemme, in *Comets and the Origin and Evolution of Life* (Springer, New York, NY, 1997), pp. 29–67.

26. P. Hartogh *et al.*, Ocean-like water in the Jupiter-family comet 103P/Hartley 2. *Nature*. **478**, 218–220 (2011).

27. K. R. Grazier, Jupiter: Cosmic Jekyll and Hyde. *Astrobiology*. **16**, 23–38 (2016).

28. A. Morbidelli, J. I. Lunine, D. P. O'Brien, S. N. Raymond, K. J. Walsh, Building terrestrial planets. *Annual Reviews of Earth and Planetary Sciences*. **40**, 251–275

(2012).

29. A. Morbidelli *et al.*, Source regions and timescales for the delivery of water to the Earth. *Meteoritics & Planetary Science*. **35**, 1309–1320 (2000).

30. D. P. O'Brien, K. J. Walsh, A. Morbidelli, S. N. Raymond, A. M. Mandell, Water delivery and giant impacts in the "Grand Tack" scenario. *Icarus*. **239**, 74–84 (2014).

31. K. J. Walsh, A. Morbidelli, S. N. Raymond, D. P. O'Brien, A. M. Mandell, A low mass for Mars from Jupiter's early gas-driven migration. *Nature*. **475**, 206–209 (2011).

32. S. A. Wilde, J. W. Valley, W. H. Peck, C. M. Graham, Evidence from detrital zircons for the existence of continental crust and oceans on the Earth 4.4 Gyr ago. *Nature*. **409**, 175–178 (2001).

33. J. E. Chambers, Planetary accretion in the inner Solar System. *Earth and Planetary Science Letters*. **223**, 241–252 (2004).

34. T. Kleine *et al.*, Hf–W chronology of the accretion and early evolution of asteroids and terrestrial planets. *Geochimica et Cosmochimica Acta*. **73**, 5150–5188 (2009).

35. Y. Chen *et al.*, Water, fluorine, and sulfur concentrations in the lunar mantle. *Earth and Planetary Science Letters*. **427**, 37–46 (2015).

36. E. H. Hauri, T. Weinreich, A. E. Saal, M. C. Rutherford, J. A. Van Orman, High pre-eruptive water contents preserved in lunar melt inclusions. *Science*. **333**, 213–215 (2011).

37. P. Lucey *et al.*, *Understanding the Lunar Surface and Space-Moon Interactions* (Reviews in Minerology and Geochemistry, Chantilly, Virginia, 2006), vol. 60.

38. A. E. Saal *et al.*, Volatile content of lunar volcanic glasses and the presence of water in the Moon's interior. *Nature*. **454**, 192–195 (2008).

39. L. E. Borg, J. N. Connelly, M. Boyet, R. W. Carlson, Chronological evidence that the Moon is either young or did not have a global magma ocean. *Nature*. **477**, 70–72 (2011).

40. A. R. Sarafian, M. F. Roden, A. E. Patiño Douce, The nature of volatiles in eucrites: Clues from apatite. *Meteoritics & Planetary Science*. **48**, 2135–2154 (2013).

41. M. Touboul, P. Sprung, S. A. Aciego, B. Bourdon, T. Kleine, Hf-W chronology of the eucrite parent body. *Geochimica et Cosmochimica Acta*. **73**, 5150–5188 (2015).

42. A. R. Sarafian *et al.*

43. Y. Amelin, U–Pb ages of angrites. *Geochimica et Cosmochimica Acta*. **72**, 221–232

(2008).

44. K. Keil, Angrites, a small but diverse suite of ancient, silica-undersaturated volcanic-plutonic mafic meteorites, and the history of their parent asteroid. *Chemie der Erde - Geochemistry*. **72**, 191–218 (2012).

45. M. Schiller, J. N. Connelly, A. C. Glad, T. Mikouchi, M. Bizzarro, Early accretion of protoplanets inferred from a reduced inner solar system 26 Al inventory. *Earth and Planetary Science Letters*. **420**, 45–54 (2015).

46. D. W. Mittlefehldt, M. M. Lindstrom, Geochemistry and genesis of the angrites. *Geochimica et Cosmochimica Acta*. **54**, 3209–3218 (1990).

47. P. L. King *et al.*, Redox History of Early Solar System Planetismals Recorded in the D'Orbigny Angrite. *Lunar and Planetary Science Conference*. **43**, 2436 (2012).

48. N. Shirai, M. Humayun, K. Righter, Moderately siderophile element abundances in angrites. *Meteoritics and Planetary Science Supplement*. **43**, 5294 (2008).

49. E. R. D. Scott, W. F. Bottke, Impact histories of angrites, eucrites, and their parent bodies. *Meteoritics & Planetary Science*. **46**, 1878–1887 (2011).

50. S. L. Hwang, P. Shen, H. T. Chu, T. F. Yui, Tsangpoite: The Unknown Calcium Silico Phosphate Phase in the Angrite D'Orbigny. *Lunar and Planetary Science Conference* (2016).

51. G. Kurat *et al.*, D'Orbigny: A non-igneous angritic achondrite? *Geochimica et Cosmochimica Acta*. **68**, 1901–1921 (2004).

52. J. W. Delano, Pristine lunar glasses: Criteria, data, and implications. *Journal of Geophysical Research: Solid Earth*. **91**, 201–213 (1986).

53. J. J. Barnes *et al.*, Accurate and precise measurements of the D/H ratio and hydroxyl content in lunar apatites using NanoSIMS. *Chemical Geology*. **337-338**, 48–55 (2012).

54. K. P. Jochum *et al.*, MPI-DING reference glasses for in situ microanalysis: New reference values for element concentrations and isotope ratios. *Geochemistry, Geophysics, Geosystems*. **7**, 1–44 (2006).

55. K. P. Jochum, M. Willbold, I. Raczek, B. Stoll, K. Herwig, Chemical Characterisation of the USGS Reference Glasses GSA-1G, GSC-1G, GSD-1G, GSE-1G, BCR-2G, BHVO-2G and BIR-1G Using EPMA, ID-TIMS, ID-ICP-MS and LA-ICP-MS. *Geostandards Newsletter*. **29**, 285–302 (2005).

56. A. Gale, C. A. Dalton, C. H. Langmuir, Y. Su, J. G. Schilling, The mean composition of

ocean ridge basalts. *Geochemistry, Geophysics, Geosystems*. **14**, 489–518 (2013).

57.   S. N. Thomson, G. E. Gehrels, J. Ruiz, R. Buchwaldt, Routine low-damage apatite U-Pb dating using laser ablation–multicollector–ICPMS. *Geochemistry, Geophysics, Geosystems*. **13**, 1–23 (2012).

58.   D. M. Chew, J. A. Petrus, B. S. Kamber, U–Pb LA–ICPMS dating using accessory mineral standards with variable common Pb. *Chemical Geology*. **363**, 185–199 (2014).

59.   B. Shaulis, T. J. Lapen, A. Toms, Signal linearity of an extended range pulse counting detector: Applications to accurate and precise U-Pb dating of zircon by laser ablation quadrupole ICP-MS. *Geochemistry, Geophysics, Geosystems*. **11**, 1–12 (2010).

60.   E. Hauri *et al.*, SIMS analysis of volatiles in silicate glasses: 1. Calibration, matrix effects and comparisons with FTIR. *Chemical Geology*. **183**, 99–114 (2002).

61.   M. E. Varela *et al.*, Glasses in the D'Orbigny angrite. *Geochimica et Cosmochimica Acta*. **67**, 5027–5046 (2003).

62.   D. M. Chew, P. J. Sylvester, M. N. Tubrett, U–Pb and Th–Pb dating of apatite by LA-ICPMS. *Chemical Geology*. **280**, 200–216 (2011).

63.   E. Füri, E. Deloule, New Constraints on the Production Rate of Cosmogenic Deuterium at the Moon's Surface. *Lunar and Planetary Science Conference*. **47**, 1351 (2016).

64.   R. Tartèse *et al.*, Apatites in lunar KREEP basalts: The missing link to understanding the H isotope systematics of the Moon. *Geology*. **42**, 363–366 (2014).

65.   R. Tartèse, M. Anand, K. H. Joy, I. A. Franchi, H and Cl isotope systematics of apatite in brecciated lunar meteorites Northwest Africa 4472, Northwest Africa 773, Sayh al Uhaymir 169, and Kalahari 009. *Meteoritics & Planetary Science*. **49**, 2266–2289 (2014).

66.   L. Merlivat, M. Lelu, G. Nief, E. Roth, Spallation deuterium in rock 70215. *Lunar and Planetary Science Conference* (1976).

67.   H. Busemann, S. Lorenzetti, O. Eugster, Noble gases in D'Orbigny, Sahara 99555 and D'Orbigny glass—Evidence for early planetary processing on the angrite parent body. *Geochimica et Cosmochimica Acta*. **70**, 5403–5425 (2006).

68.   R. P. Binzel, S. Xu, Chips off of Asteroid 4 Vesta; evidence for the parent body of basaltic achondrite meteorites. *Science*. **260**, 186–191 (1993).

69.   T. B. McCord, J. B. Adams, T. V. Johnson, Asteroid Vesta: Spectral reflectivity and compositional implications. *Science*. **168**, 1445–1447 (1970).

70.   C. T. Russell, C. A. Raymond, R. Jaumann, H. Y. McSween, (University of Arizona Press, 2012), vol. 43, p. 1633.

71.   T. H. Burbine, T. J. McCoy, R. P. Binzel, Spectra of angrites and possible parent bodies. *Lunar and Planetary Science Conference*. **32**, 1857 (2001).

72.   S. Sahijpal, P. Soni, G. Gupta, Numerical simulations of the differentiation of accreting planetesimals with 26Al and 60Fe as the heat sources. *Meteoritics & Planetary Science*. **42**, 1529–1548 (2007).

73.   B. Baghdadi, G. Godard, A. Jambon, Evolution of the angrite parent body: Implications of metamorphic coronas in NWA 3164. *Meteoritics & Planetary Science*. **48**, 1873–1893 (2013).

74.   B. Baghdadi, A. Jambon, J.-A. Barrat, Metamorphic Angrite Northwest Africa 3164/5167 Compared to Magmatic Angrites. *Geochimica et Cosmochimica Acta*. **168**, 1–21 (2015).

75.   L. Wilson, K. Keil, Consequences of explosive eruptions on small solar system bodies: the case of the missing basalts on the aubrite parent body. *Earth and Planetary Science Letters*. **104**, 505–512 (1991).

76.   K. Keil *et al.*, A composite Fe,Ni-FeS and enstatite-forsterite-diopside-glass vitrophyre clast in the Larkman Nunatak 04316 aubrite: Origin by pyroclastic volcanism. *Meteoritics & Planetary Science*. **46**, 1719–1741 (2011).

77.   A. Rosenthal, E. H. Hauri, M. M. Hirschmann, Experimental determination of C, F, and H partitioning between mantle minerals and carbonated basalt, CO2/Ba and CO2/Nb systematics of partial melting, and the CO2 contents of basaltic source regions. *Earth and Planetary Science Letters*. **412**, 77–87 (2015).

78.   E. H. Hauri, G. A. Gaetani, T. H. Green, Partitioning of water during melting of the Earth's upper mantle at H2O-undersaturated conditions. *Earth and Planetary Science Letters*. **248**, 715–734 (2006).

79.   J. E. Dixon, E. M. Stolper, J. R. Holloway, An experimental study of water and carbon dioxide solubilities in mid-ocean ridge basaltic liquids. Part I: Calibration and solubility models. *Journal of Petrology*. **36**, 1607–1631 (1995).

80.   M. M. Hirschmann, A. C. Withers, P. Ardia, N. T. Foley, Solubility of molecular hydrogen in silicate melts and consequences for volatile evolution of terrestrial planets. *Earth and Planetary Science Letters*. **345**, 38–48 (2012).

81.   J. R. Holloway, J. Sigurdur, Volatile solubilities in magmas: Transport of volatiles from mantles to planet surfaces. *Journal of Geophysical Research*. **91**, 1–4 (1986).

82. P. Ardia, M. M. Hirschmann, A. C. Withers, B. D. Stanley, Solubility of CH4 in a synthetic basaltic melt, with applications to atmosphere-magma ocean-core partitioning of volatiles and to the evolution of the Martian atmosphere. *Geochimica et Cosmochimica Acta*. **114**, 52–71 (2013).

83. B. O. Mysen, K. Kumamoto, G. D. Cody, M. L. Fogel, Solubility and solution mechanisms of C-O-H volatiles in silicate melt with variable redox conditions and melt composition at upper mantle temperatures and pressures. *Geochimica et Cosmochimica Acta*. **75**, 6183–6199 (2011).

84. Y. Morizet, M. Paris, F. Gaillard, B. Scaillet, C–O–H fluid solubility in haplobasalt under reducing conditions: An experimental study. *Chemical Geology*. **279**, 1–16 (2010).

85. G. J. CONSOLMAGNO S J, D. T. Britt, The density and porosity of meteorites from the Vatican collection. *Meteoritics & Planetary Science*. **33**, 1231–1241 (1998).

86. D. T. Britt, G. J. Consolmango, Stony meteorite porosities and densities: A review of the data through 2001. *Meteoritics & Planetary Science*. **38**, 1161–1180 (2003).

87. C. T. Russell *et al.*, Dawn at Vesta: Testing the protoplanetary paradigm. *Science*. **336**, 684–686 (2012).

88. G. McKay, L. Le, J. Wagstaff, G. Crozaz, Experimental partitioning of rare earth elements and strontium: Constraints on petrogenesis and redox conditions during crystallization of Antarctic angrite Lewis Cliff 86010. *Geochimica et Cosmochimica Acta*. **58**, 2911–2919 (1994).

89. Z. D. Sharp, F. M. McCubbin, C. K. Shearer, A hydrogen-based oxidation mechanism relevant to planetary formation. *Earth and Planetary Science Letters*. **380**, 88–97 (2013).

90. L. V. Danyushevsky, P. Plechov, Petrolog3: Integrated software for modeling crystallization processes. *Geochemistry, Geophysics, Geosystems*. **12**, 1–32 (2011).

91. R. J. Kinzler, T. L. Grove, S. I. Recca, An experimental study on the effect of temperature and melt composition on the partitioning of nickel between olivine and silicate melt. *Geochimica et Cosmochimica Acta*. **54**, 1255–1265 (1990).

92. A. E. Saal, E. H. Hauri, C. H. Langmuir, M. R. Perfit, Vapour undersaturation in primitive mid-ocean-ridge basalt and the volatile content of Earth's upper mantle. *Nature*. **419**, 451–455 (2002).

93. P. Michael, Regionally distinctive sources of depleted MORB: Evidence from trace elements and H2O. *Earth and Planetary Science Letters*. **131**, 301–320 (1995).

94.   B. J. Wood, Carbon in the core. *Earth and Planetary Science Letters.* **117**, 593–607 (1993).

95.   M. R. Carroll, J. D. Webster, in *Volatiles in Magmas, Reviews in Mineralogy*, M. R. Carroll, J. R. Holloway, Eds. (Washington, DC, 1994), vol. 30, pp. 231–279.

96.   C. Dalou, K. T. Koga, N. Shimizu, J. Boulon, J.-L. Devidal, Experimental determination of F and Cl partitioning between lherzolite and basaltic melt. *Contributions to Mineralogy and Petrology.* **163**, 591–609 (2012).

97.   S. Newman, S. Epstein, E. Stolper, Water, carbon dioxide, and hydrogen isotopes in glasses from the ca. 1340 AD eruption of the Mono Craters, California: constraints on degassing phenomena and initial volatile content. *Journal of Volcanology and Geothermal Research.* **35**, 75–96 (1988).

98.   T. Mikouchi, K. Sugiyama, W. Satake, Y. Amelin, Mineralogy and crystallography of calcium silico-phosphate in Northwest Africa 4590 angrite. *Lunar and Planetary Science Conference.* **42**, 2026 (2011).

99.   R. Tartèse, M. Anand, Late delivery of chondritic hydrogen into the lunar mantle: Insights from mare basalts. *Earth and Planetary Science Letters.* **361**, 480–486 (2013).

100.   T. Kleine, U. Hans, A. J. Irving, B. Bourdon, Chronology of the angrite parent body and implications for core formation in protoplanets. *Geochimica et Cosmochimica Acta.* **84**, 186–203 (2012).

101.   D. W. Mittlefehldt, M. Killgore, M. T. Lee, Petrology and geochemistry of D'Orbigny, geochemistry of Sahara 99555, and the origin of angrites. *Meteoritics & Planetary Science.* **37**, 345–369 (2002).

102.   L. J. Hallis, G. J. Taylor, K. Nagashima, G. R. Huss, Magmatic water in the martian meteorite Nakhla. *Earth and Planetary Science Letters.* **359**, 84–92 (2012).

103.   S. V. S. Murty, R. K. Mohapatra, Nitrogen and heavy noble gases in ALH 84001: Signatures of ancient Martian atmosphere. *Geochimica et Cosmochimica Acta.* **61**, 5417–5428 (1997).

104.   T. Usui, C. M. Alexander, J. Wang, J. I. Simon, J. H. Jones, Meteoritic evidence for a previously unrecognized hydrogen reservoir on Mars. *Earth and Planetary Science Letters.* **410**, 140–151 (2015).

105.   F. A. J. Abernethy *et al.*, Stable isotope analysis of carbon and nitrogen in angrites. *Meteoritics & Planetary Science.* **48**, 1590–1606 (2013).

106.   C. M. O. Alexander *et al.*, The provenances of asteroids, and their contributions to the

65

volatile inventories of the terrestrial planets. *Science.* **337**, 721–723 (2012).

107.   C. Arpigny *et al.*, Anomalous nitrogen isotope ratio in comets. *Science.* **301**, 1522–1524 (2003).

108.   D. Bockelée-Morvan *et al.*, Searches for HCl and HF in comets 103P/Hartley 2 and C/2009 P1 (Garradd) with the Herschel Space Observatory. *Astronomy & Astrophysics.* **562**, A5 (2014).

109.   A. H. Delsemme, The Chemistry of Comets. *Philosophical Transactions of the Royal Society of London A: Mathematical, Physical and Engineering Sciences.* **325**, 509–523 (1988).

110.   D. Hutsemékers *et al.*, Isotopic abundances of carbon and nitrogen in Jupiter-family and Oort Cloud comets. *Astronomy & Astrophysics.* **440**, L21–L24 (2005).

111.   J. F. Kerridge, Carbon, hydrogen and nitrogen in carbonaceous chondrites: Abundances and isotopic compositions in bulk samples. *Geochimica et Cosmochimica Acta.* **49**, 1707–1714 (1985).

112.   E. Lellouch *et al.*, The deuterium abundance in Jupiter and Saturn from ISO-SWS observations. *Astronomy & Astrophysics.* **370**, 610–622 (2001).

113.   A. Meibom *et al.*, Nitrogen and carbon isotopic composition of the Sun inferred from a high-temperature solar nebular condensate. *ApJL.* **656**, L33–L36 (2007).

114.   J. A. Eddy, R. Ise, New Sun: The Solar Results From Skylab. NASA SP-402. *NASA Special Publication.* **402** (1979).

115.   B. Marty *et al.*, Origins of volatile elements (H, C, N, noble gases) on Earth and Mars in light of recent results from the ROSETTA cometary mission. *Earth and Planetary Science Letters.* **441**, 91–102 (2016).

116.   B. Marty, N. Dauphas, Formation and early evolution of the atmosphere. *Geological Society, London, Special Publications.* **199**, 213–229 (2002).

117.   B. Marty, K. Hashizume, M. Chaussidon, R. Wieler, Nitrogen isotopes on the Moon: Archives of the solar and planetary contributions to the inner Solar System. *Space Sci Rev.* **106**, 175–196 (2003).

118.   Y. Miura, N. Sugiura, Nitrogen isotopic compositions in three Antarctic and two non-Antarctic eucrites. *Antarctic Meteorite Research.* **6**, 338 (1993).

119.   L. I. Cleeves *et al.*, The ancient heritage of water ice in the solar system. *Science.* **345**, 1590–1593 (2014).

120. M. J. Mumma, S. B. Charnley, The Chemical Composition of Comets—Emerging Taxonomies and Natal Heritage. *Annual Reviews.* **49**, 471–524 (2011).

121. F. Capaccioni *et al.*, The organic-rich surface of comet 67P/Churyumov-Gerasimenko as seen by VIRTIS/Rosetta. *Science.* **347**, aaa0628–aaa0628 (2015).

122. D. P. Glavin, A. Kubny, E. Jagoutz, G. W. Lugmair, Mn-Cr isotope systematics of the D'Orbigny angrite. *Meteoritics & Planetary Science.* **39**, 693–700 (2004).

123. A. J. V. Riches *et al.*, Rhenium–osmium isotope and highly-siderophile-element abundance systematics of angrite meteorites. *Earth and Planetary Science Letters.* **353**, 208–218 (2012).

124. S. Newman, J. B. Lowenstern, VolatileCalc: a silicate melt–H2O–CO2 solution model written in Visual Basic for excel. *Computers & Geosciences.* **28**, 597–604 (2002).

125. J. E. Dixon, Degassing of alkalic basalts. *American Mineralogist.* **82**, 368–378 (1997).

126. B. O. Mysen, P. Richet, Silicate glasses and melts: properties and structure. **10** (2005).

127. R. Dasgupta, Ingassing, Storage, and Outgassing of Terrestrial Carbon through Geologic Time. *Reviews in Mineralogy and Geochemistry.* **75**, 183–229 (2013).

128. R. Dasgupta, H. Chi, N. Shimizu, A. S. Buono, D. Walker, Carbon solution and partitioning between metallic and silicate melts in a shallow magma ocean: Implications for the origin and distribution of terrestrial carbon. *Geochimica et Cosmochimica Acta.* **102**, 191–212 (2013).

3.10 Figures and Tables

Figure 1

Backscatter electron (BSE) image of D'Orbigny (A), Sahara 99555 (B). (C) Secondary electron image of D'Orbigny glass bead with SIMS pits present. 1 mm scale bar is for images A, B and C. (D) Reflected light image of D'Orbigny highlighting late stage melt region containing silicophosphates; field of view is 500 μm. Major minerals and analysed phases labeled: Ol – olivine, Plg – plagioclase, Di – diopside, Spl, - spinel, Tro – troilite, and SiP – silicophosphate. I and E are indium and epoxy, respectively.
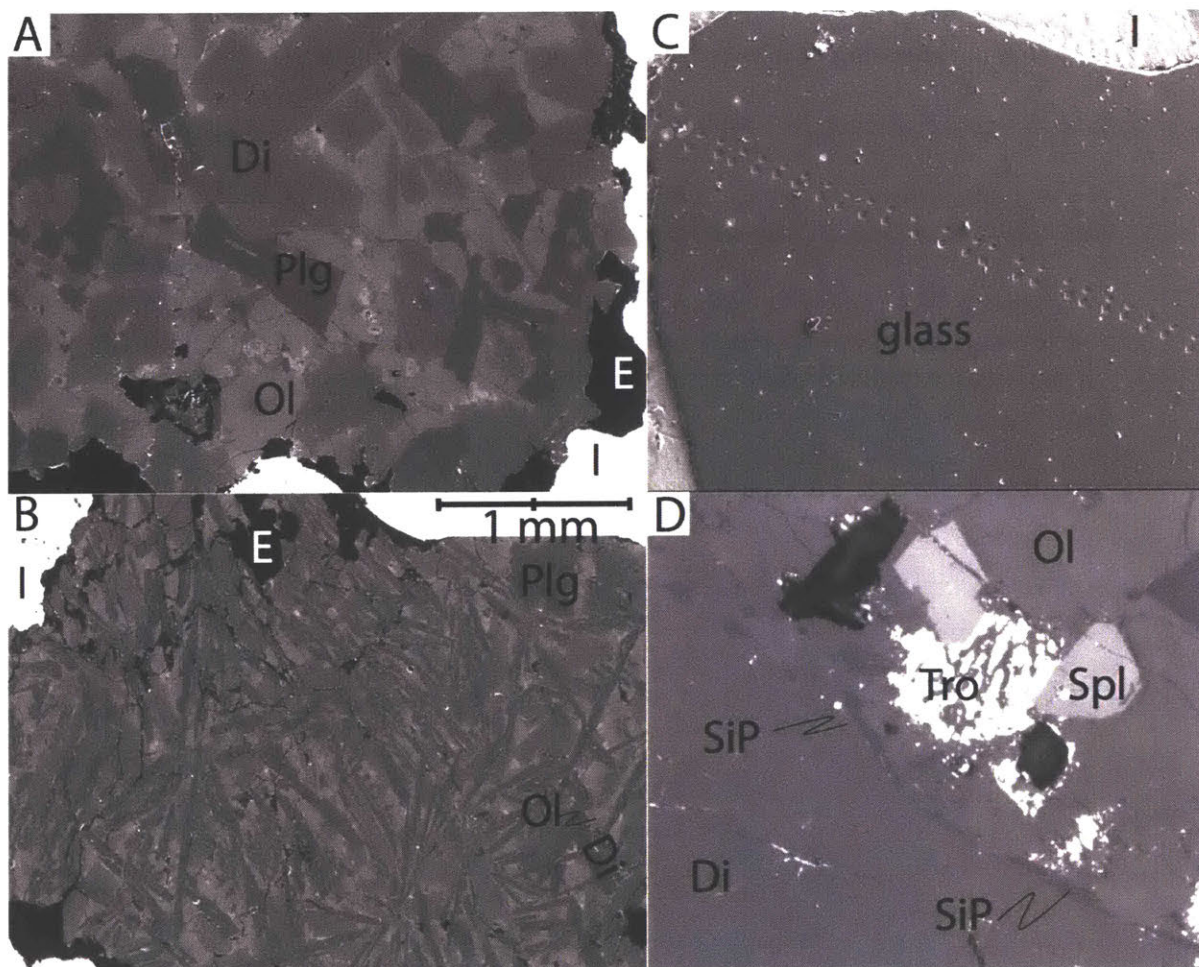
Figure 2

^{207}Pb-^{206}Pb ages of silicophosphates in D'Orbigny with 2σ error bars. Mean age (horizontal line) is 4568 ±20 Ma (2 SE)
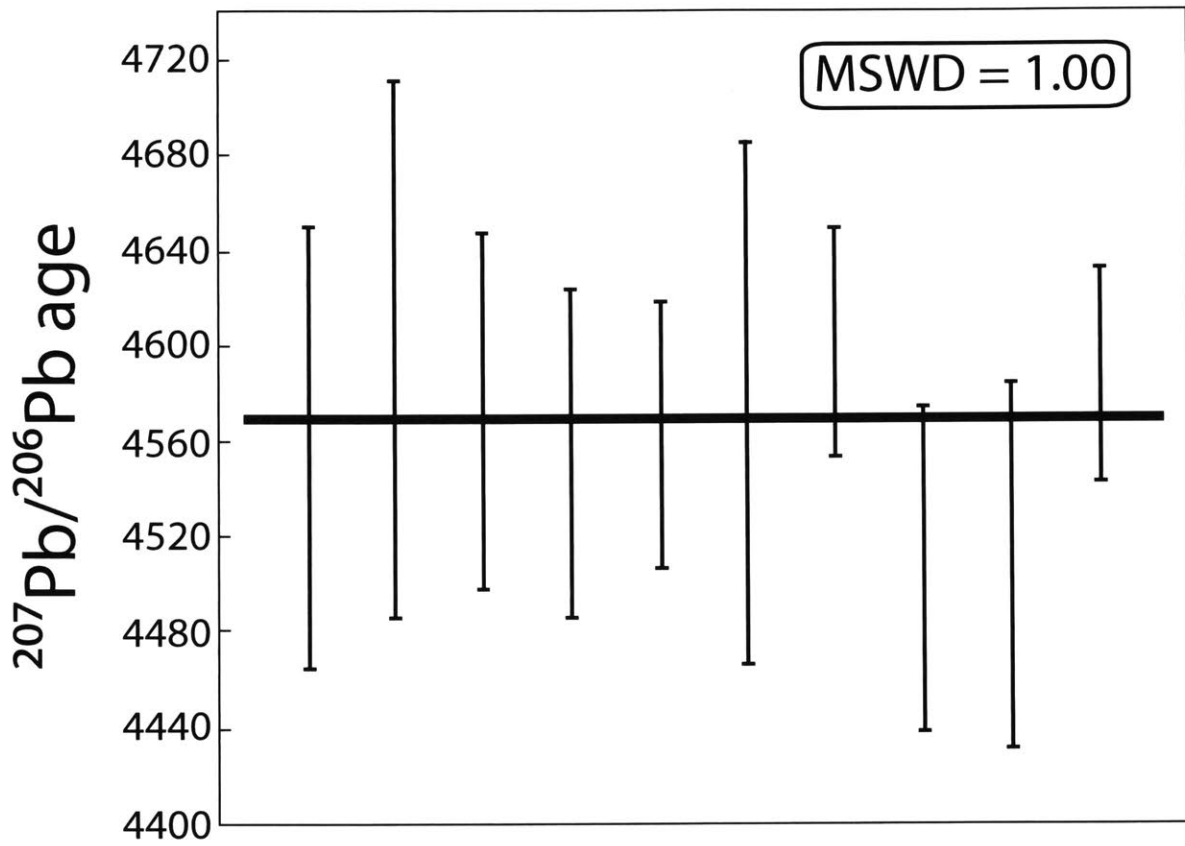
Figure 3

Hydrogen isotopic composition of analysed samples. D'Orbigny glass is a weighted mean of all analyses (n=29). Error bars not visible are smaller than the symbol size.
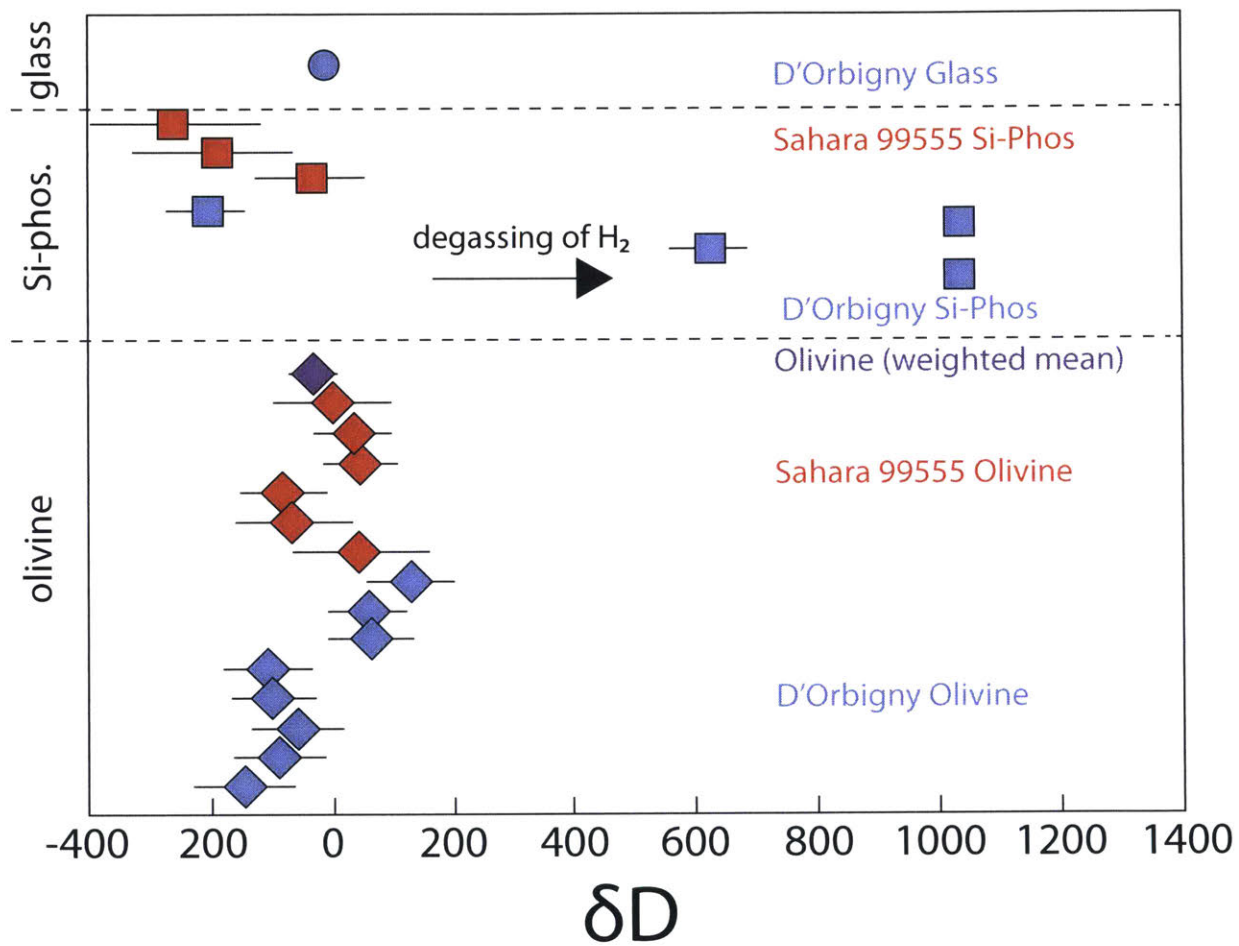
Figure 4

Depth of melting vs. size of body. The fraction of core (by radius) is listed for each curve. The forbidden zone is an area in which the planetesimal is not large enough for melting to occur in the mantle, i.e., silicate melting would have to occur in core of the body.
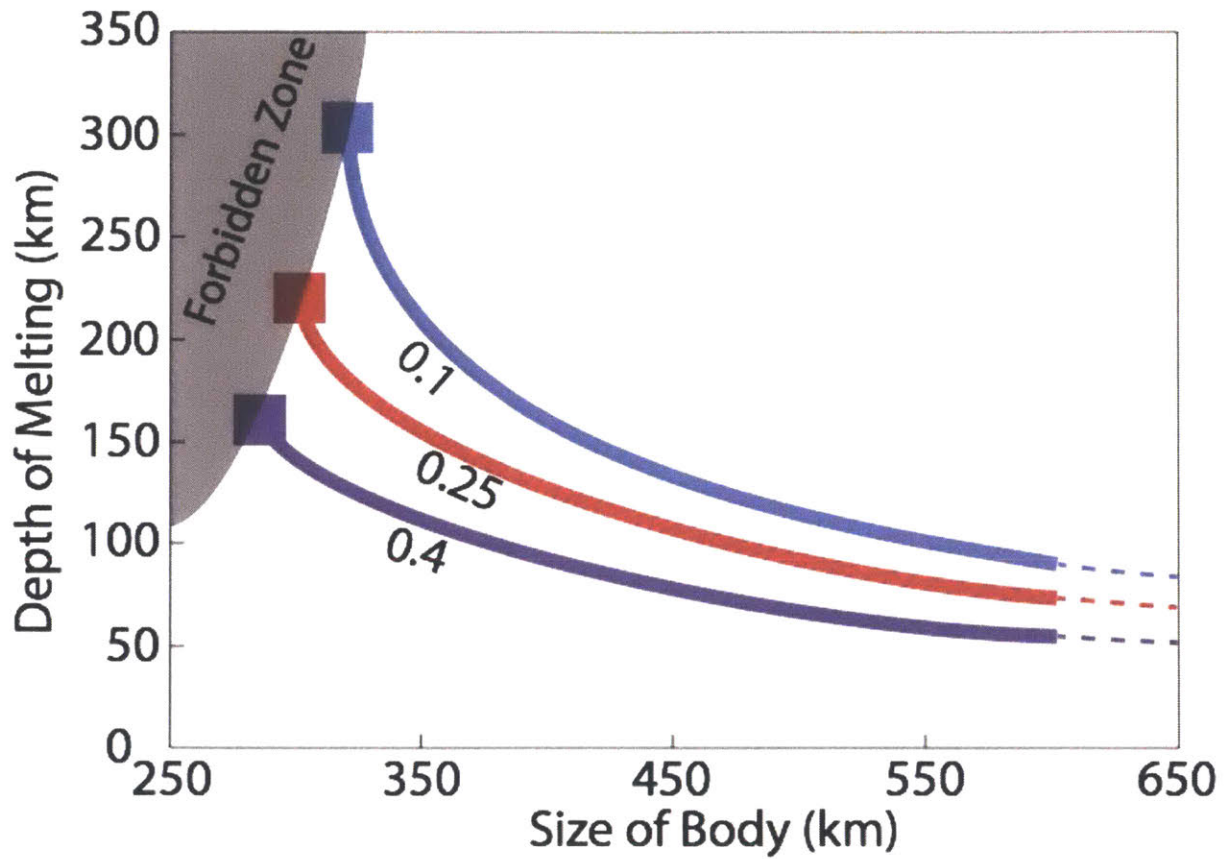
Figure 5

Composition of D'Orbigny glass bead normalized to the D'Orbigny whole rock composition vs nebular condensation temperature of elements. Note volatile elements are systematically depleted relative to the refractory elements. Data from refs (*51, 101, 122, 123*).
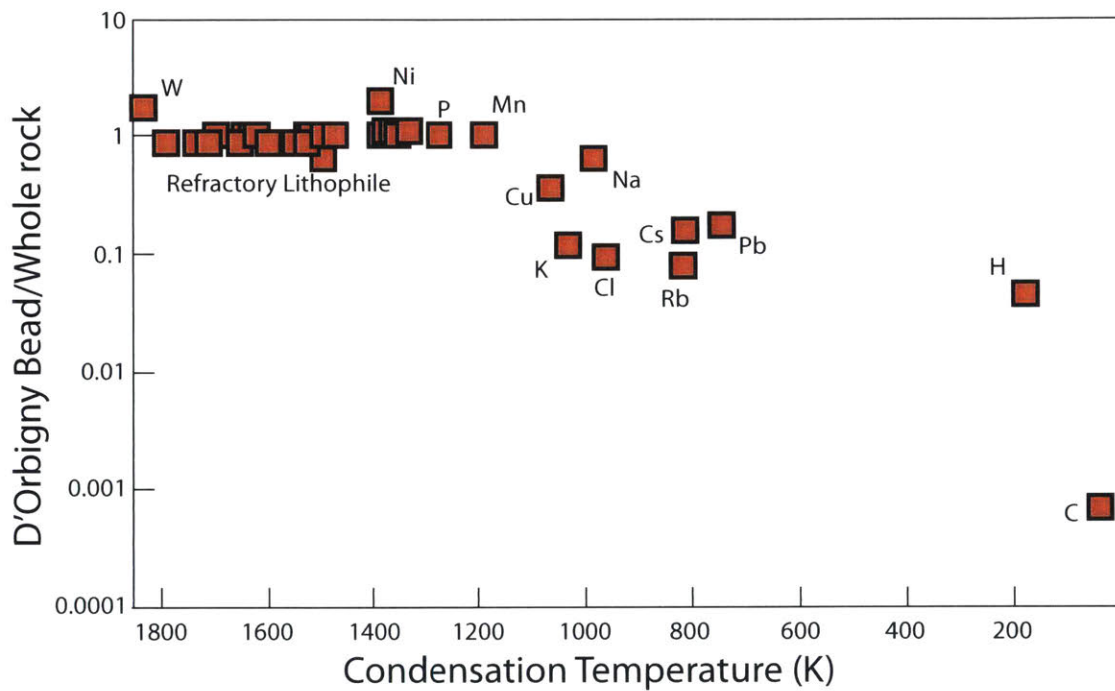
Figure 6

δD vs. water content. Modeled degassing paths with different H_2:H_2O ratios for each line. Best fit is a 17:83 ratio.

Figure 7

D/H, or δD vs. [15]N/^{14}N, or δ^{15}N. Note that degassing a gaseous nebular H source, blue line from ref (20), and mixing a protosolar source (red line) with comets cannot produce a carbonaceous chondrite H and N isotopic signature.
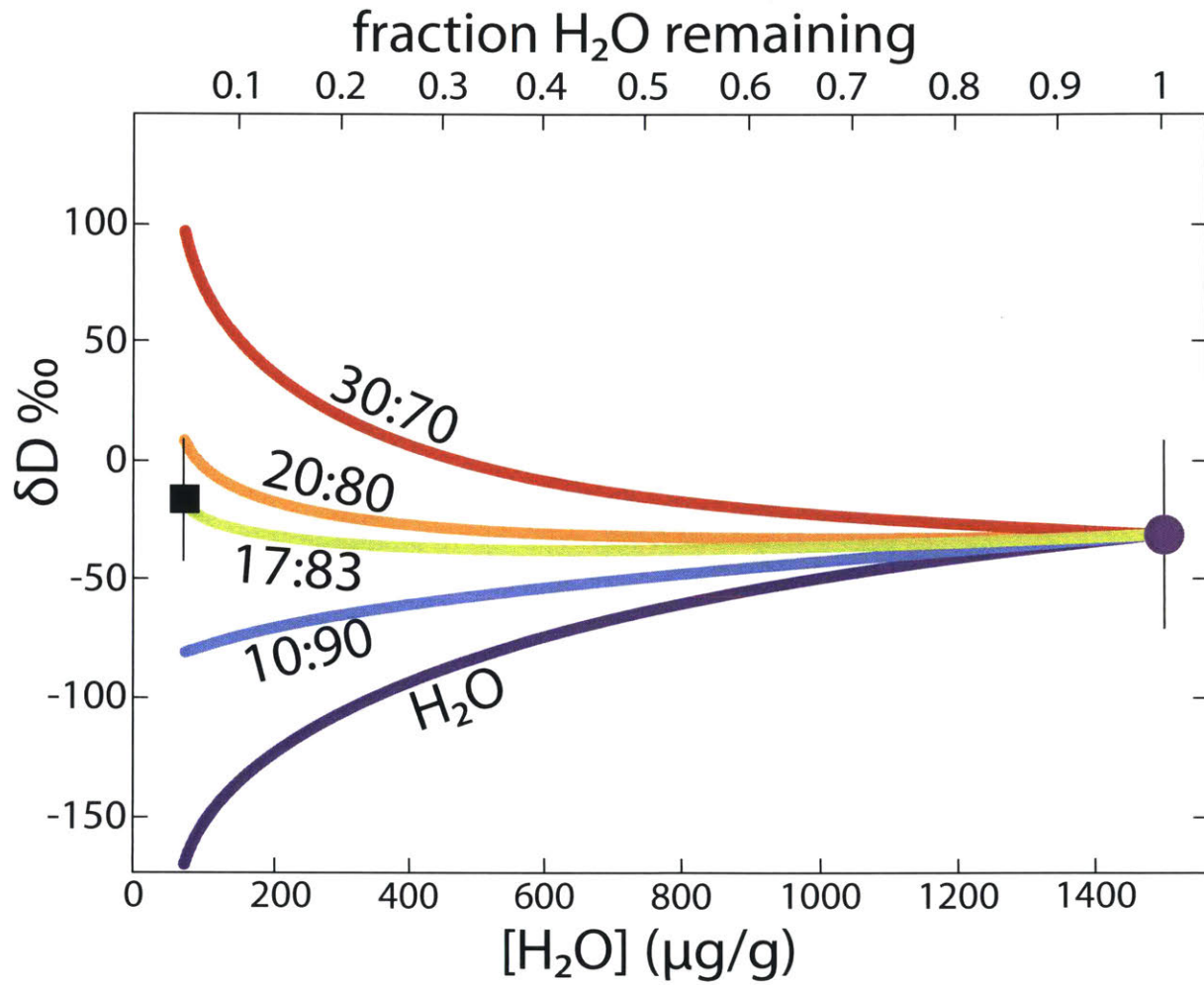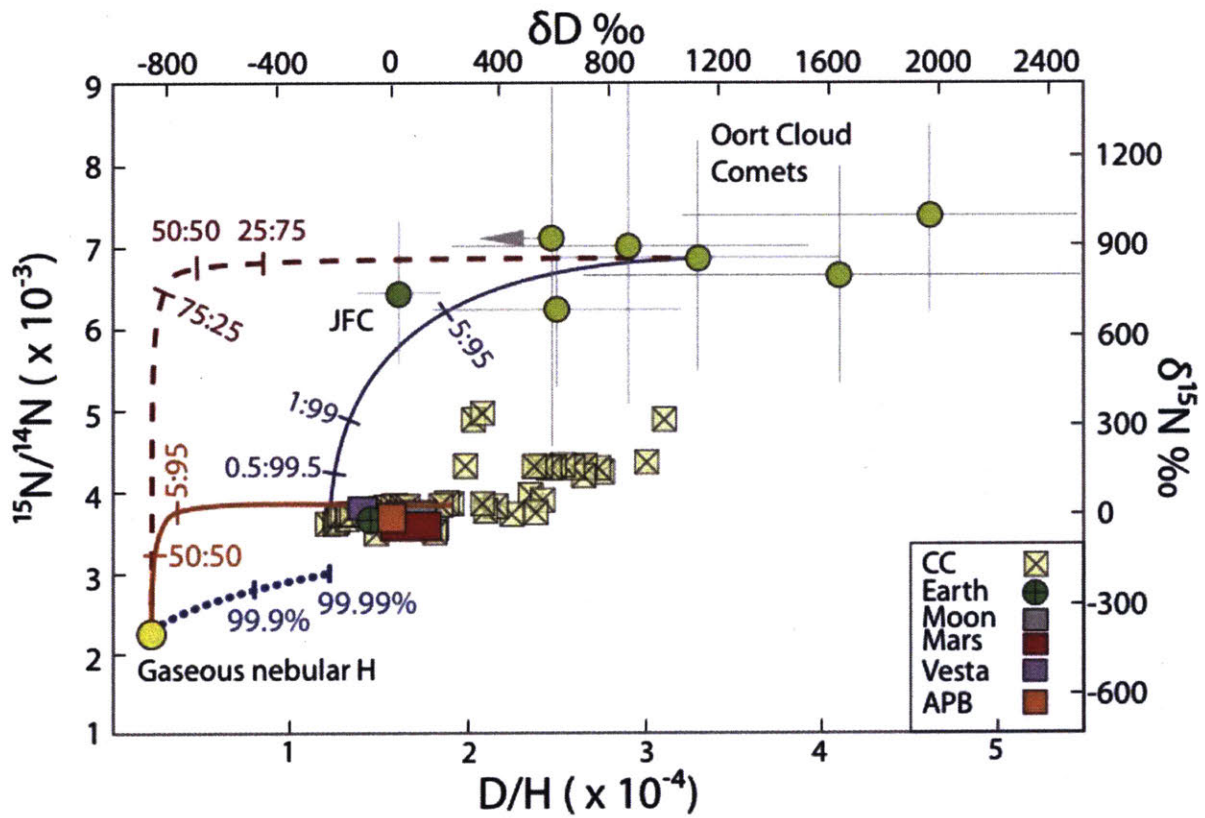
Figure 8

D/H, or δD vs. $^{15}N/^{14}N$, or $\delta^{15}N$. Note that mixing a gaseous nebular H source (orange line) or a comet (purple line) source with a carbonaceous chondrite source rapidly drives the mixture away from the carbonaceous chondrite field.
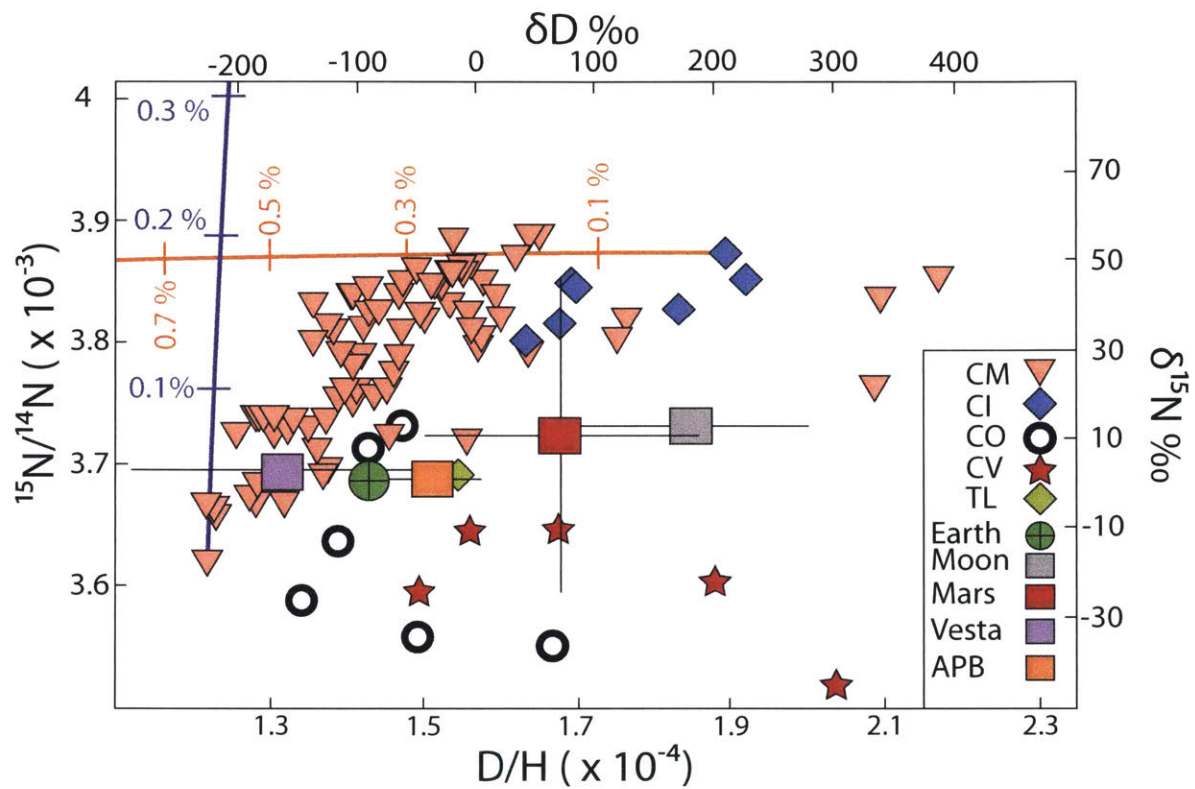
Table 1

Table 1. Major element content for D'Orbigny glass bead measured by election probe (N = 159), D'Orbigny and Sahara 99555 whole rock from (*51, 101, 122, 123*).

Oxides	Average	1σ	D'Orbigny WR	Sahara 99555 WR
SiO_2	39.85	0.25	37.54	38.51
TiO_2	0.85	0.03	0.83	0.90
$Al2O_3$	12.41	0.25	12.35	12.71
Cr_2O_3	0.05	0.01	0.04	0.31
FeO	24.91	0.32	24.58	24.16
MnO	0.27	0.01	0.24	0.26
MgO	7.64	0.22	6.47	6.91
CaO	14.38	0.19	15.74	15.20
Na_2O	0.03	0.05	0.018	0.016
K_2O	0.01	0.01	0.008	0.053
P_2O_5	0.17	0.01	0.165	0.165
Total	100.55	0.25		

Table 2

Table 2. Major and trace element content of D'Orbigny glass bead (D'O glass) measured by LA-ICP-MS. All values are listed in μg/g unless otherwise denoted. D'Orbigny and Sahara 99555 (SAH 99555) whole rock from (*51, 101, 122, 123*).

mass	element	D'O glass	1σ (n=25)	D'Orbigny	SAH 99555
23	Na_2O%	0.0114	0.0006	0.0177	0.0164
26	MgO%	7.61	0.15	6.47	6.91
27	Al_2O_3%	12.18	0.17	12.35	12.71
29	SiO_2%	39.85	0.00	37.54	38.51
39	K_2O%	0.001	0.0001	0.008	0.053
43	CaO%	14.32	0.21	15.74	15.20
45	Sc	42.5	0.7	42.5	48.8
49	TiO_2%	0.86	0.02	0.83	0.90
51	V	126	2	126	132
52	Cr	361	6	301	308
55	MnO%	0.24	0.003	0.24	0.26
57	FeO*%	24.84	0.34	24.58	24.16
59	Co	36.3	0.64	33.2	32.05
60	Ni	122	10.9	63	86
63	Cu	4.34	0.14	11.73	12.7
66	Zn	4.09	2.09	-	-
85	Rb	0.03	0.003	0.42	0.85
88	Sr	117	1.9	119	100
89	Y	18.4	0.42	20.1	19.6
90	Zr	54.26	1.29	60.58	57.3
93	Nb	3.09	0.07	3.72	3.64
133	Cs	0.0037	0.001	0.0223	-
137	Ba	29.9	0.67	48.1	41.1
139	La	3.21	0.07	3.46	3.37
140	Ce	8.53	0.19	8.82	8.71
141	Pr	1.27	0.03	1.32	1.29
146	Nd	6.12	0.12	6.32	6.70

147	Sm	1.87	0.05	2.08	2.12
153	Eu	0.76	0.02	0.81	0.83
157	Gd	2.48	0.07	2.59	2.70
159	Tb	0.44	0.01	0.48	0.51
163	Dy	2.95	0.07	2.95	3.40
165	Ho	0.66	0.01	0.67	0.76
166	Er	1.88	0.04	2.01	2.16
169	Tm	0.28	0.01	0.32	0.33
172	Yb	1.85	0.05	1.99	2.12
175	Lu	0.28	0.01	0.29	0.32
177	Hf	1.37	0.04	1.50	1.64
181	Ta	0.17	0.01	0.19	0.20
182	W	0.41	0.01	0.23	0.33
208	Pb	0.08	0.01	-	0.45
232	Th	0.42	0.01	0.41	0.43
238	U	0.11	0.004	0.09	0.11

Table 3

[207]Pb-[206]Pb ages of silicophosphates in D'Orbigny. * Isotope data were corrected for instrumental element and isotope fractionations with an in-house standard of Bear Lake apatite (958±13 Ma; 57) and Madagascar apatite (473.5 ±0.7 Ma; 62). Terrestrial standards were corrected for common Pb by monitoring [204]Pb and applying the Pb evolution model of (Stacey and Kramers, 1975). Corrections for common Pb of the angrite phosphates using Solar System initial Pb isotope compositions were not applied because [204]Pb count rates were too low for sufficiently precise [206]Pb/[204]Pb isotope ratio measurements. Instrumental mass fractionation factors applied to the measured [207]Pb/[206]Pb isotope ratios were based on long-term measured values of 0.990 ± 0.005 (2SD). Random and systematic uncertainties were propagated following methods outlined in Shaulis et al. (59). -- indicates no meaningful age can be calculated.

Sample	^{204}Pb/^{206}Pb	2SD	^{207}Pb/^{206}Pb*	2SD	^{207}Pb/^{235}U*	2SD	^{206}Pb/^{238}U*	2SD	error Corr	^{206}Pb/^{238}U Age	2SD	^{207}Pb/^{235}U Age	2SD	^{207}Pb/^{206}Pb Age	2SD
D'Orbigny															
1	0.0007	0.0011	0.6209	0.0396	119.6	14.1	1.384	0.137	0.841	5604	372	4867	119	4558	92
2	0.0170	0.0161	0.6388	0.0496	116.9	13.0	1.314	0.104	0.715	5414	291	4844	112	4599	112
3	0.0030	0.0021	0.6274	0.0324	100.4	8.9	1.149	0.083	0.812	4935	248	4690	89	4573	75
4	0.0010	0.0013	0.6200	0.0294	96.6	9.3	1.119	0.093	0.870	4844	285	4651	97	4556	69
5	0.0003	0.0006	0.6230	0.0238	95.0	7.7	1.095	0.078	0.881	4772	240	4635	81	4563	55
6	0.0005	0.0009	0.6287	0.0475	109.2	13.8	1.221	0.124	0.803	5149	361	4775	128	4576	109
7	0.0030	0.0010	0.6401	0.0210	114.8	6.7	1.288	0.062	0.827	5339	175	4825	59	4602	48
8	0.0087	0.0094	0.5995	0.0281	120.2	14.0	1.439	0.154	0.915	5754	407	4871	118	4507	68
9	0.0215	0.0196	0.6000	0.0315	93.9	9.0	1.124	0.090	0.837	4860	274	4623	96	4508	76
11	0.0147	0.0073	0.6336	0.0198	118.9	6.5	1.357	0.060	0.819	5531	166	4861	55	4587	45
wtd avg										--		--		4568	20

Yates Mine

1	0.0068	0.0017	0.0256	0.0231	0.55	0.49	0.1530	0.0083	0.060	919	47	443	335	--	--
2	0.0038	0.0017	0.0826	0.0175	1.84	0.40	0.1597	0.0084	0.239	956	46	1059	145	1261	415
3	0.0066	0.0031	0.0220	0.0351	0.46	0.73	0.1489	0.0090	0.038	896	51	381	558	--	--
4	0.0061	0.0018	0.1283	0.0230	0.86	0.16	0.1569	0.0084	0.286	941	47	632	88	2075	316
5	0.0024	0.0015	0.0979	0.0135	2.18	0.32	0.1596	0.0079	0.337	955	44	1174	102	1585	258
6	0.0061	0.0025	0.0467	0.0283	0.99	0.60	0.1525	0.0085	0.091	916	48	699	318	32	1454
wtd avg										932	19	--		--	

Table 4

Table 4. Hydrogen isotope composition of olivine. Weighted average is that of D'Orbigny and Sahara 99555.

D'Orbigny	δD	2σ	spallation corrected δD	spallation corrected 2σ	[H_2O] $\mu g/g$
Ol2b	-77	84	-146	84	11
Ol2c	-10	79	-93	79	12
Ol2a	29	76	-59	76	13
Ol13c	-48	70	-99	70	16
Ol3	-60	71	-107	71	16
Ol13a	133	71	61	71	15
Ol13b	116	67	56	67	17
Ol13c -meso	229	74	127	74	13
Sahara 99555					
Ol5	225	115	46	115	8
Ol2a	-13	99	-63	99	8
Ol2b	-66	70	-83	70	18
Ol10a	88	62	44	62	19
Ol10b	74	65	32	65	18
Ol10c	76	100	-1	100	7
wtd avg			-31	39	

Table 5

Table 5. Hydrogen isotope composition of silicophosphates.

Sample	δD	2σ	spallation corrected δD	spallation corrected 2σ	[H2O] μg/g
D'Orbigny					
Si-Phos1	1036	16	1034	16	1892
Si-Phos2	664	63	624	63	100
Si-Phos3	-158	93	-205	93	85
Si-Phos4	1034	19	1032	19	1701
Sahara 99555					
Si-Phos1	-129	135	-192	135	36
Si-Phos2	-209	132	-262	132	42
Si-Phos3	-25	88	-35	88	255

Table 6

Table 6. Volatile element content of D'Orbigny glass bead in $\mu g/g$.

Number	H_2O	1σ	CO_2	1σ	F	1σ	Cl	1σ
1	72	3	2.5	0.2	4.7	0.1	2.7	0.3
2	67	3	2.6	0.2	4.4	0.1	2.2	0.2
3	70	3	2.5	0.2	4.6	0.1	2.5	0.3
4	69	3	2.8	0.2	4.7	0.1	2.9	0.3
5	68	3	2.5	0.2	4.6	0.1	2.9	0.3
6	70	3	2.5	0.2	4.7	0.1	2.4	0.2
7	69	3	2.5	0.2	4.6	0.1	2.4	0.2
8	73	3	2.6	0.2	4.7	0.1	2.2	0.2
9	73	3	6.3	0.5	4.7	0.1	2.2	0.2
10	73	3	2.5	0.2	4.7	0.1	2.2	0.2
11	74	3	2.4	0.2	4.7	0.1	2.2	0.2
12	74	3	2.8	0.2	4.7	0.1	2.2	0.2
13	74	3	2.7	0.2	4.8	0.1	2.3	0.2
14	73	3	2.7	0.2	4.7	0.1	2.1	0.2
15	69	3	2.5	0.2	4.5	0.1	2.1	0.2
16	73	3	2.5	0.2	4.7	0.1	2.2	0.2
17	68	3	2.4	0.2	4.6	0.1	2.1	0.2
18	69	3	2.5	0.2	4.6	0.1	2.1	0.2
19	69	3	2.3	0.2	4.6	0.1	2.1	0.2
20	69	3	2.4	0.2	4.7	0.1	2.0	0.2
21	69	3	2.6	0.2	4.6	0.1	2.1	0.2
22	71	3	2.5	0.2	4.7	0.1	2.1	0.2
23	72	3	2.7	0.2	4.6	0.1	2.1	0.2
24	66	3	2.2	0.2	4.5	0.1	2.1	0.2
25	66	3	2.3	0.2	4.5	0.1	2.1	0.2
26	66	3	2.6	0.2	4.5	0.1	2.2	0.2
27	66	3	2.2	0.2	4.5	0.1	2.2	0.2
28	66	3	2.3	0.2	4.5	0.1	2.2	0.2

29	65	3	2.3	0.2	4.6	0.1	2.6	0.3
30	66	3	2.2	0.2	4.6	0.1	2.3	0.2
31	63	3	2.1	0.2	4.6	0.1	2.3	0.2

Table 7

Table 7. H isotope composition of D'Orbigny glass bead and spallation corrected H isotope composition.

Number	δD	2σ	spallation corrected	spallation corrected 2σ
1	-7	69	-25	69
2	-140	66	-154	66
3				
4	-57	65	-71	65
5	-37	70	-54	70
6	-50	69	-66	69
7	0	68	-17	68
8	-47	78	-70	78
9				
10	-61	70	-77	70
11	-4	70	-22	70
12	-6	74	-26	74
13	-4	72	-23	72
14	-27	71	-46	71
15	-77	67	-92	67
16	-109	66	-123	66
17	10	76	-12	76
18	-2	78	-25	78
19	29	75	7	75
20	-12	78	-35	78
21	146	82	115	82
22	81	79	55	79
23	-5	72	-24	72
24	55	77	30	77
25	-8	73	-28	73
26	39	81	11	81

27	56	81	28	81
28	93	87	59	87
29	50	81	23	81
30	119	80	91	80
31	116	83	85	83
Wtg avg			-16	26

Chapter 4

Vestigial volatile-bearing melts in the Vestan crust and the filiation of Stannern Trend eucrites

4.1 Abstract

In this paper, we present a combined petrographic and geochemical study of the residual eucrite Elephant Moraine 90020 (EET 90020), which is a meteorite derived from the crust of an asteroid, most likely 4-Vesta. We propose a melt-rock interaction model to describe the textures and chemical composition of EET 90020 and suggest a possible origin of the chemically distinct Stannern-trend eucrite group. This meteorite contains an ophitic coarse-grained domain, characterized by a typical magmatic texture that gradually transitions into an equigranular fine-grained domain, which we interpret as a thermally annealed portion of the sample. In addition, an apatite-rich subdomain (ARS) was identified in the equigranular fine-grained domain. The trace-element composition of a basaltic melt in equilibrium with the ARS was determined using mineral trace-element composition in combination with published mineral–melt partition coefficients.

Stannern-trend melts are successfully modeled as a ~88:12 mixture of a main-group eucritic composition (Juvinas) and the melt composition in equilibrium with ARS. The occurrence of hydroxyl-bearing fluor-apatite demonstrates that water probably played a role in melt generation on the asteroid.

4.2 Introduction

The howardite, eucrite, and diogenite (HED) clan are a group of achondrite meteorites that probably originate from the same asteroid, namely 4-Vesta, or from similar asteroids (*1-5*). Basaltic eucrites can be separated into three geochemical groups: (1) the main group, (2) the Stannern-trend, and (3) residual eucrites (e.g., *6, 7*). (1) Main-group eucrites show a range in Mg# [= Mg/(Mg+Fe)], Sc abundances, and other magmatic differentiation indices, and are enriched in incompatible elements with increasing differentiation (Fig. 1). This was interpreted as a fractional crystallization trend (*8*), which was later confirmed by trace element systematics (*9*). (2) Stannern-trend eucrites show little variation in their differentiation indices and are enriched in incompatible elements (Fig. 1). Stannern-trend eucrites could have formed from melts generated by variable degrees of partial melting of the Vestan mantle (*8*) or from complex magma mixing due to *in situ* crystallization (*10*), but they probably formed from incorporation of partial melts derived from the eucritic crust (*7, 11, 12*). (3) Residual eucrites are the most recently classified geochemical group of basaltic eucrites (*7*) and are depleted in incompatible elements, but their major elements are similar to the main group (Fig. 1). Residual eucrites are interpreted to be residues of low-degree partial melting, resulting in the depletion of incompatible elements (*7, 11, 13*). In this paper we expand on a partial melting model that links all three of these geochemical groups.

Thermal metamorphism on Vesta is ubiquitous (*7, 14-17*). Thermal metamorphism is caused by heat conduction out of the interior of the asteroid and by burial of surface material by subsequent lava flows (*7*). Intense thermal metamorphism probably led to partial melting of the eucritic crust at deeper levels and adjacent to ascending magma bodies, where heat flux was high (*7, 11*). Recently, evidence of partial melting of the eucritic crust has been presented in the form of trace-element systematics in zircons (*18*), an enrichment in ^{56}Fe in some eucrites (*12*), and Fe-rich veins in eucrites (*19*). Additionally, the mobility and composition of eucritic partial melts have been examined (*13*). With the above observations and experiments, we set forth to determine if melt–

rock reaction can explain the genesis of the Stannern trend by studying the residual eucrite Elephant Moraine 90020 (EET 90020).

EET 90020 was initially classified as an unbrecciated main group eucrite (*16*), then as an anomalous main group eucrite (*20*), and finally as a residual eucrite (*7*). We accept the most recent classification of EET 90020 as a residual eucrite. Residual eucrites provide insight into partial melting of the eucritic crust. Two lithologies in EET 90020 have been described, a coarse-grained lithology and a fine-grained lithology (*16*). The two lithologies are thought to have experienced varying degrees of melting and melt-rock interaction (*7; this study*).

In this paper, we use the petrogenesis of EET 90020 to provide further evidence in support of the partial melt model to explain the genesis of Stannern trend eucrites (*11, 12, 18, 19*). We argue that the partial melt that was extracted from EET 90020 was phosphate saturated, generating an apatite-rich region. We further suggest that partial melts with the same composition mixed with main-group magmas, resulting in the composition of the enriched, Stannern-trend magmas. This relatively simple model can explain all three eucrite chemical groups/trends. We also suggest from the composition of apatite that H_2O played a vital role in crustal partial melting on Vesta.

4.3 Sample description

EET 90020 is a residual eucrite that has been extensively studied (*7, 16, 20-22*). The two described lithologies are a subophitic "coarse-grained lithology" and an equigranular "fine-grained lithology". We will hereafter refer to the "coarse-grained lithology" as the **ophitic coarse-grained domain** and to the "fine-grained lithology" as the **equigranular fine-grained domain** (Fig. 2 & 3). A sub-domain of the equigranular fine-grained domain is extremely rich in apatite (Fig 2; *21*) and will be called the **apatite-rich sub-domain** (ARS). These revised petrographic subdivisions are required and useful because the equigranular fine-grained domain is coarser grained than the ARS, whereas the

89

ophitic coarse-grained and equigranular fine-grained domains really have similar grain sizes (Figs. 2 & 3); also, both domains have varying grain sizes on the hand-sample scale and among different thin sections (*16*). However, we elect to keep the terms "fine-grained" and "coarse-grained" to maintain consistency with the nomenclature of ref (*16*). This paper focuses on key differences among these three domains, but more detailed descriptions can be found elsewhere (*16, 20, 21, 23*).

4.3.1 Macroscopic description

We investigated the main mass of EET 90020, a ~ 5.3 x 4.5 x 4.8 cm^3 spheroidal meteorite (see supplemental). Weathering and fracturing of EET 90020 is minimal, although meandering cavities that are several mm in size are present throughout the sample. Two different textures can be discerned in hand sample, one with more milky white minerals than the other. The ophitic coarse-grained domain and equigranular fine-grained domain were easily distinguished when using a hand lens, but they appear to grade into one another on the mm scale.

4.3.2 Microscopic description

EET 90020 (,16 ,17, 20) were carefully examined by light and electron microscopy and examined in thin section (,7) by light microscopy and with element map mosaics (*22*). We also quantitatively examined several photomicrographs and backscattered electron images of EET 90020 (,18), (, 28) (*16*). EET 90020, 17 was the focus of our study, as this section contained all three described domains.

4.3.2.1 Ophitic coarse-grained domain: The ophitic coarse-grained domain has ophitic plagioclase (An 87–91), which is ~0.7 mm in the long direction (Figs. 2 & 3). Plagioclase has abundant SiO_2 inclusions (probably tridymite) in the core. Orthopyroxene with 1–3 μm wide lamella of augite in the ophitic fine-grained domain is ~0.7 mm in the long direction and is generally interstitial to the plagioclase. The ophitic coarse-grained

domain has ~0.5 % (modal abundance by volume) opaque phases (troilite, metal, and ilmenite). These phases occur as interstitial subhedral grains along with the volatile-free phosphate, merrillite. Silica, presumably tridymite, occurs as anhedral interstitial grains ~0.4 mm in length.

4.3.2.2 The equigranular fine-grained domain: The equigranular fine-grained domain consists of sub-ophitic to equigranular plagioclase with an annealed texture (0.5–1 mm grain diameters) and equigranular pyroxene (0.1–1.2 mm grain diameters). These plagioclase grains have an An content of 87–91. The equigranular fine-grained domain has ~0.1 % (modal abundance by volume) opaque phases (troilite, metal, ilmenite). These phases occur as interstitial subhedral grains. Silica occurs as anhedral interstitial grains up to 1 mm in length. Silica is more abundant in the equigranular fine-grained domain than in the ophitic coarse-grained domain and the opaque phases are less abundant.

4.3.2.3 The apatite-rich subdomain (ARS): The ARS has equigranular plagioclase, 0.1 mm in diameter. No SiO_2 inclusions were found in the ARS. Pyroxene in the ARS is equigranular and ~0.4 mm long in the longest dimension. No opaque phases were observed in the ARS, but the ARS does have a high abundance of apatite, which importantly is a volatile bearing phosphate. Subhedral apatite is up to 1 mm long and does not appear to be oriented. Apatite grains oriented with their crystallographic c-axes at right angles relative to each other and many grains at intermediate angles have been identified within the space of 1 mm. Silica in the ARS is found as ~50 μm grains interstitial to plagioclase.

4.4 Analytical Methods

4.4.1 Electron probe microanalysis (EPMA)

Plagioclase, pyroxene, and tridymite were measured with the JEOL 8600 electron microprobe at the University of Georgia. An accelerating voltage of 15 kV, a beam current of 15 nA, a 1 μm spot for pyroxene and tridymite, and a 5 μm spot for plagioclase were used. Natural and synthetic standards (albite, olivine, spinel, diopside, orthoclase, sphene, rutile, spessartine, fayalite, chromite) were used. We analyzed plagioclase, pyroxene, and tridymite from the ARS to supplement the extensive mineral analyses for the ophitic coarse-grained domain and the equigranular fine-grained domain available from the literature (16, 22).

4.4.2 Laser ablation inductively coupled plasma mass spectrometry (LA-ICP-MS)

Plagioclase, pyroxene, and apatite were measured at the University of Maryland using a Nu Wave Nd-YAG laser (213 nm) coupled to a thermo Finnigan Element 2 single-collector inductively coupled plasma mass spectrometer (LA-ICP-MS) using low mass resolving power, $M/\Delta M = 300$. A laser pulse rate of 7 Hz and an energy of ~2.6 J/cm^2 was used. LA-ICP-MS has been proven through many analytical studies as a robust method measure trace elements in small volumes from a variety of matrix materials (24-32). Some studies have examined elemental fractionation as a function of wavelength of laser used (33), and found this effect is <10 % for 213 nm and 193 nm lasers, and less elemental fractionation occurs when target minerals are relatively opaque to the laser used, such as plagioclase and pyroxene. We used a 3 cm^3 ablation cell, with a washout time of >120 s, and was flushed with He gas to enhance production. Each analysis was 60 s, consisting of 20 s of background followed by 40 s of laser ablation. Data were collected in time-resolve mode so effects of inclusions and ablating through the thin section could be accounted for. Counts vs. time was plotted for each analysis and integration intervals for the background and sample analysis was determined using LAM-TRACE software. Oxide interferences were mitigated by ensuring ^{232}Th^{16}O/^{232}Th <0.02. Thus, ^{137}Ba^{16}O interference on ^{153}Eu contributes a maximum of 4 % of total signal for the most Ba-rich plagioclase measured, 0.05 % for ^{130}Ba^{16}O on ^{146}Nd making a negligible contribution to total Eu and Nd contents. Standard reference material NIST 610 glass was used as a primary standard, as matrix matched trace element standards (e.g., plagioclase

and pyroxene) are not widely available. LA-ICP-MS has been shown to be matrix tolerant (*25, 34*), allowing for silicate glasses to be used as primary and secondary reference materials for silicates and phosphates. We used a secondary reference material, BHVO-2G, to ensure our calibration was accurate. We reproduced the published values of BHVO-2G (*30, 31*) on average within 8%, but as poorly as 22% for W and 13–19% for the HREE. Thus, the LA-ICP-MS is accurate to at least 22 %, but more commonly to approximately 8 %. We preformed 16 analyses of BHVO-2G throughout the analytical session which yielded a reproducibility of 2–18 % with a mean of 6 % (1σ); worse precision occurred in unknowns with lower elemental concentrations than our secondary standard. Analyzed masses (table 1) were normalized to Ca, which was measured by EPMA. Detection limits were determined by using 3 σ of the background (table 1). Laser spot size varied (20–60 μm) based on grain size. Larger spots were used on exsolved pyroxenes to obtain their average, re-integrated compositions. Smaller spot sizes were used on plagioclase grains with abundant inclusions in order to avoid mineral inclusions within the plagioclase.

4.5 Results

4.5.1 Plagioclase

The shape of the trace-element patterns in plagioclase in the equigranular coarse-grained domain and ophitic fine-grained domain generally agree with previous SIMS data (*16*), but the concentrations reported here are approximately 15 % higher (table 2, Fig. 4c). These 15 % are not outside the combined analytical uncertainties of the two techniques used, i.e., ICP-MS in this study and SIMS by ref (*16*) for most elements (Fig. 4). Multi-element plots are presented normalized to the concentrations reported for the whole-rock composition of CI chondrite (Fig. 4) (*35*).

Positive anomalies exist for Sr, Ba, and Eu, i.e., elements that are compatible in plagioclase and typically substitute for Ca (Fig. 4c). Plagioclase major element compositions in the ARS are indistinguishable from those of plagioclase in the

93

equigranular fine-grained and ophitic coarse-grained domains (table 3) (*16*). However, there are notable differences in their respective trace-element concentrations.

4.5.2 Pyroxene

The shape of the trace-element patterns in pyroxene in the equigranular fine-grained and ophitic coarse-grained domains also generally agree with previous SIMS data (table 2) (*16*), but the absolute concentrations reported here (table 2, Fig. 4b) are again approximately 15 % higher than previously reported data for most elements. The major element composition of pyroxene of the ARS is indistinguishable from those of the equigranular fine-grained and ophitic coarse-grained domains (table 3) (*16*). Trace-element abundances in pyroxene are also similar among lithologies, but pyroxene in the ARS has a less pronounced negative Ba anomaly (table 2).

4.5.3 Apatite

Trace-element data for apatite are presented in table 1, and the CI-normalized trace-element pattern is displayed in Fig. 4a. The shape of the trace-element patterns of apatite in the ARS domain generally agrees with previous SIMS data (*16*), apart from slightly lower La/Lu (La/Lu = 52 this study; La/Lu = 71; Yamaguchi et al 2001). In addition, we analyzed the apatite for actinides and found notably high abundances of Th and U (table 2). We use the data of Sarafian, Roden and Patiño Douce (*21*) for the halogen and H_2O content of apatite in EET 90020, which were derived from the same thin section investigated here (,17). Of the 14 meteorites examined for halogens and H_2O in eucritic apatite, EET 90020 has the lowest Cl content of any eucrite measured and has a higher average OH content than most eucrites (*21, 36*).

4.6 Discussion

4.6.1 The origin of the equigranular fine-grained domain, ophitic coarse-grained domain, and the ARS – A melt–rock reaction model

Our model is a refinement of previously proposed partial-melt models (*7, 11-13*), where we take into account the presence of the ARS, the textures observed in the meteorite, the mineral compositions, and the bulk chemical composition of EET 90020. In our melt–rock interaction model, focused silicate melt channels ascended through the Vestan crust and heated the surrounding crust (Fig. 5). Heat emanating from the melt conduits led to textural annealing of the country rock of the melt channel. The equigranular fine-grained domain observed in EET 90020 is interpreted as a sample of the texturally annealed rocks adjacent to one of these melt channels. The thermally annealed equigranular fine-grained domain continuously grades into texturally unequilibrated rock (the ophitic coarse-grained domain; Fig. 2 & 3), which is consistent with the thermal influence of the melt conduit dissipating with distance from the conduit. The thermal gradient in such a system would have resulted in the two domains preserved in EET 90020. Thermal gradients and annealing textures near channelized melt-flows are common and have been thoroughly studied in terrestrial mafic and ultramafic settings (*37-39*)

High degrees of thermal annealing was accompanied by partial melting in some eucrites (see supplement; *7, 11*). Low degree eucritic partial melts are mobile, highly enriched in incompatible trace elements, but not enriched in compatible trace elements (*13*). Most importantly, low degree partial melting may not effect the major mineral texture of the basalt compared to the igneous protolith (*13*). Low degrees of basalt partial melting mobilizes the mesostasis, which includes the phosphates (*13*). Thus, the P content of low degree basalt partial melts should be elevated. In the following paragraph we will discuss observations and implications of melts with very high P contents.

The ARS has apatite grains up to 1 mm in length, with a modal abundance of 18 % apatite, which translates to 8.2 wt% P_2O_5; this dwarfs the 0.04-0.11 wt% P_2O_5 usually reported for eucrites (*40*). According to P saturation models (*41, 42*), eucritic melts cannot dissolve more than approximately 0.4 wt% P_2O_5 at near-solidus temperatures. Consequently, the ARS cannot represent a bulk portion of crystallized melt. Hence, either (1) the ARS must be a cumulate in which apatite, plagioclase and pyroxene were liquidus

phases, or (2) apatite is grossly over-sampled in the examined thin sections of the ARS. Our thin section of ARS (EET 90020,17) is more apatite-rich than EET 90020,18, which has ~5.4 % modal abundance of apatite, corresponding to 2.4 wt% P_2O_5 (*16*), which is still above the P_2O_5 saturation predicted from apatite saturation experiments. Partial melting experiments show that a eucrite with a bulk P_2O_5 content of 300 µg/g can produce low degree melts with 3.8 wt% P_2O_5 (*13*). A decrease in temperature or silica activity or an increase in CaO activity in a melt with such a high abundance of P_2O_5 would lead to apatite saturation and crystallization. Continuous recharging of low-degree melts percolating through surrounding rocks would lead to a significant accumulation of apatite, similar to that found in the ARS. The extreme abundance of apatite in the ARS suggests that the apatite was formed by accumulation of co-crystallizing phases (mainly apatite and plagioclase).

Evidence for the co-precipitation of apatite and plagioclase is provided by approximately equal abundances of Sr in the two phases combined with the similar compatibility of Sr in plagioclase and apatite as determined by experiments (Table 1; *34*). Note that apatite in terrestrial magmatic rocks is typically depleted in Sr relative to plagioclase (e.g., *43*). This is probably caused by Sr depletion of the melt by early crystallization of plagioclase, leaving subsequently crystallized apatite depleted in Sr (*43*). Hence, similar Sr abundances in apatite and plagioclase in the ARS are evidence for co-crystallization of the two phases.

In our melt reaction model the ARS is in between the equigranular fine-grained and ophitic coarse-grained domains, or the ARS could also occur within the equigranular fine-grained domain. The highly mobile low degree P- and incompatible element-rich partial melts (*13*) migrated through the equigranular fine-grained and ophitic coarse-grained domains and equilibrated with the silicate phases (Figs. 4 & 6). Differences in the trace element content of pyroxenes and plagioclase between our data and previously reported data could be due to variable amounts of partial melting in EET 90020 (Fig 4). The ARS melt would be undersaturated with respect to apatite in the hotter equigranular

fine-grained domain, which would be close to the magma conduit, and could be saturated with respect to apatite while migrating through the colder ophitic coarse-grained domain further from the magma conduit, as apatite saturation is a strong function of temperature (*41, 42*). The accumulation of apatite and plagioclase could also result in minor changes in melt composition, as apatite saturation is a function of T, P_2O_5, SiO_2, and CaO (*41, 42*). In turn, if our model is correct, then other pockets of ARS should be present at relatively colder parts of the system, either the transition from the equigranular fine-grained domain to the ophitic coarse-grained domain, or within the ophitic coarse-grained domain where minor changes in melt composition occurred.

To summarize, all three (sub)domains in EET 90020 can be described with magmatic, annealing, partial melting, and apatite saturation processes. Our genetic model suggests that EET 90020 was located adjacent to a magma conduit on its parent asteroid; intense thermal annealing generated the equigranular fine-grained domain, whereas the ophitic coarse-grained domain was texturally unaffected. Melt flux in the passing magma conduit caused small degrees of partial melting in the adjacent wall rock. This partial melt was apatite saturated, which caused the crystallization of abundant apatite.

4.6.2 Trace-element composition of ARS-forming melt

Mineral compositions in combination with published mineral-melt partition coefficients (*D*) were used to determine the trace-element composition of the melt in equilibrium with the ARS. Three independent estimates of the melt composition can be derived using mineral-melt partition coefficients for apatite, plagioclase, and pyroxene, respectively. However, experimentally determined partition coefficients for some elements in some minerals have high uncertainties. In particular, partition coefficients larger than ~1000 or smaller than ~0.001 bear larger uncertainties due to analytical difficulties with measuring glass (melt) and mineral compositions that are vastly different. Thus for the determination of the concentrations of different trace element in the melt, we selectively favored the phases for which partition coefficients are relatively close to unity, as we

consider those values more robust (table 1). We were able to estimate the melt composition using the above partition coefficients, and we used the Stannern-trend eucrite Bouvante as a reference for a Stannern-trend melt composition (Fig. 6a).

The calculated melt is enriched in all incompatible trace elements with respect to the bulk rock (20). Uranium and Th contents in the melt (289 µg/g U; 100 µg/g Th) calculated from apatite/melt partition coefficient (D(Ap/melt) = 0.17 for U and 0.7 for Th; 34) are two to three orders of magnitude higher than the expected levels for a eucritic melt (0.09 µg/g U; 0.4 µg/g Th; 11). This suggests that either (1) the partition coefficients for U and Th between apatite and eucrite melts are two orders of magnitude higher than between apatite and basaltic melt, (2) the melt was highly enriched in U and Th, or (3) apatite was not in equilibrium with a melt with respect to U and Th. Regarding option (1), partition coefficients for apatite-melt are well established, they are close to 1, and while they vary with respect to melt composition, they do not vary by more than a factor of 5 between basaltic and basaltic andesite melts (34). (2) Estimated melt compositions from minerals that crystallize close to the solidus generally overestimate the abundances of incompatible trace elements in the initial bulk melt. However, if the extent of crystallization is known, a primitive melt composition can still be reconstructed (44). Apatite in EET 90020 appears to be a liquidus phase judging form petrographic evidence and from the comparable Sr contents in coexisting apatite and plagioclase. Hence, no correction is required to estimate the trace-element composition of the initial melt. Consequently, U and Th could have been highly enriched in the melt. (3) An alternative scenario to apatite crystallization in equilibrium with a melt is that it crystallized from a fluid. D(apatite/fluid) values for Th and U are significantly higher than D(apatite/melt) values (45, 46). Lower solubility of U in fluids at reducing conditions may be expected to produce lower U/Th ratios in potential fluid-precipitated apatite on Vesta. However, the U/Th ratio in EET 90020 apatite is extremely high, suggesting that the apatite did not crystallize from an oxidizing fluid. The reason for the anomalously high U and Th concentrations in apatite is unclear, thus, we do not calculate a melt U or Th content.

Water content of the apatite could be telling of the water content of the ARS melt if reliable, pressure-dependent exchange coefficients were available for OH and F between apatite and melt. However, these data are not available to date, and the pressure for the formation of the ARS is not constrained, so we cannot determine the water content of the melt. However, if the apatite in the ARS melt crystallized under similar conditions as apatite in other eucrites, we can qualitatively say that the ARS melt had a higher H_2O/F ratio than the melts from which most other eucrites formed (47). This is expected from our model, as water is more incompatible in eucritic silicates compared to F (48, 49) and is enriched along with the other incompatible elements.

Our calculated melt trace-element composition is similar to the composition produced by the 10 % crustal partial-melt model of ref (11). Minor differences exist for some elements (Fig. 6a), but the agreement between our calculated melt and the melting model of Barrat et al. (11) is striking. The melt calculated here is slightly enriched in Rb and LREE compared to previous models (11).

4.6.3 Origin of Stannern-trend eucrites

Stannern-trend eucrites are distinct among eucrites for their major and trace element compositions (11, 18), and isotopes (12, 50). Barat et al (11) suggested that the Stannern trend represents a main-group magma contaminated by a melt generated by partial melting of the crust. Partial melting of the crust is relatively common among eucrites (7, 12, 18, 19) and one might surmise that partial melting of the crust could play a role in the genesis of the Stannern trend. Our observations support the partial melting model for the origin of residual eucrites (7, 11), but we suggest a melt-rock interaction mechanism rather than a simple melt-extraction model. The accumulation of apatite and plagioclase evident in EET 90020 is likely the result of melt–rock reaction, and this modification to previous models can help describe the P content of Stannern trend rocks (see below). In the terrestrial mantle, similar melt–rock reactions processes occur where basaltic melts are extracted from peridotite (37-39, 51, 52); for example, the melts typically dissolve

clinopyroxene in the surrounding rock and precipitate orthopyroxene or olivine. This melt-rock reaction does not significantly change the major element and compatible trace-element composition of the residual rock (with the exception of Ca), but it leads to a strong depletion of the incompatible trace-elements in the residual rock. Similarly, the major and compatible trace elements (e.g., Sc and Sr) in residual eucrites are virtually unchanged by this melt–rock reaction, but the incompatible trace elements are highly depleted (e.g., REE; *7, 20*) (Fig. 1). The decoupling of major elements from incompatible trace elements has been a long-standing conundrum (*9-11*) that could be explained by a melt–rock reaction process.

The mixing ratio required to create a Stannern-like melt from the melt in equilibrium with the ARS with the main group eucrite Juvinas can be estimated from their respective trace-element abundances. A mixture of ~12 % ARS-forming melt and ~88 % melt of Juvinas composition matches the trace-element pattern of the Stannern-trend eucrite Bouvante (Figs. 1 & 6b). Thus, the Stannern-trend eucrites could originate from melt that reacted with the eucritic crust during ascent and subsequently mixed with a primitive magma (modeled here by using the composition of the well-studied basaltic main group eucrite Juvinas). This hypothesis is in general agreement with, and an extension of, the conclusions of ref (*11*).

Ref (*11*) mentions that P concentrations in Stannern-trend eucrites are highly variable, yet P should behave similar to the LREE. This unpredictable behavior of P may have been caused by variable amounts of apatite fractionation during the melt-rock interaction process. These variations could be due to changes in P solubility due to minor changes in the Si and Ca content of partial melts, as low degree (<7 %) partial melts are enriched in Si and depleted in Ca (*53, 54*), or the variations in P concentration could be due to exhaustion of P-rich phases, like apatite and merrillite during the low degree partial melting event.

4.7 Concluding remarks

We identified a petrographic subdomain in the rock, the ARS, which we interpret as a product of melt–rock reaction. The model suggests that heat emanated from a channelized melt conduit thermally annealed the surrounding basaltic crust with radially decreasing intensity, and partially melted the crust to a low degree. This low-degree melt produced the ARS co-precipitated mainly apatite and plagioclase and was enriched in trace elements compared to the most enriched group of eucrites, the Stannern-trend eucrites. The Stannern trend can be modeled as a 88:12 mix of the main group eucrite Juvinas and the enriched melt in equilibrium with the ARS. This model extends and refines the model of ref (*11*). Apatite in the ARS contains significant amounts of OH, showing that melting on Vesta was not anhydrous. The high abundances of U and Th in apatite appear to be inconsistent with apatite–melt equilibrium during melt–rock interaction, but the cause of this inconstancy remains unresolved.

4.8 Acknowledgements

4.9 References

1. T. B. McCord, J. B. Adams, T. V. Johnson, Asteroid Vesta: Spectral reflectivity and compositional implications. *Science* **168**, 1445 (1970).

2. G. J. Consolmango, M. J. Drake, Composition and evolution of the eucrite parent body: Evidence from rare earth elements. *Geochimica et Cosmochimica Acta* **41**, 1271-1282 (1977).

3. E. R. D. Scott, R. C. Greenwood, I. A. Franchi, I. S. Sanders, Oxygen isotopic constraints on the origin and parent bodies of eucrites, diogenites, and howardites. *Geochimica et Cosmochimica Acta* **73**, 5835-5853 (2009).

4. J. M. D. Day, R. J. Walker, L. Qin, D. Rumble III, Late accretion as a natural consequence of planetary growth. *Nature Geoscience* **5**, 614-617 (2012).

5. H. Y. McSween Jr, D. W. Mittlefehldt, A. W. Beck, R. G. Mayne, T. J. McCoy, in *The Dawn Mission to Minor Planets 4 Vesta and 1 Ceres*. (Springer, 2012), pp. 141-174.

6. Bvsp, *Basaltic Volcanism on the Terrestrial Planets*. (Pergam Press Inc., New York, 1981), pp. 1286.

7. A. Yamaguchi, J.-A. Barrat, R.C. Greenwood, N. Shirai, C. Okamoto, T. Setoyanagi, M.Ebihara, I.A. Franchi, M. Bohn. Crustal partial melting on Vesta: Evidence from highly metamorphosed eucrites. *Geochimica et Cosmochimica Acta* **73**, 7162-7182 (2009).

8. E. Stolper, Experimental petrology of eucritic meteorites. *Geochimica et Cosmochimica Acta* **41**, 587-611 (1977).

9. P. H. Warren, E. A. Jerde, Composition and origin of Nuevo Laredo trend eucrites. *Geochimica et Cosmochimica Acta* **51**, 713-725 (1987).

10. J. A. Barrat, J. Blichert-Toft, P. Gillet, F. Keller, The differentation of eucrites: The role of in situ crystallization. *Meteoritics & Planetary Science* **35**, 1087-1100 (2000).

11. J-A. Barrat, A. Yamaguchi, R.C. Greenwood, M. Bohn, J. Cotton, M. Benoit, I.A. Franchi. The Stannern trend eucrites: Contamination of main group eucritic magmas by crustal partial melts. *Geochimica et Cosmochimica Acta* **71**, 4108-4124 (2007).

12. K. Wang, F. Moynier, N. Douhpas, J.-A. Barrat, P. Craddock, C.K. Sio, Iron isotope fractionation in planetary crusts. *Geochimica et Cosmochimica Acta*, (2012).

13. A. Yamaguchi, T. Mikouchi, M. Ito, N. Shirai, J.-A. Barrat, S. Messenger, M. Ebihara. , Experimental evidence of fast transport of trace elements in planetary basaltic crusts by high temperature metamorphism. *Earth and Planetary Science Letters* **368**, 101-109 (2013).

14. H. Takeda, A. Graham, Degree of equilibration of eucritic pyroxenes and thermal metamorphism of the earliest planetary crust. *Meteoritics* **26**, 129-134 (1991).

15. A. Yamaguchi, G. J. Taylor, K. Keil, Global crustal metamorphism of the eucrite parent body. *Icarus* **124**, 97-112 (1996).

16. A. Yamaguchi *et al.*, Post-crystallization reheating and partial melting of eucrite EET90020 by impact into the hot crust of asteroid 4Vesta 4.50 Ga ago. *Geochimica et Cosmochimica Acta* **65**, 3577-3599 (2001).

17. L. Nyquist, H. Wiesmann, Y. Reese, C. Y. Shih, L. Borg, Samarium-neodymium age and manganese-chromium systematics of eucrite Elephant Moraine 90020. *Meteoritics and Planetary Science Supplement* **32**, 101 (1997).

18. M. K. Haba, A. Yamaguchi, K. Horie, H. Hidaka, Major and trace elements of zircons from basaltic eucrites: Implications for the formation of zircons on the eucrite parent body. *Earth and Planetary Science Letters* **387**, 10-21 (2014).

19. J. Roszjar, K. Metzler, A. Bischoff, J.-A. Barrat, T. Geisler, R.C. Greenwood, I.A. Franchi, S. Kelmme, Thermal history of Northwest Africa 5073—A coarse grained Stannern trend eucrite containing cm sized pyroxenes and large zircon grains. *Meteoritics & Planetary Science* **46**, 1754-1773 (2011).

20. D. W. Mittlefehldt, M. M. Lindstrom, Geochemistry of eucrites: genesis of basaltic eucrites, and Hf and Ta as petrogenetic indicators for altered antarctic eucrites. *Geochimica et Cosmochimica Acta* **67**, 1911-1934 (2003).

21. A. R. Sarafian, M. F. Roden, A. E. Patiño Douce, The nature of volatiles in eucrites: Clues from apatite. *Meteoritics and Planetary Science* **48**, 2135-2154 (2013).

22. R. G. Mayne, H. Y. McSween Jr., T. J. McCoy, A. Gale, Petrology of the unbrecciated eucrites. *Geochimica et Cosmochimica Acta* **73**, 794-819 (2009).

23. D. Bogard, D. Garrison, in *28th Lunar and Planetary Science Conference*. (1997), pp. 127-128.

24. N. J. Pearce *et al.*, A compilation of new and published major and trace element data for NIST SRM 610 and NIST SRM 612 glass reference materials. *Geostandards newsletter* **21**, 115-144 (1997).

25. S. Eggins, R. Rudnick, W. McDonough, The composition of peridotites and their minerals: a laser-ablation ICP–MS study. *Earth and Planetary Science Letters* **154**, 53-71 (1998).

26. S. M. Eggins, J. M. G. Shelley, Compositional Heterogeneity in NIST SRM 610-617 Glasses. *Geostandards Newsletter* **26**, 269-286 (2002).

27. M. Norman, W. Griffin, N. Pearson, M. Garcia, S. O'reilly, Quantitative analysis of trace element abundances in glasses and minerals: a comparison of laser ablation inductively coupled plasma mass spectrometry, solution inductively coupled plasma mass spectrometry, proton microprobe and electron microprobe data. *Journal of Analytical Atomic Spectrometry* **13**, 477-482 (1998).

28. K. Jochum, B. Stoll, K. Herwig, M. Willbold, Validation of LA-ICP-MS trace element analysis of geological glasses using a new solid-state 193 nm Nd: YAG laser and matrix-matched calibration. *Journal of Analytical Atomic Spectrometry* **22**, 112-121 (2007).

29. K. P. Jochum, B. Stoll, K. Herwig, M. Willbold, A.W. Hoffmann, M. Amini, S Aarburg, MPI-DING reference glasses for in situ microanalysis: New reference values for element concentrations and isotope ratios. *Geochemistry, Geophysics, Geosystems* **7**, 1-44 (2006).

30. K. P. Jochum, M. Willbold, I. Raczek, B. Stoll, K. Herwig, Chemical Characterisation of the USGS Reference Glasses GSA-1G, GSC-1G, GSD-1G, GSE-1G, BCR-2G, BHVO-2G and BIR-1G Using EPMA, ID-TIMS, ID-ICP-MS and LA-ICP-MS. *Geostandards and Geoanalytical Research* **29**, 285-302 (2005).

31. S. Gao, X. Liu, H. Yuan, B. Hattendorf, L. Chen, S. Hu. , Determination of forty two major and trace elements in USGS and NIST SRM glasses by laser ablation-inductively coupled plasma-mass spectrometry. *Geostandards Newsletter* **26**, 181-196 (2002).

32. F. E. Jenner, H. S. C. O'Neill, Major and trace analysis of basaltic glasses by laser-ablation ICP-MS. *Geochemistry, Geophysics, Geosystems* **13**, (2012).

33. M. Guillong, I. Horn, D. Günther, A comparison of 266 nm, 213 nm and 193 nm produced from a single solid state Nd: YAG laser for laser ablation ICP-MS. *Journal of analytical atomic spectrometry* **18**, 1224-1230 (2003).

34. S. Prowatke, S. Klemme, Trace element partitioning between apatite and silicate melts. *Geochimica et Cosmochimica Acta* **70**, 4513-4527 (2006).

35. J.-A. Barrat, A. Yamaguchi, A. Jambon, C. Bollinger, O. Boudouma., Geochemistry of CI chondrites: Major and trace elements, and Cu and Zn Isotopes. *Geochimica et Cosmochimica Acta* **83**, 79-92 (2012).

36. A. R. Sarafian, S. G. Nielsen, H. R. Marschall, F. M. McCubbin, B. D. Monteleone, Early accretion of water in the inner solar system from a carbonaceous chondrite–like source. *Science* **346**, 623-626 (2014).

37. P. B. Kelemen, H. J. B. Dick, J. E. Quick, Formation of harzburgite by pervasive melt/rock reaction in the upper mantle. *Nature* **358**, 635-641 (1992).

38. Y. Liang, A. Schiemenz, M. A. Hesse, E. M. Parmentier, J. S. Hesthaven, High-porosity channels for melt migration in the mantle: Top is the dunite and bottom is the harzburgite and lherzolite. *Geophysical Research Letters* **37**, (2010).

39. E. Tursack, Y. Liang, A comparative study of melt-rock reactions in the mantle: laboratory dissolution experiments and geological field observations. *Contributions to Mineralogy and Petrology* **163**, 861-876 (2012).

40. T. S. McCarthy, L. H. Ahrens, A. J. Erlank, Further evidence in support of the mixing model for howardite origin. *Earth and Planetary Science Letters* **15**, 86-93 (1972).

41. N. Tollari, M. Toplis, S. J. Barnes, Predicting phosphate saturation in silicate magmas: An experimental study of the effects of melt composition and temperature. *Geochimica et Cosmochimica Acta* **70**, 1518-1536 (2006).

42. T. M. Harrison, E. B. Watson, The behavior of apatite during crustal anatexis: equilibrium and kinetic considerations. *Geochimica et Cosmochimica Acta* **48**, 1467-1477 (1984).

43. E. Jennings, H. Marschall, C. Hawkesworth, C. Storey, Characterization of magma from inclusions in zircon: Apatite and biotite work well, feldspar less so. *Geology* **39**, 863 (2011).

44. F. M. McCubbin *et al.*, Nominally hydrous magmatism on the Moon. *Procedings of the National Academy of Sciences of the United States of America* **107**, 11223-11228 (2010).

45. H. J. Lippolt, M. Leitz, R. S. Wernicke, B. Hagedorn, (Uranium+ thorium)/helium dating of apatite: experience with samples from different geochemical environments. *Chemical Geology* **112**, 179-191 (1994).

46. L. K. Sha, B. W. Chappell, Apatite chemical composition, determined by electron microprobe and laser-ablation inductively coupled plasma mass spectrometry, as a probe into granite petrogenesis. *Geochimica et Cosmochimica Acta* **63**, 3861-3881 (1999).

47. A. E. Patiño-Douce, M. Roden, Apatite as a probe of halogen and water fugacities in the terrestrial planets. *Geochimica et Cosmochimica Acta* **70**, 3173-3196 (2006).

48. C. Dalou, K. T. Koga, N. Shimizu, J. Boulon, J.-L. Devidal, Experimental determination of F and Cl partitioning between lherzolite and basaltic melt. *Contributions to Mineralogy and Petrology* **163**, 591-609 (2012).

49. E. H. Hauri, G. A. Gaetani, T. H. Green, Partitioning of water during melting of the Earth's upper mantle at H2O-undersaturated conditions. *Earth and Planetary Science Letters* **248**, 715-734 (2006).

50.   J. Blichert-Toft, M. Boyet, P. Télouk, F. Albarède, 147Sm–143Nd and 176 Lu–176 Hf in eucrites and the differentiation of the HED parent body. *Earth and Planetary Science Letters* **204**, 167-181 (2002).

51.   M. Daines, D. Kohlstedt, The transition from porous to channelized flow due to melt/rock reaction during melt migration. *Geophysical Research Letters* **21**, 145-148 (1994).

52.   P. B. Kelemen, J. Whitehead, E. Aharonov, K. A. Jordahl, Experiments on flow focusing in soluble porous media, with applications to melt extraction from the mantle. *Journal of Geophysical Research: Solid Earth (1978–2012)* **100**, 475-496 (1995).

53.   M. B. Baker, E. M. Stolper, Determining the composition of high-pressure mantle melts using diamond aggregates. *Geochimica et Cosmochimica Acta* **58**, 2811-2827 (1994).

54.   M. Baker, M. Hirschmann, M. Ghiorso, E. Stolper, Compositions of near-solidus peridotite melts from experiments and thermodynamic calculation. *Nature* **375**, 308-311 (1995).

55.   E. H. Hauri, T. P. Wagner, T. L. Grove, Experimental and natural partitioning of Th, U, Pb and other trace elements between garnet, clinopyroxene and basaltic melts. *Chemical Geology* **117**, 149-166 (1994).

56.   G. A. Snyder, L. A. Taylor, C. R. Neal, A chemical model for generating the sources of mare basalts: Combined equilibrium and fractional crystallization of the lunar magmasphere. *Geochimica et Cosmochimica Acta* **56**, 3809-3823 (1992).

57.   T. Green, S. Sie, C. Ryan, D. Cousens, Proton microprobe-determined partitioning of Nb, Ta, Zr, Sr and Y between garnet, clinopyroxene and basaltic magma at high pressure and temperature. *Chemical Geology* **74**, 201-216 (1989).

58.   P. H. Warren, G. W. Kallemeyn, H. Huber, F. Ulff-Møller, W. Choe, Siderophile and other geochemical constraints on mixing relationships among HED-meteoritic breccias. *Geochimica et Cosmochimica Acta* **73**, 5918–5943 (2009).

59.   J. A. Barrat, A. Yamaguchi, B. Zanda, C. Bollinger, M. Bohn, Relative chronology of crust formation on asteroid Vesta: Insights from the geochemistry of diogenites. *Geochimica et Cosmochimica Acta* **74**, 6218-6231 (2010).

60.   J. Barrat, A. Yamaguchi, A. Jambon, C. Bollinger, O. Boudouma, Low-Mg rock debris in howardites: Evidence for KREEPy lithologies on Vesta? *Geochimica et Cosmochimica Acta* **99**, 193-205 (2012).

61.   D. Rosner, Thermal/Soret/diffusion effects on interfacial mass transport rates. *physicochemical Hydrodynamics* **1**, 159-185 (1980).

62.   C. Lesher, Effects of silicate liquid composition on mineral-liquid element partitioning from Soret diffusion studies. *Journal of Geophysical Research* **91**, 6123-6141 (1986).

63.   A. G. Whittington, A. M. Hofmeister, P. I. Nabelek, Temperature-dependent thermal diffusivity of the Earth's crust and implications for magmatism. *Nature* **458**, 319-321 (2009).

64.   T. Iizuka, A. Yamaguchi, M.K. Haba, Y. Amlin, P. Holden, M.H. Huykens, T.R. Ireland, Timing of global crustal metamorphism on Vesta as revealed by high-precision U–Pb dating and trace element chemistry of eucrite zircon. *Earth and Planetary Science Letters* **409**, 182-192 (2015).

65.   A. H. Treiman, A. Lanzirotti, D. Xirouchakis, Ancient water on asteroid 4 Vesta: Evidence from a quartz veinlet in the Serra de Magé eucrite meteorite. *Earth and Planetary Science Letters* **219**, 189-199 (2004).

66.   J. A. Barrat A.Yamaguchi, T.E. Bunch, M. Bohn, C. Bollinger, G. Ceuleneer, Possible fluid-rock interactions on differentiated asteroids recorded in eucritic meteorites. *Geochimica et Cosmochimica Acta* **75**, 3839–3852 (2011).

67.   A. H. Treiman, The perils of partition: Difficulties in retrieving magma compositions from chemically equilibrated basaltic meteorites. *Geochimica et Cosmochimica Acta* **60**, 147-155 (1996).

68.   A. Pun, J. J. Papike, Unequilibrated eucrites and the equilibrated Juvinas eucrite: Pyroxene REE systematics and major, minor, and trace element zoning. *American Mineralogist* **81**, 1438-1451 (1996).

69.   D. Cherniak, REE diffusion in feldspar. *Chemical Geology* **193**, 25-41 (2003).

70.   R. P. Rapp, E. B. Watson, Monazite solubility and dissolution kinetics: implications for the thorium and light rare earth chemistry of felsic magmas. *Contributions to Mineralogy and Petrology* **94**, 304-316 (1986).

4.10 Figures and Tables

Figure 1

Nd vs. Sc plot for eucrites (*7, 10, 11, 40, 58*). Juvinas and EET 82600 are presented to show slight variations in magma composition for mixing relations with the enriched melt. Black box is EET 90020.
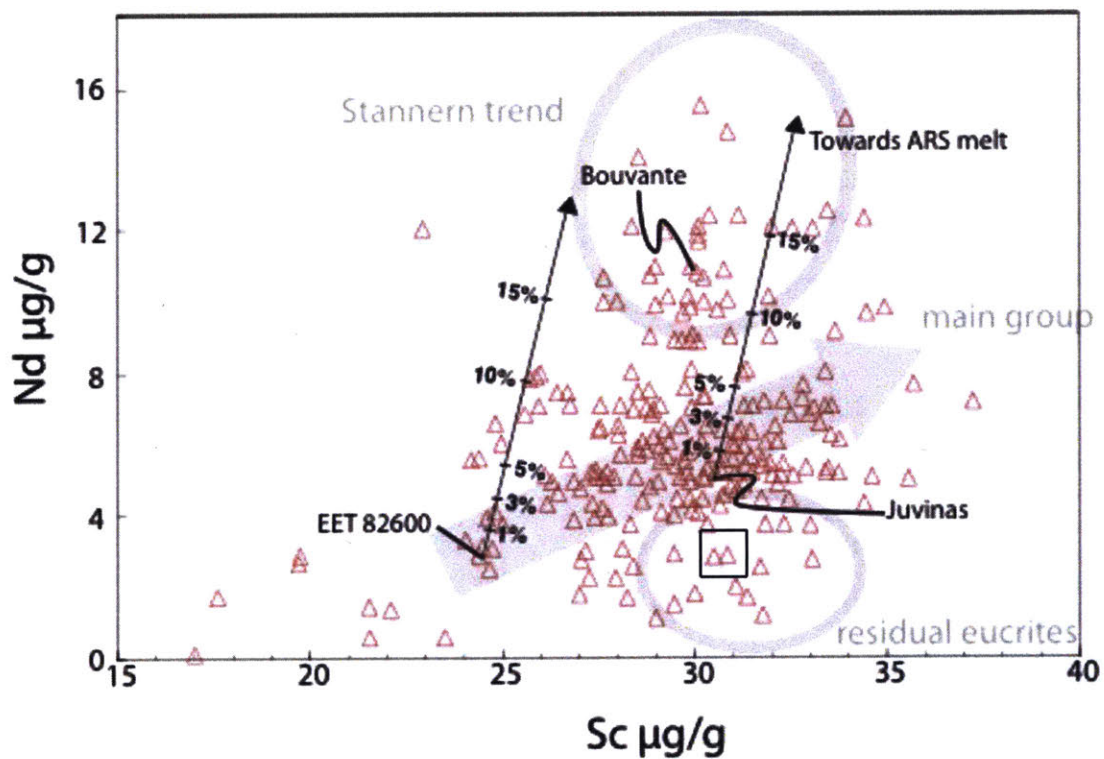
Figure 2

Plane-polarized light photomosaic of EET 90020 with spatial relationships among the ophitic fine-grained domain, equigranular coarse-grained domain, and ARS.
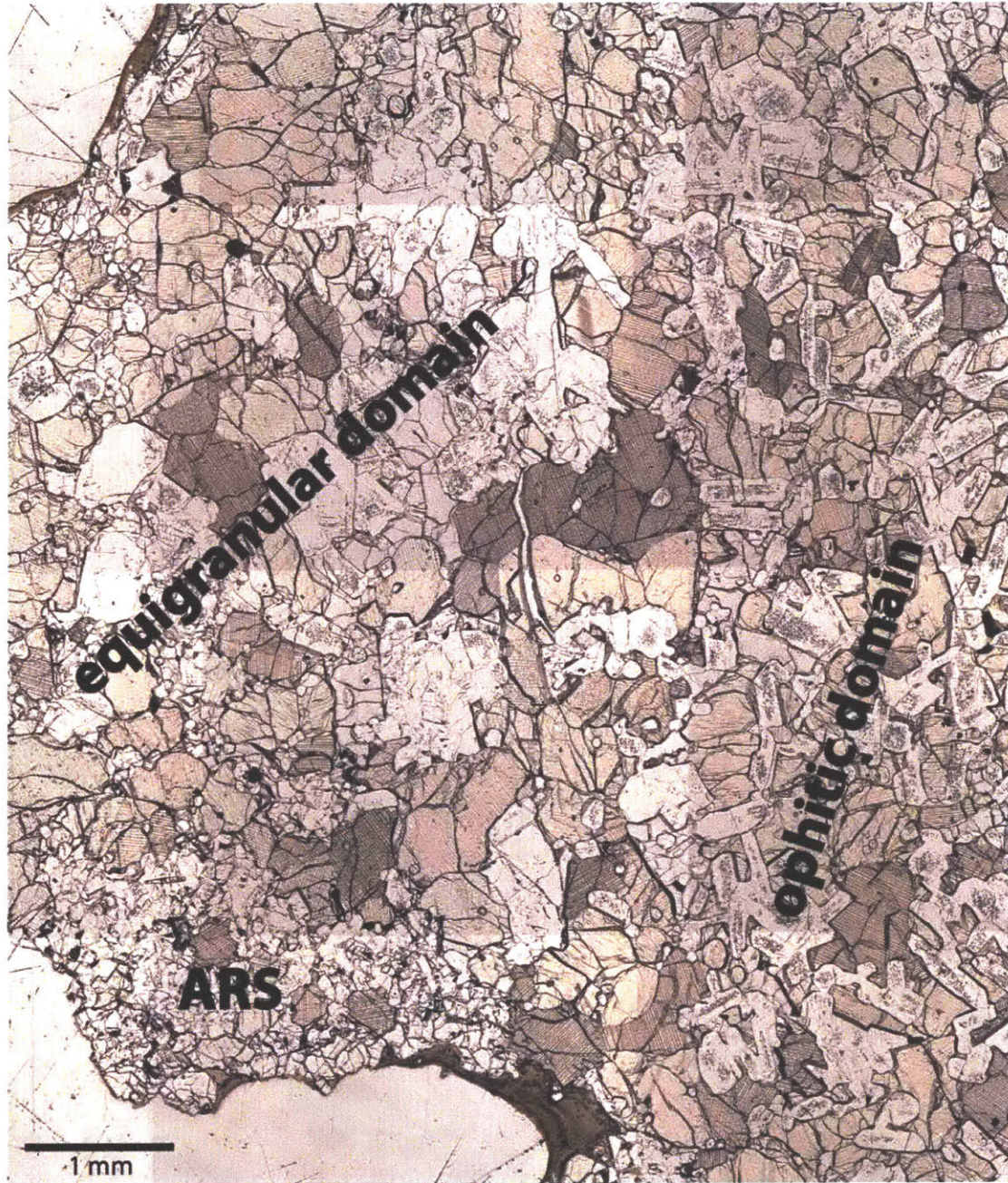
Figure 3

(a) Plane-polarized light image of the equigranular fine-grained domain. (b) Crossed-polarized light image of the equigranular fine-grained domain. (c) Plane-polarized light image of the ophitic coarse-grained domain. (d) Crossed-polarized light image of the ophitic coarse-grained domain. (e) Plane-polarized light image of the equigranular fine-grained domain adjacent to the coarse-grained domain Plagioclase is ~0.7 mm in the long direction in all images. Plagioclase is opaque/white in plane polarized light (a,c, and e) and 1st order gray in crossed-polarized light (b and d). Pyroxene is pinkish in plane-polarized light with sub-parallel exsolution lamellae (a, c, and e) and has high-order colors in crossed polarized light (b and d). Note abundant SiO_2 inclusions in ophitic plagioclase, but relatively few inclusions in recrystallized equigranular plagioclase. The scale is the same in all images
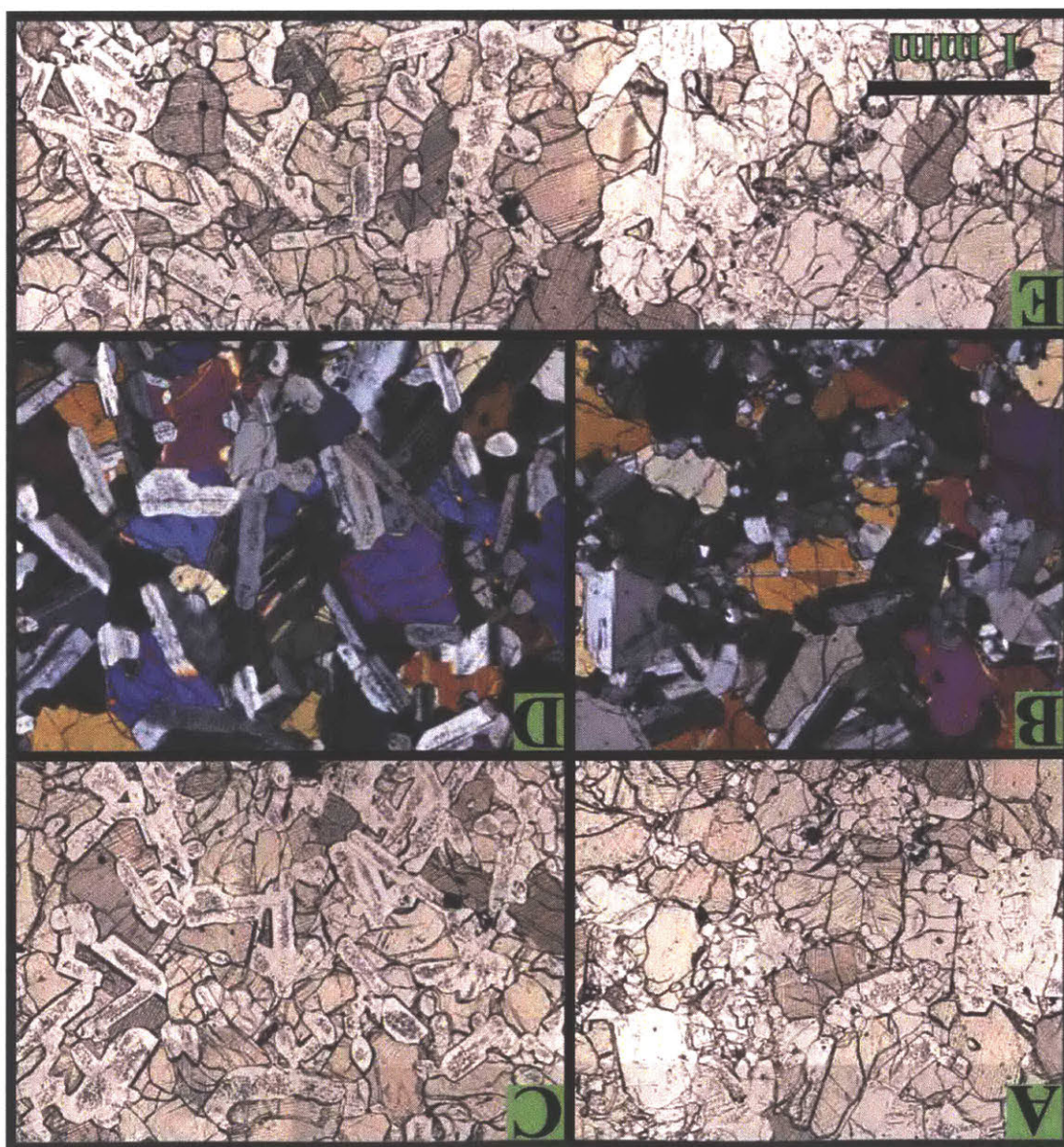
Figure 4

CI-normalized trace-element patterns for (a) apatite, (b) pyroxene, and (c) plagioclase in the ophitic coarse-grain domain (OD), equigranular fine-grain domain (ED), and apatite-rich subdomain (ARS). CI chondrite from (*35*).
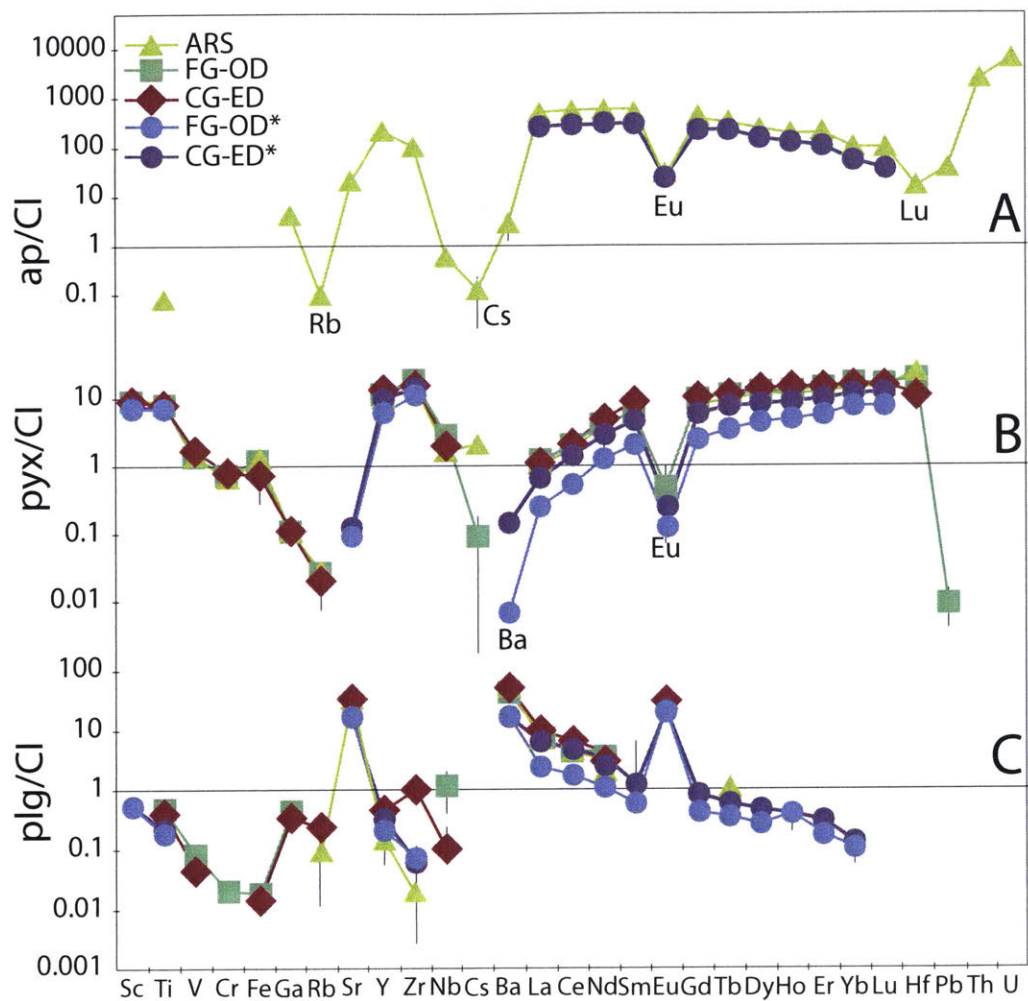
Figure 5

Conceptual model of the genesis of EET 90020, the main group and Stannern-trend eucrites. Modified from ref (*11*).
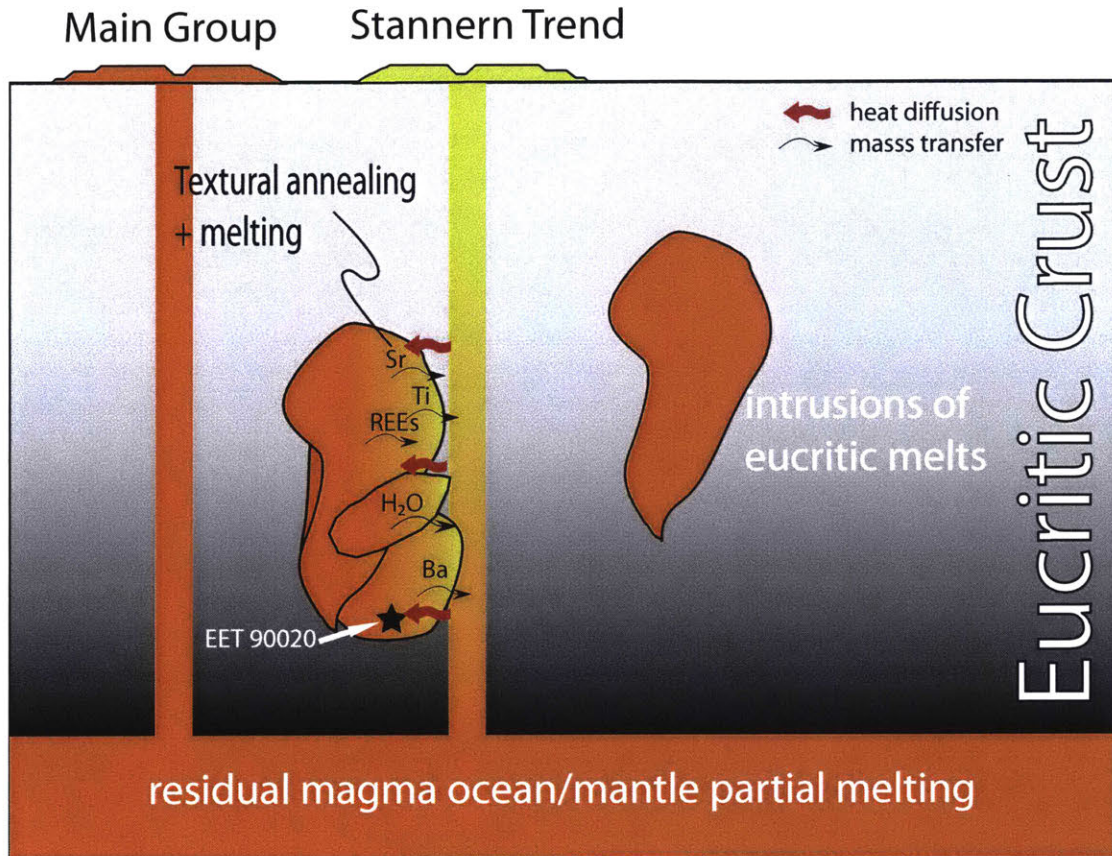
Figure 6

(a) Juvinas-normalized trace-element patterns for the calculated melt in equilibrium with the ARS (shaded region), Bouvante, and a 10 % partial melt from the model of (*11*). Bouvante data are from (*11*). (b) CI-normalized trace-element patterns for a 12:88 mix of the ARS melt and Juvinas (shaded region). Juvinas composition from (*11*).

Table 1

Trace element compositions of BHVO determined by LA-ICP-MS.

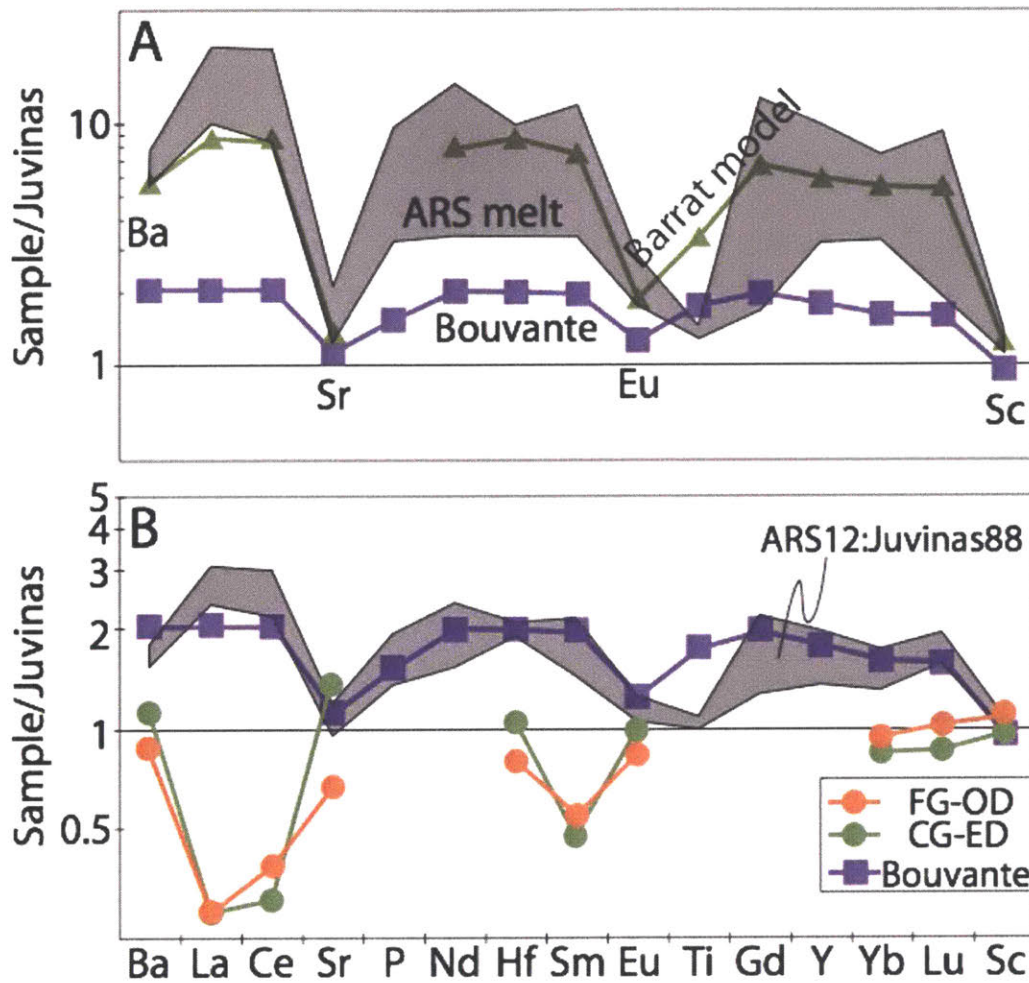| element (µg/g)	mass	D (plg)	D (pyx)	D (ap)	BHVO UMD	1 stdev	Reference*	detection limit
Sc	45	-	**0.808**[a]	-	29.8	0.684	33	0.256
Ti	49	-	**0.451**[a]	-	15500	450	16300	0.946
V	51	-	**1.810**[a]	-	322	5.33	308	0.072
Cr	53	-	**1.660**[a]	-	295	4.56	293	1.27
FeO	57	-	-	-	11.0	0.311	11.3	0.002
Ga	71	-	-	-	22.2	0.646	22	0.083
Rb	85	**0.080**[b]	0.003[b]	0.001[c]	9.39	0.353	9.2	0.029
Sr	86	**1.610**[b]	0.002[b]	**1.370**[c]	383	6.01	396	2.570
Y	89	-	-	**2.910**[c]	21.0	0.592	26	0.015
Zr	90	-	**0.063**[b]	0.056[c]	148	3.70	170	0.037
Nb	93	**0.005**[b]	**0.020**[b]	0.002[c]	17.7	0.693	18.3	0.012
Cs	133	-	-	-	0.100	0.018	0.1	0.012
Ba	137	**0.686**[b]	0.013[b]	0.060[c]	130	5.84	131	0.070
La	139	**0.042**[b]	0.001[b]	**2.940**[c]	14.6	0.499	15.2	0.009
Ce	140	**0.030**[b]	0.002[b]	**3.230**[c]	36.8	0.810	37.6	0.004
Pr	141	-	-	**3.860**[c]	5.18	0.274	5.35	0.018
Nd	146	**0.024**[b]	0.006[b]	**4.801**[c]	23.2	1.00	24.5	0.025
Sm	147	0.017[b]	0.011[b]	**5.860**[c]	5.62	0.362	6.1	0.011
Eu	153	**1.200**[b]	0.007[b]	-	1.99	0.132	2.07	0.007
Gd	157	0.011[b]	0.021[b]	**5.130**[c]	5.46	0.276	6.16	0.043
Tb	159	**0.010**[b]	0.027[b]	**4.497**[c]	0.75	0.049	0.92	0.002
Dy	163	0.009[b]	0.034[b]	**4.068**[c]	4.50	0.212	5.28	0.015
Ho	165	-	-	**3.576**[c]	0.83	0.061	0.98	0.003
Er	167	**0.008**[b]	0.055[b]	**3.046**[c]	2.08	0.116	2.56	0.011
Tm	169	-	-	**2.439**[c]	0.29	0.031	0.34	0.004
Yb	173	0.007[b]	0.087[b]	**1.753**[c]	1.72	0.147	2.01	0.008
Lu	175	0.007[b]	0.110[b]	**1.220**[c]	0.24	0.012	0.279	0.005
Hf	179	0.013[b]	**0.013**[b]	0.014[c]	3.81	0.278	4.32	0.014
Pb	206	-	**0.010**[a]	0.100[c]	1.67	0.120	1.7	0.026
Th	232	-	**0.014**[a]	0.700[c]	1.09	0.073	1.22	0.002
U	238	-	-	**0.170**[c]	0.40	0.038	0.403	0.001

Partition coefficients (D) are taken from: a - Hauri, Wagner and Grove (*55*), b -Snyder, Taylor and Neal (*56*), c - Prowatke and Klemme (*34*), d - Green, Sie, Ryan and Cousens (*57*). **Bold** typeface indicates that specific partition coefficient was used. If two partition coefficients are bolded, then the average calculated melt composition was used. n.d. is not detected.

Table 2

Table 2. Trace element content of phases in EET 90020. The 1σ precision is a maximum

value, using internal precision or deviation from the mean of multiple analyses,

whichever is larger. plg is plagioclase, pyx is pyroxene, ap is apatie. n.d. is not detected.

element (µg/g)	OD				ED				ARS					
	plg	1 σ	pyx	1 σ	plg	1 σ	pyx	1 σ	plg	1 σ	pyx	1 σ	ap	1 σ
Sc	n.d.		54.8	1.81	n.d.	-	54.4	1.12	n.d.	-	62.5	3.87	n.d.	-
Ti	225	12.7	3960	117	179	51.5	3610	134	148	19.8	3880	321	39.1	7.32
V	4.50	0.212	80.1	1.63	2.43	0.156	92.3	8.56	n.d.	-	76.8	8.56	n.d.	-
Cr	54.3	1.09	1890	38.7	n.d.	-	2090	71.79	n.d.	-	1760	197	n.d.	-
FeO	0.448	0.659	28.9	3.68	0.340	0.556	17.3	10.7	n.d.	-	30.4	4.94	n.d.	0.325
Ga	4.48	0.340	1.09	0.206	3.32	0.294	1.08	0.174	n.d.	-	1.06	0.180	41.7	5.79
Rb	n.d.	-	0.061	0.029	0.550	0.087	0.046	0.029	0.219	0.193	0.066	0.030	0.241	0.06
Sr	234	10.5	n.d.	-	240	27.5	n.d.	-	249	32.7	n.d.	-	154	22.3
Y	n.d.	-	19.2	2.85	0.717	0.268	20.7	0.606	0.225	0.141	15.1	1.80	339	59.3
Zr	n.d.	-	71.4	3.91	3.56	0.263	59.0	7.944	0.076	0.039	58.9	6.63	392	69.4
Nb	0.299	0.210	0.693	0.111	0.025	0.035	0.477	0.086	n.d.	-	0.4	0.124	0.155	0.042
Cs	n.d.	-	0.017	0.017	n.d.	-	n.d.	-	n.d.	-	0.385	0.06	0.024	0.02
Ba	101	5.14	n.d.	-	122	10.3	n.d.	-	124	31.5	n.d.	-	7.05	3.99
La	1.78	0.666	0.289	0.103	2.39	0.163	0.274	0.055	1.73	0.568	0.246	0.057	126	14.9
Ce	2.83	0.690	1.31	0.158	4.04	0.755	1.33	0.127	2.87	0.606	1.11	0.128	345	46.8
Pr	0.425	0.143	0.294	0.059	0.417	0.097	0.336	0.060	0.301	0.173	0.254	0.052	55.3	7.14
Nd	1.75	1.31	1.97	0.425	1.41	0.317	2.29	0.382	0.952	0.461	1.79	0.337	273	35.3
Sm	n.d.	-	0.941	0.289	n.d.	-	1.36	0.324	n.d.	-	0.956	0.297	77.1	7.32
Eu	1.86	0.206	0.028	0.030	1.76	0.234	n.d.	-	1.77	0.329	n.d.	-	1.82	0.660
Gd	n.d.	-	2.07	0.495	n.d.	-	2.11	0.406	n.d.	-	1.63	0.359	82.3	12.3
Tb	n.d.	-	0.425	0.067	n.d.	-	0.417	0.067	0.04	0.023	0.346	0.078	12	1.97
Dy	n.d	-	3.04	0.581	n.d.	-	3.42	0.380	n.d.	-	2.88	0.486	62	7.42
Ho	n.d.	-	0.731	0.153	n.d.	-	0.809	0.145	n.d.	-	0.613	0.120	11.4	1.09
Er	n.d.	-	2.32	0.344	n.d.	-	2.41	0.334	n.d.	-	2.05	0.559	33	5.46
Tm	n.d.	-	0.414	0.080	n.d.	-	0.357	0.062	n.d.	-	0.342	0.063	3.05	0.652
Yb	n.d.	-	2.73	0.435	n.d.	-	2.55	0.419	n.d.	-	2.45	0.599	16.8	3.70
Lu	n.d.	-	0.41	0.069	n.d.	-	0.382	0.072	n.d.	-	0.348	0.063	2.42	0.479
Hf	n.d.	-	2.05	0.404	n.d.	-	1.13	0.387	n.d.	-	2.59	0.468	1.74	0.606
Pb	n.d.	-	0.023	0.013	n.d.	-	n.d.	-	n.d.	-	n.d.	-	96.1	3.63
Th	n.d.	-	n.d	-	n.d.	-	n.d.	-	n.d.	-	n.d.	-	70.3	14.7
U	n.d.	-	n.d	-	n.d.	-	n.d.	-	n.d.	-	n.d.	-	49.2	3.97

Table 3

Representative major element composition of ARS silicate minerals. Low and hi Ca-pyx are analyzed from exsolved pyroxene.

	plagioclase	low Ca-pyx	high Ca-pyx	tridymite
SiO_2	46.70	48.49	49.68	99.03
TiO_2	n.d	0.56	1.00	0.21
Al_2O_3	33.51	0.40	1.22	0.57
MgO	0.03	11.74	10.01	0.02
FeO	0.45	35.48	17.63	0.14
MnO	0.05	1.28	0.57	0
CaO	18.18	1.84	19.38	0.05
K2O	0.07	n.d.	n.d.	0.30
Na_2O	1.25	n.d.	0.03	0.03
Cr_2O_3	n.d.	0.17	0.67	n.d.
Sum	100.23	99.95	100.19	100.36

Chapter 5

The water and Fluorine content of 4 Vesta

5.1 Abstract

The processes that controlled accretion of water and volatiles to the inner solar system remains enigmatic. This is because determining in the absolute concentrations of volatile elements for planetary bodies is difficult. In this contribution we study rare unequilibrated eucrites, derived from the asteroid 4 Vesta, to determine the water and fluorine content of 4 Vesta. We establish minimum water and F content of 4 Vesta by using newly established partition coefficients. We also confirm that the D/H of eucrites matches that of carbonaceous chondrites.

5.2 Introduction

Eucrites are a large group of mafic meteorites that, together with howardites and diogenites, form a suit of rocks dubbed the HEDs. HEDs are thought to be derived from the asteroid 4 Vesta. Eucrites can be subdivided into basaltic and cumulate, or Mg-rich, where the basaltic eucrites are thought to represent a primitive crust on the asteroid 4 Vesta and other associated asteroids (*1*). Eucrites can be further subdivided based on their bulk chemical composition into a main group, which likely represents fractional crystallization, and an incompatible element-rich group named the Stannern trend.

The origins of the main group and Stannern trend have been debated. Some argue that the main group represents fractional crystallization of a magma ocean, where the most Mg-rich basaltic eucrites represent the earliest products of the magma ocean and the most Mg poor basalt eucrites represent the evolved magma ocean (*2*). Others have hypothesized that the main group resulted from varying degrees of partial melting of the Vestan mantle (*3*). Importantly, there is evidence that the hypothesized magma ocean degassed several volatile species during solidification, including H, Cl, K, and Zn (*4, 5*). Therefore, while magma ocean crystallization can be successfully modeled using bulk refractory element concentrations in eucrites, this is not the case for volatile elements (*2, 4*). The Stannern trend was likely formed from magma interacting with the eucritic crust prior to emplacement or eruption (*6, 7*).

All eucrites are depleted in volatile elements relative to Earth and carbonaceous chondrites. For example, the K/U of, eucrites, Earth, and CI carbonaceous chondrites are 4,000, 12,000 and 74,000 respectively (*8, 9*), which suggests that Vesta contains at most a third of the volatile element complement of Earth. Despite this strong volatile element depletion in Vesta, there are multiple lines of evidence that volatile elements, including H, affected the geological history of eucrites. For example, fluids may have precipitated veins consisting of apatite, Fe-rich olivine and quartz (*10-13*). While the source of these relatively late stage fluids may be exotic or local, hydrogen in magmatic apatite grains in eucrites has been shown to have a carbonaceous chondrite-like δD (δD is the deviation of the sample from standard mean ocean water in parts per

1000) (*4, 14, 15*), which implies that Vesta accumulated some amount of water during its early accretion history. However, none of these studies were able to determine the volatile-element content of 4 Vesta. Sarafian et al. (*4*) offered two poorly constrained estimates, an upper bound based on the K/U of Vesta, the Moon and Earth and a lower bound based on apatite hygrometery (*16*). Both of these estimates are highly unsatisfactory for several reasons. First, when extrapolating a K/U in order to calculate a H_2O content one must assume that K and H_2O are depleted in a systematic way, which is not the case in some planetary bodies (*17, 18*) and thus could render this approach incorrect by orders of magnitude (A. R. Sarafian et al, 2017c). Second, apatite hygrometry uses a late crystallizing phase to estimate primitive melt contents, which by definition must include an estimate of exactly when during the crystallization sequence the studied apatite grain crystallized, or assume H and F have the same partition coeffecients for the major crystallizing phases (*16*). For apatite this is generally not realistic and the calculated water content of the primitive melt will change by an order of magnitude if the apatite crystallized after 99% relative to 90% magma crystallization. In addition, degassing could take place prior to apatite saturation, which would lower the water content compared to the primitive melt and thus render apatite hygrometry a minimum estimate (Hauri et al., 2015). Lastly, OH exchange between apatite and melt has not been determined at the very low pressures (<1000 MPa) that are found within the crust of small planetary bodies like Vesta (*19*). A better method to determine the H_2O and volatile element contents of primitive achondrites in general and 4 Vesta in particular is to examine the nominally anhydrous phases (*17*), where volatile elements are present in trace quantities. Given that mineral-melt partition coefficients for the earliest crystallizing minerals olivine and pyroxene are relatively well established (*20-22*) these can in turn be used to calculate primitive magma contents.

Here we present H and F concentration data along with the hydrogen isotope composition of 4 unequilibrated eucrite meteorites in an attempt to better constrain the volatile element content and H-isotope composition of 4-Vesta. We compare our data to one equilibrated eucrite to assess the effects of late stage diffusive equilibration. We also report the first water and F partition coefficients in pyroxene at low pressure that in turn allows us to place robust constraints on the H content of the eucrite parent body, 4 Vesta.

5.3 Samples

We measured four chips of Antarctic polymict breccias from the National Institute of Polar Research (NIPR–Japan) collection, Yamato (Y)-74450,113, Y-75011,114, Y-793548,66, Y-82210,101. The samples were selected because these polymict eucrites are reported to have a high abundance of unequilibrated eucrite clasts. All of the polymict breccias that we measured contained plagioclase and pyroxene that are highly internally fractured at the 100s of nm to 10s of μm level, making surface-contamination-free volatile element measurements arduous. In addition, we measured one equilibrated eucrite, Juvinas, to establish the effects of equilibration on pyroxene on Vesta.

5.3.1 Y-74450

The 2 x 4 mm^2 unequilibrated eucrite clast displays some dendritic intergrowths of plagioclase and pyroxene that is zoned Fe and Mg, although most pyroxene is blocky and subhedral, and plagioclase laths separate abundant mesostasis. Pyroxene ranges from several tens of μm to 100s of μm in the long direction. Mesostasis is commonly present and consists primarily of a SiO$_2$ polymorph, Ca-phosphate, metal, and troilite (Fig. 1).

5.3.2 Y-75011

The 0.5 mm x 0.5 mm^2 unequilibrated eucrite clast displays dendritic intergrowths of plagioclase and pyroxene. Additionally, subhedral plagioclase and interstitial pyroxene is present. Mesostasis is abundant in interstitial regions and between plagioclase laths. Mesostasis consists of a SiO$_2$ polymorph, ilmenite, troilite, and Ca-phosphates.

5.3.3 Y-793548:

The 1 x 2 mm^2 unequilibrated eucrite clast displays dendritic intergrowths of plagioclase and pyroxene that are zoned Fe and Mg, and subhedral pyroxene with plagioclase laths. Mesostasis

is abundant and SiO_2 rich. Pyroxene ranges from several tens of μm to 100s of μm in the long direction.

5.3.4 Y-82210:

The 1.5 x 2 mm^2 unequilibrated eucrite clast displays dendritic intergrowths of plagioclase and pyroxene that is zoned Fe and Mg. Pyroxene ranges from several tens of μm to 100s of μm in the long direction. Mesostasis is present and consists primarily of a SiO_2 polymorph, Ca-phosphate, metal and troilite.

5.3.5 Juvinas:

Juvinas is a well-studied monomict breccia that has been thermally equilibrated (12, 23, 24). Juvinas can be classified as a type 5 eucrite, meaning that the major elements in pyroxene grains have been homogenized, pyroxene grains are clouded, and the pyroxene pigeonite has exsolved to augite and orthopyroxene (24).

5.3.6 Pyroxene-melt experiments

Four low-pressure basalt melting experiments (three at 200 MPa and one at 0.1 MPa) were measured for H-partitioning between pyroxene and melt. All charges consisted of glass as well as euhedral olivine, clinopyroxene, spinel ± plagioclase. Further details describing these experiments can be found in (25). For the 200 MPa experiments, glass is ~80 wt% of the capsule with ~10% pyroxene, while the 0.1 MPa experimental capsule contained ~50 wt% glass, and ~9 wt% clinopyroxene (Gaetani et al., 1994). All mineral phases are generally 5-20 μm.

5.4 Methods
5.4.1 Preparation

Rock chips of the brecciate eucrites and fresh chips of experimental charges were prepared by first embedding the samples in epoxy resin. The chips were polished using SiC followed by water-based diamond suspensions. Samples were polished to 0.25μm quality and finished with colloidal silica to ensure the best possible polish to the highly internally fractured pyroxenes. All eucrites were removed from epoxy and embedded in a single indium metal sample holder along with three reference materials: Suprasil 3002 pure SiO_2 glass (1 μg/g H_2O, purchased from Heraeus Quarzglas, Switzerland), Herasil 102 pure SiO_2 glass (55 μg/g H_2O, purchased from Heraeus), and ALV 519-4-1 mid-ocean ridge basalt glass (1700 μg/g H_2O). Experimental chips were prepared in a separate indium metal sample holder that also contained the above standards.

5.4.2 SEM:

Scanning electron microscope (SEM) mapping was conducted on all eucrite chips. We used the JEOL 8600F field emission SEM at the NASA Johnson Space Center in Houston equipped with an energy dispersive spectroscopy (EDS) detector. Prior to analysis samples were coated with a ca. 10 nm layer of carbon using a sputter coater. Backscatter electron (BSE) and EDS maps were collected and processed with the JEOL manufacturer's software. Element maps were used to identify mesostasis phases. Maps were collected using 15 kV and 700 nA accelerating voltage and beam current, respectively.

5.4.3 EPMA:

Major and minor element compositions of pyroxene in all eucrite chips were determined using the Cameca SX100 electron microprobe (EPMA) at NASA-Johnson Space Center, Houston, TX. Accelerating voltage of 20 kV and a beam current of 40 nA were used for quantitative major and minor element concentration analyses throughout. The elements Al, Ca, Ti, Cr, Fe, Mn, Si, and Mg were measured and calibrated with natural and synthetic reference materials: oligoclase, diopside, rutile, chromite, fayalite, rhodonite, NiO, fayalite and forsterite, respectively.

5.4.4 NanoSIMS:

124

Volatile element (H, C, F, and Cl) concentrations, along with P were measured for all eucrite chips and the isotopes of H (deuterium, D and H) were measured in some pyroxene (Y-74450) and apatite (Y-74450, Y-75011, Y-82210) grains where sufficiently large areas free of internal fractures were found. NanoSIMS measurements were conducted on a Cameca NanoSIMS 50L at the Carnegie Institution of Washington. Prior to measuring, our indium metal sample mount was cleaned with distilled water and ethanol and dried in a vacuum oven for a week at 50°C then an additional week at ultra high vacuum lower than 7×10^{-7} Pa (~5 $\times$ 10^{-9} torr). The samples were then taken out of the vacuum oven and gold coated. After gold coating, the sample was placed into the instrument to obtain a pressure of lower than 9×10^{-8} Pa (~7 $\times$ 10^{-10} torr) in the analysis chamber.

Isotope compositions and concentrations were determined in two separate analytical sessions lasting one week each and we used previously described methods (26) to measure H isotopes and volatile concentrations. Briefly, a focused ~15 nA Cs^+ primary beam was rastered to produce a 20 x 20 μm^2 pre-sputter crater. During our analysis we used a 10 x 10 μm^2 raster and used the Cameca software to eliminate the outer portions of our crater such that we counted ions from the central 4 x 4 μm^2 of the SIMS pit. Mass resolving power was nominally 2000 for isotope measurements and 6000 for concentration measurements. Separation of H_2 from D is unnecessary, as production of H_2 is less than 1.5×10^{-3}, which permits high precision (2–3 ‰) measurements at low mass resolving power (27). Using multi-collection mode, we counted on masses ^1H, ^2H, and ^{12}C for isotope ratio measurements and ^{12}C, $^{16}O^1H$, ^{19}F, ^{30}Si, ^{31}P and ^{35}Cl for the concentration measurements. We used the count rates on ^{30}Si to normalize the elemental concentrations. Hydrogen (^1H) backgrounds measured throughout the isotope session were ~ 3 x $10^3 \pm 5\%$ (2se, n=10) counts/s, which translates to ~8 $\mu g/g$ H_2O, and the D/H of the background was roughly terrestrial (-67 ‰ $\pm$ 200). Backgrounds for the concentration session were <2 $\mu g/g$ H_2O, background for CO_2 was ~0.5 $\mu g/g$, and backgrounds for F, P, and Cl were negligible (17). Backgrounds were corrected by subtracting counts from both standards and samples. All errors were propagated from measured backgrounds and analytical uncertainties. Instrumental drift and D/H instrumental mass fractionation was corrected daily by measuring an internal reference basaltic glass, ALV 519-4-1 (1700 $\mu g/g$ H_2O, δD = -72 ‰) at regular intervals throughout each

analytical session. Basaltic glass was used to establish the instrumental mass fractionation (α) because basaltic glass and apatite has been shown to have the same α at the 50-100‰ level of precision (28). For the unequilibrated eucrites uncertainty on individual concentration analyses is difficult to assess because the internal fracturing of pyroxenes complicated measurements. We used the reproducibility of a low H and F reference material, Herasil, to determine the reproducibility of our measurements. We estimate the H measurements are certain within ~10% for H and ~5% for F (2sd). Our D/H standard, 519-4-1, yielded a δD of 52 ± 53 ‰ (2sd).

5.5 Results

5.5.1 Major elements:

The pryoxenes in unequilibrated eucrites were zoned with respect to Fe and Mg (Fig. 2 and Table S1). This zoning has been previously interpreted as magmatic zonation (24) and forms the basis for the interpretation that these eucrites experienced metamorphic temperatures <700 degrees C and are, therefore, unequilibrated (29).

5.5.2 Volatile element concentrations and D/H ratios in eucrites:

Overall the concentrations of H_2O and F in pyroxenes vary between 4-11 µg/g and 0.12-0.23 µg/g, respectively (Table 1). Due to the limited number of analyses in each pyroxene grain we found no systematic variation in the H and F content of pyroxenes with respect to distance along an individual grain (Fig. 2.). Our sample set is limited because of the immense internal fracturing of the pyroxenes. Most (>70%) of all analyses were aborted due to abundant surface contamination originating from internal fracturing cracks. Of the analyses that ran to completion, >80% of all analyses contained unacceptable abundances of contamination as judged from aberrantly high C or Cl abundances. We discarded analyses with an apparent C and/or Cl concentrations greater than 1 and/or 0.02 µg/g, respectively. Fluorine display a negative correlation with MgO as would be expected for fractional crystallization (Fig. 3a). Similarly, H_2O increases with decreasing MgO (Fig. 3b). The H_2O and F contents of pyroxene from

Juvinas do not vary from core to rim and display 4.0 ± 0.2 (2se, n=8) H_2O and 0.07 ± 0.01 μg/g F (2se, n=8) (Table 2).

The H isotope composition of pyroxene and apatite vary from δD = -133‰ to -127‰ and δD = -239‰ to -73‰, respectively. On average, these values are within error of one another although there is significant variation outside of analytical error for the apatite analyses (Table 3). We did not attempt to correct our data for D produced by spallation (cf. Saal et al., 2013) because exposure ages of the eucrites we measured are unknown. As previously suggested (14), the spallation correction would be relatively small for the apatite because of the high water content of the apatites and the young exposure ages of most eucrites (30). The pyroxene would require a larger spallation correction, but this would still be relatively small (e.g. 10s of permil) due to the likely young exposure ages (31).

5.5.3. Concentrations in experimental charges:

The pyroxene in the 200 MPa pyroxene-melt experiments contained ~330 μg/g H_2O and the melt contained 4 wt% H_2O (Table 4). The partition coefficient obtained from these 200 MPa experiments agree with the parameterization for pyroxene-melt water partitioning presented by O'Leary et al. (21). The pyroxenes in the 0.1 MPa experiments contained 20 μg/g H_2O and the glass contains 200 μg/g H_2O (Table 4), which is a higher partition coefficient than those expected based on the parameterization by O'Leary et al. (21).

5.6 Discussion

5.6.1. Water and F concentrations in primary magmatic eucrite pyroxene

Although unequilibrated eucrites have largely preserved primary magmatic zonation for major elements this does not imply that no thermal metamorphism took place for these samples. At the TEM scale the pyroxenes have exsolved into augite and orthopyroxene (24), which requires that the samples experienced some amount of thermal metamorphism. This observation is important

127

because H diffusion is particularly fast at temperatures ~600°C or higher (*32*) and it is, therefore, possible that at least some of the samples were affected by diffusive re-equilibration for H. In addition, H in the form of either water or H_2 readily degasses during late stages of magmatic evolution where one or both of these species could have been saturated in Vestan magmas (*4*). Hence, pyroxene rims could also have been affected by H degassing. The diffusivity of F is likely much slower than H (*33*) although still significantly faster than Mg (*34*). Magmatic F zonation is, therefore, more likely for F than for water. In addition, F degasses less than H (*35*), which suggests that late stage degassing of F should be much less prevalent than H.

The observations that the MgO contents for all pyroxene analyses weakly correlate negatively with F (Fig. 3a) and with water from 25% to 15% MgO (Fig. 3) is consistent with retention of at least some magmatic zonation for both F and water. One can estimate where the unequilibrated eucrites lie on the main group/Stannern trend by using the Mg and Fe content of pyroxenes with Mg-Fe exchange coefficients between pyroxene and melt to determine the Mg# (where Mg# = molar MgO/(MgO+FeO)) of the melt (*36*). In addition we used the Ti concentration of cores of pyroxenes in conjunction with partition coefficients (*37*), we determine the Ti content of the primitive eucrite melt (Fig. 4). With these observations, only for the lowest MgO contents do we observe low water concentrations, which could be caused by either partial diffusive re-equilibration or late stage magmatic degassing.

This interpretation would suggest that the F and water contents recorded for the highest MgO contents of >20% provide the best estimate for the primitive H and F contents of a eucrite melt. The H_2O and F contents of the five most MgO-rich pyroxene analyses vary from 5-7 µg/g and 0.12-0.19 µg/g, respectively. Although evolution from 25% to 20% MgO in pyroxenes could represent ~15% of magma crystallization (*38*) the water and F concentration of a primitive melt would increase by only ~5%, which is minor compared with the overall scatter of the correlations between MgO, F and water (Fig. 3).

128

By comparing the unequilibrated pyroxenes with our analyses of pyroxene in Juvinas we can estimate the general effects on water and F concentrations in pyroxene during thermal alteration on Vesta. We find that both H and F are depleted in Juvinas pyroxenes (4.0 ± 0.2 (2se, n=8) H_2O and 0.07 ± 0.01 µg/g F (2se, n=8)) compared to cores of pyroxene in unequilibrated eucrites (5-7 µg/g H_2O and 0.12-0.19 µg/g F). The lower abundances of H and F in Juvinas pyroxenes suggest that thermal alteration of eucrites is an open system with respect to H and F, and that H and F are lost. Therefore, the H_2O and F concentrations of Juvinas pyroxene may serve as lower limits for the original contents in magmatic pyroxene. Given that any potential degassing that occurred before the thermal alteration would have further lowered the overall H_2O and F budgets in the pyroxene we conclude that the Juvinas data provides a robust lower limit for the original H_2O and F contents of the magmatic pyroxenes in eucrites. This lower limit is consistent with the concentrations inferred for the magmatic cores of the pyroxenes in the unequilibrated eucrites.

5.6.2 Partitioning of water and F in pyroxene at conditions relevant to asteroids

In order to calculate H and F concentrations in melt from the analysis of mineral compositions, partition coefficients are needed. Most literature partition coefficients are derived by using experiments conducted at high pressure (~1 GPa) and high water contents (~5 wt%) (*20*). Partition coefficients are known to be a function of pressure, temperature, and phase composition (*39*). Therefore, using partition coefficients calibrated for very different conditions than the samples investigated may yield erroneous results. Here we have measured four phase equilibria experiments conducted at relatively low pressures of 200 MPa and 0.1 MPa. The H partition coefficient determined from the 200 MPa experiments agree with the parameterization of O'Leary et al., (*21*):

$$lnD_{H_2O}^{cpx-melt} = -5.0(\pm0.4) + 6.3(\pm0.5)X_{V_{Al}}^{cpx} - 1.2(\pm0.3)X_{ca}^{cpx} + \frac{1600(\pm700)}{T}$$

while the significantly drier and lower pressure 0.1 MPa experiments yielded a higher H partition coefficient (Table 3). The elevated partition coefficient for the relatively dry 0.1 MPa experiment is consistent with olivine H partitioning, where partitioning experiments with variable water contents at the same pressure yield significantly higher partition coefficients at lower water contents (20, 40). One possible explanation for the increase in partition coefficient is that the melt OH/H_2O drastically increases as the melt water content decreases (41). Since only OH is likely to partition into pyroxene, the change in water speciation might explain the increase in water partitioning at lower water contents. However, there are large uncertainties regarding how to quantify hydrous melt speciation (41-49), which renders this explanation difficult to test with current data. Detailed studies are needed to establish the exact behavior of H partitioning for nominally anhydrous minerals at varying H_2O contents as well as low pressures. Regardless, we here use the water partition coefficient determined at low pressure and low water contents because these conditions are most appropriate for asteroidal settings. For basaltic melts, the existing F partitioning data is not systematic (20, 21, 50-53), therefore, we use our F partitioning data.

5.6.3 Vesta water and fluorine content:

We can use the water and F contents of the most primitive pyroxene cores together with the preferred partition coefficients to calculate their respective concentrations in the melt from which these pyroxene cores crystallized. This yields a range for the primitive melt of 50-70 µg/g H_2O and 1.5-2.4 µg/g F. In order to use these values to further constrain the bulk Vesta concentrations we must consider the two leading hypotheses that generated the eucrites, which are mantle partial melting and extraction from a magma ocean (2, 3). For the mantle partial melting hypothesis (3, 54, 55), we assume that eucrites formed from a single 20-30% batch partial melting event leaving just olivine in the residua (55). If we use mineral melt partition coefficients for olivine (20), then we can calculate bulk mantle water and F content. The range of 20-30% batch melting then produces bulk concentrations for the Vesta mantle of 10-20 µg/g H_2O and 0.3-0.7 µg/g F. The largest uncertainty for the partial melt calculation is the water olivine-melt partition coefficient, which we have shown could be drastically higher at low water content and

low pressure. If this partition coefficient is higher, then our estimate of the water content of Vesta would be erroneously high.

For the magma ocean hypothesis, we take the primitive melt H and F composition as the magma ocean H and F composition at time of melt extraction. It has been proposed that some degassing of water and other volatile elements took place during magma ocean crystallization (*4*), which would render our estimate of the primitive magma ocean based on our unequilibrated eucrites lower than the true value. We cannot account for this degassing process because the rate of H degassing is unknown and H isotopes may not necessarily have fractionated during the degassing process (*4, 31*). Irrespective, these considerations suggest that our calculated initial magma ocean values will be minima. If we assume that eucritic melts were extracted after 20-80% crystallization of a magma ocean, where the liquidus phases were orthoyroxene and olivine in roughly 30:70 proportions (*2*), then 4 Vesta initially had at least 10-70 μg/g H_2O and 0.3-2 μg/g F. One must consider though, that these are lower limits due to (1) potential magma ocean degassing, (2) potential magma degassing during eruption, and (3) diffusional loss of H and/or F from pyroxenes. The only possible processes that could cause the estimated minima values to be higher than the true value is from surface contamination during analysis, and/or the water partition coefficients may be inappropriate for low-water and/or low pressure conditions.

5.6.4 Water retention on planetary bodies:

We are starting to obtain better estimates on the H content of several planetary bodies in the inner solar system. The estimates of H abundances are still crude, for example, estimates of Earth's H_2O varies from 300 to 3000 μg/g (*56, 57*), and vigorous debate on the water content of the Moon is ongoing (*18, 58, 59*). Here we examine the possibility that gravitational retention of volatiles is an important factor in controlling the water and highly volatile element content of a planetary body. Gravitational retention could be important, as strong evidence exists of volatile loss during the magma ocean phase of planetary formation (*4, 60, 61*). Therefore, we compare our estimated bulk water content of 4 Vesta from the unequilibrated eucrites with the bulk water content of the angrite parent body (APB) (*17*), Mars (*16*) and Earth (*56, 57*) with respect to the

131

radius of the planetary body (Fig. 5). We elect to exclude the moon from our regression, because the moon likely formed by giant impact (*62, 63*) It can be seen that a well-defined exponential relationship exists when comparing 4 Vesta, the APB, Mars, and Earth, which may imply that planetary bodies accumulate water during primary accretion and retain water and possibly other volatile elements proportional to their size. An alternate hypothesis could be that larger planetary bodies have a larger gravitational cross section and therefore accrete more wet material at later stages of planetary accretion when the inner solar system possibly became seeded with water rich bodies such as comets or carbonaceous chondrites (*62, 64, 65*).

With strong correlation between size of body and water content, one could speculate on the water and volatile content of the other inner solar system bodies, Venus and Mercury. Using our regression from figure 5, Venus should contain roughly the same amount of water, and likely other volatile elements as Earth. Mercury should contain ~200 μg/g H_2O. The exospheres of Earth and Venus have similar abundances of C (67, *66*), where Earth's C reservoir is mainly stored in sediment (*67*) and Venus' reservoir is mainly stored as atmospheric CO_2 (*66*).

5.6.5 The H isotope ratio of 4 Vesta:

The H isotope ratio of apatite in equilibrated eucrites has been previously studied (*4, 14, 15*). Given that water diffusion almost certainly occurred during thermal metamorphism in equilibrated eucrites, we here use our new H isotope data for unequilibrated eucrites (table s2) to test the hypothesis that eucrite water has a D/H similar to carbonaceous chondrites. The D/H of apatites and pyroxenes match that of previous studies (table S2), which suggests that the previously inferred carbonaceous chondrite origin of H and other volatiles in Vesta is likely correct. The diffusive re-equilibration of water in the equilibrated eucrites appears to have had little effect on the D/H ratio.

5.6.6 Timing of water addition to the inner solar system:

Recent evidence has shown that volatile elements with a carbonaceous chondrite heritage have accreted to inner solar system bodies within the first few million years of solar system history (14, 15, 17, 31). In addition, the most likely source of water for the Earth, Moon, and Mars is carbonaceous chondrites (26, 68-72). Therefore, one can question: when did water enter the inner solar system? Based on meteorite evidence, inner solar system materials with evidence of live ^{26}Al accreted water with a chondritic D/H (14, 17), and some evidence from lunar samples exists that chondritic water continued to accrete to the inner solar system 10s or 100 of millions of years after the start of the solar system (64, 69). If we view these observations in light of the most recent successful dynamic models, pebble accretion and giant planet formation, two possible scenarios exist.

Pebble accretion is an enticing new method of efficient planetary growth, where cm to m sized pebbles drift radially and accrete to larger planetary bodies (73-75). This method is favored because accretion of pebbles is extremely efficient compared to significantly larger bodies and allows for the giant planets to grow quickly (75). Pebbles in the outer solar system are thought to drift radially inward (76), accrete to planetary bodes, and those that do not accrete to planets/planetecimals would accrete to the Sun. The pebbles that form in the outer solar system, beyond a water ice line, could be expected to contain water ice, and thus provide a water delivery mechanism to the inner solar system prior to Jupiter formation. After Jupiter formation, outer solar system material is generally not expected to enter the inner solar system (77, 78), although recent dynamic simulations may provide a solution to the "Jupiter barrier" problem (79). Pebble accretion prior to Jupiter formation is a possible mechanism to deliver relatively small amounts of volatile elements to the inner solar system extremely early, but problems with this hypothesis exist. For example, based on the different H-isotope composition of inner solar system bodies, e.g., Earth, Moon, Mars, astroidal basalts, compared to the H-isotope composition of an outer solar system body like Saturn's moon Enceladus, Alexander et al (80) suggested that outer solar system bodies accreted a distinct H isotope reservoir. Therefore, early accreted pebble derived water should have a high D/H, which implies eucrites and angrites should have a high D/H, and this is not the case (4, 14, 15, 31).

The second plausible mechanism that could have brought significant water to the inner solar system is giant planet migration. Giant planet migration, like the Grand Tack (*81*) where the cores of Jupiter and Saturn form, migrate inward, and migrate outward, can be an efficient mechanism of water delivery to the inner solar system (*82*). The timing of the Grand Tack is poorly constrained, but it likely occurred within the first few million years of solar system history (or CAI formation) (*83*).

Evidence of extremely early volatile element accretion comes from eucrite (*4, 14, 15*) and angrite (*17, 31*) meteorites, both of which crystallized and locked in their water-bearing geochemical signature within the first few million years after CAI formation (*84, 85*). If the pebbles provided the water and volatile elements to these early formed bodies, then early accreted pebbles had carbonaceous chondrite H-, N-, and C- isotope signatures (*14, 31*), as well as carbonaceous chondrite relative abundances of volatile elements (*17*).

5.6 Conclusions

We report the H and F composition of unequilibrated eucrites as well as the equilibrated eucrite Juvinas. Appropriate partition coefficients were determined and used to determine a primitive melt composition. The bulk composition for H and F of the eucrite parent body, 4 Vesta, was calculated using the partial melt and magma ocean models. Given our assumptions, 4-Vesta has about 10-70 $\mu g/g$ H_2O and 0.3-2 $\mu g/g$ F. The isotopic composition of unequilibrated eucrites is consistent with a chondritic source of volatile elements to early-forming 4-Vesta. Comparison of the estimated bulk H_2O of differentiated objects in the inner solar system with their radii suggests that gravitational attraction plays a primary role in the accretion and retention of volatiles during the assembly and evolution of objects in the inner solar system.

5.7 Acknowledgements

5.8 References

1. R. P. Binzel, S. Xu, Chips off of Asteroid 4 Vesta; evidence for the parent body of basaltic achondrite meteorites. *Science*. **260**, 186–191 (1993).

2. B. E. Mandler, L. T. Elkins-Tanton, The origin of eucrites, diogenites, and olivine diogenites: Magma ocean crystallization and shallow magma chamber processes on Vesta. *Meteoritics & Planetary Science*. **48**, 2333–2349 (2013).

3. E. Stolper, Experimental petrology of eucritic meteorites. *Geochimica et Cosmochimica Acta*. **41**, 587–611 (1977).

4. A. R. Sarafian, T. John, J. Roszjar, M. J. Whitehouse, Chlorine and hydrogen degassing in Vesta's magma ocean. *Earth and Planetary Science Letters*. **459**, 311–319 (2017).

5. R. C. Paniello *et al.*, Zinc isotopes in HEDs: clues to the formation of 4-Vesta, and the unique composition of Pecora Escarpment 82502. *Geochimica et Cosmochimica Acta*. **86**, 76–87 (2012).

6. J. A. Barrat *et al.*, The Stannern trend eucrites: Contamination of main group eucritic magmas by crustal partial melts. *Geochimica et Cosmochimica Acta*. **71**, 4108–4124 (2007).

7. A. Yamaguchi *et al.*, Crustal partial melting on Vesta: Evidence from highly metamorphosed eucrites. *Geochimica et Cosmochimica Acta*. **73**, 7162–7182 (2009).

8. W. F. McDonough, S. S. Sun, The Composition of the Earth. *Chemical Geology*. **120**, 223–253 (1995).

9. D. W. Mittlefehldt, Asteroid (4) Vesta: I. The howardite-eucrite-diogenite (HED) clan of

meteorites. *Chemie der Erde - Geochemistry.* **75**, 155–183 (2014).

10. J. Roszjar *et al.*, Thermal history of Northwest Africa 5073—A coarse grained Stannern trend eucrite containing cm sized pyroxenes and large zircon grains. *Meteoritics & Planetary Science.* **46**, 1754–1773 (2011).

11. J. A. Barrat *et al.*, Possible fluid-rock interactions on differentiated asteroids recorded in eucritic meteorites. *Geochimica et Cosmochimica Acta.* **75**, 3839–3852 (2011).

12. A. R. Sarafian, M. F. Roden, A. E. Patiño Douce, The nature of volatiles in eucrites: Clues from apatite. *Meteoritics & Planetary Science.* **48**, 2135–2154 (2013).

13. A. H. Treiman, A. Lanzirotti, D. Xirouchakis, Ancient water on asteroid 4 Vesta: Evidence from a quartz veinlet in the Serra de Magé eucrite meteorite. *Earth and Planetary Science Letters.* **219**, 189–199 (2004).

14. A. R. Sarafian, S. G. Nielsen, H. R. Marschall, F. M. McCubbin, B. D. Monteleone, Early accretion of water in the inner solar system from a carbonaceous chondrite–like source. *Science.* **346**, 623–626 (2014).

15. T. J. Barrett *et al.*, The abundance and isotopic composition of water in eucrites. *Meteoritics & Planetary Science.* **51**, 110–1124 (2016).

16. F. M. McCubbin *et al.*, Heterogeneous distribution of H2O in the Martian interior: Implications for the abundance of H2O in depleted and enriched mantle sources. *Meteoritics & Planetary Science*, 1–25 (2016).

17. A. R. Sarafian *et al.*, Angrite meteorites record the onset and flux of water to the inner solar system. *Geochimica et Cosmochimica Acta.* **212**, 156–166 (2017).

18. E. H. Hauri, A. E. Saal, M. J. Rutherford, J. A. Van Orman, Water in the Moon's interior: Truth and consequences. *Earth and Planetary Science Letters.* **409**, 252–264 (2015).

19. F. M. McCubbin *et al.*, Experimental investigation of F, Cl, and OH partitioning between apatite and Fe-rich basaltic melt at 1.0–1.2 GPa and 950–1000 C. *American Mineralogist.* **100**, 1790–1802 (2015).

20. E. H. Hauri, G. A. Gaetani, T. H. Green, Partitioning of water during melting of the Earth's upper mantle at H2O-undersaturated conditions. *Earth and Planetary Science Letters.* **248**, 715–734 (2006).

21. J. A. O'Leary, G. A. Gaetani, E. H. Hauri, The effect of tetrahedral Al 3+ on the partitioning of water between clinopyroxene and silicate melt. *Earth and Planetary Science Letters.* **297**, 111–120 (2010).

22. H. Keppler, N. Bolfan-Casanova, Thermodynamics of water solubility and partitioning. *Reviews in Mineralogy and Geochemistry*. **62**, 193–230 (2006).

23. K. Metzler, K. D. Bobe, H. Palme, B. Spettel, D. Stöffler, Thermal and impact metamorphism on the HED parent asteroid. *Planetary and Space Science*. **43**, 499–525 (1995).

24. H. Takeda, A. L. Graham, Degree of equilibration of eucritic pyroxenes and thermal metamorphism of the earliest planetary crust. *Meteoritics*. **26**, 129–134 (1991).

25. G. A. Gaetani, T. L. Grove, W. B. Bryan, (Ocean Drilling Program, 1994), vol. 135, pp. 557–563.

26. A. E. Saal, E. H. Hauri, J. A. Van Orman, M. J. Rutherford, Hydrogen Isotopes in Lunar Volcanic Glasses and Melt Inclusions Reveal a Carbonaceous Chondrite Heritage. *Science*. **340**, 1317–1320 (2013).

27. E. Hauri *et al.*, SIMS analysis of volatiles in silicate glasses: 1. Calibration, matrix effects and comparisons with FTIR. *Chemical Geology*. **183**, 99–114 (2002).

28. S. Hu *et al.*, Measurements of water content and D/H ratio in apatite and silicate glasses using a NanoSIMS 50L. *Journal of Analytical Atomic Spectrometry*. **30**, 967–978 (2015).

29. A. Yamaguchi, G. J. Taylor, K. Keil, Global crustal metamorphism of the eucrite parent body. *Icarus*. **124**, 97–112 (1996).

30. J. A. Cartwright *et al.*, The quest for regolithic howardites. Part 1: Two trends uncovered using noble gases. *Geochimica et Cosmochimica Acta*. **105**, 395–421 (2013).

31. A. R. Sarafian *et al.*, Early accretion of water and volatile elements to the inner Solar System: evidence from angrites. *Philosophical Transactions of the Royal Society of London A: Mathematical, Physical and Engineering Sciences*. **375**, 1–27 (2017).

32. H. Skogby, Water in Natural Mantle Minerals I: Pyroxenes. *Reviews in Mineralogy and Geochemistry*. **62**, 155–167 (2006).

33. A. M. Koleszar *et al.*, The volatile contents of the Galapagos plume; evidence for H2O and F open system behavior in melt inclusions. *Earth and Planetary Science Letters*. **287**, 442–452 (2009).

34. Y. Zhang, D. J. Cherniak, Diffusion in minerals and melts. *Reviews in Mineralogy and Geochemistry*. **72**, 1–4 (2010).

35. M. R. Carroll, J. D. Webster, in *Volatiles in Magmas, Reviews in Mineralogy*, M. R. Carroll, J. R. Holloway, Eds. (Washington, DC, 1994), vol. 30, pp. 231–279.

36.   R. L. Nielsen, P. M. Davidson, T. L. Grove, Pyroxene-melt equilibria: an updated model. *Contributions to Mineralogy and Petrology.* **100**, 361–373 (1988).

37.   R. L. Nielsen, W. E. Gallahan, F. Newberger, Experimentally determined mineral-melt partition coefficients for Sc, Y and REE for olivine, orthopyroxene, pigeonite, magnetite and ilmenite. *Contributions to Mineralogy and Petrology.* **110**, 488–499 (1992).

38.   L. V. Danyushevsky, P. Plechov, Petrolog3: Integrated software for modeling crystallization processes. *Geochemistry, Geophysics, Geosystems.* **12**, 1–32 (2011).

39.   S. R. Hart, K. E. Davis, Nickel partitioning between olivine and silicate melt. *Earth and Planetary Science Letters.* **40**, 203–219 (1978).

40.   E. K. Sarafian, Geophysical and petrological constraints on ocean plate dynamics (2017), doi:10.1575/1912/9003.

41.   E. Stolper, The speciation of water in silicate melts. *Geochimica et Cosmochimica Acta.* **46**, 2609–2620 (1982).

42.   J. W. Tomlinson, *A note on the solubility of water in a molten sodium silicate* (J. Soc. Glass Technol, 1956).

43.   D. L. Hamilton, C. W. Burnham, E. F. Osborn, The solubility of water and effects of oxygen fugacity and water content on crystallization in mafic magmas. *Journal of Petrology* (1964).

44.   C. Aubaud, E. H. Hauri, M. M. Hirschmann, Hydrogen partition coefficients between nominally anhydrous minerals and basaltic melts. *Geophys. Res. Lett.* **31**, L20611 (2004).

45.   P. Ardia, M. M. Hirschmann, A. C. Withers, B. D. Stanley, Solubility of CH4 in a synthetic basaltic melt, with applications to atmosphere-magma ocean-core partitioning of volatiles and to the evolution of the Martian atmosphere. *Geochimica et Cosmochimica Acta.* **114**, 52–71 (2013).

46.   E. Stolper, Water in silicate glasses: An infrared spectroscopic study. *Contributions to Mineralogy and Petrology.* **81**, 1–17 (1982).

47.   J. E. Dixon, E. M. Stolper, J. R. Holloway, An experimental study of water and carbon dioxide solubilities in mid-ocean ridge basaltic liquids. Part I: Calibration and solubility models. *Journal of Petrology.* **36**, 1607–1631 (1995).

48.   H. Ni, H. Keppler, H. Behrens, Electrical conductivity of hydrous basaltic melts: implications for partial melting in the upper mantle. *Contributions to Mineralogy and Petrology.* **162**, 637–650 (2011).

49. F. Gaillard, Laboratory measurements of electrical conductivity of hydrous and dry silicic melts under pressure. *Earth and Planetary Science Letters*. **218**, 215–228 (2004).

50. C. Beyer, S. Klemme, M. Wiedenbeck, A. Stracke, C. Vollmer, Fluorine in nominally fluorine-free mantle minerals: Experimental partitioning of F between olivine, orthopyroxene and silicate melts with implications for magmatic processes. *Earth and Planetary Science Letters*. **337-338**, 1–9 (2012).

51. C. Dalou, K. T. Koga, N. Shimizu, J. Boulon, J.-L. Devidal, Experimental determination of F and Cl partitioning between lherzolite and basaltic melt. *Contributions to Mineralogy and Petrology*. **163**, 591–609 (2012).

52. C. Dalou, K. T. Koga, M. Le Voyer, N. Shimizu, Contrasting partition behavior of F and Cl during hydrous mantle melting: implications for Cl/F signature in arc magmas. *Prog. in Earth and Planet. Sci.* **1**, 26 (2014).

53. D. Bernini, M. Wiedenbeck, D. Dolejš, H. Keppler, Partitioning of halogens between mantle minerals and aqueous fluids: implications for the fluid flow regime in subduction zones. *Contributions to Mineralogy and Petrology*. **165**, 117–128 (2013).

54. H. O. Ashcroft, B. J. Wood, An experimental study of partial melting and fractional crystallization on the HED parent body. *Meteoritics & Planetary Science*. **50**, 1912–1924 (2015).

55. J. H. Jones, The composition of the mantle of the eucrite parent body and the origin of eucrites. *Geochimica et Cosmochimica Acta*. **48**, 641–648 (1984).

56. F. Albarède, Volatile accretion history of the terrestrial planets and dynamic implications. *Nature*. **461**, 1227–1233 (2009).

57. B. Marty, The origins and concentrations of water, carbon, nitrogen and noble gases on Earth. *Earth and Planetary Science Letters*. **313**, 56–66 (2012).

58. E. H. Hauri, T. Weinreich, A. E. Saal, M. C. Rutherford, J. A. Van Orman, High pre-eruptive water contents preserved in lunar melt inclusions. *Science*. **333**, 213–215 (2011).

59. F. M. McCubbin *et al.*, Magmatic volatiles (H, C, N, F, S, Cl) in the lunar mantle, crust, and regolith: Abundances, distributions, processes, and reservoirs. *American Mineralogist*. **100**, 1668–1707 (2015).

60. J. W. Boyce *et al.*, The chlorine isotope fingerprint of the lunar magma ocean. *Science Advances*. **1**, e1500380–e1500380 (2015).

61. J. J. Barnes *et al.*, Early degassing of lunar urKREEP by crust-breaching impact (s). *Earth and Planetary Science Letters*. **447**, 84–94 (2016).

62. W. F. Bottke, R. J. Walker, J. M. D. Day, D. Nesvorny, L. Elkins-Tanton, Stochastic late accretion to Earth, the Moon, and Mars. *Science*. **330**, 1527–1530 (2010).

63. R. M. Canup, E. Asphaug, Origin of the Moon in a giant impact near the end of the Earth's formation. *Nature*. **412**, 708–712 (2001).

64. R. Tartèse, M. Anand, Late delivery of chondritic hydrogen into the lunar mantle: Insights from mare basalts. *Earth and Planetary Science Letters*. **361**, 480–486 (2013).

65. R. Gomes, H. F. Levison, K. Tsiganis, A. Morbidelli, Origin of the cataclysmic Late Heavy Bombardment period of the terrestrial planets. *Nature*. **435**, 466–469 (2005).

66. C. Lecuyer, S. Laurent, F. Guyot, Comparison of carbon, nitrogen and water budgets on Venus and the Earth. *Earth and Planetary Science Letters*. **181**, 1–8 (2000).

67. M. M. Hirschmann, R. Dasgupta, The H/C ratios of Earth's near-surface and deep reservoirs, and consequences for deep Earth volatile cycles. *Chemical Geology*. **262**, 4–16 (2009).

68. F. Robert, The origin of water on Earth. *Science*. **293**, 1056–1058 (2001).

69. J. J. Barnes et al., An asteroidal origin for water in the Moon. *Nature Communications*. **7**, 11684 (2016).

70. J. J. Barnes et al., The origin of water in the primitive Moon as revealed by the lunar highlands samples. *Earth and Planetary Science Letters*. **390**, 244–252 (2014).

71. T. Usui, C. M. Alexander, J. Wang, J. I. Simon, J. H. Jones, Meteoritic evidence for a previously unrecognized hydrogen reservoir on Mars. *Earth and Planetary Science Letters*. **410**, 140–151 (2015).

72. L. J. Hallis, G. J. Taylor, K. Nagashima, G. R. Huss, Magmatic water in the martian meteorite Nakhla. *Earth and Planetary Science Letters*. **359**, 84–92 (2012).

73. S. J. Weidenschilling, Radial drift of particles in the solar nebula: implications for planetesimal formation. *Icarus*. **165**, 438–442 (2003).

74. A. Johansen et al., Rapid planetesimal formation in turbulent circumstellar disks. *Nature*. **448**, 1022–1025 (2007).

75. H. F. Levison, K. A. Kretke, M. J. Duncan, Growing the gas-giant planets by the gradual accumulation of pebbles. *Nature*. **524**, 322–324 (2015).

76. S. J. Weidenschilling, Aerodynamics of solid bodies in the solar nebula. *Mon Not R Astron Soc*. **180**, 57–70 (1977).

77.   K. R. Grazier, Jupiter: Cosmic Jekyll and Hyde. *Astrobiology*. **16**, 23–38 (2016).

78.   G. W. Wetherill, Possible consequences of absence of "jupiters" in planetary systems. *Astrophys Space Sci*. **212**, 23–32 (1994).

79.   S. N. Raymond, A. Izidoro, Origin of water in the inner Solar System: Planetesimals scattered inward during Jupiter and Saturn's rapid gas accretion. *Icarus*. **297**, 134–148 (2017).

80.   C. M. O. Alexander *et al.*, The provenances of asteroids, and their contributions to the volatile inventories of the terrestrial planets. *Science*. **337**, 721–723 (2012).

81.   K. J. Walsh, A. Morbidelli, S. N. Raymond, D. P. O'Brien, A. M. Mandell, A low mass for Mars from Jupiter's early gas-driven migration. *Nature*. **475**, 206–209 (2011).

82.   D. P. O'Brien, K. J. Walsh, A. Morbidelli, S. N. Raymond, A. M. Mandell, Water delivery and giant impacts in the "Grand Tack" scenario. *Icarus*. **239**, 74–84 (2014).

83.   T. S. Kruijer, C. Burkhardt, G. Budde, T. Kleine, Age of Jupiter inferred from the distinct genetics and formation times of meteorites. *Proceedings of the National Academy of Sciences*. **114**, 6712–6716 (2017).

84.   U. Hans, T. Kleine, B. Bourdon, Rb–Sr chronology of volatile depletion in differentiated protoplanets: BABI, ADOR and ALL revisited. *Earth and Planetary Science Letters*. **374**, 204–214 (2013).

85.   M. Touboul, P. Sprung, S. M. Aciego, B. Bourdon, Hf–W chronology of the eucrite parent body. *Geochemica et Cosmochimica Acta*. **156**, 106–121 (2015).

86.   A. Pun, J. J. Papike, Unequilibrated eucrites and the equilibrated Juvinas eucrite: Pyroxene REE systematics and major, minor, and trace element zoning. *American Mineralogist*. **81**, 1438–1451 (1996).

5.11 Figures

Figure 1

Backscatter image of Yamato 74450. Grey scale gradation in pyroxene is zoning in Mg-Fe.
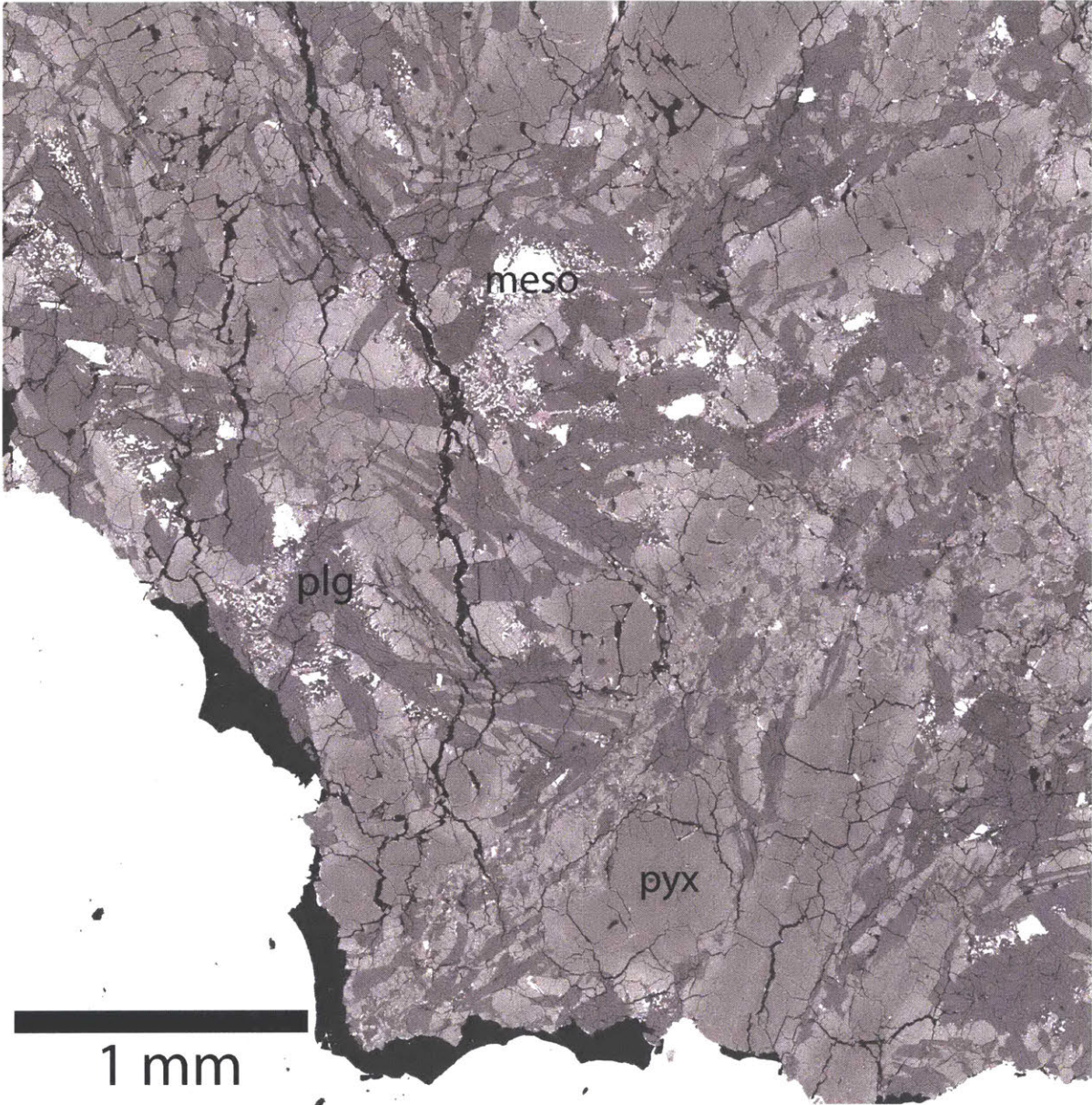
Figure 2

Electron probe and ion probe transect of pyroxene from Yamato 74450. Ion probe analyses could not be spaced as closely because of abundant internal fracturing of pyroxene.
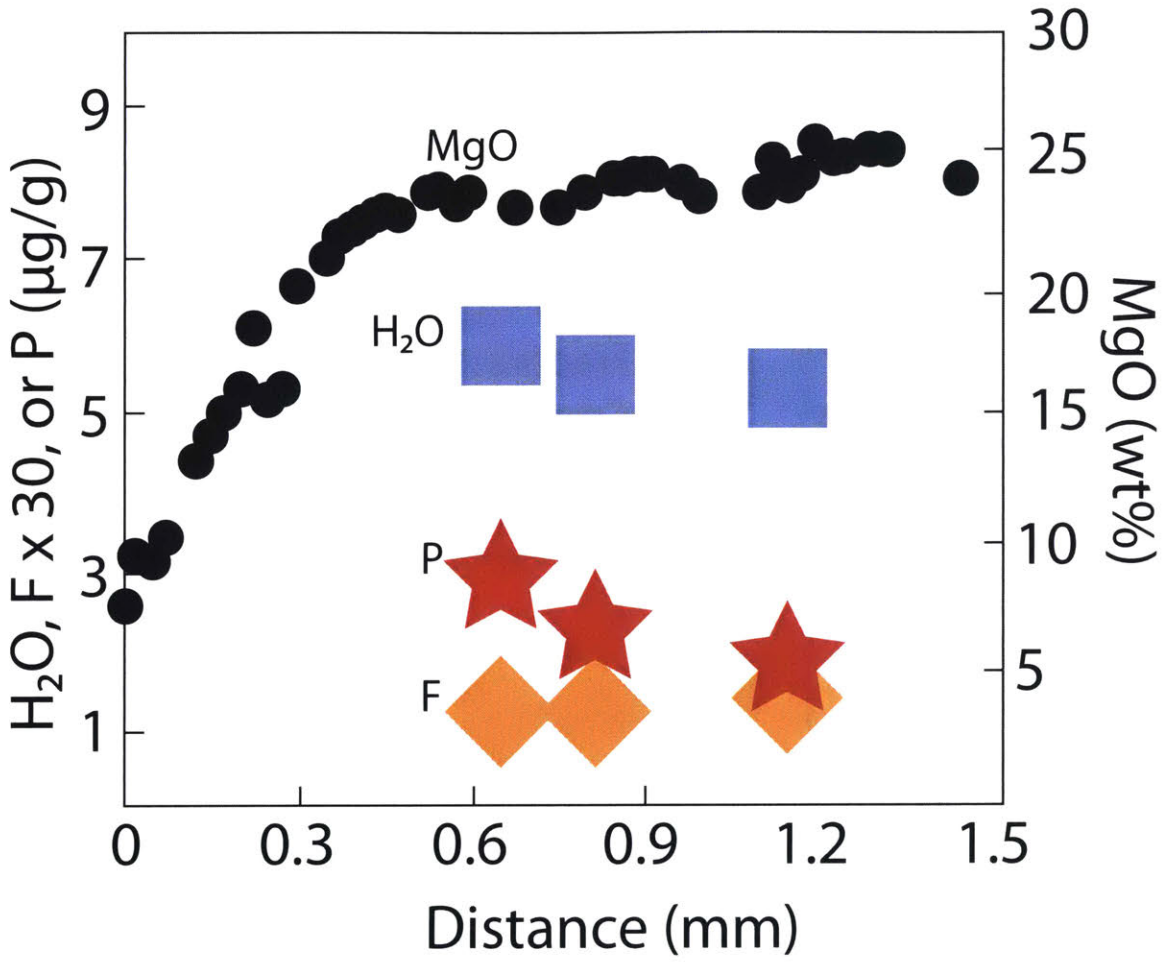
Figure 3

(a) Water vs MgO in pyroxenes from eucrites. Black outlined point is Juvinas. (b) F vs MgO in pyroxenes from eucrites. Black outlined point is Juvinas. Juvinas MgO content taken from Pun and Papike (1996).
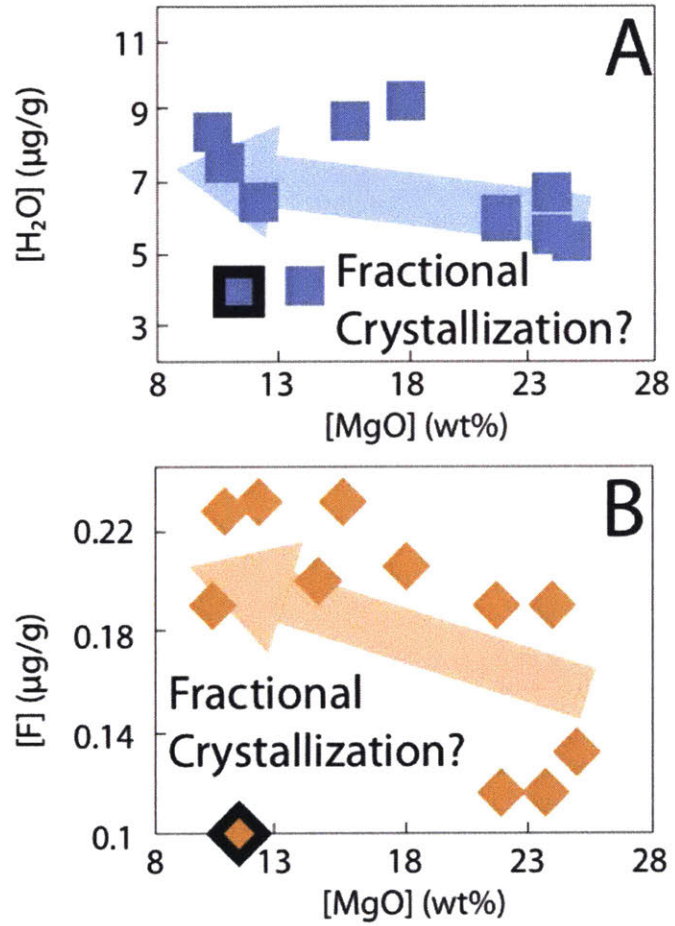
Figure 4

Ti vs. Mg#. Ti content and Mg# were determined from analyses of cores pyroxenes from unequilibrated eucrites in conjunction with a Ti partition coefficient and Mg-Fe exchange coefficient (Nielsen et al., 1992; 1988) .
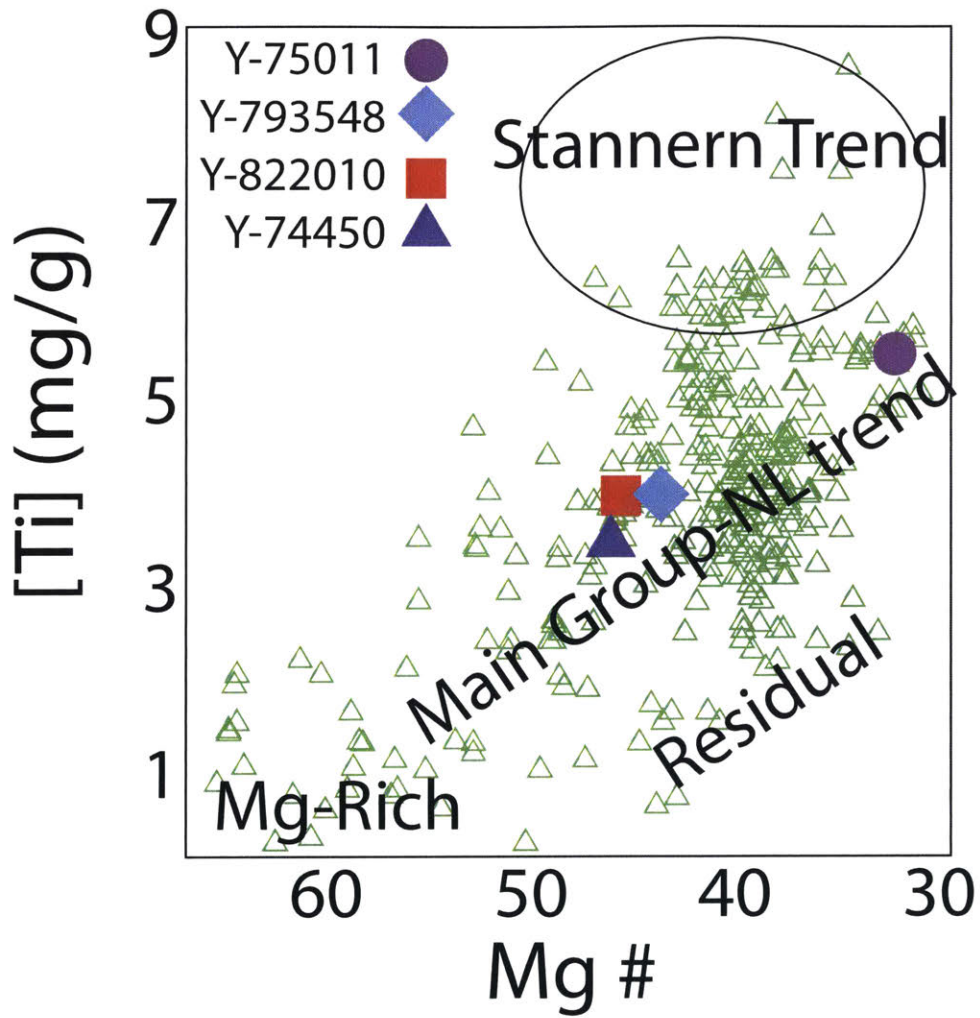
Figure 5

Bulk water content vs. size of planetary body. A strong exponential correlation exists between 4 Vesta, Mars, and Earth. Data from this study and (Albarède, 2009; Marty, 2012; McCubbin et al., 2016). Average water concentrations in black and acceptable ranges in color for each body. Angrite parent body plotted for comparison.
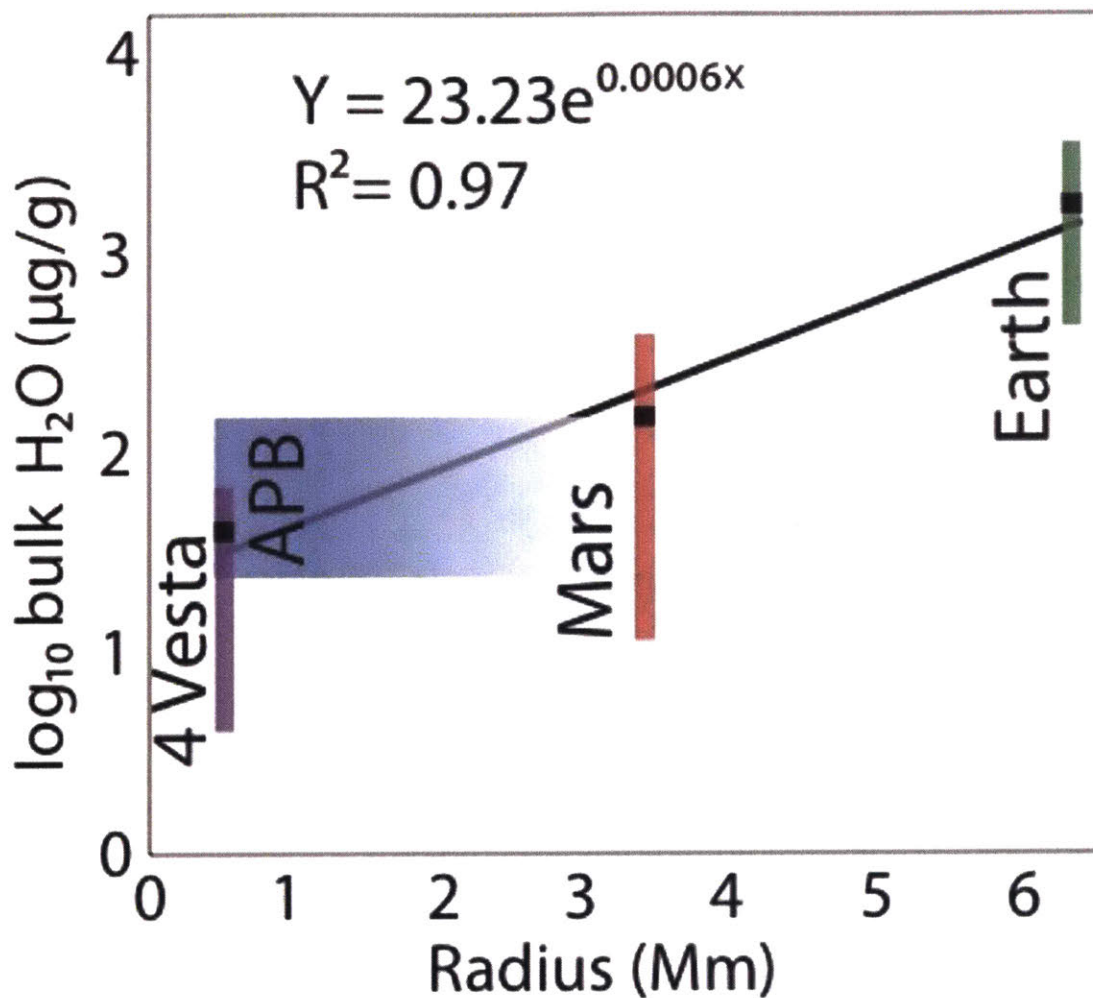
Table 1

Acceptable SIMS analysese of unequlibrated eucrites and coordinated EPMA analyses.

Sample	pyroxene	H2O	CO2*	F	P	Cl*	MgO	Al2O3	SiO2	CaO	TiO2	MnO	FeO	Cr2O3	Total
Y-793548-66	pyx1	9.3	2	0.18	2	0.007									
Y-793548-66	pyx1	9.9	3	0.18	3	0.003									
Y-793548-66	pyx2	6.0	2	0.17	2	0									
Y-793548-66	pyx3	1.8	3	0.19	2	0.02									
Y-793548-66	pyx3	2.7	2	0.17	4	0.004									
Y-793548-66	pyx3	2.5	1	0.18	3	0.003									
Y-82210-101	pyx1	4.0	2	0.21	4	0.019	13.9	1.4	49.6	5.4	0.4	1.0	27.6	0.7	100.0
Y-82210-101	pyx1+	7.0	2	0.19	8	0.00	23.7	1.6	52.3	2.4	0.2	0.7	18.0	0.9	99.9
Y-82210-101	pyx1	7.6	3	0.23	12	0.006	10.7	0.9	48.5	8.0	0.4	1.0	29.5	0.5	99.6
Y-82210-101	pyx1+	8.5	2	0.19	2	0.004	10.3	1.5	48.9	9.8	0.5	0.9	27.6	0.7	100.4
Y-82210-101	pyx2	6.1	2	0.19	7	0.019	21.9	2.1	51.0	3.5	0.2	0.7	19.7	0.9	100.0
Y-82210-101	pyx3	6.5	2	0.23	7	0.002	12.1	1.2	48.9	5.7	0.4	1.0	29.5	0.6	99.5
Y-82210-101	pyx3	9.3	2	0.21	6	0.002	18.1	1.9	51.3	4.0	0.3	0.8	23.1	1.2	100.8
Y-75011-114	pyx4	6.8	2	0.14	3	0.009									
Y-75011-114	pyx4	8.5	3	0.16	4	0.004									
Y-75011-114	pyx4	9.0	2	0.15	3	0.004									
Y-74450-113	pyx3+	5.9	2	0.12	3	0.004	21.8	1.2	52.1	2.3	0.2	0.6	21.3	0.8	
Y-74450-113	pyx3+	5.5	2	0.12	2	0.001	23.6	1.1	52.7	2.3	0.2	0.6	18.5	0.7	100.3
Y-74450-113	pyx3+	5.4	2	0.13	2	0.002	24.9	1.0	52.9	1.9	0.2	0.6	17.4	0.6	99.8
	average pyx	6.4	2	0.18	4	0.00									99.4
	2se	1.1	0.2	0.02	1	0.002									
	2Rse	0.17	0.08	0.09	29	0.41									
	average melt	62		2.2											
	2se	11		0.2											

Table 2

Sample	pyroxene	H2O	F	P
Juvinas	cpx1	3.8	0.07	8
Juvinas	cpx1	4.2	0.08	4
Juvinas	cpx2	3.9	0.07	10
Juvinas	cpx2	4.2	0.08	9
Juvinas	cpx2	3.7	0.06	9
Juvinas	cpx2	3.8	0.07	3
Juvinas	cpx2	4.4	0.08	20
Juvinas	cpx2	3.9	0.06	2
	average cpx	4.0	0.1	8.0
	2se	0.2	0.01	4.15
	2Rse	0.04	0.07	0.52

Table 3

Sample	P (MPa)	n	cpx H2O	cpx F	H2O (1se)	F (1se)
G7a 200	200	6	311	10	9	2
G4 200	200	5	332	11	14	2
g5 200	200	3	371	16	35	3
g17 0.1	0.1	5	22		1	
			glass H2O	glass F	H2O (1se)	F (1se)
G7a 200	200	6	39559	144	269	2
G4 200	200	5	40279	157	225	2
g5 200	200	6	41035	167	262	2
g17 0.1	0.1	8	215		22	
			D H2O	D F	H2O (1se)	F (1se)
G7a 200	200		0.008	0.070	0.0005	0.02
G4 200	200		0.008	0.072	0.0007	0.02
g5 200	200		0.009	0.093	0.0017	0.03
g17 0.1	0.1		0.103		0.02	

149

Chapter 6

Early accretion of water in the inner Solar System from a carbonaceous chondrite-like source

6.1 Abstract

Determining the origin of water and the timing of its accretion within the inner Solar System is important for understanding the dynamics of planet formation. The timing of water accretion to the inner Solar System also has implications for how and when life emerged on Earth. We report in-situ measurements of the hydrogen isotopic composition of the mineral apatite in eucrite meteorites, whose parent body is the main-belt asteroid 4-Vesta. These measurements sample one of the oldest hydrogen reservoirs in the Solar System and show that 4-Vesta contains the same hydrogen isotopic composition as that of carbonaceous chondrites. Taking into account the old ages of eucrite meteorites and their similarity to Earth's isotopic ratios of hydrogen, carbon, and nitrogen, we demonstrate that these volatiles could have been added early to Earth, rather than gained during a late accretion event.

6.2 Main text

Hydrogen (H) is vitally important in cosmochemical and geochemical processes. For example, water (H_2O) plays a critical role in plate tectonics on Earth (*1*) and has likely shaped the surface of Mars (*2*). Despite the abundance of water on Earth and evidence of water on the Moon, Mars and the asteroid 4-Vesta (*2-4*), these planetary bodies are often thought to have accreted dry (*5-8*). This prompts the questions: Where did the water come from? And when was it present in the inner Solar System? Answers to these key questions may reveal information about accretion processes in terrestrial planets. Additionally, the extent and importance of lateral water transport throughout the history of the Solar System are debated (*9, 10*).

The source of water in planetary bodies can be investigated by measuring the ratio between the isotopes of hydrogen (deuterium, D or ^2H, and hydrogen, ^1H), because different regions of the Solar System vary widely in measured D/H ratios (*11*). Thus, determining D/H in meteorites with well-known ages and planetary origins can help constrain the timing of water delivery to accreting planetary bodies. Such analysis provides an ideal opportunity to study the provenance of water in bodies throughout the Solar System, including Earth, the Moon, Mars and the asteroid belt (*12-14*).

Eucrites, a class of asteroidal basaltic meteorites, can provide unique information about the timing of water delivery to planets because most of these rocks crystallized 4559-4547 million years before present (Ma), or ~8-20 million years after the first solids in the Solar System, calcium aluminum rich inclusions (CAIs) (*15, 16*). Eucrites belong to the howardite-eucrite-diogenite group of meteorites (HEDs) that are derived from the asteroid belt, dominantly from the protoplanet 4-Vesta (*17-19*). Determining the source of water in eucrites can constrain the time at which water existed in the inner Solar System, because these ancient rocks are some of the oldest igneous rocks in the Solar System. However, until recently, it was believed that eucrites were completely anhydrous and, therefore, could provide no insight into the D/H ratio of 4-Vesta (*4, 6*).

Here we report the concentration and isotopic composition of structurally bound water in the mineral apatite $(Ca_5(PO_4)_3(OH,F,Cl))$ from five different basaltic eucrite samples: Juvinas, Pasamonte, Cachari, Stannern, and Pecora Escarpment (PCA) 91078 (Figs. S1 & S2). We measured the D/H and water contents simultaneously in-situ using a Cameca 1280 ion microprobe. The water concentration in these apatites ranges from 668 to 2624 µg/g, which agrees with calculated water contents from electron probe measurements (Table S1) (4, 20). We measured δD values ranging from -231‰ to -37 ‰ (Table 1) (21). No systematic variation in D/H exists between samples or between different apatite grains in the same meteorite (Fig. 1). The weighted mean hydrogen isotopic composition for eucritic apatite from the five different investigated samples is δD = -162±127‰ (n = 11, 2 standard deviation (σ)).

There are three processes that could have modified the hydrogen isotopic composition of the apatite we analyzed from that of the parental magma: (1) hydrous degassing prior to or during apatite crystallization, (2) equilibrium stable isotope fractionation between hydrous phases and melt, and (3) contamination/assimilation of exogenous H or D, presumably from the regolith of 4-Vesta. Degassing is unlikely due to the small observed spread in δD with the relatively large spread of water contents of the analyzed apatite (23, 24). Apatite is the only hydrous mineral phase in eucrites, and stable isotope fractionation between apatite and melt is expected to be small (~20‰) at high temperature, thus apatite-melt fractionation should be minor compared to the variation in δD observed (22). Contamination by exogenic H from solar wind and/or by D produced during spallation processes is unlikely due to the young exposure ages and high water contents of the apatite and the fact that the apatites have a small range of δD with varying exposure ages and metamorphic grades (20). In summary, we conclude that none of these processes have substantially affected the H isotopic compositions measured in the present study (20).

The weighted mean δD of the apatites analyzed in the present study, and hence eucrite magmatic water is -162‰, which is the value we adopt for bulk 4-Vesta (20). This value is within the combined uncertainties of the value for the bulk Earth (~ -90‰) (23) and possibly the Moon (~

+90‰; Fig. 2) (3, 24). The fact that Earth and Vesta have indistinguishable δD values suggests that they have the same source of water. Our new D/H data, in combination with published bulk nitrogen (N) isotope data for eucrites, shows that the most likely common source of volatiles for Earth and eucrites (4-Vesta) is carbonaceous chondrites (13, 25). It is important to note that N isotopes exclude the Jupiter family comets as a potential source of water for Earth and 4-Vesta. Nitrogen isotopes also exclude Oort cloud comets as a source of water for the inner solar system planetary bodies as well. Kinetic isotope fractionation during both accretion and magmatic processes would not allow the H and N isotope systems as currently measured on Earth and Vesta to have evolved from the material implied by the signature of the Jupiter family comets or of the Oort cloud comets (Fig. 2). Although we propose that carbonaceous chondrites provided water for the inner Solar System, there is significant evidence to show that at least Earth accreted from a heterogeneous mixture of hydrous and anhydrous materials, which rules out carbonaceous chondrites as the only terrestrial building blocks (8).

The hypothesis that inner Solar System water came from a carbonaceous chondrite source is further supported by bulk carbon (C) isotope data. The C isotopic compositions of Earth and Vesta are very similar and overlap with that of carbonaceous chondrites but not with the solar composition (Fig. 3). Thus, the isotopic compositions of three different volatile elements as well as their concentration ratios for Earth and Vesta are consistent with the composition of carbonaceous chondrites.

Earth and Vesta have indistinguishable H, C, and N isotopic compositions, and thus likely have the same volatile source. This source must have had an H isotopic composition similar to or lower than the values measured in our samples, because possible magmatic fractionation processes could only lead to a relative enrichment and not a depletion in deuterium (20). One important reservoir that has low D/H and low $^{15}N/^{14}N$ is the Sun (Fig. 2), which could theoretically be an alternative source of volatiles in the inner Solar System, assuming such a solar-derived reservoir would have been later altered by a secondary degassing process. Degassing is modeled here using the most conservative input values, which causes the largest

isotope fractionations for N and H isotopes and reflects degassing of a 1:1 mixture of NH_4 and H_2. It is evident that degassing alone cannot realistically evolve solar H and N isotope ratios to values measured in Vesta (Fig. 2). Degrees of degassing in excess of 99.99% are required to evolve N and H isotope ratios of the Sun to ratios close to those of the inner Solar System. Additionally, if this extreme degassing also involved volatile loss of C, then C isotopes would significantly disagree with a solar source of volatiles because the Solar C isotopic composition would become heavier than that of Earth, Moon and Vesta (Fig. 3). It is highly unlikely that accretion and degassing would strongly fractionate H and N isotopes, yet would allow C isotopes on Vesta to remain isotopically light. Consequently, we rule out a solar source of volatiles for the bodies in the inner Solar System.

The H, C and N isotopic similarities between eucrites, Earth, and potentially the Moon allow us to place important limits on the timing of water delivery to the inner Solar System. Earth cannot provide timing of water delivery because it is currently geologically active. The Moon likely accreted its water at or before ~200 million years after CAIs, or around 4367 Ma (3, 24), but such a constraint is not very rigorous given that all the planets in the inner Solar System are thought to have fully accreted by this time. Eucrites provide a significantly earlier data point suggesting that the same source of water as the Earth was present very early in Solar System history, ~8–20 million years after CAIs (15, 16). This evidence moves back the time at which the terrestrial water reservoir is thought to exist and have been available for accretion. Additionally, this reservoir was present between 1–2.4AU and perhaps throughout the inner Solar System. Late-stage addition of water to planets from outer parts of the Solar System is, therefore, unlikely to have affected the water budgets of inner Solar System bodies. Thus, the bulk of the highly volatile elements H, C, and N now present in Earth and the asteroid belt most likely arrived from a local source, i.e. carbonaceous chondrite-like material, very early in Solar System history. The limited variation in δD over a large range of heliocentric distances (1–2.4AU) supports the notion of a uniform source of water in the inner Solar System. Our findings cannot preclude a late addition of water for Earth with a carbonaceous chondrite-like D/H, but the observation indicates that a late addition of water is not necessary.

155

Our geochemical results are in agreement with several dynamic Solar System models for planetary water delivery. These models indicate that carbonaceous chondritic planetesimals delivered water during primary accretion of the Earth (*9, 26, 27*). In addition, Earth's water is believed to have condensed in the outer asteroid belt and giant planet regions and then transported to the Earth by dynamical processes related to giant planet migration (*27*). The implications are that (1) the migration of water in the inner Solar System must have started by 8-20 million years after CAIs, or (2) water was always present in the inner Solar System and no water migration is needed to satisfy the H-isotopic composition of terrestrial planets (*10*).

6.3 Acknowledgements

6.4 References

1. I. Campbell, S. Taylor, No water, no granites, no oceans, no continents. *Geophysical Research Letters* **10**, 1061-1064 (1983).

2. M. H. Carr, J. W. Head III, Geologic history of Mars. *Earth and Planetary Science Letters* **294**, 185-203 (2010).

3. A. E. Saal, E. H. Hauri, J. A. Van Orman, M. J. Rutherford, Hydrogen Isotopes in Lunar Volcanic Glasses and Melt Inclusions Reveal a Carbonaceous Chondrite Heritage. *Science* **340**, 1317-1320 (2013).

4. A. R. Sarafian, M. F. Roden, A. E. Patiño Douce, The nature of volatiles in eucrites: Clues from apatite. *Meteoritics and Planetary Science* **48**, 2135-2154 (2013).

5. F. Albarede, Volatile accretion history of the terrestrial planets and dynamic implications. *Nature* **461**, 1227-1233 (2009).

6. J. J. Papike, in *Reviews in Mineralogy: Planetary Materials*, J. J. Papike, Ed. (Mineralogical Society of America, Washington, D.C., 1998), chap. 7, pp. 7-01-07-10.

7. P. Lucey, et al., *Understanding the Lunar Surface and Space-Moon Interactions*. B. L. Jolliff, M. A. Wieczorek, C. K. Shearer, C. R. Neal, Eds., New Views of the Moon (Reviews in Minerology and Geochemistry, Chantilly, Virginia, 2006), vol. 60.

8. M. Schönbächler, R. Carlson, M. Horan, T. Mock, E. Hauri, Heterogeneous accretion and the moderately volatile element budget of Earth. *Science* **328**, 884-887 (2010).

9. A. Morbidelli, J. I. Lunine, D. P. Obrien, S. N. Raymond, K. J. Walsh, Building terrestrial planets. *Annual Reviews of Earth and Planetary Sciences* **40**, 251-275 (2012).

10. H. King et al., Computer simulations of water interactions with low-coordinated forsterite surface sites: implications for the origin of water in the inner solar system. *Earth and Planetary Science Letters* **300**, 11-18 (2010).

11. F. Robert, D. Gautier, B. Dubrulle, The solar system D/H ratio: observations and theories. *Space Science Reviews* **92**, 201-224 (2000).

12. C. O. D. Alexander et al., The provenances of asteroids, and their contributions to the volatile inventories of the terrestrial planets. *Science* **337**, 721-723 (2012).

13. F. Robert, The origin of water on Earth. *Science* **293**, 1056-1058 (2001).

14. L. Hallis, G. Taylor, K. Nagashima, G. Huss, Magmatic water in the martian meteorite Nakhla. *Earth and Planetary Science Letters* **359**, 84-92 (2012).

15. Q. Zhou et al., SIMS Pb–Pb and U–Pb age determination of eucrite zircons at< 5μm scale and the first 50Ma of the thermal history of Vesta. *Geochimica et Cosmochimica Acta* **110**, 152-175 (2013).

16. K. Misawa, A. Yamaguchi, K. Hiroshi, U-Pb and 207Pb-206Pb ages of zircons from basaltic eucrites: Implications for early basaltic volcanism on the eucrite parent body. *Geochimica et Cosmochimica Acta* **69**, 5847-5861 (2005).

17. R. N. Clayton, N. Onuma, T. K. Mayeda, A classification of meteorites based on oxygen isotopes. *Earth and Planetary Science Letters* **30**, 10-18 (1976).

18. T. B. McCord, J. B. Adams, T. V. Johnson, Asteroid Vesta: Spectral reflectivity and compositional implications. *Science* **168**, 1445 (1970).

19. H. Y. McSween Jr, D. W. Mittlefehldt, A. W. Beck, R. G. Mayne, T. J. McCoy, in *The Dawn Mission to Minor Planets 4 Vesta and 1 Ceres*. (Springer, 2012), pp. 141-174.

20. Materials and methods are available as supplementary material on *Science* Online.

21. $\delta D = [([(D/Hunknown/(D/HVSMOW)]-1)*1000]$; where VSMOW=Vienna standard mean ocean water.

22. T. Chacko, D. R. Cole, J. Horita, Equilibrium oxygen, hydrogen and carbon isotope fractionation factors applicable to geologic systems. *Reviews in mineralogy and geochemistry* **43**, 1-81 (2001).

23. Z. D. Sharp, F. M. McCubbin, C. K. Shearer, A hydrogen-based oxidation mechanism relevant to planetary formation. *Earth and Planetary Science Letters* **380**, 88-97 (2013).

24. R. Tartèse et al., Apatites in lunar KREEP basalts: The missing link to understanding the H isotope systematics of the Moon. *Geology* **42**, 363-366 (2014).

25. Y. Miura, N. Sugiura, Nitrogen isotopic compositions in three Antarctic and two non-Antarctic eucrites. *Antarctic Meteorite Research* **6**, 338 (1993).

26. A. Morbidelli et al., Source regions and timescales for the delivery of water to the Earth. *Meteoritics & Planetary Science* **35**, 1309-1320 (2000).

27. D. P. O'Brien, K. J. Walsh, A. Morbidelli, S. N. Raymond, A. M. Mandell, Water delivery and giant impacts in the 'Grand Tack'scenario. *Icarus*, (2014).

28. B. Marty, The origins and concentrations of water, carbon, nitrogen and noble gases on Earth. *Earth and Planetary Science Letters* **313**, 56-66 (2012).

29. G. A. Gaetani, J. A. O'Leary, N. Shimizu, C. E. Bucholz, M. Newville, Rapid reequilibration of H2O and oxygen fugacity in olivine-hosted melt inclusions. *Geology* **40**, 915-918 (2012).

30. F. M. McCubbin et al., Hydrous melting of the martian mantle produced both depleted and enriched shergottites. *Geology* **40**, 683-686 (2012).

31. J. Stormer, M. Pierson, R. Tacker, Variation of F and Cl X-ray intensity due to anisotropic diffusion in apatite. *American Mineralogist* **78**, 641-664S (1993).

32.   F. M. McCubbin et al., Fluorine and chlorine abundances in lunar apatite: Implications for heterogeneous distributions of magmatic volatiles in the lunar interior. *Geochimica et Cosmochimica Acta* **75**, 5073-5093 (2011).

33.   E. R. D. Scott, R. C. Greenwood, I. A. Franchi, I. S. Sanders, Oxygen isotopic constraints on the origin and parent bodies of eucrites, diogenites, and howardites. *Geochimica et Cosmochimica Acta* **73**, 5835-5853 (2009).

34.   D. Bogard, G. Taylor, K. Keil, M. Smith, R. Schmitt, Impact melting of the Cachari eucrite 3.0 Gy ago. *Geochimica et Cosmochimica Acta* **49**, 941-946 (1985).

35.   J. Roszjar et al., Thermal history of Northwest Africa 5073—A coarse grained Stannern trend eucrite containing cm sized pyroxenes and large zircon grains. *Meteoritics & Planetary Science* **46**, 1754-1773 (2011).

36.   P. M. Piccoli, P. A. Candela, Apatite in igneous systems. *Reviews in Mineralogy & Geochemistry* **48**, 255-292 (2002).

37.   E. Stolper, Experimental petrology of eucritic meteorites. *Geochimica et Cosmochimica Acta* **41**, 587-611 (1977).

38.   K. Righter, M. J. Drake, A magma ocean on Vesta: Core formation and petrogenesis of eucrites and diogenites. *Meteoritics & Planetary Science* **32**, 929-944 (1997).

39.   R. C. Greenwood, I. A. Franchi, A. Jambon, P. C. Buchanan, Widespread magma oceans on asteroidal bodies in the early Solar System. *Nature* **435**, 916-918 (2005).

40.   J. A. Barrat, A. Yamaguchi, B. Zanda, C. Bollinger, M. Bohn, Relative chronology of crust formation on asteroid Vesta: Insights from the geochemistry of diogenites. *Geochimica et Cosmochimica Acta* **74**, 6218-6231 (2010).

41.   T. J. McCoy et al., Formation of vesicles in asteroidal basaltic meteorites. *Earth and Planetary Science Letters* **246**, 102-108 (2006).

42.   A. Yamaguchi et al., Crustal partial melting on Vesta: Evidence from highly metamorphosed eucrites. *Geochimica et Cosmochimica Acta* **73**, 7162-7182 (2009).

43.   A. Yamaguchi, G. J. Taylor, K. Keil, Global crustal metamorphism of the eucrite parent body. *Icarus* **124**, 97-112 (1996).

44.   A. Yamaguchi et al., Post-crystallization reheating and partial melting of eucrite EET90020 by impact into the hot crust of asteroid 4Vesta 4.50 Ga ago. *Geochimica et Cosmochimica Acta* **65**, 3577-3599 (2001).

45.   BVSP, *Basaltic Volcanism on the Terrestrial Planets*. (Pergam Press Inc., New York, 1981), pp. 1286.

46.   J. Barrat et al., The Stannern trend eucrites: Contamination of main group eucritic magmas by crustal partial melts. *Geochimica et Cosmochimica Acta* **71**, 4108-4124 (2007).

47. H. Takeda, A. Graham, Degree of equilibration of eucritic pyroxenes and thermal metamorphism of the earliest planetary crust. *Meteoritics* **26**, 129-134 (1991).

48. M. Wadhwa, Redox conditions on small bodies, the Moon and Mars. *Reviews in Mineralogy and Geochemistry* **68**, 493-510 (2008).

49. T. K. Kyser, J. R. O'Neil, Hydrogen isotope systematics of submarine basalts. *Geochimica et Cosmochimica Acta* **48**, 2123-2133 (1984).

50. R. C. Wiens, P. Bochsler, D. S. Burnett, R. F. Wimmer-Schweingruber, Solar and solar wind isotopic compositions. *Earth and Planetary Science Letters* **226**, 549-565 (2004).

51. O. Eugster, Cosmic-ray exposure ages of meteorites and lunar rocks and their significance. *Chemie der Erde-Geochemistry* **63**, 3-30 (2003).

52. R. Reedy, in *Lunar and Planetary Science Conference Proceedings*. (1982), vol. 12, pp. 1809-1823.

53. K. L. Robinson, G. J. Taylor, Heterogeneous distribution of water in the Moon. *Nature Geoscience* **7**, 401–408 (2014).

54. J. J. Barnes et al., The origin of water in the primitive Moon as revealed by the lunar highlands samples. *Earth and Planetary Science Letters* **390**, 244-252 (2014).

55. J. Brenan, Kinetics of fluorine, chlorine and hydroxyl exchange in fluorapatite. *Chemical Geology* **110**, 195-210 (1993).

56. F. Tosi et al., Global Resolved Temperature Maps of Vesta. *LPI Contributions* **1773**, 2026 (2014).

57. F. DeMeo, B. Carry, Solar System evolution from compositional mapping of the asteroid belt. *Nature* **505**, 629-634 (2014).

58. F. M. McCubbin et al., Nominally hydrous magmatism on the Moon. *Procedings of the National Academy of Sciences of the United States of America* **107**, 11223-11228 (2010).

59. J. W. Boyce et al., Lunar apatite with terrestrial volatile abundances. *Nature*, 466-469 (2010).

60. K. E. Vander Kaaden, F. M. McCubbin, E. Whitson, E. H. Hauri, J. Wang, in *43rd Lunar and Planetary Science Conference*. (2012).

61. E. A. Mathez, J. D. Webster, Partitioning behavior of chlorine and fluorine in the system apatite–silicate melt–fluid. *Geochimica et Cosmochimica Acta* **69**, 1275-1286 (2005).

62. J. D. Webster, C. M. Tappen, C. W. Mandeville, Partitioning behavior of chlorine and fluorine in the system apatite-melt-fluid. II: Felsic silicate systems at 200 MPa. *Geochimica et Cosmochimica Acta* **73**, 559-581 (2009).

63. J. Boyce, S. Tomlinson, F. McCubbin, J. Greenwood, A. Treiman, The Lunar Apatite Paradox. *Science* **344**, 400-402 (2014).

64. J. P. Greenwood, S. Itoh, N. Sakamoto, E. P. Vicenzi, H. Yurimoto, Hydrogen isotope evidence for loss of water from Mars through time. *Geophysical Research Letters* **35**, L05203 (2008).

65. N. Boctor, C. Alexander, J. Wang, E. Hauri, The sources of water in Martian meteorites: Clues from hydrogen isotopes. *Geochimica et Cosmochimica Acta* **67**, 3971-3989 (2003).

66. L. L. Watson, I. D. Hutcheon, S. Epstein, E. M. Stolper, Water on Mars: Clues from deuterium/hydrogen and water contents of hydrous phases in SNC meteorites. *Science* **265**, 86-90 (1994).

67. L. A. Leshin, Insights into martian water reservoirs from analyses of martian meteorite QUE94201. *Geophysical Research Letters* **27**, 2017-2020 (2000).

68. T. Usui, C. M. D. Alexander, J. Wang, J. I. Simon, J. H. Jones, Origin of water and mantle–crust interactions on Mars inferred from hydrogen isotopes and volatile element abundances of olivine-hosted melt inclusions of primitive shergottites. *Earth and Planetary Science Letters* **357**, 119-129 (2012).

69. C. B. Agee et al., Unique meteorite from Early Amazonian Mars: water-rich basaltic breccia Northwest Africa 7034. *Science* **339**, 780-785 (2013).

70. C. Arpigny et al., Anomalous nitrogen isotope ratio in comets. *Science* **301**, 1522-1524 (2003).

71. A. Meibom et al., Nitrogen and carbon isotopic composition of the Sun inferred from a high-temperature solar nebular condensate. *The Astrophysical Journal Letters* **656**, L33 (2007).

72. E. Lellouch et al., The deuterium abundance in Jupiter and Saturn from ISO-SWS observations. *ASTRONOMY AND ASTROPHYSICS-BERLIN-* **370**, 610-622 (2001).

73. K. Tucker, R. Hervig, P. Mane, S. Romaniello, M. Wadhwa, Hydrogen Isotope Systematics of Maskelynites in the Shergottites Zagami, QUE 94201 and Tissint: Terrestrial Contamination or Deuteric Alteration? *Lunar and Planetary Institute Science Conference Abstracts*. (2014), vol. 45, pp. 2190.

74. J. F. Kerridge, Carbon, hydrogen and nitrogen in carbonaceous chondrites: Abundances and isotopic compositions in bulk samples. *Geochimica et Cosmochimica Acta* **49**, 1707-1714 (1985).

75. S. Murty, R. Mohapatra, Nitrogen and heavy noble gases in ALH 84001: Signatures of ancient Martian atmosphere. *Geochimica et cosmochimica acta* **61**, 5417-5428 (1997).

76. B. Marty, K. Hashizume, M. Chaussidon, R. Wieler, Nitrogen isotopes on the Moon: Archives of the solar and planetary contributions to the inner Solar System. *Space science reviews* **106**, 175-196 (2003).

77. M. M. Grady, C. Pillinger, Carbon and nitrogen stable isotope analyses of two lunar meteorites. *LPI Contributions* **712**, 72 (1989).

78. M. M. Grady, I. Wright, C. Pillinger, Carbon in howardite, eucrite and diogenite basaltic achondrites. *Meteoritics & Planetary Science* **32**, 863-868 (1997).

79. M. M. Grady, I. P. Wright, Elemental and isotopic abundances of carbon and nitrogen in meteorites. *Space science reviews* **106**, 231-248 (2003).

80. M. Sephton, A. Verchovsky, P. Bland, I. Gilmour, M. Grady, I. Wright, Investigating the variations in carbon and nitrogen isotopes in carbonaceous chondrites. *Geochimica et Cosmochimica Acta* **67**, 2093-2108 (2003).

81. P. Deines, The carbon isotope geochemistry of mantle xenoliths. *Earth-Science Reviews* **58**, 247-278 (2002).

6.5 Figures

Figure 1

Hydrogen isotopes vs. water content of eucrite apatites. Note the large variation in water content that contrasts with a small range in the hydrogen isotopic compositions. Error bars are 2σ, when error bars are not present they are smaller than the symbol.
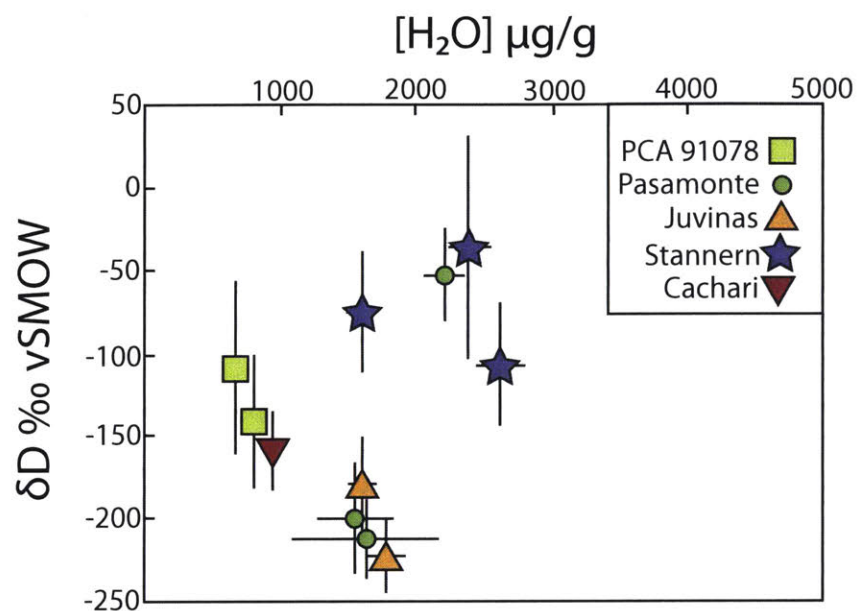
Figure 2

Nitrogen isotopes vs. hydrogen isotopic compositions of objects in the Solar System. Note that the fields for the Moon and Mars are large, these represent all D/H data as the hydrogen isotopic compositions for the bulk Moon and Mars are debated. For carbonaceous chondrites, ice in equilibrium with bulk clays has a $\delta D \approx -400 - 100‰$ see ref (12). Early carbonaceous chondrite ice could be another source of water for the inner Solar System. The degassing model line originating at protosolar values does not intersect Vesta, Earth, or the Moon. Figure modified from refs (3, 28). See (20) for details and data.

Figure 3

Carbon vs hydrogen isotopes. Note that Earth, Moon, and Vesta plot within the carbonaceous chondrite field. Because carbon isotopes vary from -250‰ to 200‰ in comets, C-isotopes are not useful to exclude comets as a source of C for inner Solar System bodies.
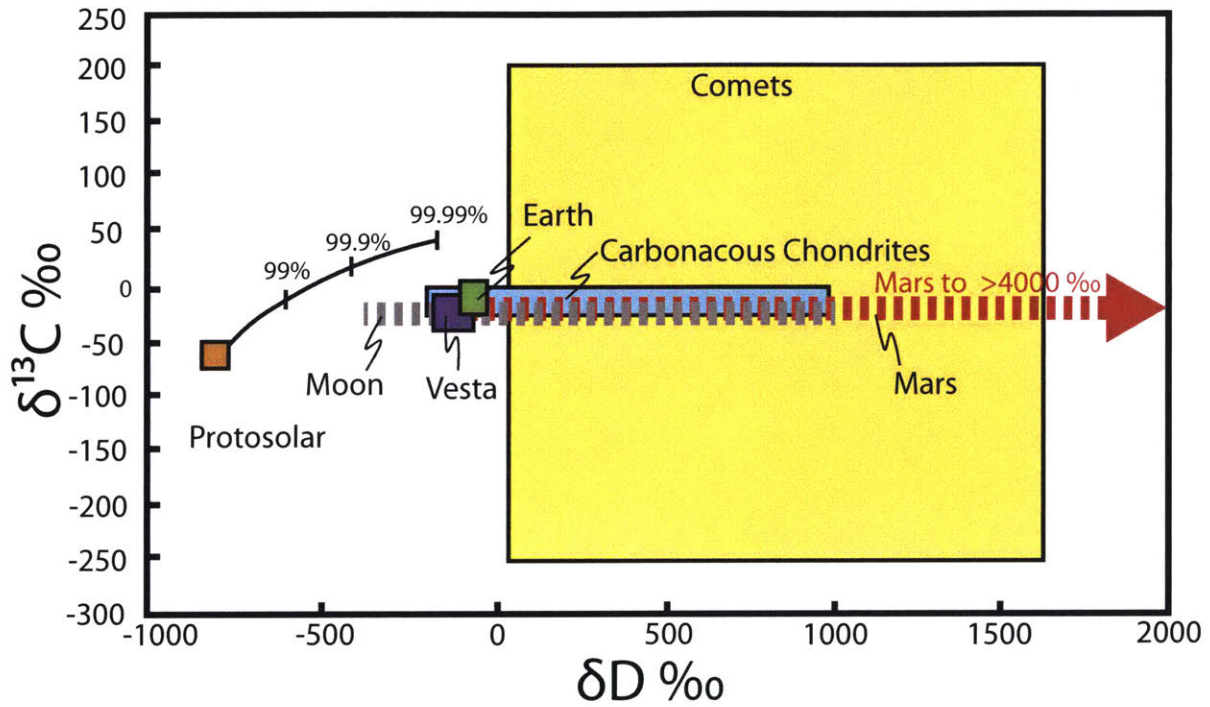
Table 1

Hydrogen isotope and water analyses of apatite and epoxy.

Sample	δD ‰	2SD	H_2O μg/g	2SD
PCA 91078 ap1	-141	40	804	60
PCA 91078 ap2	-109	53	668	52
Pasamonte ap1	-53	29	2207	153
Pasmonte ap2	-231	25	1630	584
Pasamonte ap3	-200	34	1545	295
Juvinas ap1	-223	21	1781	152
Juvinas ap2	-179	29	1594	107
Stannern ap1	-107	38	2624	182
Stannern ap2	-37	68	2390	157
Stannern ap1 51	-75	36	1595	107
Cachari ap1	-158	24	932	62
PCA epoxy	-174	9	140000	9000
Weighted mean apatite	**-162**	**127**	**1748**	**1689**

Chapter 7

Chlorine and hydrogen degassing in Vesta's magma ocean

7.1 Abstract

The hydrophilic nature of halogens makes these elements ideal for probing potential hydrous geologic processes. Generally, in magmatic settings the stable isotopes of Cl may fractionate when H is in low concentrations and little fractionation occurs when the H concentration is high. We determined the Cl isotope composition and halogen content (F, Cl, Br, and I) of apatite and merrillite in seven basaltic eucrites, which are meteorites linked to the asteroid 4-Vesta, by using secondary ion mass spectrometry. We compare our halogen results with H isotope data, existing bulk rock concentrations, and petrologic models. The inferred Cl isotope composition of eucrites from this study, expressed in standard $\delta^{37}Cl$ notation, which ranges from -3.8 to 7.7‰, correlates with the bulk major- and trace-element content, e.g., the Cl isotope composition positively correlates with Mg and Sc, while Cl isotope composition negatively correlate with K, V, and Cr. Here we suggest that eucrites preserve evidence of a degassing magma ocean as evidenced by the decreasing bulk rock K content with increasing $\delta^{37}Cl$. If the eucrite parent body, 4-Vesta, accreted with a negative $\delta^{37}Cl$ of -3.8 ± 1.1‰, at least some parts of the solar nebula would have been isotopically light compared to most estimates of the Earth, which on average is close to 0‰.

7.2 Introduction

Eucrites are differentiated meteorites that group together with howardites and diogenites to from a genetically linked suite of rocks, the HED group of meteorites. Eucrites can be further subdivided into basaltic or cumulate rocks, which sample some of the some of the oldest asteroidal crusts in the solar system (e.g. *1*). Most eucrites are thought to derive from the asteroid 4-Vesta (*2* and refs. therein), but some eucrites probably sample other geochemically similar asteroids (*3-6*). Here we will use the asteroid 4-Vesta as a proxy for all eucrite parent bodies. Basaltic eucrites can be classified into three geochemical groups by plotting proxies for fractional crystallization, such as Mg# (molar Mg/(Mg+Fe)) or Sc content ([Sc]) vs. an incompatible element, e.g., [Ti] or [Hf] (Fig. 1). Main group eucrites define a trend consistent with fractional and/or equilibrium crystallization (*7, 8* Fig. 1), although their petrogenesis is subject to some debate. Some models require partial melting of the mantle (*9*), while most models predict direct extraction from a magma ocean (*2, 8, 10*). The most recent and quantitative geochemical modeling suggest that eucrites originate directly from a crystallizing magma ocean (*2, 8*). The Stannern trend eucrites are characterized by an enrichment in incompatible elements, independent of their crystallization index, e.g., Mg# or [Sc] (Fig. 1). This trend was likely generated by contamination of a main group magma with a crustal partial melt (*10, 11*), but could have been generated by low degrees of partial melting of the vestan mantle (*9*). The third group of basaltic eucrites are residual eucrites, which are depleted in incompatible trace elements and likely represent a residual crustal rock that was partially melted (*11*). Thermal alteration among eucrites is nearly ubiquitous. Eucrites can be classified into seven types on the basis of increasing thermal alteration, type 1 eucrites are extremely rare and represent no evidence of thermal alteration, whereas type 7 eucrites exhibit evidence of partial melting (*3, 11*).

Eucrites contain two phosphates, merrillite ($Ca_9NaMg(PO_4)_7$) and apatite ($Ca_5(PO_4)_3(OH,F,Cl)$, whilst the latter is mostly F-rich apatite (*6*). In eucrites apatite and merrillite generally occur in late stage melt pockets, i.e., mesostasis (*6*) since basaltic melts have a high solubility of P (*12*). , Similar to other incompatible elements, P becomes enriched during the late stages of fractional crystallization, resulting in precipitation of apatite and/or merrillite. In planetary basalts, apatite is the main carrier of halogens and H, while merrillite is nearly devoid of H, F, and Cl. Several

studies have examined H, F, and Cl exchange between apatite and melt (*13*), as well as the partitioning of halogens between apatite and fluid (*14*). Thus, the apatite H, F, Cl, Br, and I content can be related to the magmatic and hydrothermal conditions apatite formed under and/or equilibrated with.

Eucrites are systematically depleted in volatile elements compared to carbonaceous chondrites and the Earth. For example, the geochemically similar pair Ga (volatile) and Al (refractory) should remain invariant during magmatic processes, yet the Ga/Al of eucrites, Earth and carbonaceous chondrites are 0.32, 1.7, 11, respectively (*15, 16*). While eucrites are depleted in volatile elements, there are multiple lines of evidence that fluids may have interacted with the eucritic crust. For example, fluids may have precipitated observed quartz veins (*17*), apatite veins (*6*), Fe-rich olivine veins (*18*), and Fe-enrichment along pyroxene grain boundaries (*18, 19*). The source of magmatic water has been determined to have a carbonaceous chondrite signature (*5, 20*), but the source of water for fluid-generated features, such as the quartz, apatite, and Fe-rich olivine veins, are unknown.

The Cl isotope composition of planetary basalts is extremely variable compared to magmatic rocks on Earth (*21-24*). Chlorine has two stable isotopes, ^{35}Cl and ^{37}Cl, with natural abundances of 75.77% and 24.23%, respectively. Chlorine isotope ratios can be represented in standard delta notation, as: $\delta^{37}Cl = (^{37}Cl/^{35}Cl_{sample}/^{37}Cl/^{35}Cl_{SMOC} - 1) \times 1000$, where SMOC is standard mean ocean chloride, with a $\delta^{37}Cl$ value defined as zero. Multiple studies of $\delta^{37}Cl$ of lunar and martian rocks are widely used to decipher interactions between lithospheric, atmospheric and hydrospheric components. For example, $\delta^{37}Cl$ has been used to show crustal/fluid assimilation processes on Mars (*23, 25*) and degassing processes on the Moon (*22, 26, 27*). Delta ^{37}Cl is an extremely sensitive indicator of crustal contamination in martian rocks, as crustal fluids on Mars are thought to be extremely saline (*28*) and have an elevated $\delta^{37}Cl$ (*23, 25*). Chlorine isotope ratios in some lunar samples are extremely enriched in ^{37}Cl, which is thought to be due to metal-chloride degassing (*22, 26, 27*). The latter could be due to in-situ degassing of low H content of lunar magmas (*22*), or from degassing of a magma ocean (*26, 27*). If a magma ocean on 4-Vesta

169

existed and degassed, then $\delta^{37}Cl$ should correlate with key bulk rock indicators of magma ocean crystallization.

Here, we report the H, F, Cl, Br, and I content of eucritic apatite and merrillite as well as the $\delta^{37}Cl$ and H-isotope composition of eucritic apatite. We show that the Cl isotopic composition of apatite in eucrites strongly correlate with bulk rock major and trace element concentrations. We determined a light $\delta^{37}Cl$ signature for 4-Vesta that is similar to that of the unequilibrated chondrites Parnallee and NWA 8276 (23, 25, 29), the former was confirmed by in-situ analysis of apatite grains. We suggest that 4-Vesta accreted a light Cl isotope reservoir that may be distinct from other solar system bodies, like the Earth and Moon.

7.3. Sample description

We chose seven samples (Cachari, GRA 98098, Juvinas, NWA 1908, NWA 5073, Pasamonte, and Stannern) to evaluate the halogen (F, Cl, Br, and I) concentrations and stable Cl isotopes in apatite and merrillite and two samples (GRA 98098 and NWA 1908) to measure apatite D/H and water contents. Our samples are selected from the main group and Stannern trend, and represent a wide range of thermal alteration types (types 2–6). In the following sections we provide relevant petrographic descriptions of our selected samples.

7.3.1 Cachari

Cachari (N513, NHM Vienna) is a heavily-shocked monomict basaltic eucrite that has vesicular glass veins attributed to shock melting by impact (30). It is mainly composed of fractured and mosaicised pyroxenes of 0.2–2.5 mm, i.e., orthopyroxene and augite and each containing exsolution lamellae of each other, and plagioclase of 0.2–2 mm in size and with mottled extinction when viewed in cross-polarized light. Apatite and merrillite are 10–150 μm in apparent diameter and typically occur adjacent or interstitial to pyroxene, plagioclase, chromite, and zircon. Apatite grains are larger and more abundant compared to merrillite. Sarafian et al.

(2014) measured H isotopes in Cachari and found this sample to have a H isotope composition similar to other measured eucrites.

7.3.2 GRA 98098

Graves Nunataks (GRA) 98098 is an unbrecciated coarse-grained type 4 main group eucrite. Our thick section of GRA 98098,65 has 0.2–1 mm laths of plagioclase with rounded edges and 0.2–1 mm blocky exsolved pyroxene. Graves Nunataks 98098 is absent of any late stage melt pockets and merrillite, but it does contain abundant and large apatite often 100 μm in the long direction. The sample has distinctive tridymite veins throughout the main mass that are associated Cl-rich apatite (*6*).

7.3.3 Juvinas

Juvinas is a main group type 5 monomict basaltic eucrite. We analyzed two thin sections of Juvinas, WWU Münster (apatite measurements) and Juvinas AMNH 466-2 (merrillite measurements). Our sections of Juvinas have lathy plagioclase up to ca. 2 mm in the long direction and large blocky pigeonite >4 mm in some cases. The late stage melt regions of Juvinas are also relatively coarse grained and contain ulvöspinel, troilite, pigeonite, plagioclase, merrillite and apatite.

7.3.4 NWA 1908

Northwest Africa 1908 is a monomict and thermally metamorphosed basaltic eucrite with exsolved pyroxenes of ~0.1–1 mm in the long direction and subhedral to anhedral plagioclase intergrowths ca. 100–800 μm in the long direction. Apatite is typically 10–60 μm in apparent size and occurs in late stage melt pockets along with ilmenite, troilite, pigeonite, plagioclase, SiO_2 polymorph, and merrillite, or interstitial to silicates.

7.3.5 NWA 5073

171

NWA 5073 is a rare member of an unbrecciated Stannern trend eucrite and represent one of the least thermally-metamorphosed eucrite basalts. It is mainly composed of elongated, zoned pyroxene phenocrysts up to 1.2 cm, and plagioclase laths up to 0.3 cm in length, and rich in mesostasis (*18*). Abundant late-stage melt pockets are rich in (terrestrial weathered) metal, troilite, tridymite, apatite, merrillite, zircon and baddeleyite. Apatite and merrillite grains are typically 20–100 μm and either occur adjacent to or exsolved from each other.

7.3.6 Pasamonte

Pasamonte is a monomict eucrite with thermal alteration type 2 (*3*), meaning that pyroxenes maintain their magmatic Fe and Mg zonation and absent of exsolution lamellae. Pasamonte is geochemically similar to main group eucrites, but has a distinct O isotope composition (*4*). Based on O isotope compositions Pasamonte likely derived from different parent body, which has similar geochemical characteristics as 4-Vesta (*4*). Our section of Pasamonte on loan from the University of New Mexico (UNM-221) contains rounded basaltic clasts made up of subheadral lathes of plagioclase ca. 100–1000 μm in the long direction with blocky pigeonite 100–500 μm long. Abundant late–stage melt pockets contain ulvöspinel, troilite, pigeonite, plagioclase, merrillite and apatite. While it is difficult to determine petrographically which phosphates crystallized first, merrillite and apatite are present as late crystallizing phases.

7.3.7 Stannern

Stannern is a type 4 Stannern trend brecciated basaltic eucrite. Our thin section of Stannern, AMNH 554-1 exhibit plagioclase lathes 0.2–3 mm in length with intergrown pyroxenes 0.1–2 mm in the long direction. In addition, some regions have dendritic intergrown plagioclase and pyroxene, which could indicate quench growth. Late stage melt regions in Stannern are abundant and contain ilmenite, troilite, pigeonite, plagioclase, SiO_2 polymorph, chromite, merrillite, apatite and zircon. Apatite and merrillite are in the range of 10–100 μm in the long direction.

7.3.8 Parnallee

Parnallee is an unequilibrated ordinary chondrite. Apatites occur interstitial to matrix olivine and adjacent to metal grains and range in size from 15–100 μm in the long direction. The bulk $\delta^{37}Cl$ of Parnallee and NWA 8276 were previously measured and are considered to represent the unprocessed original solar system value of ca -4‰ (*23, 25, 29*).

7.4. Methods

7.4.1 Scanning election microscope

We used the JEOL JSM 6610-LV scanning electron microscope (SEM) equipped with an energy-dispersive X-ray spectrometer (EDS) at the Natural History Museum Vienna, Austria and a Hitachi TM3000 SEM equipped with an EDS at the Woods Hole Oceanographic Institution for petrographical observations and location of phosphate grains. Low beam currents and fast acquisition times were used to ensure apatites were not electron beam damaged.

7.4.2 Secondary ion mass spectrometry

7.4.2.1 Cl isotopes and halogen concentrations: Halogen concentrations (F, Cl, Br, and I) and stable Cl isotopic compositions were measured using a CAMECA IMS1280 large-geometry secondary ion mass spectrometer at the NordSIMS facility at the Swedish Museum of Natural History. The procedures used here closely follow those of (*14, 31*). Cleaned samples were coated with 30 nm of Au. Prior to spot analyses, the analytical positions were pre-sputtered for 120 s over a 25 × 25 μm^2 raster area to remove the Au coating and any remaining surface contamination. For both concentration and isotope analysis, secondary ions of halogens species were sputtered from the surface using a 2 nA Cs^+ Gaussian focused beam and a 15 × 15 μm^2 raster with an impact energy of 20 kV. An electron gun was used in conjunction with the primary Cs^+ beam to counteract any charging effects on the surface of the sample. Secondary ions were then centered in a 2000 μm field aperture, which provides a ca. 25 × 25 μm^2 field of view on the sample that is smaller than the combined spot and pre-sputter area, thus precluding admission of surface contaminant halogens to the mass spectrometer. For halogen concentration measurements, secondary ions were filtered at a mass resolving power (MRP; M/ΔM at 10%

173

peak height) of 5000 and species of $^{19}F^-$, $^{37}Cl^-$, $^{127}I^-$, and a matrix peak of $^{40}Ca^{31}P^-$ were then measured in either an electron multiplier ($<10^6$ cps) or Faraday cup ($>10^6$ cps) in mono-collection mode using a peak hopping routine. In order to measure $^{81}Br^-$, which has complex molecular interferences, a combined $^{81}Br^- + {}^{44}Ca^{35}Cl^- + {}^{46}Ca^{37}Cl^-$ peak was measured and during data reduction stripped of its CaCl interferences using the measurement of the most abundant $^{40}Ca^{37}Cl^-$ species and assuming the natural isotopic abundances of Ca and Cl. Ratios of $^{19}F^-$, $^{37}Cl^-$, $^{81}Br^-$ and $^{127}I^-$ to the matrix $^{40}Ca^{31}P^-$ species were used to calculate concentrations using relative sensitivity factors determined by analyses of the Durango apatite standard during the same session, which has F, Cl, Br, and I contents of 33500, 4099, 0.84, and 0.73 µg/g respectively.

Chlorine isotopic compositions were measured in adjacent spots in the same grains as the halogen concentrations where possible or in adjacent grains where necessary. The secondary ions $^{35}Cl^-$ and $^{37}Cl^-$ were filtered at a mass resolution of 2500 and measured simultaneously on two Faraday cups equipped with 10^{11} Ω low noise amplifiers in four blocks of ten integrations, resulting in an overall counting time of 160 s. Secondary magnet stability was maintained using an nuclear magnetic resonance (NMR) field sensor in regulation mode. Measurements of two different apatite standards, Durango and a pure, synthetic Cl-apatite of known composition, i.e., $\delta^{37}Cl$ of 0.5‰ and 2.0‰, respectively from (14), were interspersed with analyses of unknowns. To account for matrix dependent variations in instrumental mass bias (IMF) resulting from variable Cl content(s), a linear correction based on drift-corrected measured Cl intensities was made to eucrite isotopic compositions relative to intensity and isotopic composition of the bracketing apatite standards. This IMF bias correction was not made for Parnallee because those apatites were Cl-rich.

7.4.2.2 D/H and water content: The isotopes of H (deuterium, D and H) and H_2O concentrations were measured in apatite grains from GRA 98098 and NWA 1908. According SIMS measurements were conducted on a CAMECA IMS1280 ion probe at the Woods Hole Oceanographic Institution. Prior to measurements, sample mounts were cleaned with distilled water and ethanol and dried in a vacuum chamber with a pressure less than ~6.6 × 10^{-5} Pa (5 ×

174

10^{-7} Torr). The samples were then taken out of the vacuum chamber and gold coated. After gold coating, the sample was placed into the instrument to obtain a pressure of lower than 1.3×10^{-7} Pa (~5×10^{-9} Torr) in the analysis chamber.

A focused 1 nA Cs^+ primary beam was rastered to produce a 15×15 μm^2 sputter crater. During our analysis we used a physical field aperture was used, such that ions from the central 8×8 μm^2 of the SIMS pit were counted. Prior to analysis of unknowns the production rate of $^{16}O^1H^1H^-$ was determined using JD17H reference material, i.e., a natural glasses with 2.49 wt% H_2O. A MRP of 12,000 (MRP of 11,632 needed to separate $^{16}O^2H^-$ for $^{16}O^1H^1H^-$) was used for the $^{16}O^1H^1H^-$ production rate test. We found the $^{16}O^1H^1H^-$ peak is lower than our electron multiplier (EM) background (~0.01 counts per second), meaning the production of $^{16}O^1H^1H^-$ is less than 1‰ of $^{16}O^2H$. For our analyses MRP was nominally 10,000, which separates $^{17}O^1H^-$ from $^{16}O^2H^-$. Using mono-collection mode, we counted mass $^{17}O^-$, $^{16}O^1H^-$, and $^{16}O^2H^-$. Background $^{17}O^1H^-/^{17}O^-$ measured throughout the session was ca. 4.5×10^{-2}, which translates to ca. 19 $\mu g/g$ H_2O. Background was corrected by subtracting counts of $^{17}O^1H^-$ and $^{17}O^2H^-$ of our low water reference material, Suprasil 3002 (1 $\mu g/g$ H_2O, provided by Heraeus Quarzglas, Switzerland) from our apatite measurements. All uncertainties were propagated from background and analytical uncertainty.

7.5. Results

7.5.1 Halogen concentrations

The F, Cl, Br, and I content of apatite and/or merrillite was measured in all eucrite samples and representative analyses are presented in Tables S1. The merrillite F, Cl, Br, and I content vary considerably for all samples, 5.8 – 3532 $\mu g/g$, 2.73 – 546.36 $\mu g/g$, 0.28 – 78.14 $\mu g/g$, and 0.11 – 14.1 $\mu g/g$, respectively (Fig. 2). Our measurements of F and Cl in apatite from Stannern, Pasamonte, and GRA 98098 agree with previous measurements (6). Bromine and I concentrations positively correlate with Cl content, but not F. External precision (1σ, n=35) for F, Cl, Br, and I for Durango apatite were 4%, 5%, 12%, and 3%, respectively.

7.5.2 $\delta^{37}Cl$

The Cl isotopic composition of single apatite grains in all measured eucrites vary from -4.6‰ in NWA 5073 to +11.9‰ in NWA 1908 (Table 1). This large variation is similar to the variation seen on Mars (*23, 25*), but less than the variation observed on the Moon (*26, 27*) and mantle-derived magmatic rock of the Earth (*21, 24*). Apatite $\delta^{37}Cl$ from each eucrite sample correlate with its bulk rock major- and trace-element composition, e.g., Sc, Mg, V, Cr, and K content (Fig. 3A-D). Additionally, apatite $\delta^{37}Cl$ correlate with apatite Br/Cl (Fig. 3E), apatite I/Cl (Table S1), and bulk rock $\delta^{66}Zn$ (Fig. 3F). External precision on Durango apatite and the synthetic apatite were 0.17‰ (n=159) and 0.32‰ (n=40), respectively.

7.5.2.1 $\delta^{37}Cl$-Parnallee: We measured apatite grains interstitial to olivine and associated with metal grains in the ordinary chondrite Parnallee. The mean of all analyses is -4.7 ± 1.5‰ (2 sd, n=32), which is in excellent agreement with the structurally bound Cl determined by bulk measurements, -4.1 ± 0.3‰ (*29*).

7.5.3 δD

The hydrogen isotopic composition was measured in two eucrites, GRA 98098 and NWA 1908 (Table 2). No spallation correction was made because (1) no cosmic-ray exposure ages exist for GRA 98098 and NWA 1908 and (2) the H-rich nature of apatite and the render the spallation correction negligible (*5*). For example, an apatite with ca. 56 µg/g H (500 µg/g H_2O) and exposure age of 30 Myr would have a spallation correction of ca. -20‰ (*5*). Graves Nunataks 98098 and NWA 1908 show elevated D/H relative to Cachari, Juvinas, Pasamonte (*5, 20*). With the exception of Stannern, the elevated in δD corresponds to elevated $\delta^{37}Cl$ (Fig. 4).

176

7.6 Discussion

7.6.1 Phosphate saturation

The halogen content of apatite and merrillite can help determine the limiting element(s) in apatite saturation. Beside OH, F and Cl are major structural constituents in the mineral apatite, but trace elements in merrillite. Therefore, these key characteristics of halogen geochemistry can be used to determine the crystallization sequence of phosphates in eucrites. We observe the F and Cl content of merrillite vary according to the power function $F = 1.8 \times Cl^{(0.915)}$ (Fig. 2). At a F and Cl content of greater than 300 µg/g the slope steepens, i.e., F becomes enriched compared to Cl (Fig. 2). The steepening of the slope in F vs. Cl space could be the merrillite structure switching to the apatite structure, where F is extremely compatible and Cl is moderately compatible (*14*). Therefore, merrillite coexisting with apatite suggest that F, or any other anion compatible in apatite, is the limiting element in apatite saturation in eucrite basalts, not P.

7.6.2 The H content of eucrite magmas

The bulk water content of eucrite magmas can be evaluated in two ways. (1) Apatite-melt hygrometry (*13*, *32*), which uses an apatite-melt OH-F exchange coefficient (K_d) that were mostly determined at the C-CO buffer at 1 GPa, bulk F content (see supplementary material), and apatite OH and F contents (this study and Sarafian et al., 2013). Apatite-melt hygrometry, while a useful tool, is only an approximation of the melt water content, especially at low oxygen fugacity when H_2 is present in the melt. This approach assumes a closed system during crystallization, similar partition coefficients for H and F between the major crystallizing phases, i.e., plagioclase and pyroxene, and melt, and no pressure dependence on the K_d, extrapolating from 1 GPa to $\sim 10^0$–10^7 Pa - the potential pressure of crystallization for eucrite basalts. A closed system implies that no degassing took place prior to apatite crystallization, which means magmas must have crystallized under pressure and/or melts were extremely water-poor. However, this may not be the case for eucrite magmas. Additionally, the partition coefficients for H and F between the silicate crystallizing phases and melt are different (Dalou et al., 2012; Hauri et al., 2006) and poorly characterized at low pressure. Nevertheless, we provide the first estimate for

the water content of a eucritic melt. Using the OH-F exchange coefficient and F content of the bulk rock, which likely represents a melt composition, we can estimate the H content of a primitive melt (*32*):

$$C_{H_2O}^{PM} = \frac{X_{H_2O}^{ap} \times X_F^{Melt}}{K_{d_{OH-F}}^{ap-melt} \times X_F^{ap}}$$

(1)

Where $C_{H_2O}^{PM}$ is the concentration of H_2O in the primitive melt, $X_{H_2O}^{ap}$ is the H_2O content of apatite, X_F^{ap} is the concentration of F in apatite, X_F^{Melt} is the concentration of F in the melt, which is assumed to be equal to that of the bulk rock, and $K_{d_{OH-F}}^{ap-melt}$ is the exchange coefficient determined by McCubbin et al (*13*). The estimated water content of the Juvinas, Pasamonte, and Stannern primitive melts are 53 ± 14, 52 ± 13, 5 ± 1 µg/g H (470 ± 121, 460 ± 120, 40 ± 7 µg/g H_2O), respectively. These estimates should be considered minima if F is more compatible than H in pyroxene and plagioclase, if degassing took place prior to apatite crystallization, and/or if abundant H_2 was present in the melt. The large uncertainties in the calculated H_2O contents are due to the sizable variations in measured F contents in the literature. However, the eucrite melt water contents fit into petrologic models for eucrite genesis and our isotope measurements, where Pasamonte and Juvinas have similar H, major and trace element contents, and isotopic signatures (Fig. 4). The elevated δD of Stannern (Fig. 4) suggests that H degassing took place during either magma cooling or crustal interaction (*10*) and low calculated H content of the Stannern primitive melt further support the degassing hypothesis. We would like to emphasize that these are estimates of eucrite parent melt H contents and determining the H content of 4-Vesta is beyond the scope of this contribution.

(2) An alternate method to estimate the bulk H_2O content of 4-Vesta is to use bulk rock volatile-refractory elemental ratios, extrapolating them to a 4-Vesta composition. We can assume a maximum initial preserved eucrite melt H content of ca. 112 µg/g (1000 µg/g H_2O), by extrapolating the volatile element depletion of eucrites based on the K/U of Earth, the Moon and eucrites (*6*, Fig SX; *33-35*). This approach fundamentally assumes that K and U are not

fractionated from one another, which may not be the case if a magma ocean was present. We also must assume a constant depletion factor from K to H. For Earth, this assumption holds true for many elements (Lodders, 2003), except for some, e.g., Cl (Sharp and Draper, 2013). Therefore, we would like to emphasize that this is a crude estimate for the H content of eucrite melts.

The solubility of H is pressure dependent (36, 37). Using previously established H solubility models (36, 37), our upper H content limit of 112 µg/g H as OH in a vestan magma ocean is soluble at a pressure of 2.29 MPa, or at ~3 km deep; less overburden is needed for ca. 22.4 µg/g H dissolved as OH. At a depth of 6 km, ~2000 µg/g H_2O is soluble (36, 37). If we choose the initial preserved H content of 22.4–112 µg/g based on our above hygrometry calculations, and assume the vestan magma ocean crystallized 50%, then the magma ocean must be under at least 2.5 km to 11 km of crust to allow for our observed H_2O contents, which agrees with other recent crustal thickness models (38).

7.6.3 Possible Cl and H isotope fraction processes

Apatite in eucrites display an extremely wide range of $\delta^{37}Cl$ values that correlate with the bulk rock major- and trace-element content and apatite halogen content (Fig. 3A-E). Processes that can fractionate the Cl isotopes include (a) perchlorate formation (39, 40), (b) distillation (41), and (c) degassing of metal chlorides (22). (a) Perchlorate (ClO_4^-) forms by UV irradiation of Cl and generally affects samples in desert environments due to low water flux, and can impart a wide range of Cl isotopic compositions, both heavy and light (39, 40). If perchlorate caused the wide range of observed $\delta^{37}Cl$ values, then surface contamination of basalts would be the primary process driving the variation in $\delta^{37}Cl$. In this case, we may expect a correlation between $\delta^{37}Cl$ and halogen content as well as exposure age or solar wind derive noble gas content (42). However, regolithic eucrites do not exist in the meteorite collection and regolithic howardites are rare (42). Additionally, our sample with the most elevated $\delta^{37}Cl$ is an unbrecciated rock, meaning that it was likely not part of a regolith on the surface of 4-Vesta. Therefore, the observed range in $\delta^{37}Cl$ cannot be explained by perchlorates.

179

(b) Volcanic fumaroles produce vapors with high $\delta^{37}Cl$ values (41). In these fluid dominated systems, chloride ions evaporate to form HCl vapor causing $\delta^{37}Cl$ fractionation where the heavy isotope resides in the vapor, and the light isotope remains in the liquid (41). The vapor phase is isotopically heavy because the bond strength of HCl_g is stronger than the Cl^- dissolved in the liquid (41). The H isotopes also fractionate during evaporation (43). There is a strong temperature-dependence on the D/H fractionation, but at temperatures less than 230 °C the vapor is isotopically light and at temperatures between 230-360 °C the vapor is slightly heavy, <10‰. If boiling/distillation fractionated the Cl isotopes, then apatite with the most elevated $\delta^{37}Cl$ signature should be associated with the lowest D/H if the apatite equilibrated with a low-temperature fluid, or no measurable variation in D/H if the boiling/distillation event was at high temperature. Boiling/distillation was likely not the mechanism to cause $\delta^{37}Cl$ variation because we observe the highest $\delta^{37}Cl$ associated with elevated D/H (Fig. 4). Additionally, if all of the studied eucrites were the product of intense hydrothermal alteration secondary phases, e.g., clays and other phyllosilicates, would likely be pervasive.

7.6.3.1 Magma ocean degassing: (c) Degassing of high-temperature magmas causes the loss of many volatile species, including K^+, KOH, KCl, HCl, H_2O, H_2 (44). Degassing of HCl causes little if any Cl isotope fractionation (29), but degassing of metal chlorides, like KCl causes a significant increase in $\delta^{37}Cl$ (22 Fig. S1). Additionally, Br/Cl and I/Cl likely decreases during crystallization (Kusebauch et al., 2015a).

As stated above, eucrites are a sampling of the asteroid 4-Vesta and geochemically similar asteroids. The eucrite main group likely formed via extraction from an equilibrium crystalizing magma ocean into magma chambers by fractional crystallization (8). Therefore, less evolved eucrites, e.g., low [Sc] or high [Mg], were extracted from the magma ocean earlier than evolved eucrites e.g., high [Sc] or low [Mg]. Systematic trends can be observed across many major and trace elements when plotted against $\delta^{37}Cl$ (Figs. 3A-D). One trend shows K, an incompatible element in mafic/ultramafic systems, decreases with increasing Sc and $\delta^{37}Cl$ (Figs. 3A & 3D).

This correlation suggests that K either acts compatibly during magma ocean crystallization, or degassed during 4-Vesta's magma ocean phase (45). The latter is more likely, as K degases from high-temperature magmas (44). Additionally, the Br and I content of apatite decreases by a factor of ca. 3.5 and 2.3 (Tables 1, S2), respectively, from the lowest to highest $\delta^{37}Cl$ value measured. This decrease is expected, as first-order high-temperature volatilely scales with atomic number (46). The decrease in Cl content does not follow the Br and I trend, which could be because Cl is a major structural component in apatite, meaning Cl partition between apatite and melt is non-ideal, or more likely, degassing of Cl may have been rate-limited due to its high solubility in melts. Here, we suggest that the correlation between major and trace elements, and halogens with $\delta^{37}Cl$ are related to degassing of the 4-Vesta magma ocean, where increasing $\delta^{37}Cl$ with decreasing K is observed. Alternatively, the degassing event(s) could have occurred during magmatic emplacement or eruption after a magma ocean stage. This hypothesis is supported by the large variation in H isotope composition observed in apatite, but is inconsistent with the excellent correlation between bulk rock $\delta^{66}Zn$ and apatite $\delta^{37}Cl$ of the eucrites investigated (Fig S3; 47), as stable Zn isotopes do not fractionate during magmatic emplacement (48). Therefore, we suggest that while some of the isotopic variation (including Cl) are related to magmatic emplacement processes, the large-scale Cl isotope fractionation occurred during degassing of the magma ocean. In addition, the decreasing Br/Cl and I/Cl may be due to magma ocean degassing too, but also could be due to incompatible nature of Br and I relative to Cl.

During the magma ocean stage of lunar formation, it has been hypothesized that metal chloride degassing occurred because some apatite were found to have a relative enrichment of ^{37}Cl (26, 27). Likewise, we suggest that during the magma ocean stage of 4-Vesta, while eucrite magmas were segregating and erupting, degassing of metal chlorides (or metal halides) occurred. Degassing of the magma ocean could have been enhanced by impacts breaking through the crust (27), or degassing may have occurred despite the presence of a crust due to the low pressure environment on 4-Vesta. Our degassing models, which assume Rayleigh fractionation, show that a ~60% loss of Cl as KCl will evolve the $\delta^{37}Cl$ from -3.8‰ (average NWA 5073 $\delta^{37}Cl$) to 7.7‰ (average GRA 98098 $\delta^{37}Cl$; Fig. S2). Therefore, the large range in Cl isotope compositions

observed in basaltic eucrites can be explained by a simple metal chloride degassing model (Fig. 3).

It can be assumed that Cl and H species were likely degassing at the same time. The H isotope fractionation between melt and vapor is controlled by (1) the isotope fraction factor of the degassing species, H_2 and H_2O, and (2) the abundance ratio of the two species (Fig. S3). The isotope fractionation factors (α) commonly used for H_2 and H_2O are 0.816 and 1.049 (49), but the α for H_2O between melt and vapor is likely a function of melt composition and pressure and has not been fully parameterized (49). The abundance ratio, H_2:H_2O, is controlled by the oxygen fugacity of the system (50). A the oxygen fugacity of eucrite formation, IW-1 (2 and refs. therein); where IW-1 is 1 log unit below the Fe$\rightarrow$FeO oxygen buffer), low pressure and low H_2O content, the molar H_2:H_2O ratio is ~5:95 (50). If the concentrations of H_2 and H_2O in the magma ocean are above saturation, a mixture of H_2 and H_2O will degas, although H_2 may degas more rapidly than H_2O (51). Degassing will stop when the volatile species is no longer saturated in the melt. At low oxygen fugacity, the H_2 fugacity is much higher than the H_2O fugacity, meaning that H_2O will become soluble in the melt before H_2 (51). If degassing took place at a lower oxygen fugacity, or if H_2 degasses more efficiently than H_2O (Sharp et al., 2013b), then one would expect to generate greater H isotope fractionation than observed here. 4-Vesta likely accreted and underwent core formation at a very low oxygen fugacity, however this was likely prior to any volatile accretion 4-Vesta experienced.

We model the vestan magma ocean by first degassing H_2, H_2O, and metal chlorides for a period, followed by degassing of only H_2 and metal chlorides (Fig. 4). The system can switch from a mixed H_2–H_2O species, which causes little H isotope fractionation (Fig. S3) to only H_2, which causes massive H isotope fractionation, for two reasons, (1) H_2O can become soluble due to low concentrations of H_2O in the magma ocean, or (2) H_2O becomes soluble due to an increase of pressure (36, 37). Our model shows that mixed-phase degassing can explain the variations seen in the data (Fig. 4) and requires and early-formed crust at least 3-11 km in thickness, which generally agrees with recent physicochemical models of 4-Vesta (8, 38). The location of the

inflection point (where Juvinas sits, Fig. 4) is a function of absolute H_2O content and crustal thickness (pressure).

7.6.4 Stannern, the outlier

Stannern is enriched in incompatible elements relative to $\delta^{37}Cl$ compared to the other eucrites studied here (Figs. 1, 3D). Apatite in Stannern also has an elevated δD relative to other eucrites (5, 20), yet has unfractionated Cl isotopes (Fig. 3). Stannern, the namesake of the Stannern trend, was likely generated by mixing small degree crustal partial melts with main group-type magmas (10, 11). The partial melt generated would be enriched in the incompatible elements, including H and Cl, and likely degassed H_2. A loss of at least 60% of total H can account for the enrichment of D, if no H_2O degassing took place at the time of crystallization. The NWA 5073 sample is another member of Stannern trend eucrites, but likely samples a relatively primitive magma ocean. We suggest that Stannern received its Cl isotope signature from the magma ocean but underwent further processing, e.g., interaction with a crustal melt.

7.6.5 The $\delta^{37}Cl$ of 4-Vesta

Here we have shown that magma ocean degassing of mixed species (KCl, HCl, H_2O, H_2) is the likely mechanism that caused the observed enrichments in $\delta^{37}Cl$ and δD. Our best estimate for the primordial $\delta^{37}Cl$ of 4-Vesta derives from the eucrite with the lowest measured $\delta^{37}Cl$, NWA 5073, -3.8 ± 1.1‰ (2 sd, n=23) based on our bulk rock major- and trace-element content and apatite halogen content trends (Fig. 3). Our estimate (1) would be an upper limit for 4-Vesta, because magma ocean degassing increases the $\delta^{37}Cl$ of segregated magmas and we probably did not sample the most primitive lava possible (such as the primitive eucrite Sioux County); (2) is within error of some unequilibrated chondrites (23, 25, 29). The similarly low $\delta^{37}Cl$ of 4-Vesta and the chondrites Parnallee and NWA 8276 (25, 29) may suggest a primordial light Cl isotope reservoir existed, but was extremely difficult to preserve.

7.6.6 The volatile element accretion/processing in the inner solar system

4-Vesta, with a fast accretion history (*1*), likely avoided any potential isotopically heavy HCl hydrate ices (*25*), which condenses around 140–160 K (*52*). If 4-Vesta did not receive HCl hydrate ices, then it may not have received other hydrous- and carbon-bearing ices, as H and C condense at ca. 180 and 40 K, respectively (*53*), meaning 4-Vesta would be relatively depleted in H, C, Cl, and other elements contained in ice, compared to bodies with a $\delta^{37}Cl$ of 0‰. Consequently, 4-Vesta could have avoided the delivery/and or accumulation of HCl hydrate ice because the ices probably were lost once "wet" material crossed an ice line, presumably in the early inner solar system, or 4-Vesta finished primary accretion prior to ice injection into the inner solar system. Interestingly, the terrestrial mantle likely has a $\delta^{37}Cl$ value of ca. 0‰ (*29*), although some mantle reservoirs are as light as -3‰ (*21, 24*). Therefore, if the source of H is the same between Earth, the Moon and 4-Vesta (*5, 20, 54, 55*), then some processes that affected the Earth and possibly the Moon must have fractionated the Cl isotopes without fractionating the H isotopes, or 4-Vesta is missing a heavy-Cl component independent of the other volatile elements.

7.7 Conclusions

Here we have shown that F is a phase-limiting element for apatite growth in eucrite basalts. Using apatite hygrometry we have shown that the Juvinas/Pasamonte primitive melt contained ~200–600 μg/g H_2O. We have also shown large variations in apatite Br/Cl and I/Cl, and $\delta^{37}Cl$ were preserved in eucrite meteorites. Large-scale geochemical trends, interpreted to be evidence of a magma ocean on 4-Vesta, were related to apatite Br/Cl and $\delta^{37}Cl$. 4-Vesta likely had a magma ocean that degassed many volatile species, including KCl, H_2, H_2O, Br, and I. We confirm that Parnallee has a $\delta^{37}Cl$ of -4.7 ± 1.5‰, which suggests that some chondrite parent bodies and 4-Vesta accreted a depleted Cl isotope signature compared to Earth and possibly the Moon. Either these bodies are missing a heavy Cl isotope volatile-element component, or Earth accreted from material that had been geochemically processed or was isotopically distinct from the start.

7.8 Acknowledgements

7.9 References

1. M. Touboul, P. Sprung, S. A. Aciego, B. Bourdon, T. Kleine, Hf-W chronology of the eucrite parent body. *Geochimica et Cosmochimica Acta.* **73**, 5150–5188 (2015).

2. H. Y. McSween Jr, D. W. Mittlefehldt, A. W. Beck, R. G. Mayne, T. J. McCoy, in *The Dawn Mission to Minor Planets 4 Vesta and 1 Ceres*, C. Russell, C. Raymond, Eds. (Springer, New York, NY, 2012), pp. 141–174.

3. H. Takeda, A. L. Graham, Degree of equilibration of eucritic pyroxenes and thermal metamorphism of the earliest planetary crust. *Meteoritics.* **26**, 129–134 (1991).

4. E. R. D. Scott, R. C. Greenwood, I. A. Franchi, I. S. Sanders, Oxygen isotopic constraints on the origin and parent bodies of eucrites, diogenites, and howardites. *Geochimica et Cosmochimica Acta.* **73**, 5835–5853 (2009).

5. A. R. Sarafian, S. G. Nielsen, H. R. Marschall, F. M. McCubbin, B. D. Monteleone, Early accretion of water in the inner solar system from a carbonaceous chondrite–like source. *Science.* **346**, 623–626 (2014).

6. A. R. Sarafian, M. F. Roden, A. E. Patiño Douce, The nature of volatiles in eucrites: Clues from apatite. *Meteoritics & Planetary Science.* **48**, 2135–2154 (2013).

7. P. H. Warren, E. A. Jerde, Composition and origin of Nuevo Laredo trend eucrites. *Geochimica et Cosmochimica Acta.* **51**, 713–725 (1987).

8. B. E. Mandler, L. T. Elkins-Tanton, The origin of eucrites, diogenites, and olivine diogenites: Magma ocean crystallization and shallow magma chamber processes on Vesta. *Meteoritics & Planetary Science.* **48**, 2333–2349 (2013).

9. E. Stolper, Experimental petrology of eucritic meteorites. *Geochimica et Cosmochimica Acta.* **41**, 587–611 (1977).

10. J. A. Barrat *et al.*, The Stannern trend eucrites: Contamination of main group eucritic magmas by crustal partial melts. *Geochimica et Cosmochimica Acta.* **71**, 4108–4124 (2007).

11. A. Yamaguchi *et al.*, Crustal partial melting on Vesta: Evidence from highly metamorphosed eucrites. *Geochimica et Cosmochimica Acta.* **73**, 7162–7182 (2009).

12. T. M. Harrison, E. B. Watson, The behavior of apatite during crustal anatexis: equilibrium and kinetic considerations. *Geochimica et Cosmochimica Acta.* **48**, 1467–1477 (1984).

13. F. M. McCubbin *et al.*, Experimental investigation of F, Cl, and OH partitioning between apatite and Fe-rich basaltic melt at 1.0–1.2 GPa and 950–1000 C. *American Mineralogist.*

100, 1790–1802 (2015).

14.   C. Kusebauch, T. John, M. J. Whitehouse, S. Klemme, A. Putnis, Distribution of Halogens between Fluid and Apatite during fluid-mediated replacement processes. *Geochimica et Cosmochimica Acta.* **170**, 225–246 (2015).

15.   W. F. McDonough, S. S. Sun, The Composition of the Earth. *Chemical Geology.* **120**, 223–253 (1995).

16.   P. H. Warren, G. W. Kallemeyn, H. Huber, F. Ulff-Møller, W. Choe, Siderophile and other geochemical constraints on mixing relationships among HED-meteoritic breccias. *Geochimica et Cosmochimica Acta.* **73**, 5918–5943 (2009).

17.   A. H. Treiman, A. Lanzirotti, D. Xirouchakis, Ancient water on asteroid 4 Vesta: Evidence from a quartz veinlet in the Serra de Magé eucrite meteorite. *Earth and Planetary Science Letters.* **219**, 189–199 (2004).

18.   J. Roszjar *et al.*, Thermal history of Northwest Africa 5073—A coarse grained Stannern trend eucrite containing cm sized pyroxenes and large zircon grains. *Meteoritics & Planetary Science.* **46**, 1754–1773 (2011).

19.   J. A. Barrat *et al.*, Possible fluid-rock interactions on differentiated asteroids recorded in eucritic meteorites. *Geochimica et Cosmochimica Acta.* **75**, 3839–3852 (2011).

20.   T. J. Barrett *et al.*, The abundance and isotopic composition of water in eucrites. *Meteoritics & Planetary Science.* **51**, 110–1124 (2016).

21.   T. John, G. D. Layne, K. M. Haase, J. D. Barnes, Chlorine isotope evidence for crustal recycling into the Earth's mantle. *Earth and Planetary Science Letters.* **298**, 175–182 (2010).

22.   Z. D. Sharp, C. K. Shearer, K. D. McKeegan, J. D. Barnes, Y. Q. Wang, The chlorine isotope composition of the moon and implications for an anhydrous mantle. *Science.* **329**, 1050–1053 (2010).

23.   J. T. Williams *et al.*, The chlorine isotopic composition of Martian meteorites 1: Chlorine isotope composition of Martian mantle and crustal reservoirs and their interactions. *Meteoritics & Planetary Science.* **in press**, 1–19 (2016).

24.   S. A. Halldórsson *et al.*, Subducted lithosphere controls halogen enrichments in the Iceland mantle plume source. *Geology.* **44**, 679–682 (2016).

25.   Z. Sharp, J. Williams, C. Shearer, C. Agee, K. McKeegan, The chlorine isotope composition of Martian meteorites 2. Implications for the early solar system and the formation of Mars. *Meteoritics & Planetary Science.* **in press**, 1–16 (2016).

26. J. W. Boyce *et al.*, The chlorine isotope fingerprint of the lunar magma ocean. *Science Advances*. **1**, e1500380–e1500380 (2015).

27. J. J. Barnes *et al.*, Early degassing of lunar urKREEP by crust-breaching impact (s). *Earth and Planetary Science Letters*. **447**, 84–94 (2016).

28. L. P. Knauth, D. M. Burt, Eutectic brines on Mars: Origin and possible relation to young seepage features. *Icarus*. **158**, 267–271 (2002).

29. Z. D. Sharp *et al.*, The chlorine isotope composition of chondrites and Earth. *Geochimica et Cosmochimica Acta*. **107**, 189–204 (2013).

30. D. D. Bogard, G. J. Taylor, K. Keil, M. R. Smith, R. A. Schmitt, Impact melting of the Cachari eucrite 3.0 Gy ago. *Geochimica et Cosmochimica Acta*. **49**, 941–946 (1985).

31. C. Kusebauch, T. John, M. J. Whitehouse, A. K. Engvik, Apatite as probe for the halogen composition of metamorphic fluids (Bamble Sector, SE Norway). *Contributions to Mineralogy and Petrology*. **170**, 1–20 (2015).

32. F. M. McCubbin *et al.*, Heterogeneous distribution of H2O in the Martian interior: Implications for the abundance of H2O in depleted and enriched mantle sources. *Meteoritics & Planetary Science*, 1–25 (2016).

33. M. M. Hirschmann, R. Dasgupta, The H/C ratios of Earth's near-surface and deep reservoirs, and consequences for deep Earth volatile cycles. *Chemical Geology*. **262**, 4–16 (2009).

34. B. Marty, The origins and concentrations of water, carbon, nitrogen and noble gases on Earth. *Earth and Planetary Science Letters*. **313**, 56–66 (2012).

35. E. H. Hauri, A. E. Saal, M. J. Rutherford, J. A. Van Orman, Water in the Moon's interior: Truth and consequences. *Earth and Planetary Science Letters*. **409**, 252–264 (2015).

36. J. Berndt *et al.*, A combined rapid-quench and H2-membrane setup for internally heated pressure vessels: description and application for water solubility in basaltic melts. *American Mineralogist*. **87**, 1717–1726 (2002).

37. J. E. Dixon, E. M. Stolper, J. R. Holloway, An experimental study of water and carbon dioxide solubilities in mid-ocean ridge basaltic liquids. Part I: Calibration and solubility models. *Journal of Petrology*. **36**, 1607–1631 (1995).

38. J. Roszjar *et al.*, Prolonged magmatism on 4 Vesta inferred from Hf–W analyses of eucrite zircon. *Earth and Planetary Science Letters*. **452**, 216–226 (2016).

39. W. A. Jackson, J. K. Böhlke, B. Gu, P. B. Hatzinger, N. C. Sturchio, Isotopic composition

and origin of indigenous natural perchlorate and co-occurring nitrate in the southwestern United States. *Environmental science & technology*. **44**, 4869–4876 (2010).

40. K. A. Farley *et al.*, Light and variable 37 Cl/35 Cl ratios in rocks from Gale Crater, Mars: Possible signature of perchlorate. *Earth and Planetary Science Letters*. **438**, 14–24 (2016).

41. Z. D. Sharp, J. D. Barnes, T. P. Fischer, M. Halick, An experimental determination of chlorine isotope fractionation in acid systems and applications to volcanic fumaroles. *Geochimica et Cosmochimica Acta*. **74**, 264–273 (2010).

42. J. A. Cartwright *et al.*, The quest for regolithic howardites. Part 1: Two trends uncovered using noble gases. *Geochimica et Cosmochimica Acta*. **105**, 395–421 (2013).

43. J. Horita, D. J. Wesolowski, Liquid-vapor fractionation of oxygen and hydrogen isotopes of water from the freezing to the critical temperature. *Geochimica et Cosmochimica Acta*. **58**, 3425–3437 (1994).

44. L. Schaefer, B. Fegley, A thermodynamic model of high temperature lava vaporization on Io. *Icarus*. **169**, 216–241 (2004).

45. D. W. Mittlefehldt, Volatile degassing of basaltic achondrite parent bodies: Evidence from alkali elements and phosphorus. *Geochimica et Cosmochimica Acta*. **51**, 267–278 (1987).

46. R. Bunsen, XII. Flame reactions. *The London, Edinburgh, and Dublin Philosophical Magazine and Journal of Science*. **32**, 81–107 (1866).

47. R. C. Paniello *et al.*, Zinc isotopes in HEDs: clues to the formation of 4-Vesta, and the unique composition of Pecora Escarpment 82502. *Geochimica et Cosmochimica Acta*. **86**, 76–87 (2012).

48. R. C. Paniello, J. M. D. Day, F. Moynier, Zinc isotopic evidence for the origin of the Moon. *Nature*. **490**, 376–379 (2012).

49. S. Newman, S. Epstein, E. Stolper, Water, carbon dioxide, and hydrogen isotopes in glasses from the ca. 1340 AD eruption of the Mono Craters, California: constraints on degassing phenomena and initial volatile content. *Journal of Volcanology and Geothermal Research*. **35**, 75–96 (1988).

50. M. M. Hirschmann, A. C. Withers, P. Ardia, N. T. Foley, Solubility of molecular hydrogen in silicate melts and consequences for volatile evolution of terrestrial planets. *Earth and Planetary Science Letters*. **345**, 38–48 (2012).

51. Z. D. Sharp, F. M. McCubbin, C. K. Shearer, A hydrogen-based oxidation mechanism relevant to planetary formation. *Earth and Planetary Science Letters*. **380**, 88–97 (2013).

52. M. Y. Zolotov, M. V. Mironenko, (2007), LPSC vol. 38, p. 2340.

53. K. Lodders, Solar system abundances and condensation temperatures of the elements. *The Astrophysical Journal*. **591**, 1220–1247 (2003).

54. M. Clog, C. Aubaud, P. Cartigny, L. Dosso, The hydrogen isotopic composition and water content of southern Pacific MORB: A reassessment of the D/H ratio of the depleted mantle reservoir. *Earth and Planetary Science Letters*. **381**, 156–165 (2013).

55. A. E. Saal, E. H. Hauri, J. A. Van Orman, M. J. Rutherford, Hydrogen Isotopes in Lunar Volcanic Glasses and Melt Inclusions Reveal a Carbonaceous Chondrite Heritage. *Science*. **340**, 1317–1320 (2013).

56. D. D. Bogard, D. H. Garrison, (1997), LPSC vol. 38, pp. 127–128.

57. K. Metzler, K. D. Bobe, H. Palme, B. Spettel, D. Stöffler, Thermal and impact metamorphism on the HED parent asteroid. *Planetary and Space Science*. **43**, 499–525 (1995).

58. G. W. Reed, S. Jovanovic, Some halogen measurements on achondrites. *Earth and Planetary Science Letters*. **6**, 316–320 (1969).

59. R. O. Allen, P. J. Clark, Fluorine in meteorites. *Geochimica et Cosmochimica Acta*. **41**, 581–585 (1977).

60. G. Dreibus, B. Spettel, H. Wänke, Halogens in meteorites and their primordial abundances. *Physics and Chemistry of the Earth*. **11**, 33–38 (1979).

61. D. J. Sawyer, M. D. McGehee, J. Canepa, C. B. Moore, Water soluble ions in the Nakhla martian meteorite. *Meteoritics & Planetary Science*. **35**, 743–747 (2000).

7.10 Figures and Tables

Figure 1

Bulk rock Hf vs. Sc concentrations. Note that Stannern trend eucrites (Stannern and NWA 5073) are enriched in Hf compared to main group eucrites.
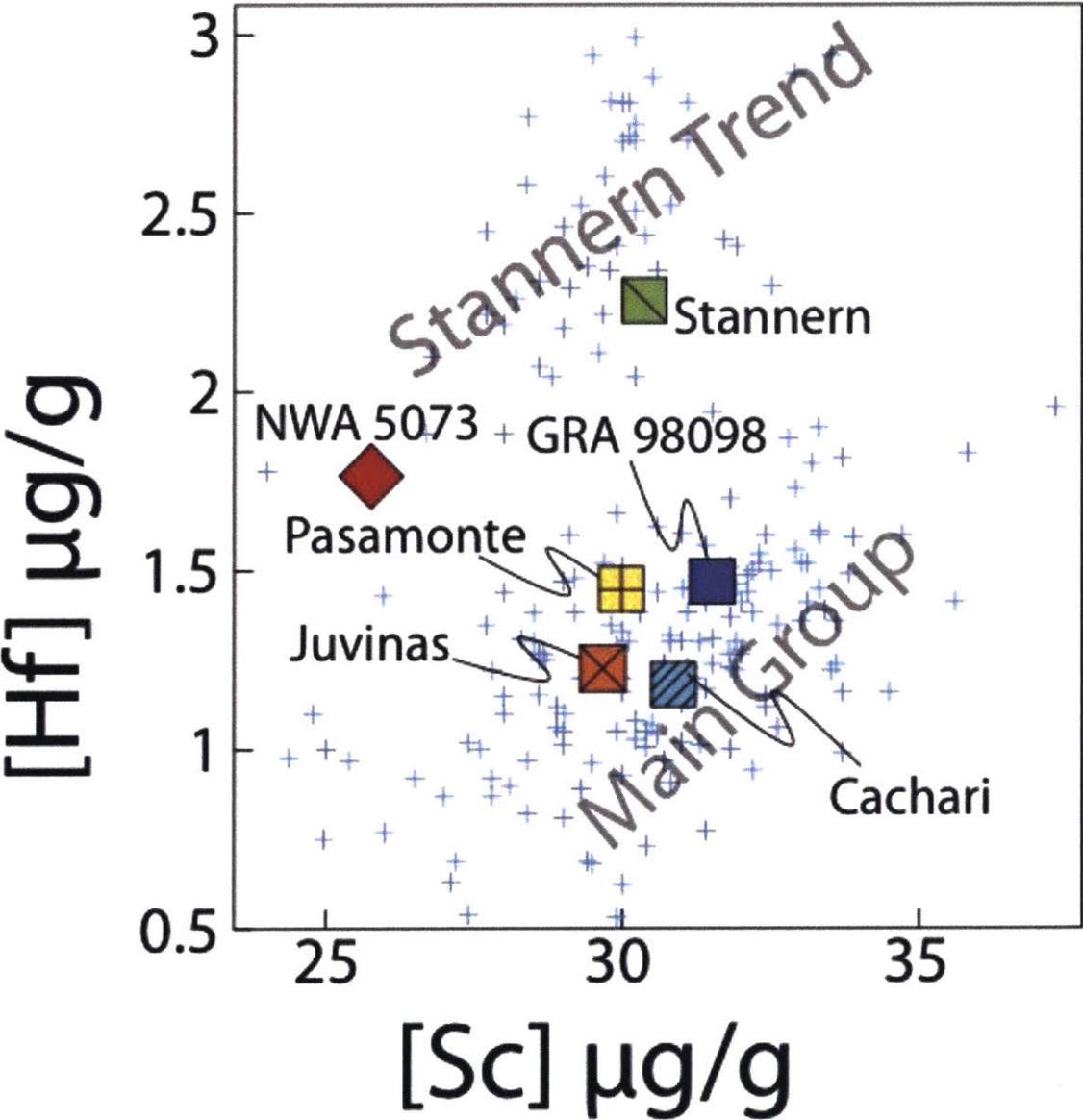
Figure 2

Fluorine vs. Cl in eucrite apatite and merrillite.
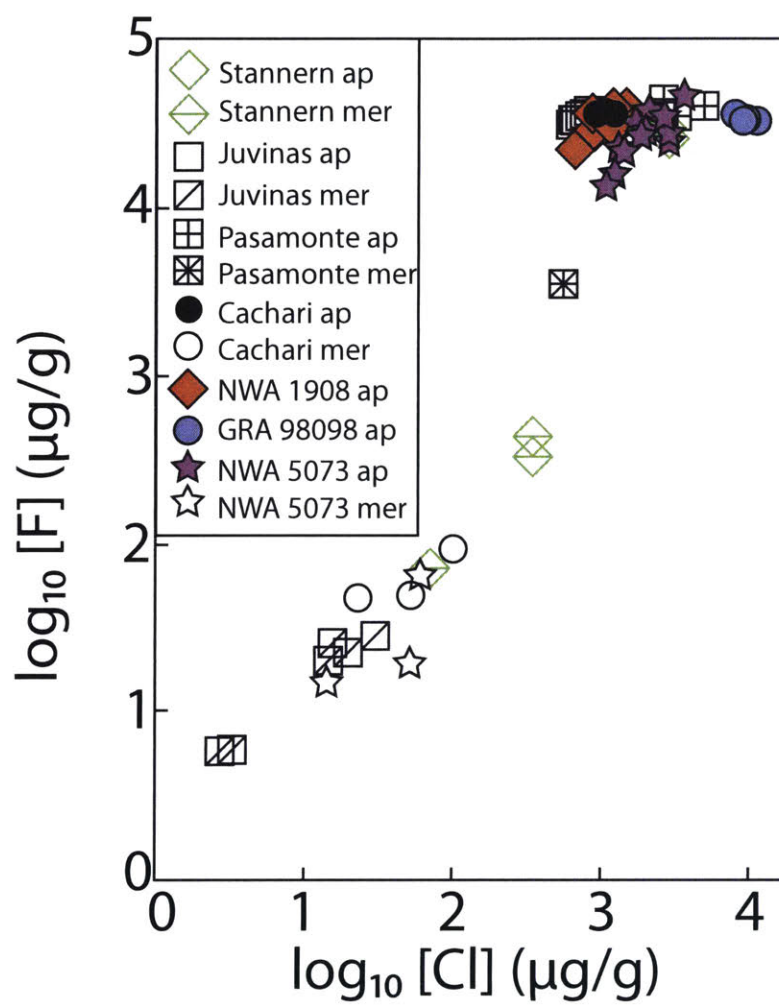
Figure 3

Figure 3. A) bulk rock Sc vs. $\delta^{37}Cl$; note the increase of Sc with $\delta^{37}Cl$, implying olivine instead of pyroxene was a major phase crystallizing during magma ocean crystallization. B) bulk rock Mg vs. $\delta^{37}Cl$ note decrease of Mg with increasing $\delta^{37}Cl$, implying olivine was a major phase crystallizing during magma ocean crystallization. C) bulk rock Cr vs. $\delta^{37}Cl$; note negative relationship between Cr and $\delta^{37}Cl$, implying spinel was crystallizing during magma ocean crystallization. D) bulk rock K vs. $\delta^{37}Cl$; note negative relationship between K and $\delta^{37}Cl$, implying loss of K during magma ocean crystallization. E). Apatite Br/Cl vs. $\delta^{37}Cl$; note negative relationship between Br/Cl and $\delta^{37}Cl$, degassing of Br and Cl during magma ocean crystallization. F) bulk rock $\delta^{66}Zn$ vs $\delta^{37}Cl$ are positively correlated. Stable Zn isotope do not fractionate during magma emplacement. Therefore, Cl and Zn must be fractionating during magma ocean cooling. Graves Nunataks 98098 gives a minimum value for $\delta^{66}Zn$ due to Antarctic weathering removing heavy Zn (*47*). See Supplementary information for references for bulk rock concentrations.

Figure 4

Hydrogen isotope composition vs. Cl isotope composition. Note positive correlation between the two isotope systems, which suggest that H and Cl were degassing contemporaneously.

Table 1

Cl isotope composition of measured apatite

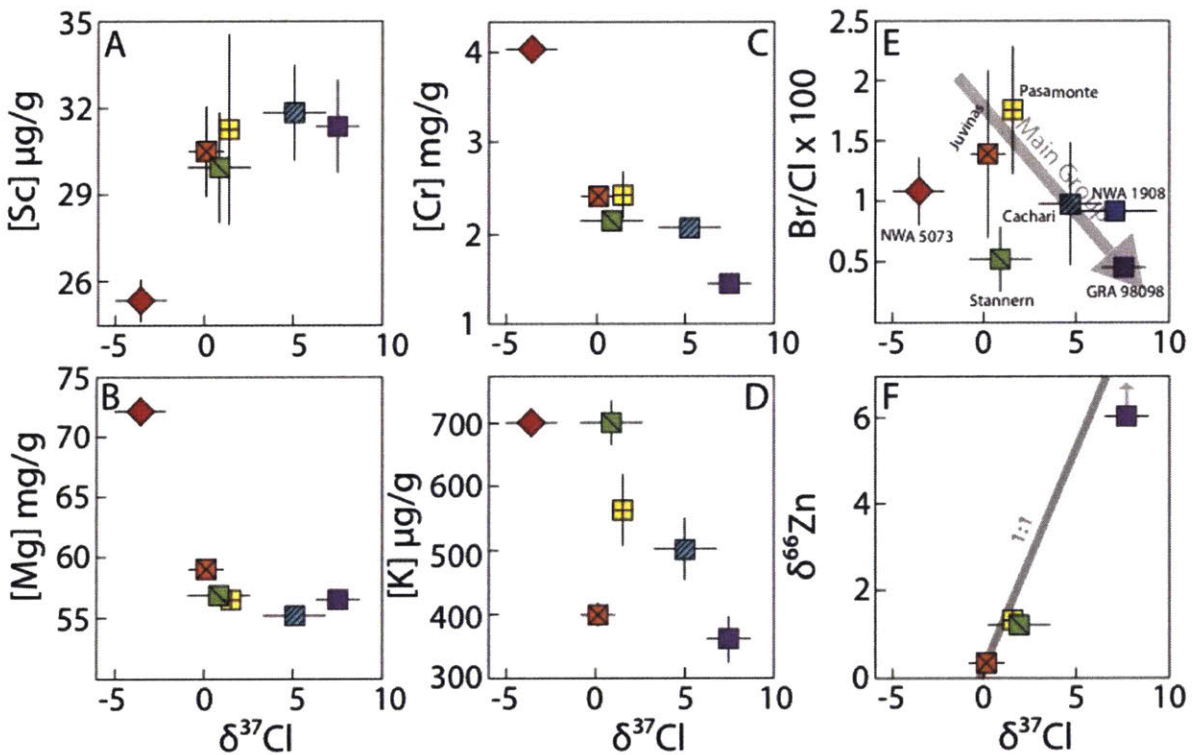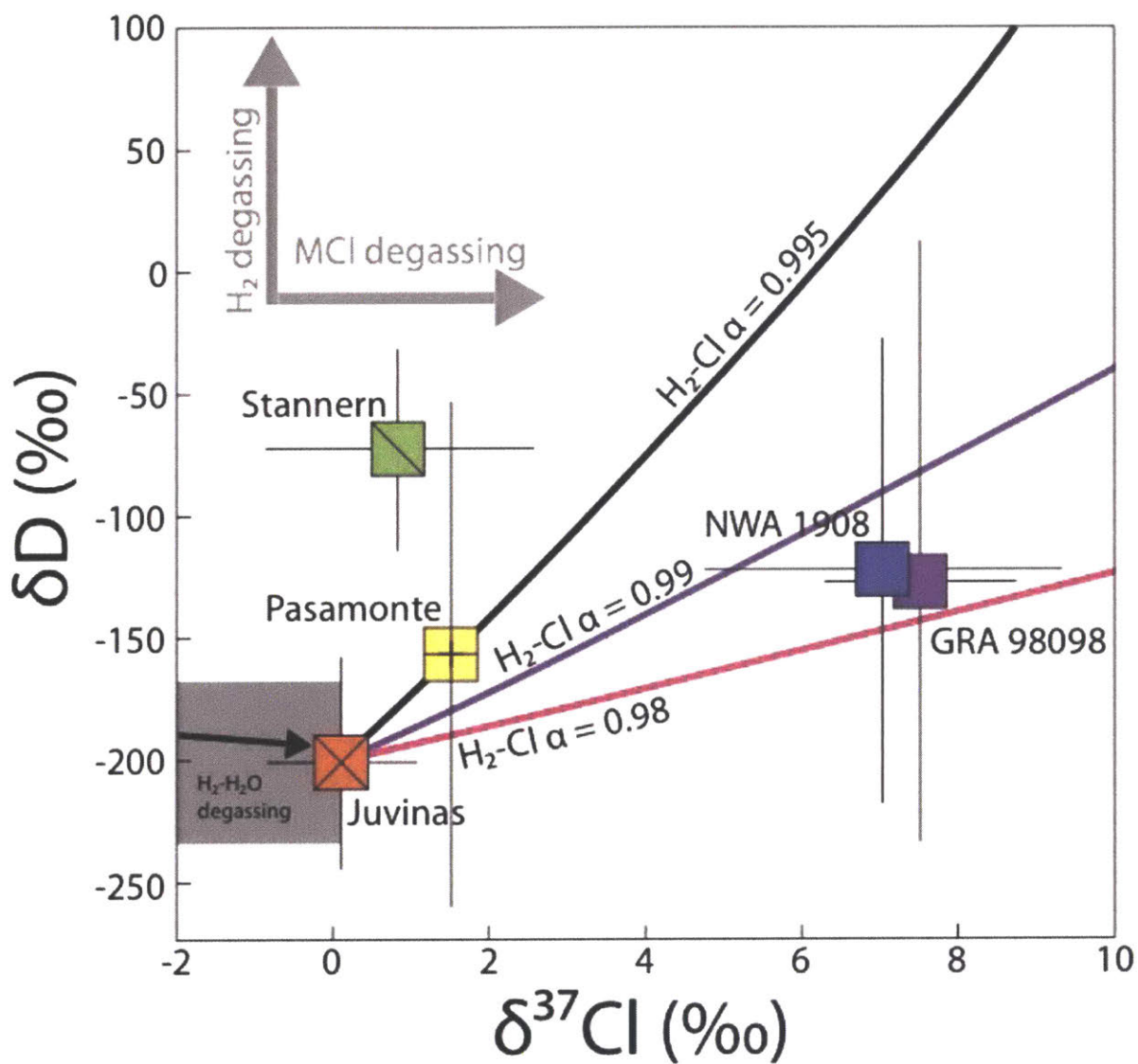| Sample	$\delta^{37}Cl$	2σ	Sample	$\delta^{37}Cl$	2σ	Sample	$\delta^{37}Cl$	2σ
Cachari			**Juvinas**					
Ap3	5.58	0.54	Ap4	-0.05	0.78	**GRA 98098**		
Ap3	6.25	0.54	Ap4	0.36	0.91	Ap2	7.66	0.31
Ap3	6.41	0.50	Ap5	1.27	0.94	Ap2	7.65	0.31
Ap3	5.12	0.44	Ap5	1.06	0.83	Ap3	6.77	0.31
Ap3	4.82	0.48	Ap2	-0.50	1.31	Ap9	8.29	0.31
Ap4	5.09	0.45	Ap2	1.22	0.90	Ap9	8.29	0.31
Ap4	5.06	0.43	Ap2	-0.94	1.22	**Average**	7.73	1.25
Ap4	6.00	0.58	Ap3	-1.18	1.80	**Stannern (AMNH)**		
Ap4	3.56	0.42	**Average**	**0.16**	**1.96**	Ap8	1.48	0.32
Ap5	4.38	0.51	**NWA 5073**			Ap8	1.08	0.35
Ap5	4.84	0.61	Ap7	-3.10	0.54	Ap4	-0.31	1.82
Ap5	6.02	0.56	Ap7	-3.08	0.54	Ap3	1.26	0.32
Ap5	4.99	0.77	Ap6	-3.37	0.56	Ap3	0.15	0.37
Ap1	4.15	0.44	Ap15	-2.94	0.56	Ap1	0.01	0.42
Ap1	6.13	0.44	Ap15	-2.26	0.70	Ap1	1.11	0.31
Ap1	4.90	0.44	Ap3	-3.70	0.51	Ap7	1.08	0.39
Ap1	4.74	0.44	Ap3	-3.22	0.56	**Stannern (WWU)**		
Ap6	4.53	0.41	Ap4	-3.91	0.56	Ap10	2.84	0.38
Ap6	2.35	0.45	Ap4	-3.51	0.53	Ap10	-0.37	0.36
Ap6	2.42	0.41	Ap2	-4.09	0.56	Ap10	2.03	0.36
Average	**4.87**	**2.25**	Ap2	-4.21	0.59	Ap10	2.03	0.34
NWA 1908			Ap10	-3.67	0.42	Ap11	2.32	0.42
Ap16	7.90	1.11	Ap10	-4.38	0.41	Ap11	2.76	0.52
Ap16	6.61	0.92	Ap11	-4.15	0.34	Ap11	3.18	0.34
Ap18	4.97	0.85	AP11	-4.61	0.38	Ap11	3.44	0.46
Ap18	4.82	0.87	Ap11	-4.36	0.35	Ap11	2.67	0.36
Ap18	11.93	0.88	Ap12	-3.61	0.35	Ap11	2.45	0.42
Ap19	8.25	0.77	Ap12	-4.25	0.52	Ap17	2.82	0.40
Ap13	4.77	0.75	Ap12	-3.96	0.36	Ap17	1.74	0.40
Ap13	5.43	0.68	Ap13	-4.14	0.37	Ap17	3.26	0.38
Ap6	7.35	0.73	Ap13	-4.31	0.35	Ap13	0.92	0.36
Ap8	8.94	1.15	Ap13	-3.94	0.33	Ap13	0.15	0.40
Average	**7.10**	**4.57**	Ap13	-3.50	0.34	Ap13	1.93	0.42
Pasamonte			**Average**	**-3.75**	**1.14**	Ap13	2.27	0.44
Ap5	1.70	0.37				**Average**	**1.69**	**2.30**
Ap4	1.41	0.34						
Ap7	1.67	0.39						
Average	**1.60**	**0.32**						

Table 2

Hydrogen isotope composition and water concentration of measured apatite.

Sample	δD	2σ	[H₂O]	2σ	Sample	δD	2σ	[H₂O]	2σ
GRA 98098					NWA 1908				
Ap1	-124	21	2182	45	Ap14	-147	20	2672	55
Ap2	-45	29	988	20	Ap15	-83	20	2505	51
Ap3	-50	67	177	4	Ap16	-78	20	2622	54
Ap4	-65	77	143	3	Ap17	-157	15	9090	186
Ap5	-238	15	7183	147	Ap17	-97	20	2706	55
Ap6	-76	25	1460	30	Ap13	-207	24	1514	31
Ap7	-77	62	250	5	Ap6	-84	20	2975	61
Ap8	-206	27	1353	28					
Ap9	-133	44	417	9					
Ap10	-145	21	2110	43					
wtd avg	**-126**	**139**			wtd avg	**-121**	**97**		

Appendix A

Supplementary materials for Chapter 2

A.1 H incorporation in olivine

The incorporation of H in olivine has been extensively studied e.g., (*21*, *78-80*). Several different H-incorporation mechanisms have been proposed based on FTIR spectra and the total H dissolved in olivine is the sum of several point defect types (*81*). The SIMS technique measures the total concentration of H in a given analysis spot, thus, even if H incorporated in olivine by more than one method, the SIMS technique will still allow us to report total H of a spot analysis of olivine (*81*).

A.2 Volatile element partitioning into olivine

The incorporation of most volatile elements in olivine has been fleetingly studied. The partition coefficient between olivine and melt for H, F and Cl have reliable values (*21*, *22*), but the partition coefficients were determined at much higher pressures compared to the crystallization pressure(s) of angrites. The largest uncertainty in the above partition coefficients is the unknown pressure dependence for volatile element partitioning. The C partition coefficient between olivine and melt is far less certain than the other elements. The partitioning experiments of Rosenthal et al. (*23*) report two partition coefficients between olivine and melt, which differ by 33 %. For this study we took the average of the two partition coefficients. Thus, for C partitioning, our two largest uncertainties are in the partition coefficient itself and the pressure dependence of C partitioning into olivine. While the above uncertainties exist, H, C, and Cl are all highly incompatible in olivine. This high degree of incompatibility means that H, C, Cl, and to a lesser degree, F, will be highly concentrated in the melt compared to olivine. The final partitioning value that we use for H, C, F, and Cl is of minor importance compared to the extreme relative enrichment in volatile elements for angrites.

Appendix B

Supplementary materials for Chapter 3

B.1 Size of the APB

As stated in the main text, the size of the APB is poorly constrained (*68-70*). Here we aim to provide a well-constrained minimum estimate of the APB. Our first minimum estimate use the CO_2 and H_2O saturation models (*124*) calibrated to relatively alkali rich mid-ocean ridge basalt (MORB) compositions (*125*). In contrast angrites are highly depleted in alkali metals, and less polymerized than MORB melts, i.e., angrite melts have a high non-bridging oxygen/tetrahedral coordinated ions (NBO/T) relative to MORB melts (*126, 127*). Melt structure, which is strongly dependent on composition (*126*), can have dramatic effects on element partitioning and the solubility of chemical species, e.g., C solubility increases with decreasing degree of polymerization (*83, 127*). In our H-C-O saturation model we assume melting occurs at the core mantle boundary and vapor saturated in order to determine the minimum size of the APB, melting shallower and vapor under saturated will only increase the size of the calculated APB. Our input values for the pressure calculation (*124*) was used a temperature of 1200 °C, SiO_2 content of 40%, CO_2 content of 4030 µg/g (which equals 1100 µg/g C), and a H_2O content of 1500 µg/g. In order to translate the pressure into a depth we must make assumptions about the physical characteristics of the APB itself. We assumed a homogenous core density of 8000 kg/m^3 and a homogenous mantle density of 3200 kg/m^3 (*85, 86*) We varied the R_{core}/R_{total} for the APB from 0.5-0.1 to gather a large range of potential planetary body internal structures (Figure). Taking into account our input parameters we obtain a pressure of 166 MPa and taking into account our assumptions about the APB we obtain a minimum size of the APB to be $\geq$270 km for a R_{core}/R_{Earth} of 0.4 (Fig. 4). The pressure and APB size calculations are only valid if the CO_2 solubility of an angrite melt is similar to that of MORB, which is likely not the case, and if H_2O and CO_2 are the degassing species. Carbonate (which degasses as CO_2) is more soluble with in depolymerized melts , but more soluble in melts with low SiO_2 contents (*124, 127, 128*). At low oxygen fugacity, such as near and below the iron-wüstite (IW) oxygen buffer, H_2, CH_4, and CO are present in the melt opposed to OH and CO_3 (which degas to H_2O and CO_2) (*80-83*). The

solubility of reduced H-C-O species are far lower than the relatively oxidized C-H-O species and therefore would require more pressure to maintain a high H and C content of an angrite magma; if we did incorporate CH_4 into our model and extrapolate the solubility from experimental data (*82*), then an exceedingly high minimum pressure of ~ 8 GPa is required to retain C. Therefore, if melting on the APB was close to the IW oxygen buffer (*47, 88, 100*), our estimates provide a robust minimum size for the APB. Using the volatile saturation model of Dixon et al (*79*), we obtain a pressure of ~500 MPa. The greater pressure required by the Dixon et al (*79*), is due to the fact that that SiO2 is not factored into the earlier Dixon model. Regardless, our estimate of 166 MPa, is a minimum pressure and the true pressure of melt extraction is likely greater.

Appendix C

Supplementary materials for Chapter 4

C.1 Additional support for partial melting of the eucritic crust

The classification of residual eucrites led to an exploration of the geochemical consequences of

crustal partial melting in the eucritic crust (7). Ref (11) modeled the trace-element pattern of a

low-degree partial melt, which is strikingly similar to the calculated melt composition in

equilibrium with the ARS presented here (Fig. 6a). Subsequently, ref (59) suggested the mixing

of a melt enriched in incompatible elements (the melt composition modeled in the 2007

contribution) to explain trace-element anomalies in diogenites. Finally, ref (60) found

"KREEPy" clasts in howardites, which were small clasts (<1 mm x 1 mm) rich in K, REE, P,

and Y. This KREEPy melt could have mixed with a diogenitic melt to create the variance in

trace-elements seen in diogenites (59). This KREEPy melt could be similar to the melt in

equilibrium with the ARS.

Additional support for partial melting of the eucritic crust comes in the form of Fe-rich olivine

veins (19), which could be evidence of low degree melting of the eucritic crust; and from trace

element systematics in zircons, which suggest that partial melting took place in eucrites (18); and

finally, an enrichment in ^{56}Fe in Stannern trend eucrites suggests that Stannern trend eucrites

were probably impregnated with a melt containing isotopically heavy Fe (12), which could be

the result of preferential melting of ilmenite, a common mesostasis phase.

C.2 Other possible petrogenetic models

C.2.1 Other possible origins of the ophitic coarse-grained domain, equigranular fine-grained domain, and ARS

The low abundance of REE in apatite and high abundances of REE in plagioclase and pyroxene were interpreted as products of solid-state or fluid-mediated diffusion on the mm to cm scale (20). However, this interpretation ignored the low abundance of incompatible elements in the bulk rock. In contrast, ref (7) argued that the low abundance of bulk-rock REE was caused by the extraction of a low-degree partial melt rich in incompatible elements. Experiments show that extraction of 1–2 % partial melt is mechanically feasible and that such a melt would be highly enriched in P, Ti, and REE (13). The experiments further demonstrate that extraction of such low-degree melts would not alter the ophitic texture of the restitic rock. This confirms that low-degree melt extraction can be pervasive without affecting the texture.

Strong thermal gradients in rocks and magmas may also cause chemical fractionation by Soret diffusion, which causes certain elements to diffuse towards a heat source, while others diffuse away from it (61). In the case of EET 90020 the heat source was adjacent to the equigranular fine-grained domain (hot end), whereas the ophitic coarse-grained domain represents the cold end. Experimental studies using terrestrial basalts show that P and the REE invariably migrate towards the cold end during Soret diffusion whereas Rb migrates to the hot end (62). Additionally, if Soret diffusion were to explain the ARS, F and H would have to have migrated towards the cold end. The apatite enrichment would be expected at the cold end of the system, i.e., close to the ophitic coarse-grained domain, which is where it is observed. Hence, Soret

202

diffusion cannot be ruled out as the process from which the textures seen in EET 90020

originated, but Soret diffusion is an unlikely possibility because (1) Soret diffusion is

inconsistent with Rb data, and (2) the thermal gradient required for Soret diffusion to operate is

very high (~50-80°C/mm) (61). The thermal diffusivity of the eucrite crust is on the order of 1

mm^2/s (63). Thus, a thermal gradient along the distance of the diameter of the main mass of EET

90020 (~4 cm) would fully relax within 1–2 hours. This is orders of magnitude faster than any

chemical diffusion in minerals or melts. With a relaxed thermal gradient, Soret diffusion would

cease. The only possibility for Soret diffusion to explain the geochemical and petrologic

observations is strong cooling in the cold end of the system and heating of the hot end of the

system to maintain the thermal gradient. This is also unlikely because the eucrite crust is thought

to be relative hot for a long duration (64), eliminating the possibility of cooling the system from

the surrounding rocks, but leaves the possibly of the surface of the asteroid to allow for cooling.

Fluid-moderated diffusion of the REE and other trace–elements is also unlikely. We see no

petrologic evidence of fluid flow in EET 90020. Some evidence one would expect to observe in

such a case would be quartz, tridymite, or apatite veining, as seen in Serra de Magé, Graves

Nunataks (GRA) 98098, and Juvinas (21, 65), or abundant Fe-rich metasomatic veining, as seen

in Pasamonte (66). No such evidence of fluid flow is present in EET90020, and fluid-moderated

diffusion is, therefore, unlikely.

Mittlefehldt and Lindstrom (20) suggested solid-state diffusion as a possible mechanism for the

heterogeneous distribution of apatite and merrillite in EET 90020. Solid-state diffusion has been

shown to highly alter the mineral chemistry of equilibrated eucrites (67, 68). However, this

mechanism is only viable where textural annealing has taken places, because diffusion of the

REE is extremely slow, such that it would take ~1.5 x 10^9 years to diffuse REE 1 cm through

plagioclase (based on D(REE, Pl) = 10-21 m2/s; *69*). Hence, if EET 90020 was completely

texturally annealed without different domains, solid-state diffusion could be considered to

explain the observed anomalies. However, because the ophitic fine-grained domain has

preserved a magmatic texture, extended periods of heating can be excluded and diffusion of the

REE is not plausible. Solid-state diffusion also cannot explain the high modal abundance of

apatite in the ARS, because diffusion of P is even slower or at least as slow as that of the REE

(e.g., *70*). In any case, diffusion models do not address the low bulk rock abundance of

incompatible elements in EET 90020 (Fig. 6b; *16*).

Appendix D

Supplementary materials for Chapter 5

D.1 Supplementary tables

Table S1. Hydrogen isotope composition of pyroxene and apatite in unequilibrated eucrites.

pyroxene	dD	1sd
Y-74450	-133	24
Y-74450	-127	34
Apatite		
Y-82210	-157	10
Y-82210	-225	7
Y-77450	-73	18
Y-77450	-239	61
Y-75011	-146	12

Appendix E

Supplementary materials for Chapter 6

E.1 Materials and Methods

E1.1 Water and D/H measurements of eucritic apatites

The studied samples were selected to represent a wide range of thermal annealing, and apatite textures. Additionally, other apatites in the same samples had been previously analyzed for Cl and F abundances by electron microprobe (Juvinas, Pasamonte, Stannern, and PCA 91078) and Cachari was selected because it is a rock chip that has never been exposed to epoxy. Juvinas, Pasamonte, Stannern, and PCA 91078 are epoxy mounted thin sections and Cachari is a rock chip that was mounted in indium metal prior to analysis. All samples were polished to 0.3μm quality with diamond paste, cleaned with distilled water, dried in a vacuum oven for over a week at 50°C, then transferred into a vacuum chamber (ca. 8×10^{-5} Pa). Immediately prior to the measurement, the sample was taken out of the chamber and gold coated to a thickness of ca. 120 nm. After gold coating, the samples were placed in a different vacuum chamber (ca. 8×10^{-7} Pa) attached to the ion probe for at least 24 hours prior to analysis.

We used a Cameca 1280 ion microprobe to measure H_2O contents and D/H in apatites and a modified analytical setup of Gaetani et al (29) was employed. A 1 nA Cs^+ beam was used to produce a 10 x 10 μm raster. We used a field aperture to decrease the measured area to 6 x 6 μm, which reduces crater edge effects and analytical background. To further eliminate the analytical background we used electronic gating, which reduces the measured area to ca. 4 x 4 μm (Fig. S1 & S2). Mass resolving power (MRP) was 9872 (m/Δm at 10 %;), sufficient to separate ^{17}O from $^{16}O^1H$ (MRP needed – 4713) and $^{17}O^1H$ from $^{16}O^2H$ (MRP needed – 8743). We measured masses ^{17}O, $^{16}O^1H$, and $^{16}O^2H$ to ensure optimal mass spectrometer tuning over a small mass range, minimal magnet movement, and sequential measurement of signals for H and D. Counting times were 3 s for ^{17}O, 5 s for $^{16}O^1H$ and 15 s for $^{16}O^2H$ and were collected for 70 cycles. Typical counting rates in our reference material Eagle County apatite, which contains 3700 μg/g of

water, were ca. 90,000 counts per second (cps) for $^{16}O^1H$ and 20 cps for $^{16}O^2H$ and counting rates for anhydrous blanks were ca. 6500 cps for $^{16}O^1H$ and 2 cps for $^{16}O^2H$. Analyses of standards and unknowns were corrected for this background.

Background correction consisted of subtracting the proportion of background from the measured D/H ratio. We did this by measuring the water concentration and D/H of dry plagioclase adjacent to each apatite analysis and used this as our background. The background did not vary substantially over the course of this study and had a composition of $\delta D \sim +900$. The corrected D/H was calculated by manipulating the following equation:

$$D/H_{measured} = D/H_{apatite} * f_{apatite} + D/H_{contamination} * f_{contamination}$$

Where f_x is the fraction of D/H signal coming from apatite or contamination. This equation yields:

$$D/H_{apatite} = [D/H_{measured} - (D/H_{contamination} * f_{contamination})] * 1/f_{apatite}$$

Using this equation, we subtracted the background D/H from the standards and unknowns and propagated the error according to the uncertainties of all four variables. We used 2 reference apatites with known D/H values to establish a calibration curve for D/H for correction of instrumental mass fractionation. After background correction, the reference materials produced a calibration curve consistent with the expected values. We also analyzed a third reference apatite (Russia, or ap018) with lower water contents (2000 μg/g), which yielded $\delta D = -74 \pm 54$ ‰ (2σ), which is in good agreement with the accepted value for this reference material of $\delta D = -90$ ± 14 ‰ (30). Background correction on eucrite apatites resulted in corrections on the raw data of between -138 and -17 ‰ for the low-OH and high-OH apatites, respectively.

There are several possible terrestrial sources of contamination for analyses of hydrogen in apatite by ion probe: (1) Water on the surface of the apatite, (2) diffusion of terrestrial water into apatite, (3) epoxy. Below we discuss these three potential sources of H contamination. (1) Surface contamination was significantly reduced by the following measures: all samples were kept at

50 °C in a vacuum oven for a week prior to analysis. After this, samples were gold coated and kept under high vacuum for at least an additional 24 h. Additionally, presputtering took place for 10 minutes prior to each ion probe analysis. Surface contamination can be identified in ion probe analyses by the occurrence of decreasing count rates during a measurement as the surface contamination is partially removed by the sputtering process over the course of the 70 analytical cycles. We did not observe this effect in any of our samples. Thus, we are confident that water contamination on the analyzed surfaces during measurement was insignificant. (2) Diffusion is discussed in detail below, but at the temperatures of terrestrial contamination (<200°C) water diffusion in apatite is far too slow for diffusive exchange between a terrestrial contaminant and apatite to occur even over timescales of the entire history of the Solar System. (3) Epoxy could potentially be a major contaminant, because it contains ca. 14 wt% H_2O. During each analysis an image of the electron multiplier was carefully watched to ensure that no heterogeneities in the spatial distribution of H were present, which could result from small pockets of epoxy in voids or cracks in the original thin section. Furthermore, if significant non-apatite water was present during an apatite measurement then the apatites would become "non-stoichiometric", whereby the sum of F, Cl and H_2O added up to more than the mineral accommodates in its structure ($Ca_5(PO_4)_3(OH,F,Cl)$). In order to assess the stoichiometry of the apatites analyzed for D/H in this study were, we determined F and Cl concentrations by electron microprobe in representative apatite grains from the same sample and used these concentrations to predict the water content of the investigated apatite (Table S1) (4). This approach is justified by a very restricted variation of Cl and F contents of apatite within individual eucrite samples (4). All samples presented in this study exhibited measured water contents that are within error of the stoichoimetric prediction based on the measured F and Cl contents. Lastly, sample Cachari, which has D/H indistinguishable from the remaining sample set, was mounted in indium and had no contact with epoxy. We are, therefore, confident that water contamination from epoxy or any other non-apatite source was insignificant. The D/H values determined by ion probe therefore must represent the composition of the eucrite apatite at the time of formation of the rocks on their parent body in the young Solar System.

E1.2 Electron probe microanalysis of eucrite apatites

209

Apatite grains from PCA 91078 were analyzed using the JEOL 8200 electron microprobe at the University of New Mexico. An accelerating voltage of 15 kV and a nominal probe current of 25 nA was used during each analysis. We analyzed for the elements Si, Ce, Y, Fe, Mn, Mg, Ca, Na, P, F, and Cl. Fluorine was analyzed using a light-element LDE1 detector crystal, and Cl was analyzed using a PET detector crystal. Calcium, P, and F were standardized using a natural fluorapatite from India. Chlorine and Na were standardized using a scapolite crystal. Cerium and Y were standardized using their respective endmember phosphates. Silicon and Mg were standardized using Taylor Olivine (from San Carlos, AZ), Mn was standardized using Spessertine garnet, and a chromite crystal was used as an Fe standard. In order to reduce or eliminate electron beam damage, we used a 10 μm spot for standardization and 1 to 10 μm diameter defocused beam for analysis of apatite grains in all the eucrite samples.

Stormer et al. (*31*) documented that F and Cl X-ray count rates change with time during electron microprobe analysis of apatite, although McCubbin et al., (*32*) showed that this problem does not apply to Cl. In addition to obtaining inaccurate F concentrations, this problem also causes difficulties in estimating structural OH by stoichiometry. Consequently, we monitored the fluorine X-ray counts in real time with the JEOL software. Some analyses did display variable F X-ray count rates, which is why some of the analyses have more than their stoichiometric fill of F + Cl (Table S1).

E.2 Supplementary Text

E.2.1 Sample Description

Apatite in Pasamonte, Stannern, and PCA 91078 are found in late-stage melt pockets associated with troilite, tridymite, and ulvöspinel (Fig. S1). The apatites in these samples are anhedral to subhedral and range in size from 1–50μm in the long direction. We analyzed the largest apatites in the sections. Pasamonte has an anomalous $\Delta^{17}O$, which may reflect it is from a different parent body (*33*). If Pasamonte is from a different eucrite-like parent body, then this study samples two distinct asteroidal bodies. Cachari has a young Ar-Ar age and is shocked eucrite with impact

melt veins throughout the meteorite (*34*), apatite in Cachari occurs between large pyroxene and plagioclase grains and is generally less <40μm in the long direction (Fig. S2). Apatite in Juvinas occurs in late-stage melt pockets (subhedral, 1-40μm), and within veins (euhedral to subhedral, 5-30μm; Fig. S1). The veins in Juvinas could be a result of incongruent melting or fluid mediated crystallization (*35*). All of the above-described textures of apatite indicate that apatite crystallized late, i.e., near the eucrite magma solidus (*36*).

E.2.2 Petrogenesis of Eucrites

Eucrites are melts that could have been formed from partial melting of an olivine-rich mantle (*19, 37*) or they could be direct melts from a magma ocean (*38-40*). Basaltic eucrites can be separated into two geochemical trends, the main group and the Stannern trend (*45*). The Stannern trend is invariant in differentiation indices, like Sc, and elevated in incompatible elements (e.g., Ti, La, Hf) (*46*). The main group is thought to represent a fractional crystallization sequence, while the Stannern trend is thought to represent crustal contamination (*46*). We selected eucrites from both geochemical trends. Some eucrites, such as cumulate eucrites crystallized deeper as orthocumulates, but none of these eucrites were measured here. We measured basaltic eucrites with varying degrees of chemical equilibration, but with no textural equilibration (*47*). The varying degree of chemical equilibrium does not correlate with the water-F-Cl content of apatite (*4*), nor does it correlate with the δD.

E.2.3 Possible factors that affect the H isotopic composition of apatite

In the following section we evaluate to what degree the H isotopic composition of the eucrite apatite is representative of the H isotopic composition of the eucrite parent body. We discuss the possible factors that could affect the D/H ratio of igneous apatite during magmatic and high temperature processes which include (1) degassing, (2) isotope fractionation between apatite and melt, and contamination/assimilation of exogenous D and H either (3) implantation of solar wind or (4) produced by cosmic ray spallation reactions.

211

(1) The dominant H–bearing species that would degas from eucrite magmas is expected to be H_2, because of the low oxygen fugacity within Vesta. The same is true for lunar magmas (*7, 48*). This speciation of H would greatly affect the D/H ratio of the magma during degassing of an H-bearing gas, because of the large relative mass difference between H_2 with and without deuterium. Degassing could take place either during accretion of the eucrite parent body or during magmatic degassing from the eucrite parental magma. Any degassing taking place prior to apatite crystallization would not be directly detectable with D/H in apatite. However, if it did occur, our measured D/H ratio would represent a maximum δD value for the source of water in the eucrite parent body, because any degassing at low oxygen fugacity would only be able to shift the δD in a positive direction, i.e., it would lead to an enrichment of deuterium in the degassed residuum. Magmatic degassing both prior to and during apatite crystallization, however, is unlikely to have been significant because we observed nearly invariant apatite δD values in our entire sample set, which display a wide range of water contents (apatite water abundances vary by a factor of ~6; Fig. 1) in samples with vastly different thermal histories.

If the D/H ratio of Vesta would have been significantly lower at initial accretion the asteroid evolved to its current H (N and C) isotope ratio through accretion-assisted planetary-scale degassing, this would also have increased the oxygen fugacity in the mantle of Vesta (*23*). Given the relatively reduced nature of the Vestan mantle (*48*), H degassing during accretion is less likely, but cannot, at present, be ruled out. However, as argued in the main text, Vesta cannot have accreted from material with a Solar H, N and C isotope composition.

(2) The isotopic fractionation between apatite and melt has not been quantified experimentally. However, experimentally determined H isotope fractionation between silicate melt and amphibole (another hydrous mineral) at 700 °C is only ca. 21 ‰ (*22*). The H isotope fractionation between apatite and melt can be expected to be of a similar value (*49*). We therefore conclude that equilibrium fractionation between apatite and melt is most likely insignificant at the level of analytical precision (ca. ±50 ‰).

(3) Solar wind (δD = ca. -1000 ‰; (*50*)) penetrates up to 100s of nm into a surface and contamination could have affected the D/H ratio of apatite if there was exchange of OH in apatite

with implanted solar wind. There are two different processes that could cause solar wind H to affect eucrite apatite grains. The first would be assimilation of solar wind H by the apatite-forming magma as the magma ascends through a solar-wind-rich regolith region on the eucrite parent body. Conversely, apatite could have been directly exposed to the solar wind once the eucrite reached the surface of 4-Vesta or during travel through space. This is highly unlikely because the studied samples are polished thin sections and chips, the polishing process removes 100s of nm, which should be sufficient to eliminate solar wind H. Also, there is no correlation between D/H ratio and exposure age of the analyzed eucrites, which range from 7–36 Ma (*51*), implying that recent solar-wind interaction with apatite was insignificant. Hence, we conclude that solar wind contributions to eucrite apatite are insignificant.

(4) Cosmic rays penetrate the upper ~3m of regolith and the resulting spallation reactions predominantly produce D, which causes elevated δD. Because the production of D is a function of exposure time and cosmic ray flux, the total amount of D produced can be calculated and removed if both these parameters are known. The effect of the spallation production is greater at lower water concentrations because D is primarily produced from target nuclei of O, Fe, Si, Al and Mg (*52*) none of which vary significantly as a function of water content in apatite. Unfortunately, the cosmic ray flux for 4-Vesta is unknown, but might be expected to be lower than the Moon due to its greater distance from the Sun. Here we use the lunar cosmic ray flux (*3, 53, 54*) to infer the magnitude of the eucrite spallation corrections. The exposure ages of eucrites are significantly younger than those of most lunar samples, and the apatites measured are all water rich (>650 μg/g water). Previous studies have found that lunar apatites require insignificant spallation corrections at water contents in excess of 500 μg/g (*53, 54*). With the younger exposure ages and higher water contents in eucrite apatites, we therefore conclude that spallation corrections are negligible in eucrite apatites.

It is also a possibility that metamorphic re-equilibration of OH in apatite with implanted H or spallation D occurred at a later time when the eucrites had come into contact with regolith material most likely through impact-related processing on the parent body. We have analyzed eucrites with a varying degree of thermal annealing, and they show the same apatite D/H ratio,

demonstrating that solar wind-derived H and spallation produced D were not incorporated in eucrite apatite.

We conclude that degassing, equilibrium isotope fractionation between apatite and melt and extraterrestrial contamination has not significantly affected the apatite D/H ratio with respect to the parental magma of the eucrites and the bulk composition of their parent body. Hence, the D/H ratio determined for eucrite apatite samples correspond closely to the D/H ratio of the eucrite parent body.

E.2.4 Diffusion in apatite

Diffusion of H can drastically change the H isotopes in apatite, obscuring the primordial H-isotope signature. Water can diffuse in or out of apatite, depending what the sources or sinks of water is. Below we discuss the timescales and temperatures needed for diffusion of H in apatite to effect eucritic apatite. Diffusion in apatite is highly anisotropic (*55*). We discuss diffusion along the crystallographic C-axis of apatite, which is the direction of fastest diffusion. This provides the most conservative estimate of the possible effects of post-crystallization diffusion in apatite. Diffusivity of H in apatite (at P = 0.1 MPa) was experimentally determined by Brennan (*55*) to be

where D is the diffusion coefficient of F, Cl and OH parallel to the C axis of apatite, R is the gas constant in kJ mol^{-1} K^{-1} and T is the temperature in kelvins. To estimate the length scale at which apatite may have been affected by diffusion, the relationship:

$$x \approx (Dt)^{1/2}$$

can be used, where x is distance in meters and t is time in seconds. The ambient equatorial temperature on Vesta is ca. 0 °C during daytime and ca. -100 °C at night, although data is

preliminary at this point (*56*). Assuming a temperature of 0 °C and a time of 4.56 Ga, OH can diffuse over a distance of $\sim 3 \times 10^{-21}$ m, which is insignificant compared to the size of an apatite grain (~ 1-50×10^{-6} m) and thus water will not diffuse at ambient temperatures. At high temperature, OH can diffuse much faster. For example, a 600 °C metamorphic event, which would have occurred for at least 1 million years would have allowed for OH in apatites to diffusively equilibrate over the distance of the typical size of the grains. However, even if such an event took place, the observed uniformity of the measured D/H in eucrites among samples that represent different metamorphic grades strongly argue against the possibility that re-equilibration of the D/H ratios of apatite under metamorphic substantially affected the analyzed samples.

E.2.5 Degassing model

If degassing took place on Vesta, the H isotopes should fractionate and change from the primordial H isotope composition that Vesta accreted with. We can evaluate the possible impact of degassing on the D/H ratio of Vesta by using degassing models. We consider Rayleigh fractionation during evaporation of various volatile molecules in the early Solar System. The model can determine if the determined D/H ratio could have evolved by degassing from another known source material (such as comets or a protosolar composition) using Rayleigh fractionation:

$$R = R_0 * F^{(\alpha - 1)}$$

where R is the isotope ratio in the degassed residue, R_0 is the initial isotope ratio, F is the fraction of the element that remains in the residue and α is the isotope fractionation factor. For ideal gasses evaporating in a vacuum the fractionation factor is the square root of the ratio of the two isotope masses. We show that under reducing conditions it is not likely for Vesta to have acceded significant cometary material (Fig. 2). Degassing of H and N ensures that the residue (Vesta) becomes more enriched in the heavy isotopes. Regardless of H isotopes, N isotopes cannot evolve from a cometary value to that of Vesta.

If we consider the protosolar nebula (Jupiter) as source of volatiles then H, C, and N isotopes would have to evolve to extreme values and would still not converge to a Vesta-like signature. If 99.99 % of all of Vesta's H is lost through the degassing of H_2 then the H isotopes could evolve from a protosolar composition to a Vesta-/Earth-/Moon-like composition. With 99.99 % degassing, the N isotopes would not evolve far from a protosolar value. Degassing of 99.9999 % of N as NH_4 is required to evolve the N isotopes from a protosolar value to eucritic values. The C isotope composition of the protosun is slightly lighter than eucrites (50); with just 99.99% degassing the protosun would evolve from -60‰ to +42‰ assuming degassing of CO_2, fractionation would be more if degassing CO (+103‰) or CH_4 (+238‰). It is highly unlikely that the degassing process that caused 99.9999% of N to degas failed to cause extreme C isotope fractionation. In addition, the pre-degassing abundances of N and H on Vesta would have been unrealistically high especially when it is considered that most models support relatively dry accretion within the inner Solar System (57).

An alternative and viable source of appreciable volatiles in the inner Solar System are carbonaceous chondrites. Carbonaceous chondrites have a very similar C and N isotopic composition as eucrites and their H isotopic compositions overlap those of eucrites. The spread in H isotopic compositions of carbonaceous chondrites could be due to degassing, as H isotopes fractionate readily during degassing of H_2.

E.2.6 The source of water for the Moon and Mars

Mars and the Moon have been extensively studied for hydrogen isotopes to determine the source of water for these planetary bodies, e.g. (*14, 24, 53, 54, 64-68*). Mars generally has high δD, ~1000s of ‰, but Martian some samples have terrestrial-like D/H (*14, 68, 69*). It could be possible that Mars accreted with the terrestrial-like D/H, but given the complexity and variation of D/H in Martian meteorites, we think it is currently premature to infer a specific isotopic composition for Mars. Secondary alteration, like spallation, solar wind, magmatic assimilation of crustal material, interaction with fractionated surface water, or recycling of water into the mantle

are possible mechanisms that could alter the D/H of Martian magmas and apatites towards both positive and negative values. Because of these complications more work needs to be done to confirm if Mars in fact did accrete with Earth-like water, or if the Earth-like D/H represent secondary processes.

The hydrogen isotope composition of the Moon is highly variable in the positive and negative direction (53). The spread in hydrogen isotopes is likely due to several processes acting at the same time, such as (1) spallation, (2) solar wind implantation, (3) input from comet material, and (4) magmatic degassing. These processes could happen in-situ (1-2), or any of them could happen during magmatic ascent through contaminated regolith. We discussed most of these four processes above, and suggest these could be the causes of the large range of measured D/H for the Moon.

E.3 Supporting information used in figures

E.3.1 Data for hydrogen and nitrogen isotopes

Hydrogen isotopes of water ice and OH- molecules and N isotopes of CN molecules were measured in comets by spectroscopy (70-72). Hydrogen isotopes from Mars are mostly ion probe measurements of hydrous and nominally anhydrous phases (14, 64, 66-68, 73), but also includes sequential step heating (69). Hydrogen isotopes for Moon are measured by ion probe of glasses and minerals (3, 24, 53). Hydrogen and N isotopes for chondrites are bulk sequential step heating measurements (12, 74). Nitrogen isotopes from Moon, Mars, and Vesta are bulk values from sequential step heating and modeling (25, 75, 76). Error bars for comets are variation in data collected, see (70) for details.

217

E.3.2 Data for carbon isotopes

Carbon isotopes from comets are measured from CN molecules. Carbon isotopes from rocks (including Earth, Moon, Mars, Vesta, and chondrites) are measured by bulk sequential heating. Data from refs (*50, 71, 77-81*).
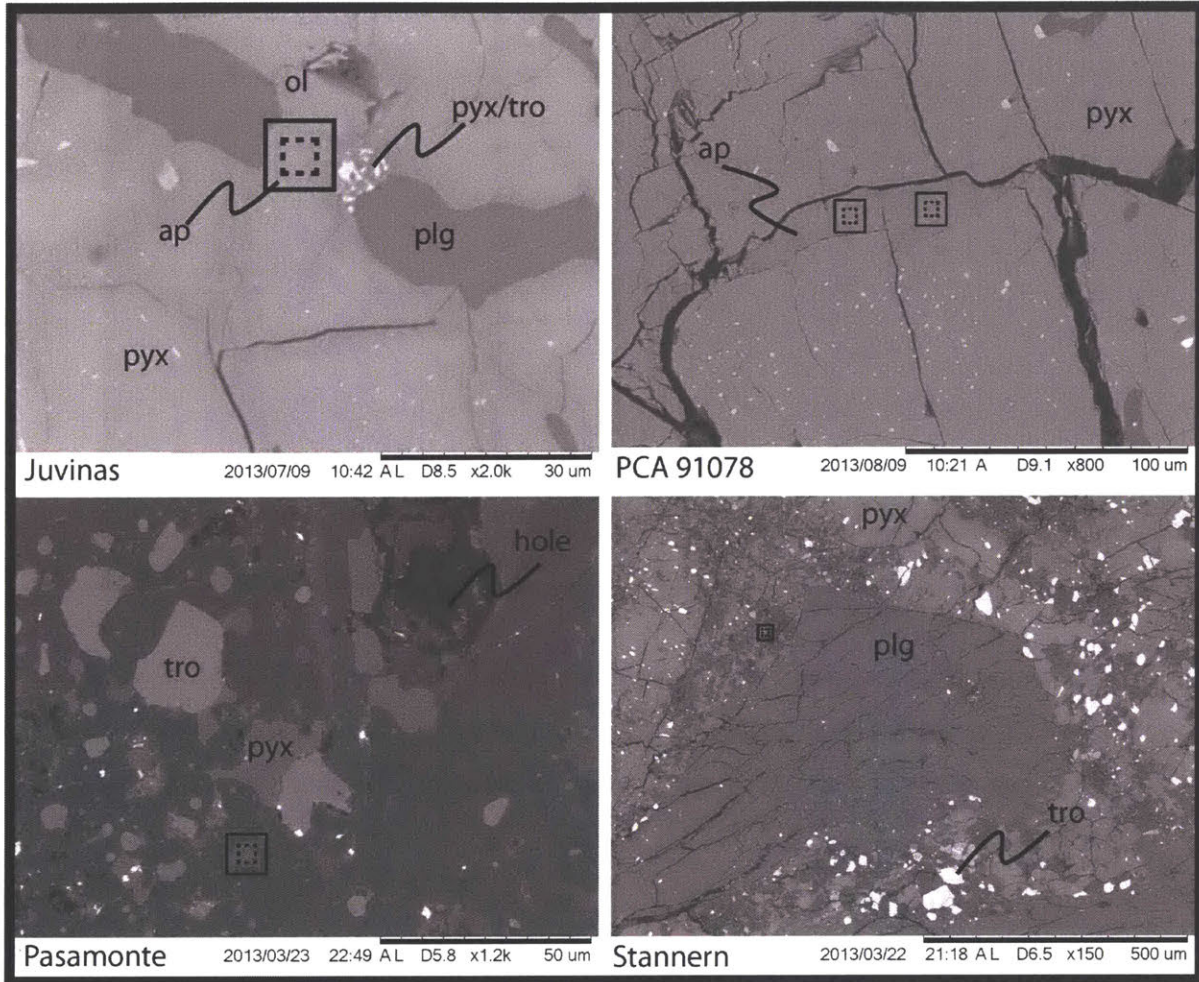
E.4 Figures and Tables

Fig. S1.

Figure S1. Backscatter electron images of selected analyzed apatites. Black boxes represent raster size of ion beam and dashed black boxes represent area measured by SIMS after electronic gate and physical (field) aperture.
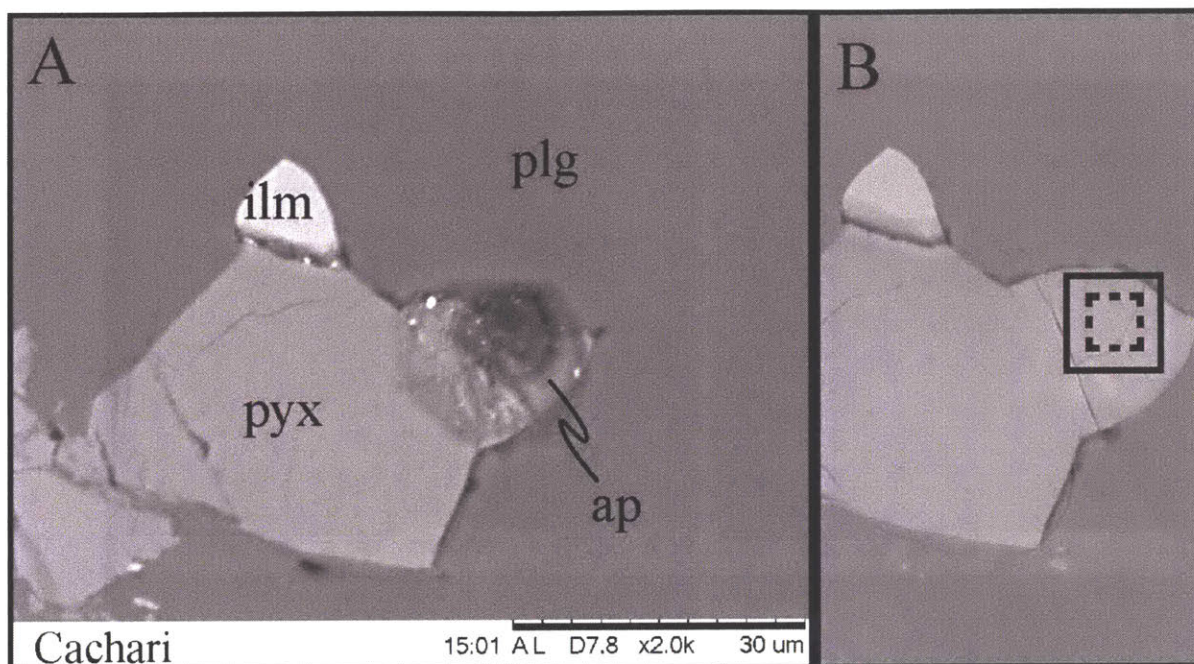
Figure S2. Backscatter electron images of Cachari after SIMS (A) and before SIMS (B). Scale is the same for both images. (B) Solid black box is raster area and dashed box is analyzed area after electronic gating and physical aperture. Note Cachari is mounted in indium meaning that no epoxy is present.

Table S1. Electron probe microanalysis of PCA91078. Fluorine counts were variable through time, which causes an overestimation of F content in apatite. *APFU = atoms per formula unit.

ap#	ap1	ap4	ap3	ap4	ap6	ap8	ap9	ap10	ap11	ap12	ap13	ap14	ap15	ap16	ap17
P_2O_5	42.47	41.85	42.07	40.94	41.81	41.88	42.13	42.51	42.48	42.14	42.01	42.45	42.51	42.69	40.82
SiO_2	0.00	0.00	0.01	0.00	0.00	0.00	0.00	0.00	0.00	0.00	0.00	0.00	0.00	0.00	0.73
Ce_2O_3	0.03	0.03	0.00	0.00	0.01	0.08	0.06	0.05	0.04	0.03	0.01	0.04	0.01	0.00	0.00
Y_2O_3	0.01	0.00	0.00	0.02	0.01	0.00	0.03	0.01	0.00	0.00	0.02	0.02	0.03	0.01	0.02
FeO	0.67	0.63	0.39	0.03	0.74	0.74	0.51	0.52	0.61	0.58	0.61	0.59	0.58	0.77	1.19
MnO	0.05	0.06	0.06	0.01	0.01	0.07	0.06	0.07	0.05	0.07	0.04	0.06	0.04	0.03	0.06
MgO	0.02	0.03	0.04	0.03	0.05	0.02	0.01	0.03	0.05	0.04	0.01	0.01	0.03	0.02	0.07
CaO	55.25	55.15	56.28	55.43	55.91	56.31	55.93	55.58	55.24	55.46	56.12	55.78	55.81	55.51	55.52
Na_2O	0.00	0.05	0.01	0.00	0.00	0.00	0.00	0.02	0.00	0.00	0.00	0.00	0.03	0.00	0.01
F*	4.17	4.23	3.35	4.26	3.98	4.24	3.31	4.43	4.19	4.56	3.59	4.22	3.82	3.73	4.56
Cl	0.01	0.00	0.09	0.07	0.08	0.07	0.11	0.13	0.10	0.09	0.07	0.09	0.10	0.08	0.12
S	0.02	0.03	0.00	0.00	0.05	0.04	0.01	0.01	0.01	0.00	0.01	0.01	0.01	0.01	0.01
F + Cl = -O	1.76	1.80	1.43	1.81	1.72	1.82	1.42	1.90	1.79	1.94	1.54	1.80	1.63	1.59	1.95
Total	100.91	100.26	100.86	98.97	100.93	101.64	100.72	101.45	100.97	101.02	100.95	101.44	101.30	101.26	101.16
APFU*															
P	3.00	2.99	2.97	2.96	2.97	2.96	2.98	3.00	3.00	2.99	2.97	2.99	2.99	3.00	2.91
Si	0.00	0.00	0.00	0.00	0.00	0.00	0.00	0.00	0.00	0.00	0.00	0.00	0.00	0.00	0.06
Ce	0.00	0.00	0.00	0.00	0.00	0.00	0.00	0.00	0.00	0.00	0.00	0.00	0.00	0.00	0.00
Y	0.00	0.00	0.00	0.00	0.00	0.00	0.00	0.00	0.00	0.00	0.00	0.00	0.00	0.00	0.00
Fe	0.05	0.04	0.03	0.00	0.05	0.05	0.04	0.04	0.04	0.04	0.04	0.04	0.04	0.05	0.08
Mg	0.00	0.00	0.00	0.00	0.01	0.00	0.00	0.00	0.01	0.00	0.00	0.00	0.00	0.00	0.01
Ca	4.94	4.98	5.03	5.08	5.02	5.04	5.01	4.96	4.94	4.98	5.02	4.97	4.97	4.94	5.01
Na	0.00	0.01	0.00	0.00	0.00	0.00	0.00	0.00	0.00	0.00	0.00	0.00	0.00	0.00	0.00
F	1.10	1.13	0.88	1.15	1.06	1.12	0.87	1.17	1.11	1.21	0.95	1.11	1.00	0.98	1.21
Cl	0.00	0.00	0.01	0.01	0.01	0.01	0.02	0.02	0.01	0.01	0.01	0.01	0.01	0.01	0.02
S	0.00	0.00	0.00	0.00	0.01	0.01	0.00	0.00	0.00	0.00	0.00	0.00	0.00	0.00	0.00
Total	7.99	8.02	8.04	8.05	8.05	8.05	8.03	8.00	7.99	8.01	8.04	8.01	8.01	8.00	8.07
F-Cl-OH	1.10	1.13	0.90	1.16	1.07	1.14	0.89	1.19	1.12	1.22	0.96	1.13	1.02	0.99	1.23
Missing component	-0.10	-0.13	0.10	-0.16	-0.07	-0.14	0.11	-0.19	-0.12	-0.22	0.04	-0.13	-0.02	0.01	-0.23

Appendix F

Supplementary materials for Chapter 7

F.1 Supplementary materials

Bulk rock data were selected from large aliquots from established labs in order to gain a representative analysis of each eucrite. Data from: Cachari (*56*), GRA 98098 (*16*), Juvinas (*10*), NWA 5073 (*18*), Pasamonte (*57*), and Stannern (*10*). Fluorine abundances were measured mostly by INAA and were taken from (*58-61*).

Figure S1: Crude estimate of the H_2O content of Vesta, in comparison of the K/U of Earth, Moon, and Vesta. Here, we obtain a maximum plausible H_2O content by rounding to 1000 µg/g H_2O, whereas apatite hygrometry likely provides a minimum.
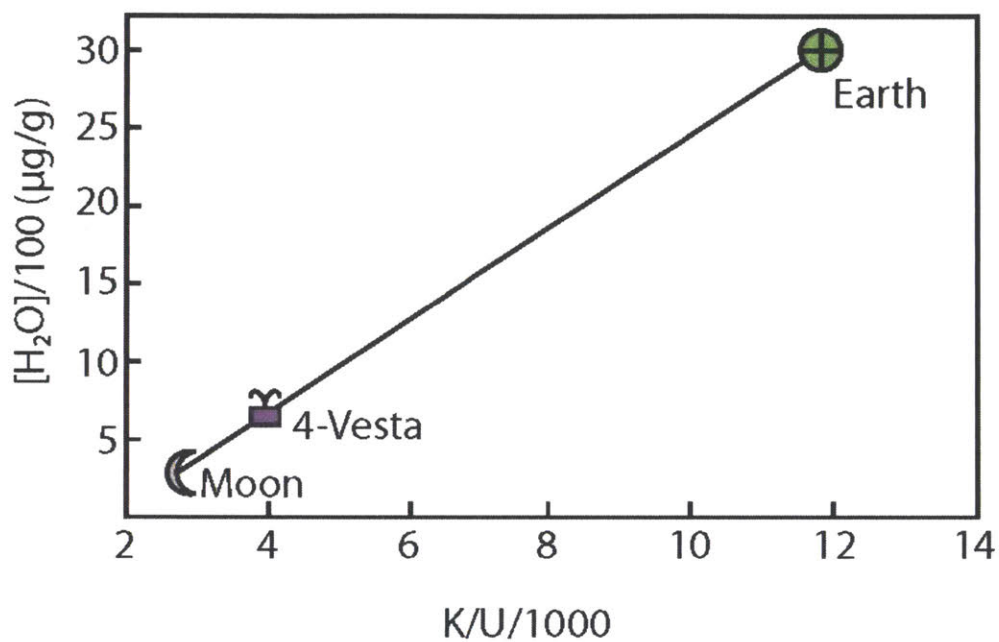
Figure S2: $\delta^{37}Cl$ vs. fraction of Cl remaining. Different alpha values are for various amounts of metal chlorides, e.g., NaCl, FeCl$_2$, ZnCl$_2$. Figure modified from Sharp et al. (*22*)
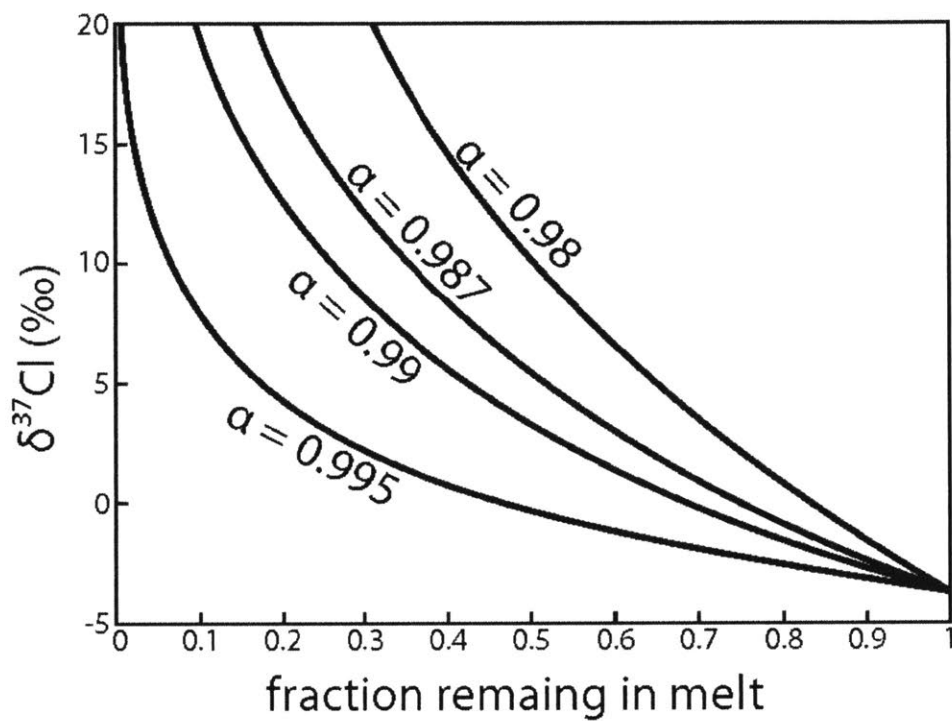
Figure S3: Degassing model for various H_2:H_2O ratios assuming that H_2 and H_2O degas at the same rate. If H_2 degases more rapidly then heavier isotope compositions are expected. Note when H_2:H_2O is low, the residual is isotopically light with 5:95, corresponding to IW-1 with 200 µg/g H.